Hydrogen Transfer in Hydrogen Bonded Solid State Materials

Marc Schmidtmann

Thesis submitted to the University of Glasgow
for the degree of Doctor of Philosophy

Department of Chemistry

submitted April 2008

Abstract

The investigation of strongly hydrogen bonded solid state materials and the hydrogen transfer processes therein are the subject of the present work. Strong hydrogen bonds are found whenever the hydrogen bonded species compete for the hydrogen atom, and are thereby on the verge of showing hydrogen transfer. Consequently, the strongly hydrogen bonded solid state materials investigated in this work are synthesised by co-crystallising chemical compounds which have a similar affinity for the proton.

The molecular complexes of isonicotinamide with oxalic acid crystallise in two hydrogenous polymorphs and, upon substituting the acidic hydrogen for deuterium, in two deuterated polymorphs, neither being isostructural to the hydrogenous forms. This phenomenon is known as isotopomeric polymorphism and is rarely observed in molecular materials. The four polymorphic forms are found to exhibit different degrees of hydron transfer. The hydrogenous forms show strong hydrogen bonding between the acid and the pyridine base. The nature of these strong hydrogen bonds is characterised by combined X-ray charge density and single crystal neutron diffraction studies and found to be covalent in nature. The covalent hydroxyl bonds are considerably elongated, to an extent that in one polymorph the hydrogen atom occupies a near central position in the strong hydrogen bond. The structural work has been complemented by ab-initio computational studies, using the plane wave and localised atomic orbital methods, to evaluate the nature and the dynamics of the strong hydrogen bonds, and to establish an energy scale for polymorphism. It is found that the atomic orbital calculations yield results in good agreement with the experiment, while the plane wave calculations fail to reproduce the experimental hydrogen bond geometries.

A strong electronic delocalisation is observed in the difference electron densities of strong acid – pyridine base hydrogen bonds. The major contribution to the delocalisation is found to originate from the nitrogen lone pair density which in this type of strong hydrogen bond is found to be observed to low experimental resolutions in standard X-ray diffraction experiments. As a consequence, such hydrogen bonds are susceptible to misinterpretation, and can be misinterpreted as hydrogen bonds with a disordered hydrogen, altering the descriptive character of materials significantly from being neutral to being ionic. It is shown that a careful examination of the difference electron densities, with the knowledge of the presence of the nitrogen lone pair density, allows a reasonably accurate determination of nuclear hydrogen positions from X-ray diffraction experiments alone.

The hydrogen transfer behaviour in a series of strongly hydrogen bonded materials has been studied. For the molecular complexes of pentachlorophenol with the series of dimethylpyridines, a correlation is established between the dissociation constants determined in solution and the degree of hydrogen transfer from phenol to the pyridine bases in the solid state. The influence of additional strong and weak hydrogen bonding interactions in the vicinity of the strong hydrogen bonds on the hydrogen transfer behaviour is rationalised. Similar studies have been carried out on the molecular complexes of oxalic acid and fumaric acid with the dimethylpyridines, and on the molecular complexes of pentachlorophenol with 1,4-diazabicyclo[2.2.2]octane. The design approach leading to these materials and the hydrogen transfer behaviour observed in these materials is critically analysed.

Declaration

The thesis has been written in accordance with the University and all work presented is original and performed by the author unless otherwise stated and referenced in the text.

Marc Schmidtmann

Acknowledgements

I'd like to thank Professor Chick C Wilson for supervising my PhD project. He has been supportive and highly motivating at all times in his unique inspiring style. I'd also like to thank Dr. Louis J Farrugia who in his function as my second supervisor served as a steady source of knowledge invaluable to this work.

I thank the original office crew Martin and Susie for helping me to settle in and making my life in Glasgow as enjoyable as it was and continues to be. They both deserve extra credits, Martin for being inimitably entertaining and Susie for being wonderfully pink. I thank Derek, the mastermind of physics and page long equations; this work, as it stands today, would not have been possible without him. I thank all past and present members of the Wilson group. Special mentions go to Duncan, the real Scot who is ginger, likes sheep and kills pints by the dozen. Extra special mentions go to Lynne, the understanding and endlessly helpful Welsh, who I thank for being the Lynne she is.

I'd like to thank Professor Achim Müller and in particular Hartmut Bögge. It seems unlikely that without these two people I would have had the opportunity to submit a PhD thesis. I'd also like to thank all members of the AC1 (the group of Prof. Müller), with whom I spent many enjoyable years in Bielefeld. One of them happened to be Lee Cronin who lured me over to Glasgow for which I would like to thank him.

I thank my parents for the obvious and for their support during my whole life essentially. I thank my sister for everything she is and for giving birth to three adorable nephews, who I'd like to thank as well in hope they let me play with their Wii. There are many more people to thank, close friends, friends, colleagues, family, and distant family, but then this is not the Academy Awards, and I actually did not win anything. So I conclude with thanking you, the reader, who, if not interested by profession, will be a close friend and surely should have deserved a special mention – lazy me.

TABLE OF CONTENTS

1. INTRODUCTION TO HYDROGEN BONDING

1.1. GENERAL CONSIDERATIONS

Since the phenomenon of *Hydrogen Bonding* started to emerge slowly in the scientific literature some 80-100 years ago,[1, 2] a vast amount of information on hydrogen bonds (HBs) has been gathered and documented. It is impossible to give a comprehensive account on all aspects of this topic here. The reader is therefore referred to some text books[3, 4, 5] while the author mentions the most basic concepts only, before giving a slightly more detailed overview on strong HBs in the solid state.

The HB is undoubtedly the most important intermolecular interaction. It can be found in an abundance of materials, from inorganic minerals to biologically active macromolecules. When present, HBs largely determine the structure, and hence also the physical properties and (bio)chemical reactivity of a wide range of materials. This huge impact is amusingly summed up by G. A. Jeffrey in the quote from the back cover of his "*An Introduction to Hydrogen Bonding*" where he states that

"*Without them, all wooden structures would collapse, cement would crumble, oceans would vaporize, and all living things would disintegrate into inanimate matter.*"[3]

This leaves us with the question of what exactly is a HB. The answer is not unequivocal because first, there simply is not just the *one* type of HB. The involved forces can have very weak *van der Waals* and dispersive to very strong covalent natures, with HB interaction energies ranging in a continuous way from 0.2 to 40 kcal/mol. Second, along with the development of analytical methods, the definition of the HB has continuously altered and evolved over the course of history. New aspects were, and still are, constantly added to the concept of hydrogen bonding, like weak C–H$\cdots\pi$ HBs, dihydrogen bonds, and inverse HBs to mention a few examples. Depending on the system under study and the analytical method applied, HB definitions may differ quite dramatically. These range from geometrical considerations to a list of numerical criteria which have to be fulfilled in the topological analysis of the electron density.[6] Two general definitions shall be quoted here, an early definition by Pauling and a more recent one by Steiner:

"*Under certain conditions an atom of hydrogen is attracted by rather strong forces to two atoms, instead of only one, so that it may be considered to be acting as a bond between them.*"[7]

"*An X–H$\cdots$A interaction is called a 'hydrogen bond', if 1. it constitutes a local bond, and 2. X–H acts as a proton donor to A.*"[8]

Throughout this work the classification of HBs into "weak", "moderate", and "strong" HBs will be used, as suggested by Jeffrey[3] and adapted by Steiner[8]. Criteria for this classification are listed in Table 1-1; they provide a rough guide and are not meant to be applied in too strict a manner. The continuous energy landscape of HBs with equally continuously varying energy contributions, means that a classification of a particular HB might not always be unambiguous. It depends to a certain extent on the point of view and the analytical method used, as we will see later.

Table 1-1: Classification of HBs into strong, moderate and weak. Table from reference [8].

	Strong	Moderate	Weak
interaction type	covalent	electrostatic	electrostatic/dispersive
bond lengths H···A / Å	1.2 – 1.5	1.5 – 2.2	> 2.2
lengthening of X–H / Å	0.08 – 0.25	0.02 – 0.08	< 0.02
X–H v H···A	X–H ≈ H···A	X–H < H···A	X–H << H···A
X···A / Å	2.2 – 2.5	2.5 – 3.2	3.2
directionality	strong	moderate	weak
bond angles / °	170 – 180	> 130	> 90
bond energy / kJ·mol^{-1}	> 60	15 – 60	< 15
relative IR shift $\Delta\nu_{XH}$ / cm^{-1}	25 %	10 – 25 %	< 10 %
^{1}H downfield shift / ppm	14 – 22	< 14	

Most HBs can be denoted in the general form X–H···A, where X–H is the H donor group and A the H acceptor (Scheme 1-1). In the classical electrostatic HB model X is sufficiently more electronegative than H and the driving force behind the HB formation is the $X^{\delta-}$–$H^{\delta+}$ dipole which is directed towards the nucleophile A (typically a lone pair of atoms like O, N, and S). The electrostatic contribution to the HB formation is undisputed and largely accounts for the most common, i.e. moderately strong, class of HBs, as found in water/ice ($HO^{\delta-}$–$H^{\delta+}$···$^{\delta-}OH_2$), between the strands of polypeptide chains in proteins or between nucleic acid base pairs in DNA. The rather long range interaction of a HB means that a particular HB can have more than one H acceptor and, vice versa, more than one H donor for one particular H acceptor. Such HBs are termed *bifurcated*, *trifurcated*, etc. HBs can be *homo*nuclear, that is X equals A, or *hetero*nuclear where X is different from A.

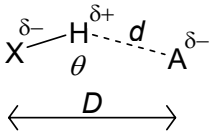

Scheme 1-1: General hydrogen bonding scheme, d = H···A, D = X···A, θ = ∠XHA

Structural evidence for the existence of a HB is a reasonably short H···A distance; historically the cut-off distance was set to the sum of the van der Waals radii of H and A, with the argument that the attractive forces (if present) exerted by the HB should overcome the repulsive forces between the atoms. The strength of a HB is structurally well defined by its bond length H···A, or alternatively, if an accurate H position is not available (see 2.1 *Diffraction Techniques*) by the donor to acceptor distance X···A. To a first approximation, the strength of a HB increases with decreasing HB distance. HB formation also leads to an elongation of the covalent X–H bond, which gets more pronounced with increasing HB strength. Spectroscopically this is reflected by a shift towards longer wavelengths for the X–H stretching frequencies in IR and a downfield shift of the ^{1}H NMR signal due to the deshielded H atom. Further evidence for hydrogen bonding can be obtained by microwave spectroscopy on gas phase adducts, which yields information like rotational constants, distances between centres of mass, dipole moments, and much more.

Weak HBs were initially identified by spectroscopic studies on systems in solution.[9] Following the electrostatic HB model, there are principally two ways to intrinsically weaken a HB, that is to reduce the dipole on the H donor side or to reduce the

nucleophilicity on the acceptor side of a HB, as for instance in C–H···A and X–H···π HBs respectively. It is also possible to "weaken" both the H donor and the H acceptor as in C–H···π HBs. However, the electrostatic contribution to such *very* weak HBs becomes very low and dispersion forces start to dominate the HB energy. Consequently the distinction between hydrogen bonding and pure van der Waals interaction becomes increasingly difficult. Whether weak HBs form in the solid state was discussed a long time before clear structural evidence by extensive analysis of known crystal structures was accumulated in favour of their existence.[10, 11] The common problem of locating weak HBs in crystal structures is that the crystal packing is usually dominated by stronger intermolecular interactions i.e. moderate or strong HBs. Therefore it is difficult to determine whether weak HBs actually contribute to the process of crystal packing or whether they are enforced by the structure. However, there are studies which document the structure determining ability of weak HBs in the absence of stronger intermolecular interactions.[12, 13] For a fully comprehensive work on weak HBs see reference [4].

1.2. STRONG HYDROGEN BONDS

Strong HBs are of particular interest because they show some unique physical and chemical properties. They are characterised by a large redshift of the X–H stretching frequency until for very strong HBs they disappear completely and are replaced by a broad absorption region in the low frequency range (absorption continuum),[14, 15] and a far downfield shift of the ^{1}H NMR signal. As mentioned before, the H···A and X···A distances become continually shortened with increasing HB strength, accompanied by an elongation of the X–H bond length. This leads to a shift of the H atom towards the centre of the HB until it is no longer possible to differentiate between H acceptor and donor, which is why strong HBs are better denoted in the more general form X–H···Y. However, not all short HBs are necessarily strong. This is especially true for *intra*molecular HBs which are often forced to be short by steric restrictions. To a lesser degree such forced short contacts are observed also for *inter*molecular HBs in the solid state, by so called "crystal field" effects. The crystal field effect in this context is vaguely defined as the sum of all intermolecular interactions and is difficult to quantify and to separate into its different energy contributions. Another indication for a strong HB is a high directionality of the X–H donor towards the acceptor, which is expressed in a near linear X–H–Y bond angle close to 180º.

So under which conditions do strong HBs form? The obvious case is when additional full or partial electric charges increase the electrostatic potential. Prime examples can be found in the hydrogendifluoride anion $[F–H–F]^-$ (with notation of partial charges $[F^{\delta-}–H^{\delta+}–F^{\delta-}]^-$) and in $[H_2O–H–OH_2]^+$. In a more general approach, the necessary condition for the formation of a strong HB is a similar proton affinity (PA) of the hydrogen bonded molecules or functional groups in case of intramolecular hydrogen bonding. In aqueous solution, proton affinities are expressed in pK_a values and strong HBs are accordingly formed for sufficiently small $\Delta pK_a = pK_a(\text{acceptor}) - pK_a(\text{donor})$. Competition for the H then leads to equilibrium structures of the type X··H··Y or its resonance structures X–H···Y $\leftrightarrow$ X···H–Y where the H atom is equally shared between donor and acceptor. In the solid state, pK_a values are obviously no longer strictly applicable but can still provide some guidance in the design of materials showing strong hydrogen bonding. The above

examples of $[HF_2]^-$ and $[H_5O_2]^+$ readily fulfil PA/pK_a matching criterion because they are acid – conjugated base systems.

As mentioned previously, strong HBs are of at least partial covalent nature. Evidence that the covalent contribution to the HB energy becomes more and more pronounced with increasing HB strength, was found by analysis of the experimental charge density in strong H···Y bonds.[16, 17] Gilli and Gilli have "unified" the electrostatic and covalent HB models into the "*Electrostatic-Covalent H-Bond Model*" (ECHBM).[18] They proposed that essentially all strong HBs could be assigned to one of four different types, three for the *homo*nuclear case, with one additional for the *hetero*nuclear:

- negative charge assisted HB ((–)CAHB), for example in $[F–H–F]^-$
- positive charge assisted HB ((+)CAHB), in $[H_2O–H–OH_2]^+$
- resonance assisted HB (RAHB), in carboxylic acid dimers or β-diketone enols
- positive/negative charge assisted HB or charge transfer HB ((±)CAHB), in acid – base systems $O–H\cdots N \leftrightarrow O^-\cdots H–N^+$

Resonance assisted HBs (RAHBs) are peculiar because a transfer of the proton from donor to acceptor is not accompanied by a charge transfer but by the adoption of another resonance form. This can be best illustrated with the resonance forms of a β-diketone enol and the carboxylic acid dimer as examples for intramolecular and intermolecular RAHBs respectively (Scheme 1-2).

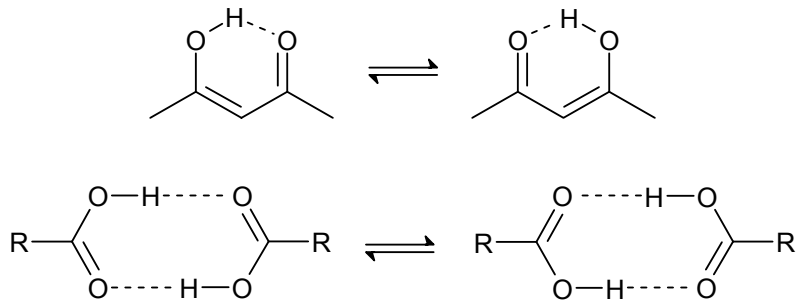

Scheme 1-2: Resonance forms of RAHBs, (top) intramolecular RAHB in a β-diketone enol, (bottom) intermolecular RAHB in the carboxylic acid dimer.

A very important aspect of strong HBs is the shape of the potential energy curve (PEC)[a] for H transfer along the HB path. It has long been recognised that a reduced distance between the hydrogen bonded atoms leads to a very broad and flat energy profile with little or no energy barrier for H transfer.[19] Typical examples of such potential energy curves are shown in Figure 1-1. In a common (moderate) HB the potential shows two distinct minima (one low and one high energy), which are well separated by a high energy barrier. The H atom almost exclusively occupies the low energy minimum. In a shortened HB the minima become less separated, more similar in energy, and the energy barrier becomes small. A HB showing such a double well potential with a low barrier for H transfer is therefore called *low barrier HB* (LBHB). Further shortening of the HB results ultimately in a single well potential and the H occupies a position close to the centre in an X–H–Y HB, hence the term *single well HB* (SWHB). In homoconjugated systems (X = Y)

[a] Potential Energy Curve (PEC) as the one dimensional equivalent to the Potential Energy Surface (PES)

the SWHB can be symmetrical and the H is located in a position equidistant to X and Y; in heteroconjugated systems (X ≠ Y) the SWHB is usually asymmetrical and the H is located off centre.

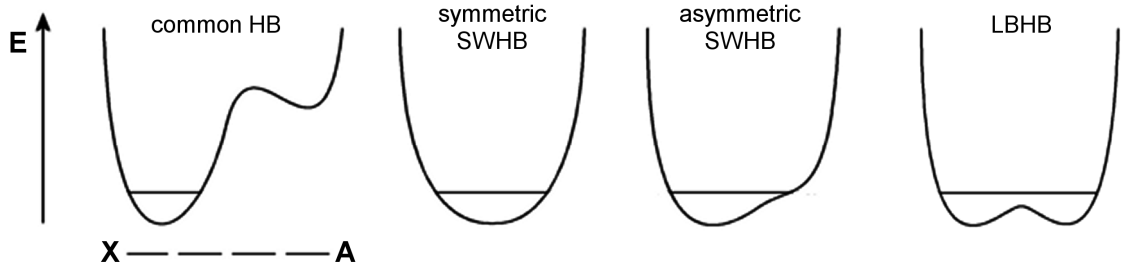

Figure 1-1: Comparison of potential energy curves (schematic) in common (moderate) and strong HBs, X = hydrogen donor, A = hydrogen acceptor.

At this point it is worth mentioning the hydrogen/deuterium (H/D) isotope effects. These are caused by the fact that the vibrational contribution to the zero point energy is mass dependent, i.e. smaller for an X–D bond compared to that of an X–H. Deuterium effectively occupies a lower energy state than hydrogen as indicated in Figure 1-2. The *intrinsic* H/D isotope effect leads to a shortening of the covalent X–H/D bond upon deuteration, a lengthening of the H/D···Y, and also a lengthening of the heteroatom distance X···Y. This isotope effect on the HB geometry is commonly known as the Ubbelohde effect,[20] and observed only in HBs with an anharmonic potential (in general, HB potentials are anharmonic, and the anharmonicity increases with HB strength); in HBs with an harmonic potential (symmetrical SWHBs, for example) no H/D isotope effect is observed. The *equilibrium* H/D isotope effect concerns equilibrium structures like O–H/D···N ↔ O^{-}···H/D–N^{+}, for which H/D populations can differ quite significantly (see Figure 1-2, right).

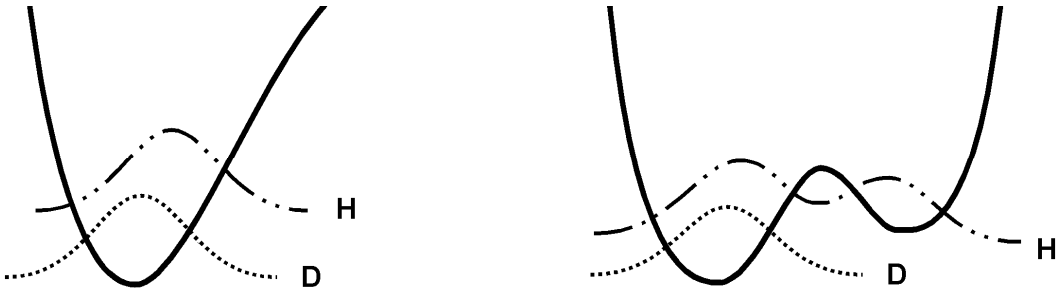

Figure 1-2: Schematic illustration of the H/D isotope effects, and probability density distributions for H/D in a moderate HB (left) and a LBHB (right).

Since all strong HB potentials show relatively low energy differences over a long range of the H pathway (usually of the order of a few kJ/mol or less), an exact statement about the shape of the potential energy curve is difficult. Energy calculations depend on the model used and assumptions made, and results might be misleading. Unless there is clear evidence for one type or the other the more general term *short, strong HB* (SSHB) is used from hereon when strong HBs are addressed, as proposed by Gerlt and Gassman.[21] The important point is that all SSHBs show broad and flat energy profiles for H transfer, that

these are susceptible to small energy changes, and that they can therefore facilitate H transfer processes.

1.3. HYDROGEN TRANSFER IN THE SOLID STATE

H transfer processes in the solid state are exemplary of structure – property relationships of hydrogen bonded systems. In hydrogen bonded materials many properties like solubility, melting point, colour and polarisation are determined by the characteristics of the HBs. On a side note, polymorphic materials (materials which crystallise in two or more different forms) often have different properties, and in case of hydrogen bonded polymorphs they almost always feature a variation in the HB pattern which determines the property change.

In materials which exhibit SSHBs H transfer can be induced comparatively easily by changing the external conditions such as temperature, pressure, electric field, etc. in a non destructive and reversible way. Two H transfer mechanisms for the solid state will be introduced here:

- H disorder – H order transition in LBHBs
- H migration in SSHBs

Well known examples for the first mechanism are carboxylic acids. They often form strongly hydrogen bonded dimers, characterised by LBHB profiles and H atoms disordered over the two energy minima. In solution or in the gas phase the HB configurations are evenly distributed between the two energetically equivalent tautomeric forms shown in Scheme 1-2, bottom. In the solid state, however, this distribution is not necessarily equal as the energy landscape is perturbed by the crystal field and one conformation can be favoured over the other. In case of the benzoic acid dimers, the H occupations are temperature dependent, and show a gradual H disorder – H order transition upon cooling.[22] Such a H disorder – H order transition can also lead to a polarisation of the material and result in a ferroelectric phase transition in which case the transition temperature is called the *Curie temperature*, T_c. In potassium dihydrogen phosphate, KH_2PO_4, as an example for an inorganic ferroelectric, the ordering of the H atoms is accompanied by a change from the paraelectric phase (space group I-42d) to the ferroelectric phase (space group Fdd2) at T_c = 123 K.[23] An example for an organic ferroelectric has been recently documented for the molecular complex of iodanilic acid with 5,5'-dimethyl-2,2'-bipyridine where H ordering results in a phase transition from $P\bar{1}$ to P1 at T_c = 268 K.[24] The Curie temperature in such ferroelectrics is strongly pressure dependent, and is found to decrease with increasing pressure (shorter HB distance leads to a lower energy barrier and consequently to a lower T_c). In the ferroelectric phase, of course, H transfer can be induced by applying an external electric field.

Thermally induced H migration in SSHBs has been observed in some hydrogen bonded complexes by variable temperature (VT) single crystal neutron diffraction experiments. For example, in the adduct of pentachlorophenol with 4-methylpyridine the H atom migrates from a position closer to the O site to one closer to the N site in a strong heteronuclear HB upon cooling (Figure 1-3).[25] Formally there is a high T molecular phase with O–H···N configuration and a low T ionic phase with $O^{-}\cdots H{-}N^{+}$ configuration. A similar H behaviour has been found for a few other materials,[26, 27, 28] but this

phenomenon is rare and the absolute shift of the time averaged H nuclear position hardly exceeds 0.1 Å. It can be reasoned that the H migration is caused by small but significant changes in the potential energy surface of asymmetric SWHBs upon variation of T, but also that the probability density distribution changes with T in a broad and flat but static potential.

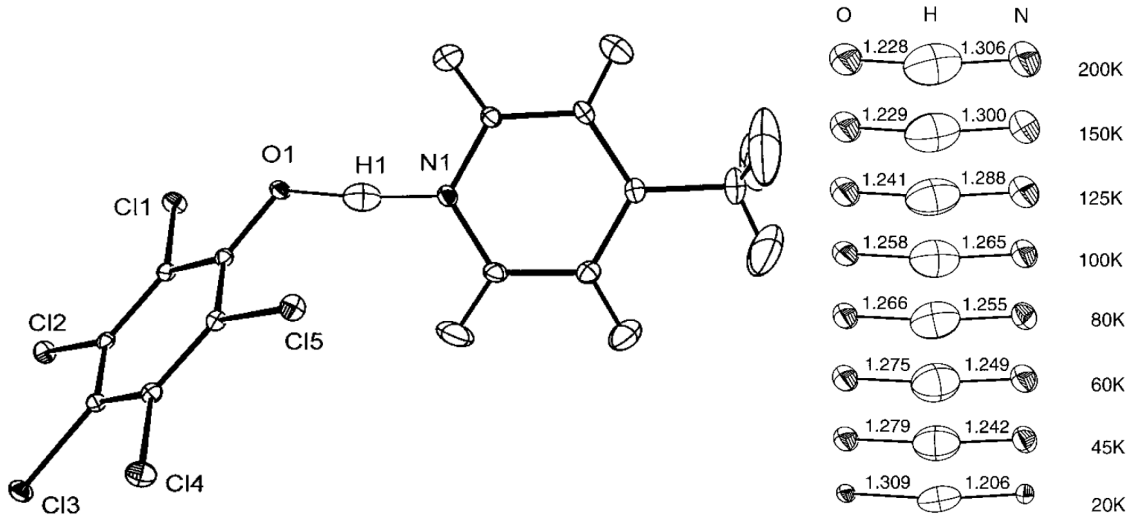

Figure 1-3: (Left) neutron structure of pentachlorophenol with 4-methylpyridine at 100 K, ellipsoids at 30 % probability level. (Right) the O1··H1··N1 HB with varying T, ellipsoids at 50 % probability level. Figures from reference [25].

From the material design or crystal engineering point of view, H transfer can be induced by changing the chemistry at the (strong) HB, or its lattice environment. For solid state materials this implies the study of chemically or structurally different compounds. H transfer processes of this nature include:

- H transfer upon chemically induced change of donor/acceptor properties
- H transfer upon isotopic substitution
- H transfer upon formation of polymorphs

The first approach includes all chemical reactions which influence the H donor and acceptor properties, i.e. their proton affinities, in such a way that they promote a H transfer reaction. This is of course rather archetypical of solution rather than of solid state chemistry. However, such H transfer processes also play a very important role in enzymatic reactions which arguably have at least partial solid state character. There is also an ongoing debate to whether SSHBs are involved in certain enzymatic reactions by stabilising intermediates and facilitating H transfer, see for example the review by Bachovchin and the references therein.[29] In the world of crystal engineering this approach is used, if in a slightly different way, to design new crystalline materials and to fine tune existing ones, and has been explored in the current work to investigate the relationship of ΔpK_a values and H transfer in Chapter 5 *Design of Strongly Hydrogen Bonded Materials*.

The possibility of H transfer upon isotopic substitution has been indicated when describing H/D isotope effects. The deuterated analogues of ferroelectrics of the H ordering type are characterised by a considerably increased T_c because the D atoms occupy

lower energy states in the LBHBs and consequently become "ordered" at higher temperatures. To revert back to the example of KH_2PO_4, this effect is expressed in a phase transition temperature rise by nearly 100 K on deuteration to T_c = 220 K for KD_2PO_4. In this context, a rather uncommon H/D isotope effect has recently been shown by Madsen *et al* for benzoylacetone.[30] Here, H in a strong intramolecular LBHB has enough thermal energy to shuttle across the barrier and occupy a position delocalised around the centre of the HB, while D in the isostructural material "orders" with equal distributions into the two LBHB minima (Figure 1-4). Aside from changing the HB configuration, isotopic H/D substitution can lead to a change in the hydron migration behaviour as observed, for example, for pyridine-3,5-dicarboxylic acid.[28] It can furthermore lead to the occurrence of "isotopomeric polymorphism" (formation of a polymorph upon isotopic substitution) as observed in the adduct of pentachlorophenol with 4-methylpyridine.[31, 32]

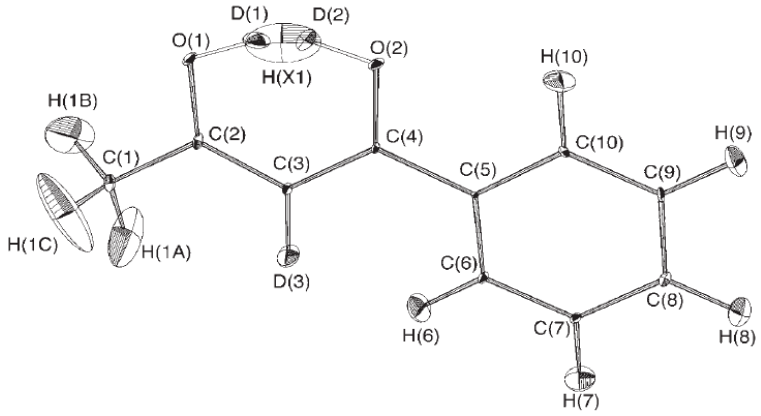

Figure 1-4: H/D isotope effect in the LBHB in benzoylacetone, ellipsoid plot of the deuterated form with overlaid H parameters of the hydrogenous form (both neutron data). Figure from reference [30]

Isotopomeric polymorphism ties in with the observation of H transfer upon formation of polymorphs. Polymorphs can be composed of, for example, neutral species in one form and ionic in the other, even if the same chemical groups are involved in the hydrogen bonding scheme. See for example reference [33] and the pronounced variation in the H transfer behaviour in the polymorphic complexes discussed in Chapter 3 *Molecular Complexes of Isonicotinamide with Oxalic Acid*.

2. METHODS

The characterisation of hydrogen bonded solid state materials, and in general of hydrogenous materials, strongly depends on the knowledge of accurate atomic hydrogen positions. The most important and versatile tool to determine the structure of crystalline solids, X-ray diffraction, while enormously powerful, often fails to locate the hydrogen atoms due to the weak interaction of hydrogen with X-rays. The alternative, neutron diffraction, solves this problem but is for reasons of sample size requirements, the limited access to neutron sources, etc not applicable on a regular basis and often not applicable at all. Another alternative, quantum mechanical calculations, is increasingly employed to add information not accessible to the experiment. This chapter is intended to give an overview of the experimental and theoretical methods applied in this work. A comprehensive account of these is available in relevant textbooks and in the literature references given, and is beyond the scope of this work. In depth details will only be given where they are relevant to this work.

2.1. DIFFRACTION TECHNIQUES

2.1.1. X-ray Diffraction

X-ray diffraction is the experimental method of choice for the determination of the electron density distribution in a crystalline material. It is commonly used to obtain the arrangement of atoms and molecules, their connectivity and conformation in real 3D space. This chapter addresses some basic aspects of the interaction of X-rays with matter, why X-rays are "diffracted" by crystals, and how this can be exploited to model the electron density in a crystalline compound. Aspects regarding crystallographic symmetry (crystal systems, space groups) as well as detailed experimental procedures will be largely ignored here. Crystallography has become a standard analytical method during the past 10 to 20 years, and there is an abundance of text books on X-ray diffraction available, of which a few are referenced here: The introductions to crystallography and X-ray structure determination "*Einführung in die Kristallographie*" by Kleber, Bautsch, and Bohm,[34] "*Kristallstrukturbestimmung*" by Werner Massa,[35] and the more in depth and detailed "*Fundamentals of Crystallography*" edited by Giacovazzo.[36] This section concludes with a more detailed description of methodologies to model the atomic electron densities in *X-ray Charge Density Analysis*.

Interaction of X-rays with Matter

When a charged particle is exposed to electromagnetic radiation, in this case to X-rays, it is forced to oscillate in the electromagnetic field. Accelerated charged particles in turn become sources of electromagnetic radiation. Hence, each such excited particle (electron, atom nucleus) acts as a point source of radiation with the same wavelength as it is exposed to – the incident radiation is "scattered" elastically. Since the phase lag between excitation and emission is well defined to π in radians, the electromagnetic wave is scattered in a

coherent fashion. This type of interaction is generally referred to as *Thomson scattering*, which in terms of intensity can be formulated as

$$I_e = I_i \frac{e^4}{m^2 r^2 c^4} P \qquad (2\text{-}1)$$

I_e and I_i are the intensities of scattered and incident radiation respectively, r the distance between oscillator and observer, and P the *polarisation factor* described later. Equation (2-1) makes clear that the contribution of the atom nuclei (they too have an electric charge and oscillate in an electromagnetic field) to the scattered intensity can be ignored because of their much higher mass. Thus, X-rays are scattered by electrons and X-ray diffraction is a tool to probe the electron density, not the nuclear density. However, most of the electrons are atom centred and the electron density maxima usually coincide well with the atomic nuclei. This is especially true for the heavier elements with many core electrons close to the nucleus, and less so for the very light elements (H, Li). Besides the elastic Thomson scattering there are other interactions of electromagnetic radiation with matter. The *Compton effect* describes the fact that a small amount of the photon energy is transferred to the electron. The scattered radiation has consequently a longer wavelength and does not contribute to the coherent scattering (resulting in inelastic scattering). Furthermore there is the *photoelectric effect* where the photon is absorbed to remove an electron from its atomic orbital. The photoelectric effect is the main contribution to the absorption of radiation.

Thomson scattering is responsible for the fact that each electron, excited by X-rays, becomes a point source of coherent radiation. According to the wave nature of electromagnetic radiation, the scattered radiation experiences interference effects; interference which naturally depends on the position of the X-ray scatterers, i.e. the electrons or, in a simpler model, the atoms. Here it becomes apparent why X-rays are used: Interference effects will only be significant if the wavelength is of the same magnitude as the interatomic distances (~ 0.5 – 2 Å). In a material with a random atom arrangement the interferences statistically cancel out, such materials are termed "X-ray amorphous"; glass is a typical example. In a crystalline material, on the other hand, the atoms are arranged in a highly ordered, regular fashion, which leads to constructive interferences in well defined scattering vectors. The X-rays become "diffracted". The scattering vectors are defined on a pure geometrical basis by the "unit cell" parameters (a, b, c, α, β, γ) as will become evident from the *Laue* and the *Bragg* equations below. An example of a unit cell is shown in Figure 2-1, it is the smallest building block necessary to build up the whole crystal by translation. By convention unit cells are chosen to have the highest possible metric symmetry which can lead to the occurrence of centred cells with larger volumes than the "reduced primitive" cells, see references [34-36].

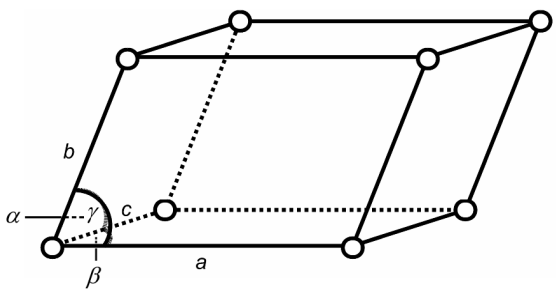

Figure 2-1: Unit cell of a crystal, circles mark the lattice points.

Figure 2-2 illustrates the relation between lattice parameters and constructive interference. The condition for constructive interference is that the path length difference ($s - t$) between the incident and scattered wave is an integer multiple of the wavelength, which can be formulated by the *Laue equations*

$$\begin{aligned} s - t &= a(\cos\varphi_s - \cos\varphi_i) = n\lambda \\ b(\cos\varphi_s - \cos\varphi_i) &= n\lambda \\ c(\cos\varphi_s - \cos\varphi_i) &= n\lambda \end{aligned} \qquad (2\text{-}2)$$

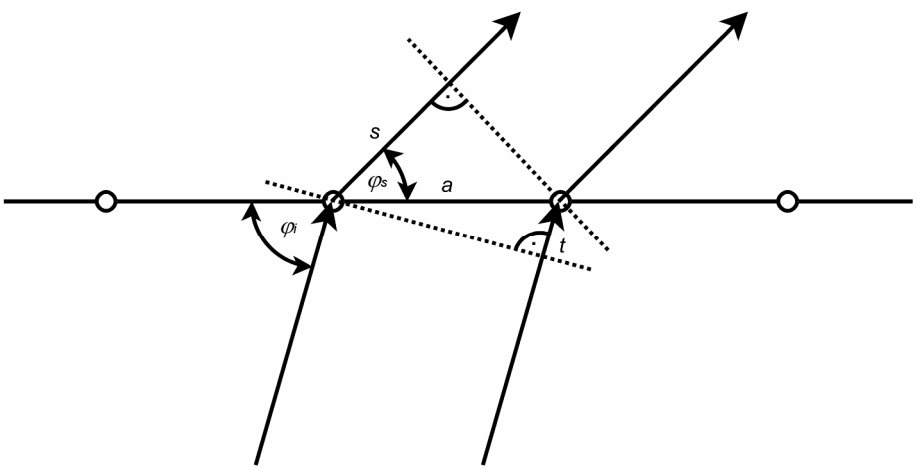

Figure 2-2: Schematic representation of the diffraction condition for the one dimensional case (unit cell vector *a* in this example).

For the three dimensional lattice all three Laue equations (2-2) have to be satisfied simultaneously. It is apparent that constructive interference is only reached for certain scattering vectors, while in all other directions the scattered waves are extinguished by destructive interference.

The above relations can furthermore be described by the *Bragg equation* (2-3). It represents the diffraction condition by "reflection" of the incident wave at sets of parallel crystallographic planes generated by the unit cell vectors. From Figure 2-3 the Bragg equation can be easily derived. Again, the path length difference ($s + s$) has to be a multiple of the wavelength:

$$s + s = 2d\sin\theta = n\lambda \qquad (2\text{-}3)$$

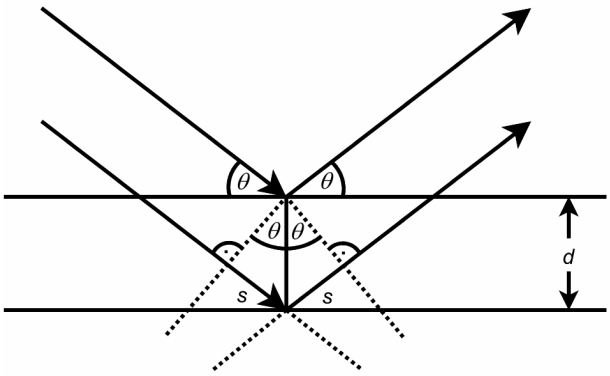

Figure 2-3: Schematic representation of the diffraction condition according to Bragg's equation.

Figure 2-4 shows how the crystallographic planes are constructed from the unit cell vectors. They are described in reciprocal space by the *Miller indices h k l*, have integer values, and can be derived from the relation

$$h : k : l = \frac{1}{a} : \frac{1}{b} : \frac{1}{c} \qquad (2\text{-}4)$$

a, *b*, *c* are here not the unit cell vectors but the intersection points of the planes with the lattice. For example the crystallographic plane (1 2 0) in Figure 2-4 relates to 1/2 : 1/1 : 1/∞, with *c* being infinite and subtending all lattice points down the paper plane.

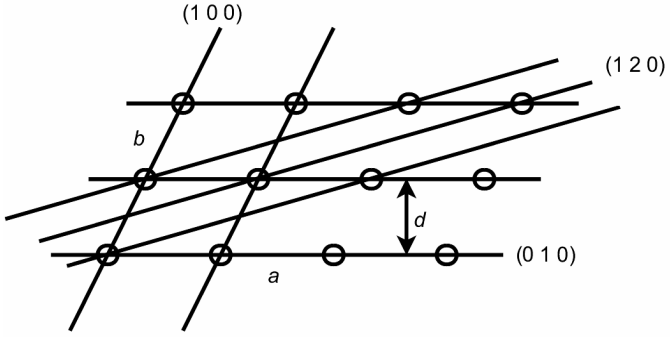

Figure 2-4: Construction of crystallographic planes from the unit cell vectors.

The overall diffraction angle 2θ depends only on the distance *d* between the crystallographic planes. In addition to defining the scattering angle, *d* is also a measure of the "resolution" of a diffraction experiment; it is given in units of Ångström (Å) and small *d* values correspond to a high resolution. From the Bragg equation (2-3) one can derive the maximum resolution to $d = \lambda/2$, which is where 2θ equals 180º, and the diffracted beam is directed back to the radiation source. The resolution is also often given in $\sin\theta/\lambda$ (= $1/2d$) in units of $Å^{-1}$. Figure 2-5 documents the relation between 2θ, *d* and $\sin\theta/\lambda$.

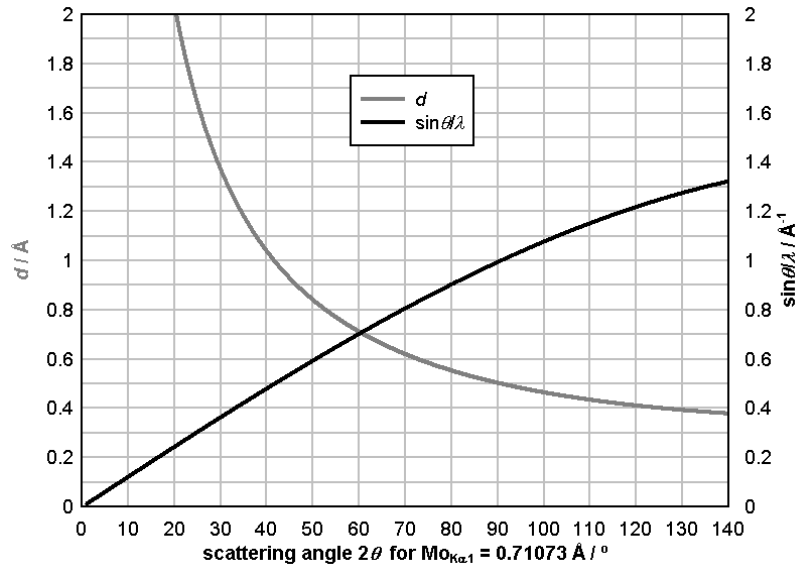

Figure 2-5: *d* spacing and $\sin\theta/\lambda$ versus scattering angle for incident radiation wavelength 0.71073 Å.

Experimental

Each "reflection" (*h k l*) corresponds to a diffracted beam whose intensity can be measured. Experimentally, there are essentially two methods to bring the crystallographic planes into reflection condition. For X-ray diffraction experiments the *crystal rotating method* is the most commonly applied. It uses monochromatic radiation (constant λ) and rotates the crystal in the beam (variable θ). The *Laue method* on the other hand exploits the high intensity of the non-monochromated radiation (variable λ), also called white beam, but keeps the crystal in a fixed position (constant θ). This method is used when the intensity of the incident beam is an issue (see *Neutron Diffraction* below).

The intensities of reflections are affected by several factors: The previously mentioned polarisation, which states that for a completely polarised incident radiation the intensity of the scattered wave is highest at an angle perpendicular to the oscillation vector and zero in its direction. Due to this effect, the intensity drops with $\cos^2 2\theta$, where 2θ is the angle between the incident beam and the contribution of the scattering vector which is parallel to the oscillation vector (the oscillation is perpendicular to the incident beam). For unpolarised radiation the *polarisation factor* is $P = (1 + \cos^2 2\theta)/2$. One has to note that the scattered radiation is always (slightly) polarised, which implies that monochromated radiation used for the diffraction experiment is also slightly polarised (usually corrected for automatically by the instrument software), and that X-rays originating from a synchrotron source are completely polarised. The *Lorentz factor*, L, depends on the experimental technique and is also corrected for automatically by the instrument software. For the crystal rotating method, for example, $L = \lambda/\sin 2\theta$. The *absorption factor*, $A = e^{-\mu d}$, corrects for the fact that electromagnetic radiation is absorbed by matter. For X-rays, the absorption coefficient μ depends on the atomic numbers (Z) of the involved elements and scales with $\sim Z^4$. The absorption naturally depends on the thickness, d, of the material, i.e. the path length of the beam through the sample, which varies during an experiment if the sample is not spherical (it hardly ever is). In addition to absorption effects, extinction weakens the primary beam and is accounted for by the *extinction factor*(s), E. There are two extinction effects; the dominant and hence most important reflects the fact that the incident beam is already considerably weakened by strong reflection at crystallographic planes in the surface regions of the crystal; the minor accounts for multiple scattering where the diffracted beam acts as a secondary incident beam and becomes itself diffracted. Extinction is difficult to correct for on an analytical basis; it is important to note that extinction is most severe for perfect crystals and affects the very strong reflections most significantly.[34-36]

Structure Factors

The intensities of the reflections hold all the information about the electron density distribution in the unit cell, which in good approximation is the distribution of atoms in the unit cell. Since usually not all atoms are located on the crystallographic planes (that is where all atoms would scatter in phase), there will be a phase shift Φ for each atom j which is dependent on its displacement away from the crystallographic plane (*h k l*), hence from its fractional coordinates, x_j, y_j, z_j.

$$\Phi_j = 2\pi(hx_j + ky_j + lz_j) \qquad (2\text{-}5)$$

The scattered wave can be expressed as a complex number whose amplitude and phase can be described for each reflection by *Fourier summation* over all atoms in the unit cell to yield the structure factor, F_{hkl}. This can be written in either exponential form (2-6) or, using *Euler's rule*, separated into real and imaginary part (2-7)

$$F_{hkl} = \sum_j f_j e^{2\pi i(hx_j + ky_j + lz_j)} \qquad (2\text{-}6)$$

$$F_{hkl} = \sum_j f_j \left[\cos 2\pi(hx_j + ky_j + lz_j) + i \sin 2\pi(hx_j + ky_j + lz_j)\right] \qquad (2\text{-}7)$$

At this point a differentiation has to be made regarding *centrosymmetric* and *non-centrosymmetric* structures. For centrosymmetric structures, the crystallographic symmetry includes a centre of inversion, projecting each atom with the general coordinates x, y, z to $-x, -y, -z$. Since the imaginary term disappears ($\sin\Phi + \sin{-\Phi} = 0$), equation (2-6) can be reduced to

$$F_{hkl} = \sum_j f_j \cos 2\pi(hx_j + ky_j + lz_j) \qquad (2\text{-}8)$$

Furthermore $|F_{hkl}| = |F_{-h,-k,-l}|$ and, ignoring anomalous dispersion, the phase is reduced to 0 or π, or, in other words, to the sign of F_{hkl}. The phase information of the structure factor cannot be directly determined from the experiment and is instead determined from methods described in *Structure Solution and Refinement* below, but the modulus, $|F_{hkl}|$, can be directly determined from its intensity. It corresponds to the amplitude of the diffracted wave, and according to the nature of electromagnetic radiation the intensity of a wave is approximately proportional to the square of its amplitude, hence

$$I_{hkl} \propto |F_{hkl}|^2 \qquad (2\text{-}9)$$

The *scattering factor*, f_j in equations (2-6) to (2-8) reflects the scattering power of the atom and is approximately proportional to the number of its electrons. The choice of the scattering factors depends on the model used to describe the electron density, they can be based on spherical or aspherical atomic densities (see *X-ray Charge Density Analysis* below). In any case, the atomic scattering power decreases with increasing resolution $\sin\theta/\lambda$ because the electron density is not located in a point but "delocalised" over a comparatively large volume element. This effect is less pronounced for heavy elements which have many well localised core electrons; and more for elements which have many delocalised (valence) electrons. Thus the scattering power fall-off is most apparent for the H atom (see Figure 2-7), and more generally speaking, for low electron density regions like those present in chemical bonds. The important implication is that all the chemical information about such low electron density regions is present in the low resolution reflections. In addition, the thermal motion of atoms (or more generally, the atomic displacement), which is ignored in the above structure factor calculation, enhances the fall-off by further "smearing out" the electron density.

The structure factors can also be calculated from a continuous electron density distribution rather than an atom centred model by integration of the electron density over the complete unit cell volume

$$F_{hkl} = \int_V \rho_{xyz} e^{2\pi i(hx+ky+lz)} \mathrm{d}V \qquad (2\text{-}10)$$

From the structure factors in turn, the electron density can be obtained for any point *x y z* in the unit cell by *Fourier synthesis*

$$\rho_{xyz} = \frac{1}{V}\sum_{hkl} F_{hkl} e^{-2\pi i(hx+ky+lz)} \qquad (2\text{-}11)$$

An accurate electron density, however, is only yielded by Fourier summation of an infinite set of *hkl* values. Because this is experimentally impossible to achieve (maximum $2\theta = 180°$), there will be "Fourier truncation effects" which lead to "Fourier ripples" in calculated electron densities. A way around this problem is the calculation of the difference electron density by *difference Fourier synthesis*.

$$\Delta\rho_{xyz} = \frac{1}{V}\sum_{hkl} (F_{\mathrm{obs},hkl} - F_{\mathrm{calc},hkl}) e^{-2\pi i(hx+ky+lz)} \qquad (2\text{-}12)$$

The calculated structure factors F_{calc} are subtracted from the measured ("observed") F_{obs} to yield $F_{\mathrm{obs}} - F_{\mathrm{calc}}$ density maps with the consequence that the Fourier truncation effects cancel out. In contrast to the total electron density, the difference density reveals only those density features which are not yet accounted for in a given structure model, hence not accounted for in the structure factor calculation. It is therefore a tool to find missing atoms to complete the structure (see *Structure Solution and Refinement* below).

2.1.2. Neutron Diffraction

According to the particle–wave duality, particles have an associated wavelength of $\lambda = h/p$; h is the *Planck constant* and $p = m \cdot v$ the momentum. Therefore, particle beams are also diffracted by crystals and the same diffraction conditions are obeyed for particle waves as for electromagnetic waves, with the same requirement that the particle wavelength lies in the same range as the interatomic distances. This can be "easily" achieved by tuning the particle speed. Electron diffraction and neutron diffraction have become the main applications and are "widely" used experiments for structure determination. Electrons are scattered by electrons, but they are easily absorbed by matter, also suffer badly from multiple scattering effects, and do not propagate very far into a material. They are therefore mainly used for probing surfaces or very small sample sizes. Neutrons on the other hand are scattered by the atomic nuclei. Here, the overall interaction with matter is very small and neutrons can propagate unhindered through large volumes of material – a problem for protection from exposure to neutrons as well as for the required sample sizes and experimental time scales. Neutrons carry a spin, and are additionally scattered by atomic spins and can thus also be used to determine the magnetic structure of a material.

The atomic scattering factors for neutrons (termed scattering lengths b) are nucleus specific and they can vary quite dramatically for elements next to each other in the periodic table, and isotopes of the same element. There is no real correlation between scattering power and the size of the nucleus or on the number of the elementary particles constituting the nucleus (see Figure 2-6). The great advantage of neutron diffraction is the fact that the scattering power (although overall low) is of the same order for almost all elements, hence the contrast for the lighter elements is much higher than that obtained by X-ray diffraction. The element of choice for probing with neutrons is naturally the H atom, which, for the reasons described earlier, cannot be determined by X-ray diffraction accurately, or not at

all when heavy elements are present in the structure. Also a distinction between H and D is possible because H has a negative scattering factor and D a positive. X-ray and neutron diffraction are two techniques which greatly complement each other.

It is also advantageous that the scattering factors do not decrease with increasing resolution because, unlike the electron density around nuclei, the nuclei themselves can be seen as point scatterers. A comparison of the resolution dependence of X-ray and neutron scattering factors is shown in Figure 2-7.

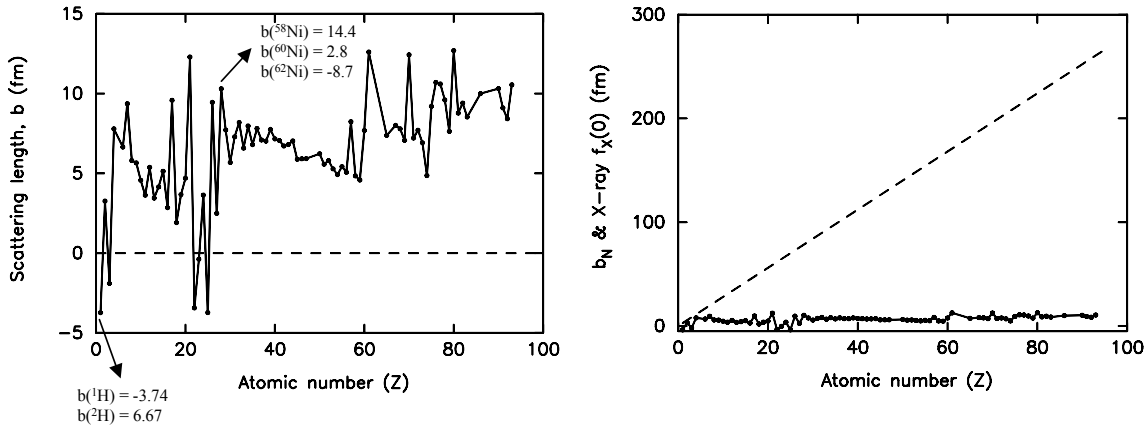

Figure 2-6: (Left) neutron scattering lengths; (right) a comparison of X-ray and neutron scattering factors. Figures from reference [37]

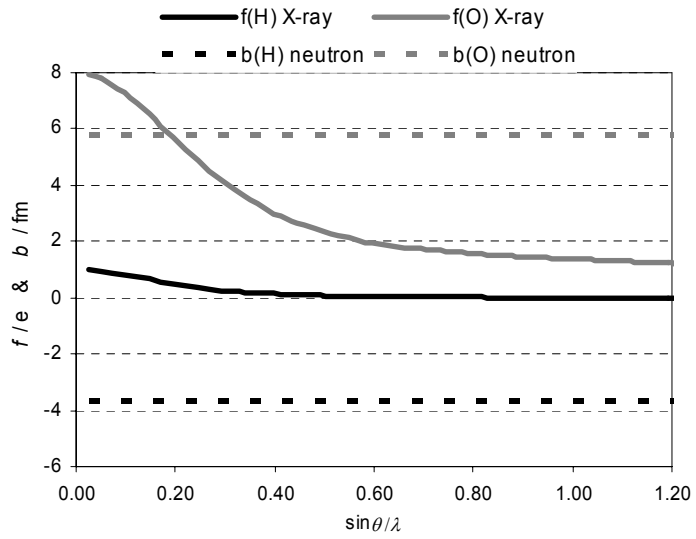

Figure 2-7: X-ray scattering factors and neutron scattering lengths plotted against $\sin\theta/\lambda$ for the elements hydrogen and oxygen.

Experimental

The main disadvantages of neutron diffraction are the scarce access to neutron sources (the "production" of neutrons is very costly and takes place only at a few central facilities dedicated to scientific use) and, as mentioned previously, the low interaction of neutrons with matter and the consequences thereof. There are two main procedures to generate neutrons. One is by reactor based *nuclear fission* which has all the technical and political difficulties associated to any commercial nuclear power plant. The other is by

"*spallation*", where protons are accelerated in a synchrotron and directed onto a heavy metal target, where neutrons are produced by particle collision at very high energies.

The small scattering power of the nuclei requires large sample sizes. This is a considerable difficulty, particularly for single crystal neutron diffraction experiments because large enough single crystals cannot be grown for all materials. However, recent advances in technology have improved the situation to an extent that a standard experiment can often be performed in a day. Such advances include optimisation of neutron sources towards the generation of neutrons in the desired wavelength range, optimisation of the neutron guides, and improvements in detector technology. Furthermore, modern experiments use the Laue method to exploit the high flux of the white beam, and cover a large section of reciprocal space with detectors in order to measure as many reflections as possible simultaneously.

The Laue method has the disadvantage that the information about the wavelength is lost and the d values cannot be calculated directly from the diffraction angle θ, thus indexing the unit cell and determining the orientation of the crystal in real 3D space becomes a problem. This means that it is advisable to know the unit cell parameters prior to the neutron diffraction experiment in order to facilitate the determination of the orientation matrix; a requirement which in practice is very often met by a preceding X-ray diffraction experiment. The *Very-Intense Vertical-Axis Laue Diffractometer* (VIVALDI), for example, located at the reactor based neutron source *Institute Laue-Langevin* (ILL), Grenoble, works according to this method. A variant of the Laue method is the *time of flight* (TOF) Laue method, which recovers the wavelength information by measuring the speed of each neutron (hence its wavelength). For pulsed neutron sources this is achieved by measuring the time between the collision event of protons with the target and the impact of the neutron on the detector – each neutron detection receives a timestamp. An example for this application is the *Single Crystal Diffractometer* (SXD) at the neutron spallation source *ISIS*, Oxfordshire. ISIS is a pulsed source where the protons are inserted into the synchrotron, accelerated, and diverted to the target in a batch like fashion at a rate of ~50 per second. For more details about neutron diffraction techniques see "*Single Crystal Neutron Diffraction From Molecular Materials*" by C. C. Wilson.[37]

2.1.3. Structure Solution and Refinement

Structure Solution

As mentioned previously, the modulus of the structure factor can be determined directly from the experiment. The phase information however, is lost, and its determination is known as the "phase problem" in structure solution. There are various ways to tackle this problem, two of which will be mentioned here briefly. Historically developed for the solution of X-ray structures, the *Patterson method* is still of importance for structure solution and has its applications. It calculates all interatomic distances by *Patterson synthesis*, which is an analogue to the Fourier synthesis but works directly with the measured intensities F_o^2, thus not requiring the phase information. The distance vectors are mapped into the so called *Patterson space*, *uvw*, which is a vector space and inherently different from the real space *xyz*.

$$P_{uvw} = \frac{1}{V^2} \sum_{hkl} F_{hkl}^2 e^{-2\pi i(hu+kv+lw)} \qquad (2\text{-}13)$$

Dependent on the size of the structure the number of the difference vectors mapped onto the generated "*Patterson map*" can be very high and difficult to interpret. Hence, the Patterson map is only a tool and a starting point to proceed with the structure solution. There are various routes to translate the vector information into real space atomic coordinates of which only the "heavy atom method" will be described here briefly. The intensity of each distance vector is proportional the product of the electrons of the contributing atom pair. That is why the Patterson method always works well if there are a few (and only a few) heavy scatterers in the structure, whose relative positions can be comparatively easily determined from the very strong distance vectors. As long as the contribution of these heavy atoms to the total electron density is sufficient, a Fourier synthesis in real space often yields sufficiently well determined phases in order to calculate a difference Fourier synthesis according to equation (2-12) and complete the structure.

It is evident that the Patterson map becomes very difficult to interpret when there are a lot of similarly strong scatterers present in the structure, for example organic compounds comprised of only C, H, N, O. Better ways to solve such structures are the "*direct methods*". They try to solve a structure "directly" from relations between the phases of groups of reflections and their intensities. This procedure requires a normalisation because intensities depend systematically on the scattering angle. Therefore the intensities are scaled to so called "expectation values", E^2, which is nowadays done by scaling to average intensities determined for different resolution ranges from the measured dataset. The most important such relation is the *triplet relation*. For centrosymmetric structures it is given by

$$E_{hkl} = E_{h',k',l'} \cdot E_{h-h',k-k',l-l'} \qquad (2\text{-}14)$$

It states that E_{hkl} has a positive sign if $E_{h',k',l'}$ and $E_{h'-h,k'-k,l'-l}$ both have the same sign; and a negative, if they differ. The relation is not exact, but is only true to a certain probability which increases with the intensities of the involved reflections (for a schematic illustration of the triplet relation see for example Figure 72 in reference [35]). A special case of (2-14) is given if $E_{h',k',l'}$ equals $E_{h'-h,k'-k,l'-l}$ stating that the higher order reflection of E_{hkl}, $E_{2h,2k,2l}$, has a positive sign if E_{hkl} is strong.

$$E_{2h,2k,2l} = E_{hkl} \cdot E_{hkl} \qquad (2\text{-}15)$$

For more relations exploited by direct methods and the treatment of non-centrosymmetric structures (where the phase information is not reduced to the sign of the structure factor), the reader is referred to references [34-36]. The phase–intensity relations only yield a starting set of phases from which the rest have to be determined by trial and error. Therefore, direct methods are computationally very intensive and have become routinely applied only since the development of computer technology. They are now, however, by far the dominant method used to solve the crystal structures of small molecule materials.

Structure Refinement

Once the phases are sufficiently determined to give an initial structure solution, the structure needs further optimisation (refinement). This process is referred to as *structure refinement*, where besides a few global parameters, the positional and displacement

parameters of atoms are refined. The atomic displacement parameters (ADPs) describe the volume element an atom averagely occupies due to thermal motion and other effects. Computationally, the structure refinement is performed iteratively by small variations of the *n* parameters in a set of *m* (number of measurements) linear equations. Mostly, the *least squares method* is applied, in which the squares of the differences between observed and calculated structure factors are minimised for all measurements:

$$\sum_{hkl} w(|F_{obs}| - |F_{calc}|)^2 \qquad (2\text{-}16)$$

$$\sum_{hkl} w(F_{obs}^2 - F_{calc}^2)^2 \qquad (2\text{-}17)$$

One can either refine against the structure factors F_{obs} (2-16), or against the squares of the structure factors F_{obs}^2, i.e. intensities of the reflections (2-17). The latter has the advantage that any negative intensities can be used directly, whilst they are not defined for the former (square root of a negative value). Such negative intensities (in theory they naturally always have positive values) can arise experimentally when for very weak reflections the background is determined to a higher value than the actual intensity. For the refinement against F_{obs} such reflections have to be omitted, or set to zero/small positive value, with the disadvantage of missing important information or introducing systematic errors respectively. During the structure refinement the structure factors are usually weighted (w in equations (2-16) and (2-17)) to account for the fact that weak reflections are systematically less reliably determined and should not be treated with the same weight as the strong reflections. There are different weighting schemes in use, the statistical one is based on the experimental standard uncertainties associated with each intensity measurement $w = 1/(\sigma(F_{obs}))^2$ and $w = 1/(\sigma(F_{obs}^2))^2$ respectively. The agreement between F_{obs} and F_{calc} is measured by residual values, the common R-values are

$$R_1 = \frac{\sum_{hkl} \| F_{obs}| - |F_{calc} \|}{\sum_{hkl} |F_{obs}|} \qquad (2\text{-}18)$$

$$wR_2 = \left(\frac{\sum_{hkl} w(F_{obs}^2 - F_{calc}^2)^2}{\sum_{hkl} w(F_{obs}^2)^2} \right)^{1/2} \qquad (2\text{-}19)$$

2.1.4. X-ray Charge Density Analysis

Spherical Atom Model

During the course of a "normal" X-ray structure analysis the electron density is modelled as a superposition of isolated, spherical atomic densities (which are allowed to follow the thermal motion of the nuclei), hence it is termed the spherical atom model. This is a reasonably good approximation since most of the electron density is concentrated near the nucleus, and due to the much higher mass of the nucleus, will rapidly adapt to any displacements of the nucleus. Ignoring thermal motion the electron density is now described as

$$\rho(\mathbf{r}) = \sum_A \rho_A(\mathbf{r} - Q_A) \qquad (2\text{-}20)$$

ρ_A is the atomic density centred at the nucleus Q_A. The disadvantage of the spherical atom model is that it does not account for charge transfer effects, mainly caused by the formation of chemical bonds, but also by the abundance of intermolecular interactions in the crystalline state. This is especially true for organic molecules, where the number of valence electrons involved in bonding is relatively high in comparison with the total number of electrons. It is most pronounced for the H atom, which has no core electrons, and the one valence electron is always involved in bonding, which consequently leads to a shift of the H electron density maximum towards the bonding partner. The shift is further enhanced by libration effects. The H atom performs bending vibrations along the X–H bond in a circular fashion around the bonding partner and thereby simulates a shorter bond distance. The discrepancy between the positional parameters of the H nucleus and electron density maximum usually sums up to about 0.1–0.2 Å. Refinement of X-ray data therefore leads to systematically incorrect H positional parameters which of course affect bond distances and angles. To a much lesser extent such biases are also known for heavier elements like C, N, O, where refined bond distances can deviate up 0.01 Å from those determined by neutron diffraction.[38]

In order to illustrate the above mentioned charge transfer effects, difference Fourier density maps (*residual density maps*), shown in Figure 2-8, have been calculated according to equation (2-12) for the pyridine ring in the molecular complex of isonicotinamide with oxalic acid (IN_2–OA Form I, discussed in Chapter 3). They have been obtained after refinement of a high resolution dataset with the spherical atom model (*spherical atom refinement*), which is the model employed by the widely used structure refinement program SHELXL.[39] Electron density (or charge) accumulation in bonding and lone pair regions is clearly visible. Also the shift of the H positional parameters upon their refinement, and the resulting reduced electron density in the X–H bonds, becomes apparent.

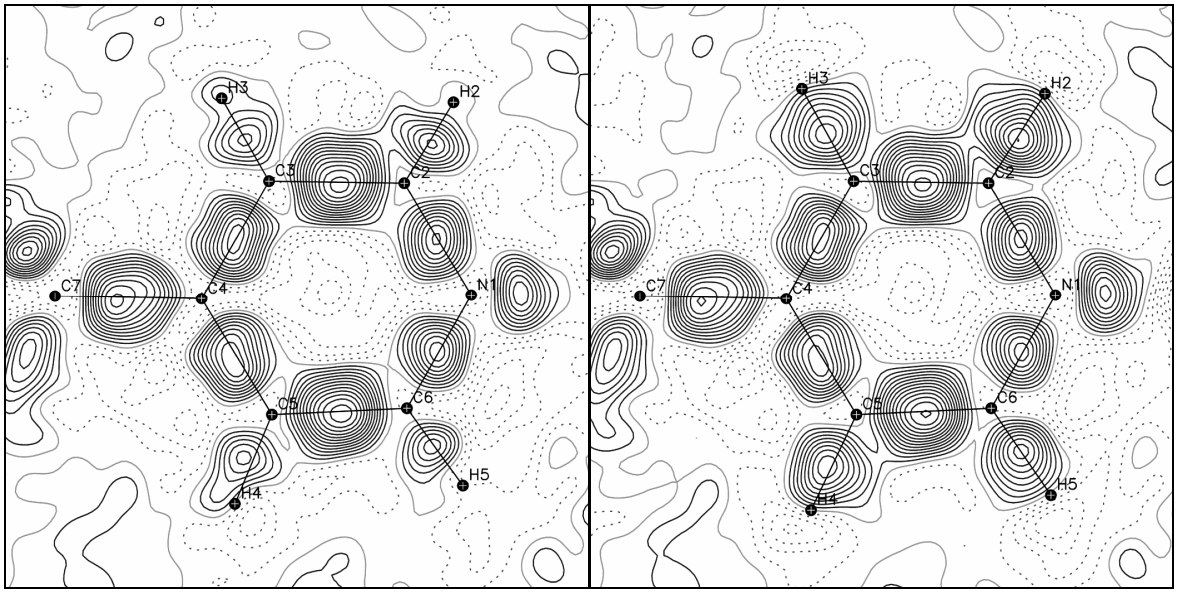

Figure 2-8: Residual density maps in the pyridine plane of IN_2–OA after the spherical atom refinement; (left) all parameters refined against X-ray data; (right) H parameters fixed to those obtained from neutron refinement; maps for $F_{obs} > 4\sigma(F_{obs})$, $\sin\theta/\lambda < 1.078$ Å^{-1}; positive contours – solid black, zero levels – solid grey, negative – dotted, contours at 0.05 eÅ^{-3}.

Aspherical Atom Model

The aim of an X-ray refinement to minimise the difference between the experimental and modelled electron density (i.e. F_{obs} and F_{calc}) means that the residual electron density should be featureless. That is evidently not optimal in the above case. Improved models are those which account for the asphericity of the electron density distribution – they are generally referred to as *aspherical atom models*. The analysis of the electron density in such a way is commonly referred to as *charge density analysis*. Its implementation, however, increases greatly the number of parameters to be refined and the experimental demands are consequently high.

The aspherical atom model implemented in the XD package[40] which has been used for this work, has been developed by Hansen and Coppens.[41] It is more specifically referred to as a *pseudoatom model*, because the valence density is modelled in a series of nucleus-centred multipole expansions around a spherical core density. The atomic electron density is now divided into a spherical core part $\rho_{c,}$ a spherical valence part ρ_v, and a valence deformation part ρ_d (the last term in the formula below).

$$\rho(\mathbf{r}) = P_c\rho_c(r) + P_v\kappa^3\rho_v(\kappa r) + \sum_{l=0}^{l\,\max} \kappa'^3 R_l(\kappa' r) \sum_{m=0}^{l} P_{lm\pm} d_{lm\pm}(\theta,\phi) \qquad (2\text{-}21)\ [42]$$

In the XD implementation the population for the core density is fixed to the number of core electrons, and the populations for the valence density P_v and P_{lm} are variable. κ and κ' are contraction–expansion parameters for the valence densities, R_l are the radial density functions, and d_{lm} the density-normalised real spherical harmonics in polar coordinates θ and ϕ. Further formalism of this method can be found in the original paper by Hansen and Coppens,[41] the monograph "*X-ray Charge Densities and Chemical Bonding*" by Coppens,[42] and a more recent review by Koritsanszky and Coppens.[43] Within the aspherical atom model, the deformation density is properly (though still not perfectly) accounted for. After refinement with the Hansen–Coppens approach (referred to as *multipole refinement*) of the same dataset as used for the above spherical atom refinement, the residual map is as shown in Figure 2-9. It is, although still slightly noisy, now featureless, and the R_1 value (2-18) for the observed reflections has dropped considerably from 0.0310 (spherical atom refinement) to 0.0159.

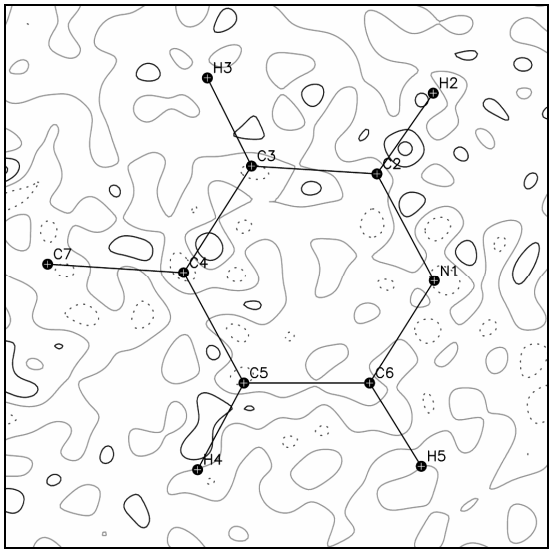

Figure 2-9: Residual density map in the pyridine plane of IN_2–OA after multipole refinement, H parameters fixed to those obtained from neutron data; for details see Figure 2-8.

Experimental

A charge density analysis requires a very accurate determination of the intensities of the reflections up to a high resolution, however the low resolution intensities are especially crucial because they hold all the information about the actual charge transfer effects as discussed earlier, and a few under- or overestimations can strongly bias the results. In addition, it is just these low resolution reflections which can be very strong and suffer most from extinction, in which case a good extinction model is required. Also, absorption is a problem. A way of getting a good model to correct for absorption is to measure reflections with a high redundancy, which in combination with the demand for a high resolution dataset means in practical terms a long experiment. Aside from highly accurate experimental data, an accurate determination of all atomic parameters (positional and displacement) is required, which for the H atoms cannot be obtained directly from the X-ray charge density experiment. Therefore, special care has to be taken with respect to the treatment of H atoms if present. Accurate H parameters are ideally obtained from a neutron diffraction study and fixed during the X-ray refinement (X+N refinement). Because various experimental factors differ in X-ray and neutron experiments, the ADPs from a neutron study are usually systematically different which has to be corrected for. The program UIJXN[44] does this by comparing the heavy element ADPs obtained from the X-ray refinement with those from the neutron, and uses this information to subsequently scale the H ADPs. In the absence of neutron data there are various possibilities to estimate the H parameters. The X–H distance, thus H positional parameters, can be fixed to standard "neutron lengths" in the X-ray refinement; the H ADPs, however, are less accessible because they highly depend on the motion of the molecular group (the rigid body) to which the H atom is bonded to. The fact that molecular groups move as a rigid body on the other hand, can be exploited to estimate the ADPs for H from a so called "rigid body model". Programs like SHADE[45] use such a model to estimate the rigid body contribution to the overall H displacement from the heavy element ADPs which belong to the same rigid group. To this the internal H vibrations are added.

Deformation Densities

The deformation density is defined as the difference electron density between the molecular density and that constructed from the spherical densities of independent atoms in the gas phase. It should reveal all charge transfer effects arising upon the formation of molecules, i.e. density accumulations in covalent bonds and lone pair regions. There are many possibilities of visualising experimental deformation densities. First of all, the combinations of X-ray and neutron data require various differentiation. In X–X maps the molecular density originates from an X-ray experiment, and the reference density from a structure refinement against X-ray data only (for example Figure 2-8, left). In X–N maps ($F_{\mathrm{x,\,obs}} - F_{\mathrm{n,\,calc}}$) all atomic parameters originate from a neutron refinement, and in X–(X+N) maps a combination of both approaches is used, where only partial information originates from the neutron refinement, usually that for light elements like H and Li (for example Figure 2-8, right). In this work, all deformation densities calculated from the charge density data follow the X–(X+N) approach with the H coordinates and ADPs taken from the neutron experiment; all deformation densities and difference Fourier maps calculated from standard X-ray data on the other hand, are X–X maps.

The *standard deformation density* (Figure 2-10, left) is the difference between the experimental density and a reference density generated from a superposition of nucleus centred spherical atomic densities (referred to as *promolecule density*). It is calculated from the structure factors ($F_{obs} - F_{calc,\ spherical}$) by Fourier synthesis according to equation (2-12). Using standard spherical atomic densities for the structure factor calculation leads to residual densities like those in Figure 2-8. For "normal" X-ray experiments carried out to a standard resolution, however, the positional, and particularly the atomic displacement parameters, are biased by the very existence of charge transfer effects in molecules. This leads to unrealistic spherical atomic densities being subtracted from the total density and subsequently to unrealistic deformation densities. A way around this problem is to use more accurate atomic parameters for the determination of F_{calc}. Such parameters can originate from a neutron refinement, a high order X-ray refinement, or an X-ray refinement using an aspherical atom model. The standard deformation density based on the latter is referred to as *experimental deformation density* in this work. An example is shown for the pyridine ring in IN_2–OA in Figure 2-10, left, which resembles qualitatively the residual density after a spherical atom refinement (Figure 2-8).

The *dynamic model deformation density* (Figure 2-10, right) is obtained by subtracting the promolecule density from a density which has been calculated from the multipole refinement, ($F_{calc,\ multipole} - F_{calc,\ spherical}$). The experimental data are only involved insofar that they have been used for the determination of the atomic parameters. This method results in noiseless maps, but the features should qualitatively be the same as those obtained from the experimental deformation density, provided that the experimental data, as well as the refined aspherical atom model, are good.

The *static model deformation density* (Figure 2-11) on the other hand, is calculated directly from the multipole populations. It implies an infinite resolution because no Fourier synthesis is involved in this process. For this reason and the fact that it does not take into account thermal motion, the charge transfer effects and charge accumulations are enhanced.

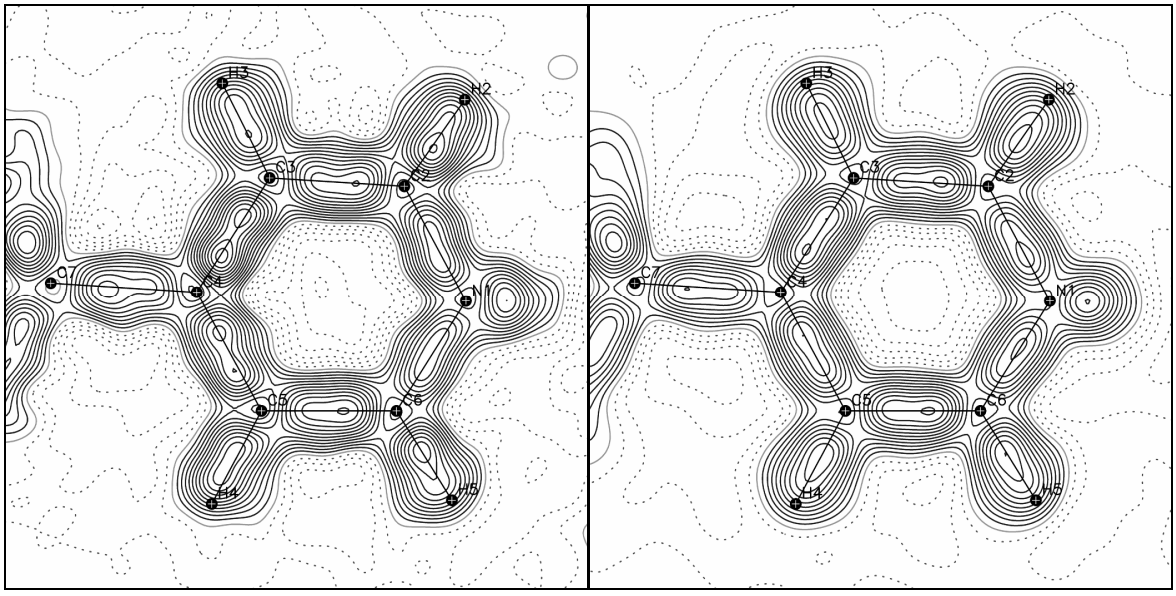

Figure 2-10: (Left) X–(X+N) experimental deformation density map, (right) X–(X+N) dynamic model deformation density map; for details see Figure 2-8.

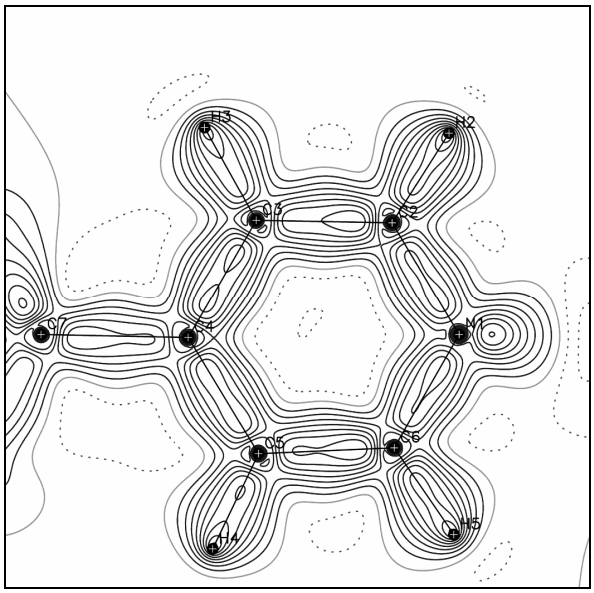

Figure 2-11: Static model deformation density map in the pyridine plane of IN_2–OA, contours at 0.1 eÅ^{-3}.

Comparison of the experimental deformation density after multipole refinement (Figure 2-10, left) with the residual density map after the spherical atom refinement (Figure 2-8, right) shows, that – although these two maps are generated essentially in the same way – it is now clearer for two main reasons. First, within the aspherical atom model, the refined atom positions and ADPs are less biased by the deformation density. Second, the better fit of modelled and experimental electron density implies that the phases of the structure factors are also determined more accurately (although for centrosymmetric structures like this one usually only a few, numerically small, structure factors are affected). The differences between the experimental and dynamic model deformation density (Figure 2-10, right) are small, as they should be for a good experimental dataset. The static model density map (Figure 2-11) yields qualitatively the same information. It is noiseless, because it is not generated by a Fourier synthesis, and its features are sharper because there is no thermal smearing. The latter effect is especially pronounced in lone pairs regions. Aside from the rather intuitive way of retrieving chemical information by visualising deformation densities, there are a number of properties that can be derived from the total electron density. This will be discussed in 2.3 *Atoms In Molecules*.

2.2. AB INITIO CALCULATIONS

Since the advent of computer technology, scientists have tried to simulate nature, encompassing all aspects from the destiny of the universe, to weather forecasting, to traffic flow. In the material science context, computer simulations provide the possibility to determine material properties (structural, energetic, vibrational, magnetic, etc.). This information can be used to support and add information to experimental data, or to make predictions regarding them. Computer simulations also provide the possibility to study materials which are experimentally not accessible, for example the state of iron at the pressures existent in the core of the earth.[46] The computational approaches can be classified into *empirical* and *ab-initio* methods. The first uses classical mechanics and

empirical data to determine, say the interaction energy between two atoms. The latter calculates (or aims to calculate) everything from *first principles* "ab-initio", i.e. based on the laws of quantum mechanics. This section focuses on ab-initio methods, and in particular on those which include the periodicity of crystalline materials since the systems studied in this work are solely of this type.

Ground State Energy Calculations

Ab-initio calculations make use of the laws of quantum mechanics and basically try to solve the *Schrödinger equation*

$$H\psi = E\psi \qquad (2\text{-}22)$$

H is the *Hamilton operator* or *Hamiltonian*, E the total energy of the system, and ψ the wave function. An *exact* solution, however, is only possible for systems constituting no more than two particles like the H atom, or the He^+ ion. The time independent Schrödinger equation for an isolated particle at any point **r** becomes

$$\left(-\frac{\hbar^2}{2m}\nabla^2 + V\right)\psi(\mathbf{r}) = E\psi(\mathbf{r}) \qquad (2\text{-}23)$$

The first term describes the kinetic energy, T, which for the example of a H atom is that of the electron; $\hbar = h/2\pi$ is the *reduced Planck constant*, m the mass of the electron, and V is the potential energy of the electron in the electric field of the proton. The *Laplace operator* ∇^2 describes the curvature of the wave function (compare with 2.3 on *The Laplacian*).

For systems with more than two particles, also known as "many body systems", the Schrödinger equation cannot be solved analytically. This is partly overcome by the *Born–Oppenheimer approximation* which states that the nuclei can be regarded as stationary because the much lighter electrons rapidly adapt to any change in nuclear positions. Therefore many body systems with more than one nucleus can be dealt with. Solving the Schrödinger equation for many electron systems, however, is the main challenge for all ab-initio calculations. The problem lies in the interaction between electrons because the electrons no longer move independently but are correlated (*electron correlation*). Contributions to the electron correlation originate from the electrostatic repulsion and from the *electron exchange* which considers the fact that two electrons with the same spin cannot occupy the same spatial part of their wave function. The Hamiltonian is then expanded to

$$H = T + V_{\text{ext}} + V_{\text{int}} + E_{II} \qquad (2\text{-}24)$$

V_{ext} is the potential exerted by the nuclei on the electrons, V_{int} the electron–electron interaction, and E_{II} the inter nuclei as well as all other energy terms which are not relevant to the electronic description.[47] As stated previously, there is no analytical way to solve the Schrödinger equation for such a many body system. There are, however, very good approximations to a solution which use numerical, iterative methods; so called *self-consistent field methods* (SCF methods), "self-consistent" because they iteratively calculate the potentials from the wave function, then starting from these potentials, calculate a new wave function, until this cycle converges and the energy is minimised. Two widely used methods to deal with the electron–electron interaction shall be mentioned here.

The *Hartree–Fock* (HF) method is an independent electron method that makes the approximation that each electron moves independently in an average, effective potential determined by the nuclei and all other electrons. Hence, the electron correlation is only treated approximately. The electron exchange on the other hand is included exactly. Therefore this method can be expected to perform well for any property in which electron correlation (important in covalent interactions) is less important than exchange. Consequently, HF performs often better for ionic systems.

Density functional theory (DFT) states that all properties of a material depend on / are a functional of the ground state density, *n*. Within the *Kohn–Sham* approach the ground state density of a many body system is assumed to be equal to that of the sum of non interacting particles. All the electron–electron interactions of the (real) many body system are covered by an *exchange–correlation* energy. The Kohn–Sham energy is expressed as a functional of the density *n*:

$$E_{\mathrm{KS}} = T[n] + \int d\mathbf{r} V_{ext}(\mathbf{r}) n(\mathbf{r}) + E_{\mathrm{Hartree}}[n] + E_{II} + E_{\mathrm{xc}}[n] \qquad (2\text{-}25)$$ [47]

E_{Hartree} is the classical electrostatic energy of the density, and E_{xc} the exchange–correlation energy. The exchange–correlation energy is calculated from first principles simulations on a uniform electron gas. It shows that it is only dependent on the electron density *n*, which in turn results from the solution of the Schrödinger equation. Once the electron density at a given point is known, the exchange–correlation energy can be calculated, in principle exactly, but not in practice due to limitations inherent to the functionals. Two widely used functionals for E_{xc} are the *local density approximation* (LDA) and the *generalised gradient approximation* (GGA). In the LDA, E_{xc} is a function of only the local density *n*, whilst the GGA also includes the gradient ∇n of the density. Furthermore, there is the possibility to mix the exchange–correlation energy with the exact exchange of the Hartree–Fock method into so called *hybrid functionals*. DFT methods are nowadays widely used for ab-initio calculations and have become standard routines in material sciences. For molecular materials especially, hybrid functionals (B3LYP[48, 49] to name an example of a widely used hybrid functional) have proved to be accurate with respect to reliably reproducing the experimental data. A general disadvantage of pure DFT functionals manifests in the determination of intermolecular binding energies: they are overestimated by the LDA and underestimated by the GGA.

A few differentiations have to be made at this point regarding the phase in which a material is modelled. It can be treated as isolated in the gas phase, dissolved in a liquid (usually subject to molecular dynamics), or as a sub-unit (commonly the crystallographic unit cell) of a periodic, crystalline solid state structure. It is obvious that the computational model has great impact on the results – a molecule in the gas phase behaves differently from that incorporated in the solid state, simply because in the former there are no intermolecular interactions whilst they are abundant in the latter. The two most commonly used DFT approaches for the calculation of periodic structures will be introduced briefly in the following.

In the *plane wave* (PW) approach the electronic structure is described by sets of plane waves (*plane wave basis sets*) which are uncoupled from the atomic nuclei. The plane waves have to obey the periodic boundary conditions determined by the unique building block of the periodic structure – often the unit cell of a crystalline material. The electron density can then be visualised as a linear combination of the plane waves. There is,

however, the disadvantage that a very large number of plane waves have to be computed in order to model the high electron densities and associated high gradients near the nuclei of atoms. This is overcome by the inclusion of *pseudopotentials*. Pseudopotentials are comprised of the nuclei and the core electrons, from which an effective coulomb potential is exerted on the remainder of the electrons, i.e. the valence electrons. Thus only the comparably low valence electron density has to be described by the plane waves. Without the use of such pseudopotentials the computational effort would be far too high to be applicable. The method is therefore often referred to as *plane wave pseudopotential DFT*. Because the calculation of the exact Fock exchange energy is computationally extremely expensive, only DFT functionals are realised in practical terms, implying that the intermolecular interaction energies obtained from pure DFT functionals are liable to be inaccurate. The great advantage of this method, however, is that it scales well with $N \cdot \log N$ (N = number of atoms) towards the computation of larger systems.

In the *atomic orbital* (AO) approach the electron density is described in atom centred orbitals (*s*, *p*, *d*, *f*, etc.) as they are known from the wave function of the H atom. The probability density functions of each atomic orbital are typically built up by sets of *Gaussian* or *Slater* type functions (*local basis sets*), which have to be constructed in such a way that they accurately describe the system under study. *Linear combination of atomic orbitals* (LCAO) then leads to the complete descriptor of the electron density of a single atom or one embedded in a molecule. To the chemist, the AO approach appears more appealing than the PW approach insofar that the electronic population in atomic/molecular orbitals is computed. Properties can be derived more intuitively and, for example, Mulliken population analyses are more naturally obtained in the AO approach. This method has the advantage that it allows the inclusion of Hartree–Fock and hybrid functionals. The disadvantage is that the computation of large systems is very expensive because of a strong scaling with N^3–N^4 (N = number of basis functions, which depends on the number of atomic orbitals to be described).

The ground state energy is obtained, independent from the methodologies described above, either by *single point energy* calculations where the wave function of a given atomic arrangement is determined with the SCF method without altering the nuclear positions; or it can be obtained by *geometry optimisation*, where the nuclei are allowed to move to lower the total energy of the system. At each optimisation step, a single point energy calculation is performed in accordance with the Born–Oppenheimer approximation, before the atomic positions are further optimised. This cycle is repeated until the global energy minimum is found for the optimised geometry.

For the current work, PW and AO calculations have been performed using the CASTEP[50] and CRYSTAL03[51] codes respectively.

Molecular Dynamics

Molecular dynamics (MD) simulations provide the possibility to study the properties of materials. This is achieved by simulating a system over a period of time at finite temperatures, unlike the previous ground state calculations which yield time independent energies at zero Kelvin. All MD works according to *Newton's law of motion*, $F = a \cdot m$, where particles are accelerated in a potential and their displacements per time step are calculated. The way the potentials are determined defines the class of MD simulations; by classical mechanical calculations (*force field molecular dynamics*, generally referred to as

just MD) or from first principles by quantum mechanical (*quantum molecular dynamics*, or QMD).

$$V(r) = 4\varepsilon\left[\left(\frac{\sigma}{r}\right)^{12} - \left(\frac{\sigma}{r}\right)^{6}\right] \qquad (2\text{-}26)$$

$$F(r) = -\frac{dV(r)}{dr} \qquad (2\text{-}27)$$

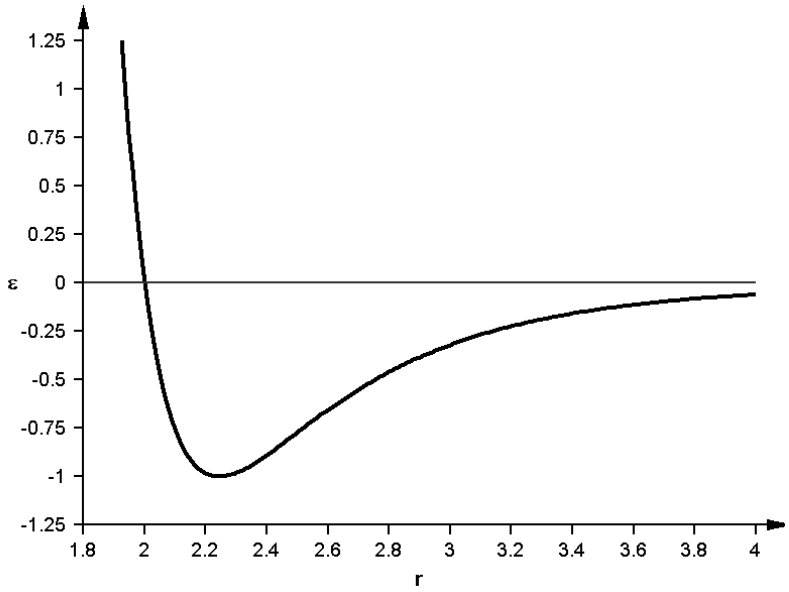

Figure 2-12: The *Lennard–Jones* potential, ε is the potential well depth and σ the value for which $\varepsilon = 0$ (here for $\varepsilon = 1$, $\sigma = 2$).

Force field MD are usually based on pair interactions, where the forces are calculated from, for example, fairly simple *Lennard–Jones* potentials (Figure 2-12, and equations (2-26) and (2-27)). For single atoms this approach is straight forward; for atoms bound to other atoms (i.e. molecules), additional interatomic potentials have to be added, which describe the stretching, bending, and torsion motions of a molecule. Each potential has to be parameterised. Since there is no general purpose parameter set, the success of a force field method depends on the quality of parameterisation for each individual problem. Furthermore, force field MD does not allow breaking or formation of covalent bonds; consequently, reaction pathways cannot be explored by this method. The great advantage of this method, however, lies in the fast processing of large systems.

In quantum molecular dynamics (QMD) the forces are directly derived from the wave function calculated ab-initio. Systems studied by MD are by definition large, and from the perspective of the computational effort, QMD is only feasible within PW DFT. In the *Car–Parrinello* approach the calculation of the wave function and classical motion is unified; both the nuclear and electronic structure evolve with time and are evaluated simultaneously.[52] In other words, the electronic wave function has not necessarily reached the ground state energy (within the energy tolerances applied) when the atomic forces are calculated, implying that the Born–Oppenheimer approximation is not obeyed. As a result, the Car–Parrinello approach is computationally fast, but justified only as long as the time steps between the energy calculations are small in comparison to the nuclear motion. A variant of this approach is implemented in the CASTEP code,[50] in which the

forces are calculated at each nuclear step from the electronic ground state wave function, obeying the Born–Oppenheimer approximation. Independent from the QMD approach used, there are various ensembles which conserve the number of particles, the energy, volume, temperature and pressure in the system during the MD simulation period. For this work, the QMD calculations have been performed with CASTEP using the NVT ensemble which keeps the number of particles (N) and the volume (V) constant, and conserves the temperature (T).

2.3. ATOMS IN MOLECULES

This section is intended to give an overview of the theory of "*Atoms In Molecules*" (AIM), which has been developed by Bader and co-workers. Comprehensive descriptions of this method are given in the monographs "*Atoms In Molecules – A Quantum Theory*" by Bader[53] and "*Atoms In Molecules – An Introduction*" by Popelier.[54] AIM is based on the topological analysis of the electron total density, $\rho(\mathbf{r})$, in any given system. It does not distinguish where the electron density information originates – it can be obtained from charge density analysis or from quantum mechanical calculations and thereby offers an ideal common platform for experiment and theory. It is also a strict and objective tool as it is solely based on the electron density, for example the answer to the question about the presence of a bond between any two atoms will be either yes or no, there will be no ambiguity. Sticking to this example, the scope for interpretation will, in the AIM formalism, be limited to the type or strength of a bond. Uncertainties do not arise from the topological analysis itself (aside from numerical errors), but from the accuracy of the method used to obtain the electron density.

Critical Points and the Gradient Vector Field

The topological analysis of the electron density is analogous to that of the surface of an object such as our planet; the difference is that the former is a 3-dimensional and the latter a 2-dimensional problem. In order to find peaks on a 2-dimensional surface, it is only necessary to find those points where the surface gradient is zero and the curvature at that point is positive. Troughs are determined by a zero gradient and a negative curvature, and there is a third point at which the gradient is zero, namely a saddle point, where the curvature is positive in one direction (for example the x direction) and negative in the other (y). In the AIM terminology, points with a zero gradient are called critical points (CPs). They are denoted by their rank *r* (dimensionality) and their signature *s*, which is the sum of the signs of the curvature at the CP (note that a positive curvature has negative sign and vice versa). In the above example, a "peak critical point" would have the (*r*, *s*) notation (2, –2), with *s* = –2 because both curvatures in the x and y directions are positive; a saddle point would be denoted as (2, 0), and a trough as (2, +2).

The gradient of the 3-dimensional electron density is defined by

$$\nabla\rho = \left(\frac{\partial\rho}{\partial x}, \frac{\partial\rho}{\partial y}, \frac{\partial\rho}{\partial z} \right) \quad (2\text{-}28)$$

There are now 4 distinct critical points where $\nabla\rho = 0$. The analogue to the peak on a surface is the *nuclear attractor* NA (3, –3), which determines the electron density maximum and therefore almost coincides with the position of the nucleus (within the limits

described earlier). The NA has rank 3 and the signature –3, because the curvature (evaluated by the Laplacian, see below) is positive in all 3 dimensions at this point. The saddle point described above becomes, in 3D, the *bond critical point* BCP (3, –1) with positive curvatures in x and y and negative in the z dimension, and the trough becomes the *ring critical point* RCP (3, +1), which has positive curvature in x, and negative in z and y dimension. The fourth critical point, the *cage critical point* CCP (3, +3) has negative curvatures in all dimensions.

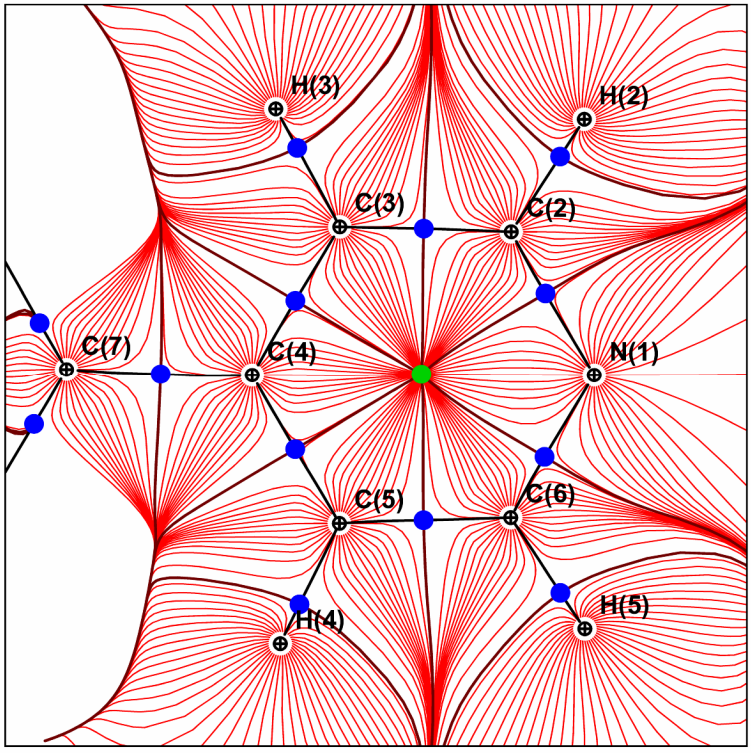

Figure 2-13: Gradient vector field map in the pyridine plane of IN_2–OA; BCP (blue), RCP (green), IAS (brown), BP (black).

It is now helpful to visualise the gradient vector field that consists of an infinite set of gradient vectors, $\nabla\rho$, or gradient paths. The rules for gradient paths are such that they go from low to high electron density, and that they always follow the steepest gradient. They are therefore perpendicular to the contour lines of an electron density map (contour lines connect points of equal electron density, in this case). Gradient paths also have a start and an endpoint; they originate at infinity or at a CP and will eventually terminate at a CP of lower signature than its origin. An example of a gradient vector field map is shown in Figure 2-13. Starting from a RCP (green), like that in the centre of the pyridine ring of the IN_2–OA example, there is an infinite set of gradient paths (red lines) of which most terminate directly at a NA, and a few (6 exactly) at a BCP (blue). Starting from a BCP, however, there are only exactly two possibilities to follow a steepest gradient. For the BCP between N(1) and C(2) for example, one gradient path leads to the nuclear attractor N(1) and the other to C(2). The line connecting two NAs via the BCP is called the *bond path* (BP), it can be curved and its length can deviate from the interatomic distance. According to AIM, the existence of such a BP (and therefore a BCP) determines whether there is a bonding interaction between two atoms or not. At this point it is worth remembering that all statements made by the AIM theory are solely based on the electron

density distribution in a system, and can thus be assumed to have a solid physical foundation. In this interpretation the BP is simply the line of maximum electron density between two atoms, with the BCP marking the point of lowest density on the BP. The interpretation of RCPs and CCPs will be left out in this short overview of AIM, other than that their presence is mandatory[55] and numerous in periodic systems, and that they are located in ring systems and cages respectively, all of which are generated by the bond paths.

The gradient vector field reveals another feature: the *interatomic surface* (IAS), projected on the map by brown lines in Figure 2-13. The mathematical definition is that at *all* points on the IAS, the normal **n** to the surface is orthogonal to the gradient of the electron density, or $\mathbf{n}\cdot\nabla\rho = 0$. In other words, the IAS is *everywhere* parallel to $\nabla\rho$, which is true for all surfaces parallel to the gradient paths in the above map, except for those which terminate at a NA. The IAS thereby readily partitions space, because not terminating at a NA means that points located on a IAS are not assigned to any NA, whereas from every other point in space the gradient path will terminate in one unique NA. The space which is allocated to a NA in this way is called the *atomic basin* Ω from which integrated properties like volumes and electronic populations of atoms can be calculated.

The Laplacian

The *Laplace operator* or *Laplacian* is the sum of the second partial derivatives, and is defined for the electron density ρ as

$$\nabla^2\rho = \nabla\cdot\nabla\rho = \left(\frac{\partial^2\rho}{\partial x^2} + \frac{\partial^2\rho}{\partial y^2} + \frac{\partial^2\rho}{\partial z^2}\right) \qquad (2\text{-}29)$$

It is determined by a 3×3 Hessian matrix which on diagonalisation yields the 3 eigenvalues λ_1, λ_2 and λ_3, which are measures for the local curvature along the 3 principal axes of curvature (λ is negative for a positive curvature). The Laplacian can also be written as $\nabla^2\rho = \lambda_1 + \lambda_2 + \lambda_3$, and is a measure of the local charge concentration or charge depletion. At a BCP for example, the electron density is depleted with respect to the BP vector, but concentrated with respect to the remaining two vectors. In order to see whether charge concentration dominates at any one point, one has to evaluate if the positive curvature dominates, that is the sum of the three λ eigenvalues has to be negative. Hence, for regions with charge concentration $\nabla^2\rho < 0$, and conversely for charge depletion $\nabla^2\rho > 0$. The Laplacian is commonly visualised as the *negative* Laplacian $L(\mathbf{r}) = -\nabla^2\rho$, "negative" because it is convenient to associate concentration with positive values. A typical example is shown in Figure 2-14.

The Laplacian as a second derivative is *very* sensitive to small changes in ρ and reveals features which pass unrecognised by looking at the total electron density itself. Regions of charge concentration appear close to the nuclei and in the valence shells of atoms, of which the latter is of course of interest from the chemical point of view. This *valence shell charge concentration* (VSCC) is pronounced in regions where the chemist would draw electron pairs, bonded and non-bonded. The Laplacian is also used to evaluate the nature of a bond. From the AIM perspective, a bond constitutes a shared interaction (is a covalent bond) when at the BCP the electron density is reasonably high ($\rho_{BCP} > \sim 0.4$ e·Å^{-3}) and the charge is locally concentrated ($\nabla^2\rho_{BCP} < 0$). Conversely, there is a closed shell interaction (non covalent) for low ρ_{BCP} and local charge depletion ($\nabla^2\rho_{BCP} > 0$). These BCP

properties are used to classify also hydrogen bonding interactions in strong, partially covalent, and moderate and weak, mainly electrostatic HBs.

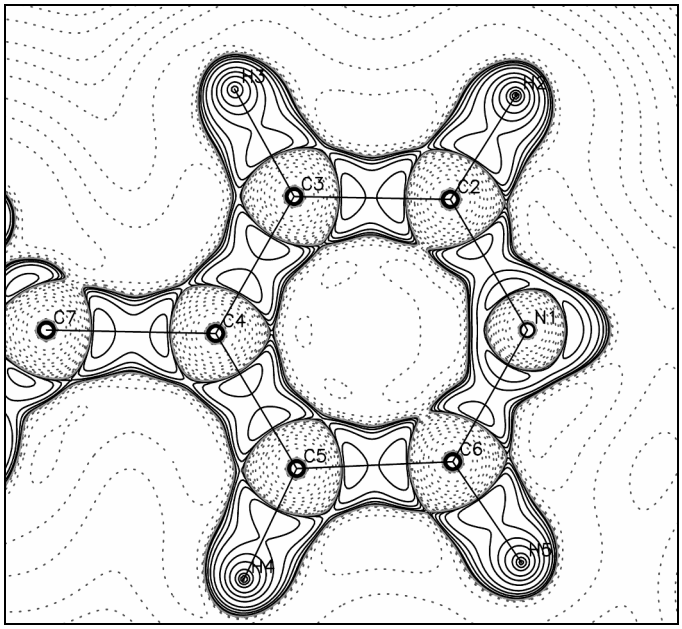

Figure 2-14: Plot of the negative Laplacian, $L(\mathbf{r})$, in the pyridine plane of IN_2–OA; positive contours – solid black, zero levels – solid grey, negative – dotted.

The Source Function

The source function, developed by Bader and Gatti,[56] allows an evaluation of the nature of bonding interactions from a different point of view. It can be obtained from theoretical and experimental charge densities and describes the contribution of a local source, LS to the electron density at any given point **r**. The integral over all local sources, usually evaluated over the atomic basins Ω which constitute the system, thereby equals $\rho(\mathbf{r})$.

$$\mathrm{LS}(\mathbf{r},\mathbf{r}') = -\frac{1}{4\pi}\frac{\nabla^2\rho(\mathbf{r}')}{|\mathbf{r}-\mathbf{r}'|} \qquad (2\text{-}30)$$

$$\text{and } \rho(\mathbf{r}) = \int \mathrm{LS}(\mathbf{r},\mathbf{r}')\,\mathrm{d}\,\mathbf{r}' = \sum_{\Omega}\int_{\Omega} \mathrm{LS}(\mathbf{r},\mathbf{r}')\,\mathrm{d}\,\mathbf{r}' \qquad (2\text{-}31)$$

LS itself, evaluated at a point **r**', corresponds to no more than a distance weighted Laplacian $(1/|\mathbf{r}-\mathbf{r}'|)$. The chemically meaningful information is obtained by integrating LS over the atomic basins, leading to the source contribution S from Ω to **r**.

$$\mathrm{S}(\mathbf{r},\Omega) = \int_{\Omega} \mathrm{LS}(\mathbf{r},\mathbf{r}')\,\mathrm{d}\,\mathbf{r}' \qquad (2\text{-}32)$$

An atom can act as a source (S > 0) or a sink (S < 0) of electron density to $\rho(\mathbf{r})$, which to a first approximation depends on whether charge concentration ($\nabla^2\rho(\mathbf{r}') < 0$) or charge depletion ($\nabla^2\rho(\mathbf{r}') > 0$) dominates in the atomic basin, but, importantly, also on the distribution of the charge concentration within the atomic basin. The absolute contribution to $\rho(\mathbf{r})$ is ultimately dependent on the distance of the atom to the reference point **r**. The reference point can be any point in space, but typically the source function is evaluated for bond critical points as they are unbiased and, of course, also of chemical interest.

The individual source contributions (S) to the electron density at a BCP are found to be characteristic of the type of bonding interaction. S is typically given in percentages of ρ_{BCP}; individual contributions can exceed 100 % since S can be negative, but all sources combined must add up to 100 % (see equation (2-31)), which is also used to check the reliability of the calculated source function. As an example, Figure 2-15 visualises the source function at the HX1···O1 BCP in the strong covalent LBHB in benzoylacetone. The observed large positive contribution of HX1 and the localisation of the source contributions at the hydrogen bonded atoms is characteristic of strong covalent HBs.

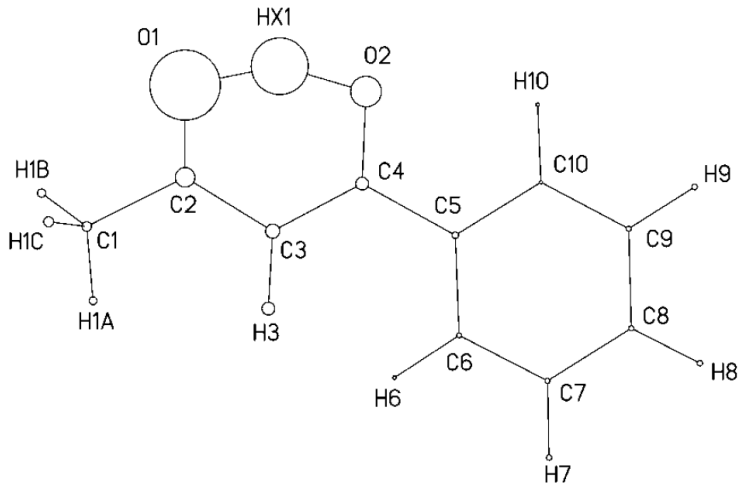

Figure 2-15: Source contributions to the HX1···O1 BCP in the LBHB in benzoylacetone (compare with Figure 1-4), the sizes of the circles representing the atoms are proportional to their source contributions. Figure from reference [78]

Energy Densities

This section describes a method which allows the extraction of hydrogen bond energies from experimental and theoretical charge densities. Abramov[57] proposed a semi quantitative evaluation of the electronic kinetic energy density $G(\mathbf{r})$ by topological analysis of the electron density at a point $\mathbf{r}$:

$$G(\mathbf{r}) = \frac{3}{10}(3\pi^2)^{2/3}\rho(\mathbf{r})^{5/3} + \frac{1}{72}\frac{\nabla\rho(\mathbf{r})^2}{\rho(\mathbf{r})} + \frac{1}{6}\nabla^2\rho(\mathbf{r}) \qquad (2\text{-}33)$$

He showed that for medium range regions (~ 0.5 – 2.1 Å away from the nuclei) the calculated kinetic energy densities using this expression are in good agreement with those calculated from Hartree–Fock wave functions. From the AIM perspective the properties at bond critical points are of special interest, which for moderate and weak HB interactions are typically located in the above medium range. Also, at CPs the gradient equals zero and the middle term in Abramov's equation vanishes. Espinosa *et al*[17] used this formulation to evaluate $G(\mathbf{r})$ of experimentally determined topological properties at intermolecular BCPs of X–H···O HBs (with X = O, N, C). According to Bader and Essen[58] the Laplacian of the electron density $\nabla^2\rho(\mathbf{r})$ is related to the local expression of the virial theorem[a] by

[a] The virial theorem states that the average kinetic energy of a particle in a bound state is in balance with its potential energy $V = -2T_{av}$.

$$V(\mathbf{r}) = \frac{\hbar^2}{4m}\nabla^2\rho(\mathbf{r}) - 2G(\mathbf{r}) \qquad (2\text{-}34)$$

Using this local form of the virial theorem, Espinosa *et al* calculated the potential energies $V(\mathbf{r})$, fitted the data, and set them in relation to the H···O distances. Their results are shown in Figure 2-16. They used this information to extrapolate to a HB distance at which the Laplacian of the electron density $\nabla^2\rho_{BCP}$ is zero. According to AIM, the HB undergoes at this point the change from a closed shell interaction to a shared, i.e. covalent bond. For the evaluated X–H···O HBs they determined this H···O distance to be ~1.33 Å. Vener *et al*[59] later confirmed this value by topological analysis of computed ground state wave functions using the quantum theory of atoms in molecules (QTAIM). They investigated strongly hydrogen bonded materials and calculated for O–H···A interactions the H···O and H···N distances at which $\nabla^2\rho_{BCP} = 0$ to be 1.35 Å and 1.42 Å respectively.

Using dissociation energies from theoretical calculations, Espinosa *et al* also deduced an empirical relation of the HB energy to the potential energy density at the BCP: $E_{HB} \sim -0.5 \cdot V = D_e$. This relation is not valid for the determination of SSHB energies though, since in those cases the BCPs are too close to the nuclei, and the medium range condition for Abramov's approximation (2-33) does not hold anymore. For details on their approach see reference [17]. They furthermore fitted the energy densities and the dissociation energy to the H···O distances, of which the latter is given by: $E_{HB} \sim 25300 \cdot \exp(-3.6 \cdot d(\text{H}\cdots\text{O}))$. Although many approximations are involved in this method, it offers a means of quickly obtaining reasonable estimates for HB energies for moderate and weak HBs from the topological analysis of experimental electron densities, and from the H···O distance.

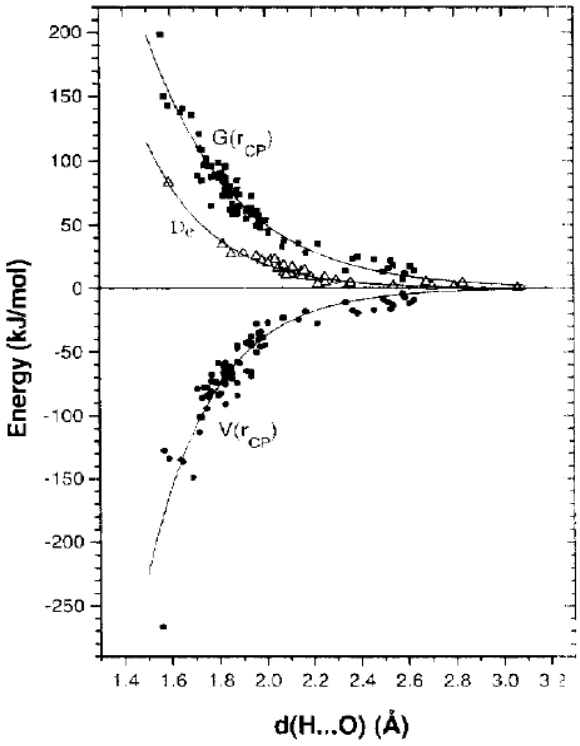

Figure 2-16: Kinetic energy density $G(\mathbf{r}_{CP})$, potential energy density $V(\mathbf{r}_{CP})$, and calculated dissociation energy D_e in dependence of the H···O distance. Figure from reference [17]

3. MOLECULAR COMPLEXES OF ISONICOTINAMIDE WITH OXALIC ACID

The molecular complexes of isonicotinamide (IN) with oxalic acid (OA) are the most thoroughly studied in this work. The system shows some unusual behaviour concerning the hydrogen bonding scheme and a tendency towards the appearance of polymorphism, both of which are enhanced upon isotopic H/D substitution. Altogether four different polymorphic forms have been found and characterised to date by X-ray diffraction, two hydrogenous and two deuterated. In addition to the standard structure determination, on the hydrogenous forms charge density analyses have also been carried out in combination with variable temperature neutron diffraction experiments. The structural work has been complemented by ab-initio ground state energy and quantum molecular dynamics studies with the aim to explain some of the unusual findings mentioned above.

IN and OA form molecular complexes in the ratio 2 : 1, abbreviated as IN_2–OA from hereon. The original crystal structure, the hydrogenous Form I, was initially determined by X-ray diffraction and published by Vishweshwar *et al*.[60] It had been part of a work in the field of crystal engineering, where rules for the prediction and formation of hydrogen bonded motifs were evaluated. Vishweshwar *et al* confirmed here that, for a series of co-crystallisation experiments of IN with *n*-alkanedicarboxylic acids, *Etter's rule*[61], [a] was obeyed. From our perspective, the strong hydrogen bonding between IN and OA was of interest, which required a more in depth structural analysis which will be described in the following.

3.1. HYDROGENOUS POLYMORPHS

3.1.1. X-ray Studies

The hydrogenous forms of the molecular complex IN_2–OA crystallise in the two polymorphs:

IN_2–OA Form I $\equiv (C_6H_6N_2O)_2 \cdot H_2C_2O_4$ [60]

IN_2–OA Form II $\equiv (C_6H_6N_2O)_2 \cdot H_2C_2O_4$ [62]

Crystals of the original structure (Form I) were obtained from a 1 : 1 mixture of water and ethanol upon slow evaporation of the solvent.[60] Upon reproduction, the previously unknown Form II was found to literally co-crystallise from the same solution. Both forms also co-crystallise from only water, precipitating slower and yielding crystals of better quality. Form I crystallises with block or plate shaped morphology in the space group C2/c; and Form II with a needle/stick shaped in $P\bar{1}$. It has been observed that the needle shaped crystals of Form II crystallise prior to Form I; and that they start to disappear, if very slowly on a timescale of weeks, once the first crystals of Form I start to appear. It appears that, at present experimental conditions, Form I is the energetically favoured and Form II the kinetically favoured polymorph.

[a] Stating that the best proton donors and acceptors remaining after intramolecular HB formation form intermolecular HBs to one another.

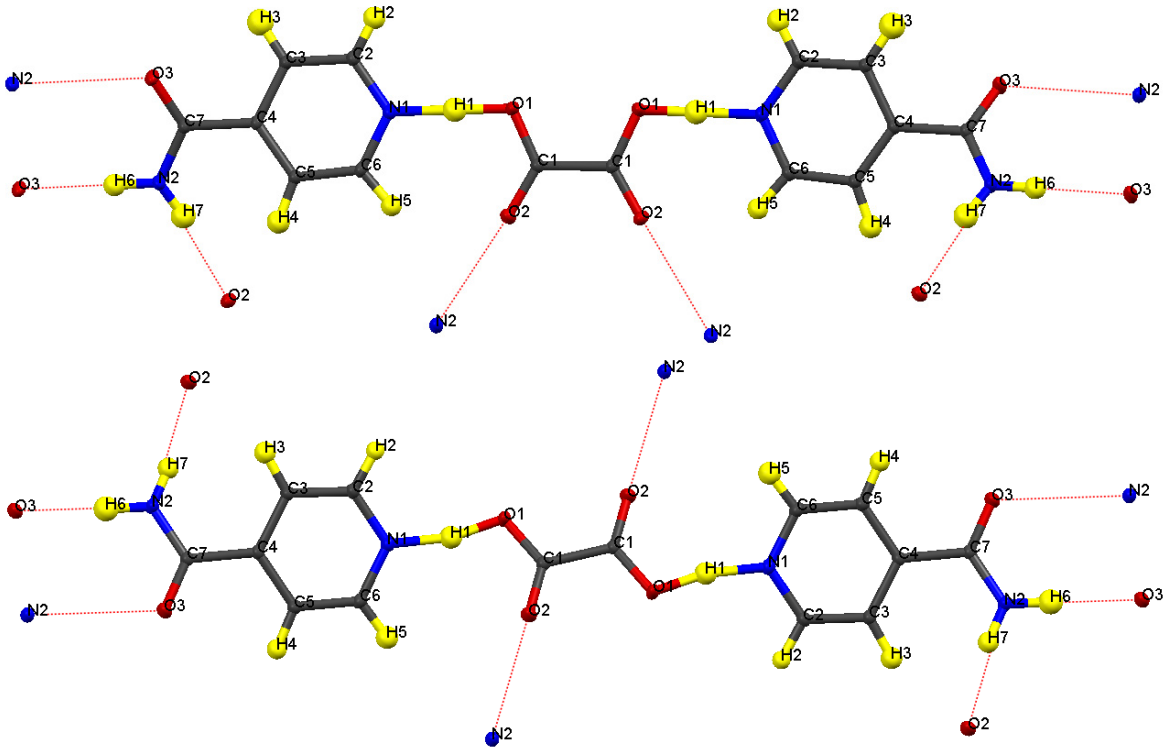

Figure 3-1: Formula units of IN_2–OA including the HB schemes indicated by dotted lines; (top) *cis*-form, Form I; (bottom) *trans*-form, Form II.

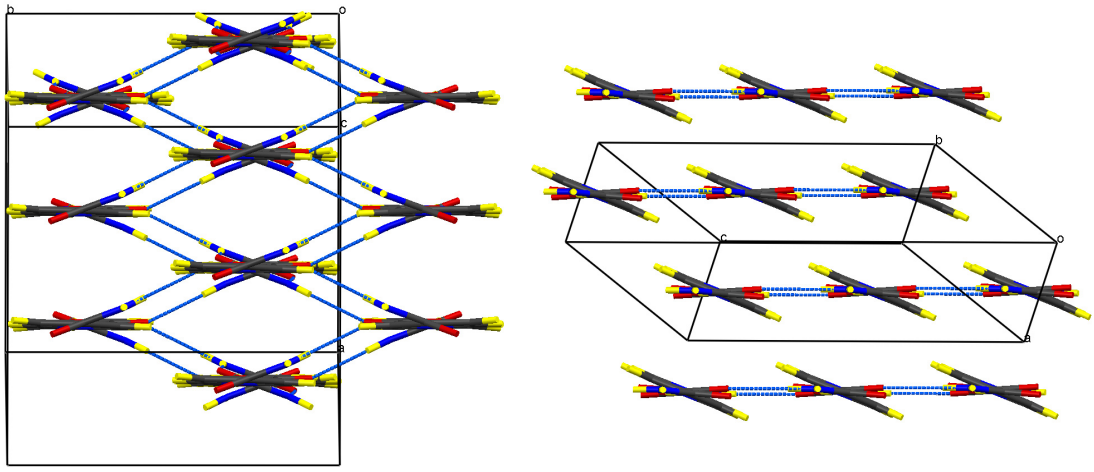

Figure 3-2: Packing schemes of IN_2–OA, viewed along the –IN–OA–IN– chains; (left) Form I, (right) Form II, HBs are shown in blue dotted lines.

Both forms have common principal features of the hydrogen bonded motif. This consists of hydrogen bonded chains in which each carboxylic acid group of OA is strongly hydrogen bonded to the pyridine N of IN, giving rise to the formation of a short, strong hydrogen bond (SSHB) O1··H1··N1. IN in turn, is hydrogen bonded to another molecule of IN via the moderate amide–amide (diamide) interaction, N2–H6···O3. The chains of $(–IN–OA–IN–)_n$ thus formed are then crosslinked by further moderate HBs, N2–H7···O2, which originate from the second amide H to the carbonyl oxygen of OA. The key

difference is a *cis*/*trans* isomerism of the oxalic acid hydroxyl groups by which the two polymorphs can intuitively be classified into a *cis*-form and a *trans*-form respectively, as shown in Figure 3-1.

The OA unit lies on a symmetry element in both polymorphs: a 2-fold axis in Form I, and an inversion centre in Form II, dictating the *cis*/*trans* isomerism of the OH group and furthermore rendering the two strong HBs formed by the OA symmetry equivalent. There are additional inversion centres situated in the centres of the diamide HBs in both forms. The main structural difference regarding possible properties of the two forms, however, manifests in the extended hydrogen bonded structure which is formed by the amide–OA HBs (N2–H7···O2). The –IN–OA–IN– chains arrange in Form I into a 3-dimensional hydrogen bonded network and in Form II into a 2-dimensional layered structure (Figure 3-2). This structural difference is reflected in the orientation of the "interchain HB" acceptor molecules OA towards the amide donor groups. In Form I, OA is roughly coplanar with the pyridine ring and thus rotated out of the plane spanned by the amide group.[a] As a result, the carbonyl O lone pair is not exactly directed towards the N–H donor and has no preferences as to whether to form a HB in a direction slightly above or below the plane in which the OA molecules and the pyridine rings lie. In Form II on the other hand, OA is rotated out of the pyridine plane by ~28º, but is coplanar with the amide group. Thus, the N–H donor group here points more directly towards the carbonyl O lone pair (see Figure 3-2), which results in a slightly stronger HB interaction and a ~0.1 Å shorter N2···O2 distance.

Form I

As indicated earlier, the original crystal structure (determined at 150 K) promised some interesting features regarding the strong hydrogen bonding between the OA hydroxyl groups and the pyridyl N atom. With a heteroatom distance of O1···N1 = 2.564(1) Å in a near linear geometry, the HB O1··H1··N1 can be regarded as a SSHB. Vishweshwar *et al* localised the H atom near the O atom but with a considerable shift towards the centre of the HB, refining the O1–H1 distance to 1.18(2) Å, and the H1···N1 to 1.38(2) Å. The refined HB parameters have been obtained from the data deposited in the Cambridge Structural Database (CSD),[63] whereas reference [60] interestingly refers to "neutron normalised" X–H distances only, and consequentially gives the H1···N1 distance as 1.58 Å.

In order to obtain a more detailed picture of the electronic structure in this SSHB, the structures have been redetermined from a low (100 K) and a high temperature (RT) X-ray diffraction experiment. For both datasets the resolution was set to d = 0.64 Å, equivalent to 2θ = 68º or $\sin\theta/\lambda$ = 0.78 Å^{-1} (for comparison of the different resolution notations see Figure 2-5). All positional and atomic displacement parameters (ADPs) including those for the H atoms have been refined – with the exception of the ADP for H1, see discussion below. The final R_1 values are 3.83 % and 6.84 % for all data, for the 100 K and RT data respectively (see Appendix B, Table B-1). On a side note, the RT data would have normally been cut off at a lower resolution, but were stretched in this case to match the resolution of the low T structure for a better comparison.

[a] The amide group in IN is generally rotated against the pyridine ring by ~25º to minimise the contact between the amide and the α-C H atoms.

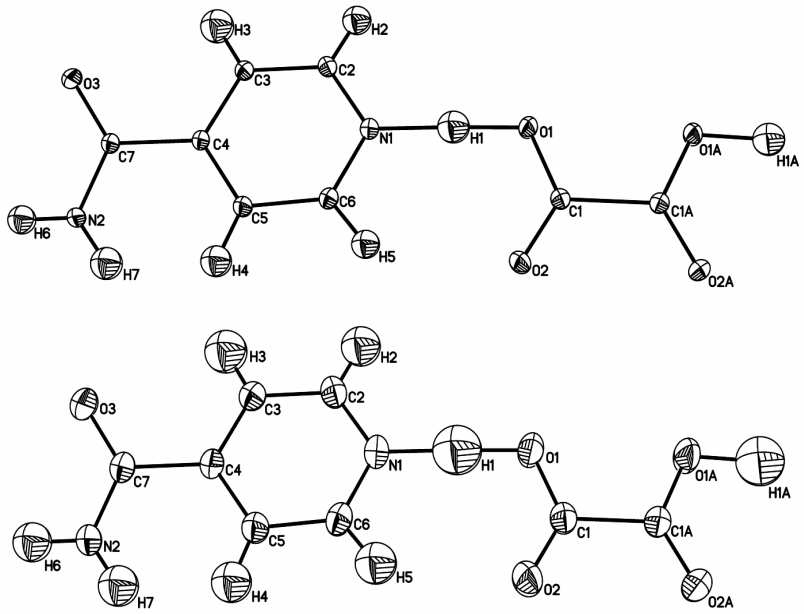

Figure 3-3: Asymmetric units of IN_2–OA Form I for the 100 K (top) and RT (bottom) data, for clarity the OA molecules have been completed by applying the corresponding symmetry, the ellipsoids are at the 50 % probability level.

A comparison of the ORTEP[a] like ellipsoid plots for the low and high temperature data is shown in Figure 3-3. Aside from the naturally higher ADPs for the RT structure, no significant structural differences can be observed between the two temperatures. The small decrease in volume per formula unit IN_2–OA ($\Delta V/Z$) of ~12 Å^3 upon cooling from RT to 100 K manifests, as expected, in shorter intermolecular distances and here in particular in a reduction of the pyridine–pyridine π–π contacts by ~0.1 Å. The moderate strength diamide and amide–carbonyl HBs, and the SSHB are less affected and only shortened by 0.02 – 0.03 Å. The corresponding HB parameters are listed in Table 3-1 at the end of this section.

The SSHB parameters for the 100 K structure refine to O1–H1 = 1.19(1), H1···N1 = 1.36(1), and D(O1···N1) = 2.549(1) Å, agreeing well with those determined by Vishweshwar *et al* for T = 150 K. At RT, the heteroatom distance is lengthened slightly to D = 2.574(1) Å, and the H atom refines to a position closer to the centre of the HB (if statistically not significant): O1–H1 = 1.23(2) and H1···N1 = 1.34(2) Å (Table 3-1). Refining H parameters often leads to biased and wrong results as described earlier. This is especially true for strong HBs where the H atom can occupy a large volume element in the broad and flat potentials typical of SSHBs (see 1.2 *Strong Hydrogen Bonds*), which then further enhances the intrinsic delocalisation of the H electron density. For this reason H1 has been refined with a constraint placed on the isotropic displacement parameter to 150 % of O1. Without this constraint, H1 consistently refines to a position in the centre of the SSHB with a large displacement parameter. The approach has been chosen to find H positional parameters which reflect a region of "highest" electron density rather than modelling as much electron density as possible, thereby improving the fit between F_{obs} and F_{calc} and lowering the R values. Despite this, H parameters refined in this way still have to be treated with care.

[a] Oak Ridge Thermal Ellipsoid Plot (ORTEP)

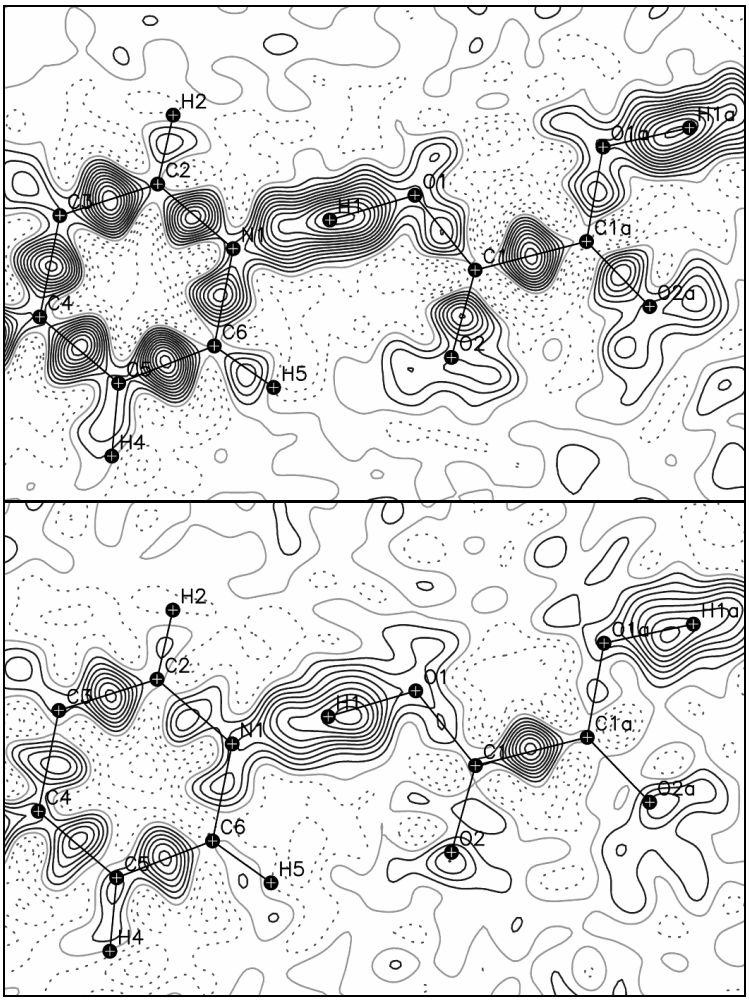

Figure 3-4: Electron difference Fourier maps for the 100 K data (top) and RT (bottom) of IN_2–OA Form I in the C1–O1–N1 plane, obtained after omitting H1 from the refinement, H1 points to the previously refined position, maps for $F_{obs} > 4\sigma(F_{obs})$, $\sin\theta/\lambda < 0.78$ Å^{-1}; positive contours – solid black, zero levels – solid grey, negative – dotted, contours at 0.05 eÅ^{-3}.

When determined on the basis of X-ray diffraction, a better way of retrieving qualitative (and quantitative!) information on H atoms is to image the H electron density by means of electron density difference Fourier maps. Such maps are generated by calculating the difference electron density after omitting the H atom(s) of interest from the refinement. For H1, this procedure results in the difference Fouriers shown in Figure 3-4 for the 100 K and RT data. They document the typical charge transfer effects giving rise to electron density accumulation in the covalent bonds, and also in the lone pair regions of the carboxylic acid oxygen atoms. They are less pronounced for the high T data, because thermal motion naturally increases the electron delocalisation; yet the features are qualitatively the same for low and high T. With respect to the electronic structure of the SSHB, the difference Fouriers reveal a very high electron density delocalisation for H1 that almost spans from the pyridyl N to the carboxylic O atoms, with a small electron density accumulation near the O atoms. A visual inspection of the maps reveals furthermore that the refined H1 positions are slightly shifted away from the electron density maxima towards the HB centres. This shift is pronounced for the high T structure. In addition to the unusual high electron density delocalisation, the total electron density in the SSHB is only marginally higher than that observed on the covalent bonds, a finding which becomes

pronounced when comparing the density for H1 with that for the other H atoms in the structure (Figure 3-5).

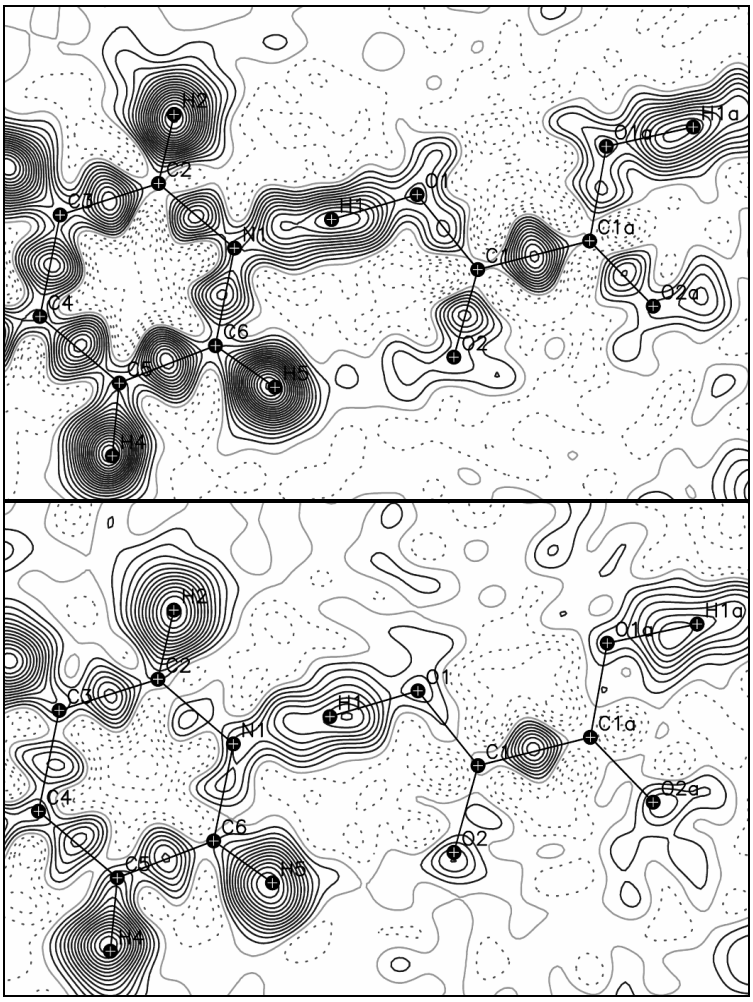

Figure 3-5: Difference Fourier maps for IN_2–OA Form I after refinement without H1–H5; (top) 100 K, (bottom) RT data; $\sin\theta/\lambda < 0.78$ Å^{-1}, for details see Figure 3-4.

The difference Fourier maps in Figure 3-5 were obtained after refinement also in the absence of the pyridine H atoms. They illustrate nicely, that in comparison with H1 in the SSHB, the pyridine H not only show more distinct density maxima, but also considerably higher absolute densities. This pronounced relative charge concentration does not seem to be caused by better localised H nuclei, as a visual estimation of the difference maps does not bear any evidence for smaller volumes for the pyridine H atoms as such. As a result, the charge on H1 in the SSHB is significantly depleted to a degree which cannot be accounted for by a delocalisation of the H nucleus only. The observations from imaging the electron density in the SSHB can be summarised as:

- a high electron density delocalisation with a small accumulation at the O site
- a low absolute electron density

The self-evident explanation to the above is that the H atom is disordered over two sites, which also makes perfect sense from the chemical point of view. The pK_a values for HOOC–COOH, HOOC–COO^-, and protonated IN are 1.2, 4.2, and 3.6 respectively. HOOC–COOH is a sufficiently strong acid to protonate IN, and HOOC–COO^- is too weak

an acid to protonate the second IN. The average structure can subsequently be formulated as IN···HOOC–COO$^-$···H$^+$IN, and the H atom will appear as delocalised over two sites as long as the H is statistically disordered and there is no long range ordering of the H atoms.[a] Refinement of an H disorder model leads to an approximate 60 : 40 disorder in favour of the O- over the N-site (the site occupation factors and coordinates have been allowed to refine, and the ADPs have been constraint to be equal for both sites). Within the limits of the method the refined positional H parameters and site occupancies appeared reasonable. In the end however, and informed by the neutron diffraction studies (H1 is not in fact disordered but well localised at the O atom! see 3.1.2 *Neutron Studies* below), the H1 parameters were refined to a single site with the isotropic ADP fixed to 150 % of O1 as described earlier.

In the absence of reliable H positions, geometrical criteria based on the parameters of the "heavier" elements C, N, and O (which are determined by X-ray diffraction with sufficient accuracy) can aid in the evaluation of the HB configurations. Here, the C–O distances of the carboxylic group and the CNC bond angle of the pyridine ring are indicative of the protonation states of the OA and IN respectively. In protonated carboxylic acids, the C–O(H) and C=O bond lengths range from 1.30 – 1.32 and 1.20 – 1.22 Å respectively, while in the resonance structure of the carboxylate anion, both distances approximate values around 1.24 – 1.26 Å. An additional margin of ±0.1 Å has to be considered if strong HB interactions are involved, or if intermolecular interactions are absent altogether. In the current low T structure, the C1–O1 and C1–O2 distances of 1.294(1) and 1.222(1) Å respectively, suggest that OA rather exists in its molecular form. Pyridine groups show CNC bond angles of ~116 – 124º in moving from unprotonated to fully protonated species, in accordance with structures deposited in the CSD.[63] The absolute values depend to a degree on substituents on the pyridine ring; for IN they range from ~116º to 122.5º of which the latter are found for fully protonated IN species in the tetrachloroplatinate and the nickel bis(dithio-oxalato) complexes.[64, 65] In IN_2–OA, the C2–N1–C6 bond angle of 119.67(6)º lies midway between the two extremes, which would indeed be supportive of the above H disorder model. The transition for these geometrical heavy atom parameters varies smoothly with the H transfer coordinate as has previously been shown for example by Majerz and Koll,[66] and as will be documented later based on quantum mechanical calculations in 3.1.4 *Ab Initio Studies*.

Form II

The interpretation of the X-ray diffraction experiments on Form II follows largely that on Form I. As for Form I, the X-ray structures have been determined at 100 K and RT, and refined to 4.74 % and 6.50 % respectively, to a resolution of $\sin\theta/\lambda$ = 0.78 Å^{-1}. The refinement procedure follows that described for Form I, which is that all parameters have been refined except that the isotropic displacement parameter for H1 has been constrained to 150 % of that of O1. The ellipsoid plots are shown in Figure 3-6.

[a] There is no crystallographic evidence for such a long range order, no additional weak reflections suggesting a superstructure are observed, and refinement with a lower symmetry (Cc) results in the same electron density delocalisation.

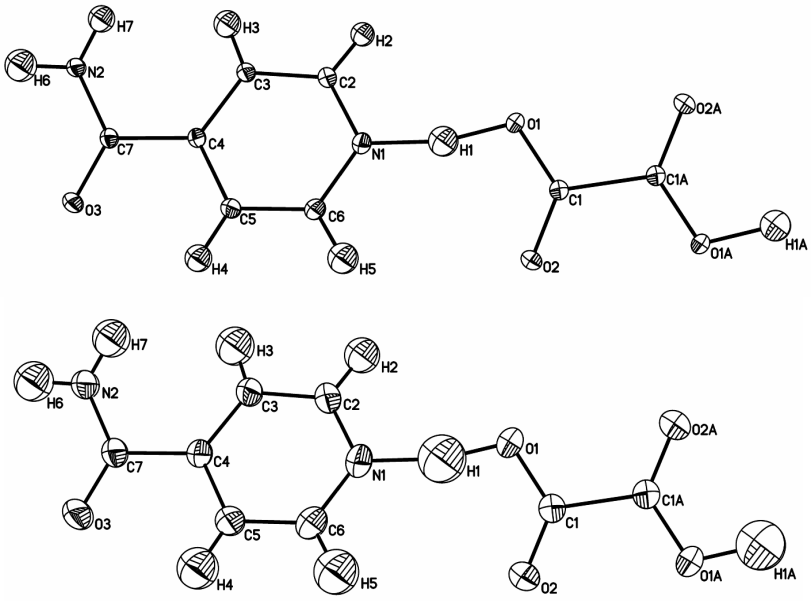

Figure 3-6: Asymmetric units of IN_2–OA Form II for the 100 K data (top) and RT (bottom), for details see Figure 3-3.

Despite the structural differences between Form I and Form II described earlier, they share many common features. The volume contraction upon cooling of $\Delta V/Z \sim 12$ Å^3 is nearly identical, and also affects the intermolecular interactions in the same way as in Form I. In Form II, the SSHB is less linear with an OHN bond angle of ~167º compared to ~176º in Form I, as apparent in Figure 3-1 and Figure 3-6. The HB parameters for the SSHB refine for the 100 K structure to D = 2.529(1), O1–H1 = 1.20(1), H1···N1 = 1.35(1) Å; and for the RT to D = 2.554(1), O1–H1 = 1.16(2), H1···N1 = 1.42(2) Å respectively (Table 3-1). Although the heteroatom separations are shorter by ~0.02 Å, the distances from H to the hydrogen bonded atoms refine to remarkably similar values to those in Form I. Adding up the O1–H1 and H1···N1 bond lengths for both forms yields 2.55 Å for the 100 K data and 2.57/2.58 Å for the RT. Thus, on the basis of the refined HB parameters, the HB strengths can be considered to be similar, and the shortened O1···N1 distance in Form I is due to a reduced linearity of the SSHB.

However, in view of the difference Fourier maps in Figure 3-7, some qualitative differentiation can be made. First, in the 100 K structure the electron density maximum for H1 is shifted towards the N site, and in the RT structure the electron density clearly shows two well separated maxima in the SSHB, strongly favouring a split site for H1. Second, the H1 atoms refine to positions closer to the O site and thereby do not coincide well with the electron density maxima as evident from Figure 3-7. Refining the H1 atom with the same disorder model used for Form I, results in a ~ 50 : 50 disorder for the RT data, and also for the 100 K.

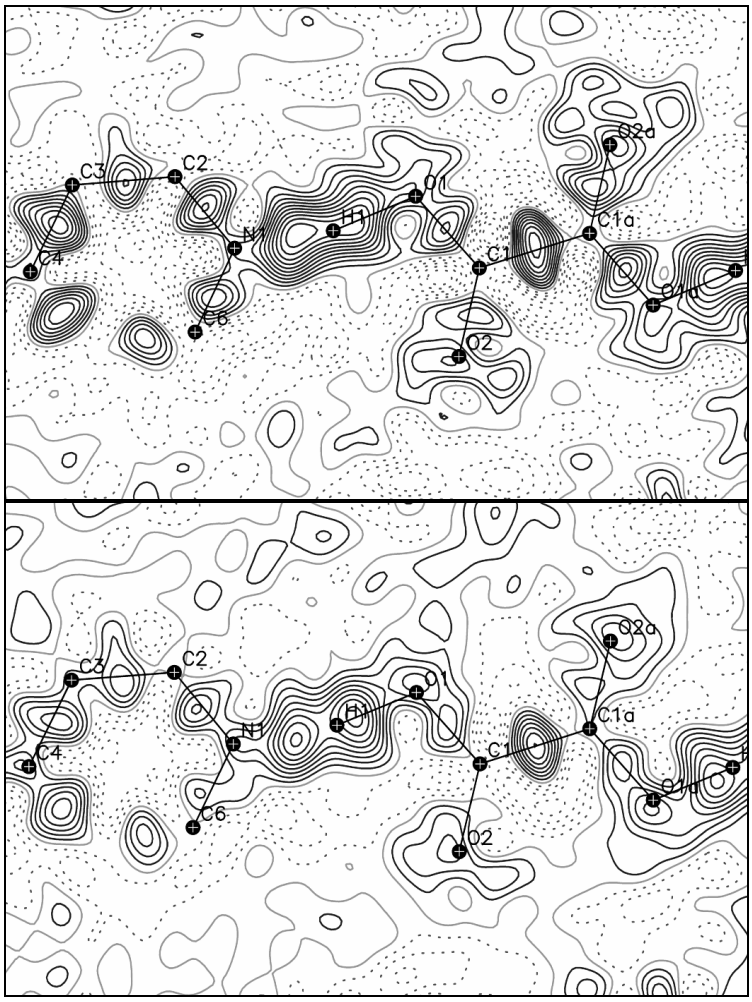

Figure 3-7: Electron difference Fourier maps for the 100 K data (top) and RT (bottom) of IN_2–OA Form II in the C1–O1–N1 plane. Note that the pyridine ring is rotated out of the OA plane by ~28º; $\sin\theta/\lambda <$ 0.78 $Å^{-1}$, for details see Figure 3-4.

Again, an interpretation of refined H parameters in the SSHBs has to be taken with care, especially when the H disorder model is used to describe the very low electron densities in the current case. For now, and in view of the neutron data, the disorder model is not pursued further at this point, but H1 is assumed to occupy a single site if situated in a more central position in the SSHB. The latter statement is not only deduced from the difference Fouriers but also from the C–O bond lengths and the CNC bond angle, which are characteristic of the protonation states of the participating molecules. They refine to C1–O1 = 1.289(1) Å, C1–O2 = 1.223(1) Å, and C2–N1–C6 = 119.92(7)º respectively, and are hence more ambiguous towards a definite localisation of the H atom in comparison with the values found for Form I. They support the above observations that the H atom occupies a more central position in the SSHB, or is indeed disordered over two sites.

Table 3-1: HB parameters for IN_2–OA (X-ray data).

	T	HB	D–H / Å	H···A / Å	D···A / Å	∠DHA / °
Form I	100K	O1–H1···N1	1.194(13)	1.357(13)	2.5493(8)	176.3(12)
		N2–H6···O3*	0.922(13)	1.987(13)	2.9026(8)	171.8(12)
		N2–H7···O2*	0.895(14)	2.104(14)	2.9933(8)	172.0(12)
	RT	O1–H1···N1	1.23(2)	1.34(2)	2.5735(12)	174.8(16)
		N2–H6···O3*	0.954(17)	1.981(17)	2.9296(12)	172.7(14)
		N2–H7···O2*	0.904(17)	2.128(18)	3.0258(14)	172.1(14)
Form II	100K	O1–H1···N1	1.200(14)	1.346(14)	2.5292(10)	166.9(13)
		N2–H6···O3*	0.975(16)	1.924(16)	2.8987(10)	177.9(14)
		N2–H7···O2*	0.925(14)	1.978(14)	2.8948(11)	170.7(13)
	RT	O1–H1···N1	1.157(18)	1.415(18)	2.5541(11)	166.5(16)
		N2–H6···O3*	0.951(16)	1.967(16)	2.9179(12)	178.5(14)
		N2–H7···O2*	0.922(16)	2.007(16)	2.9183(12)	169.7(14)

* Atoms generated by symmetry.

3.1.2. Neutron Studies

The above X-ray studies only allow comparative statements regarding the H position in the discussed SSHB O1··H1··N1. There is no clear answer to the question of whether the H has been transferred from the carboxylic acid to the pyridine base; and in case of H transfer the question remains to which degree. 50 % H transfer corresponding to the 50 : 50 H disorder model seems to be a reasonably good estimate from the analysis of the X-ray data. But there are still qualitative uncertainties, and quantitative statements like accurate H positional parameters are beyond the scope of X-ray diffraction in such ambiguous delocalised systems. The purpose of the neutron diffraction experiments was therefore to retrieve accurate positional and displacement parameters for the H1 atom (and site occupancies in case of H disorder) and to investigate any possible H transfer effects upon variation in temperature. The availability of accurate H parameters, in particular for the H atom involved in the SSHB, is furthermore very important for the charge density studies discussed later.

Form I

A variable temperature single crystal neutron diffraction experiment on Form I was performed on the SXD instrument[67] at the RAL ISIS neutron spallation source, using the time of flight (TOF) Laue method. Form I crystallises with block/plate shaped morphology and yields good quality, neutron sized crystals of which a block shaped sample with the dimensions $3 \times 2 \times 2$ mm^3 was used for the data collection. On the same crystal, datasets were collected at five temperatures 30, 100, 200, 300, and 350 K. The data were processed with the program SXD2001,[67] a dedicated software package which has specifically been designed for use with the SXD instrument. The structures were subsequently refined against the TOF multi-wavelength datasets with SHELXL.[39] The positional and anisotropic displacement parameters of all atoms, naturally including those

of the H atoms, were refined; crystallographic details for the refinement of all datasets can be found in Appendix B, Table B-2.

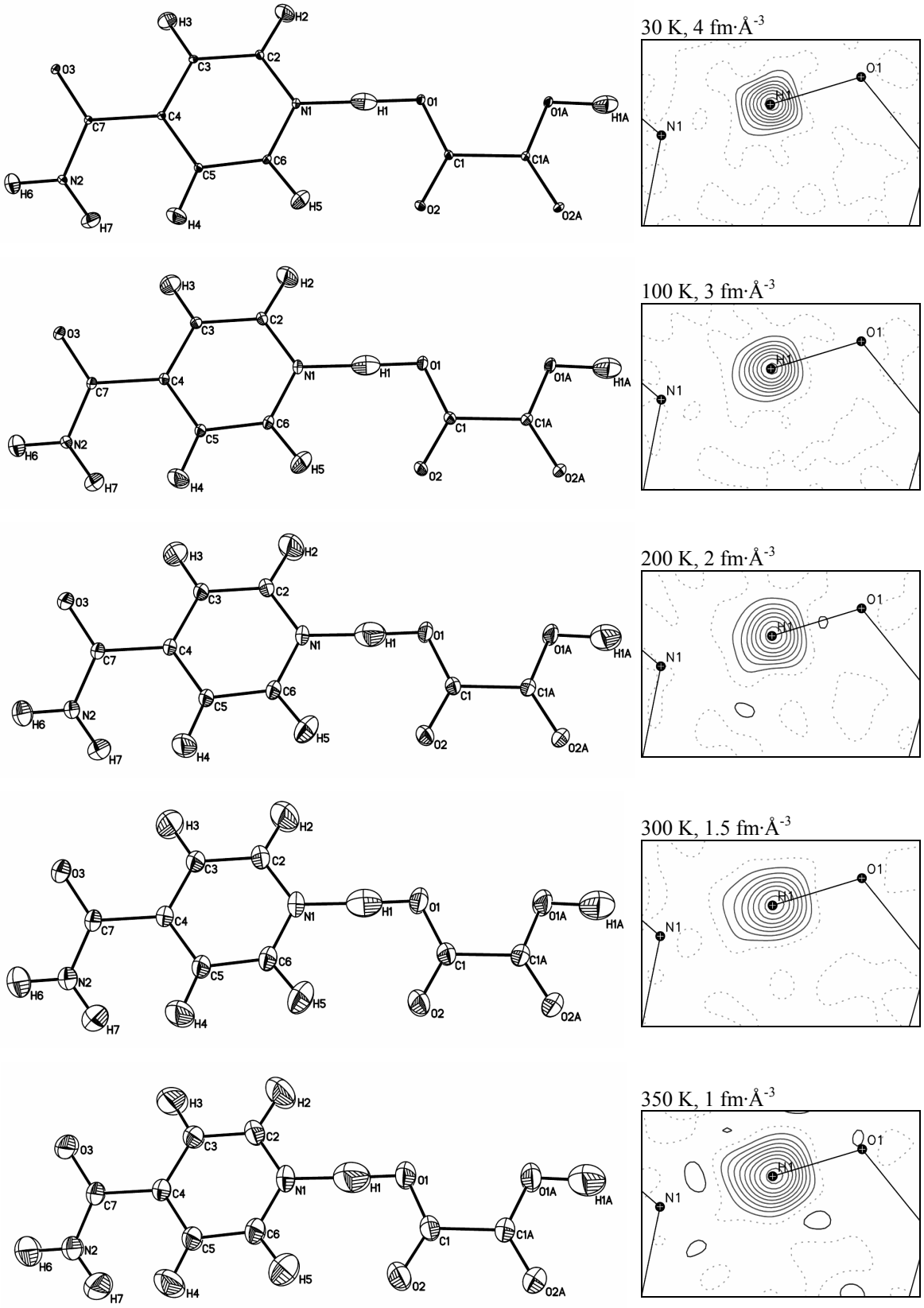

Figure 3-8: (Left) ellipsoid plots for the neutron data in IN_2–OA Form I, ellipsoids at the 50 % level. (Right) difference Fourier maps for all observed data ($F_{obs} > 4\sigma(F_{obs})$) in the C1–O1–N1 plane after omitting H1 from the refinement model; temperatures and contour levels are given above the maps; positive contours – solid black, zero levels – dotted, negative contours – solid grey.

Figure 3-8 shows the ellipsoid plots for the different temperatures alongside the difference Fourier maps for the H nucleus of interest, i.e. H1 in the SSHB. The difference Fourier maps for the nuclear densities are generated according to the same procedure described for the X-ray data above by omitting H1 from the refinement prior to calculation of the maps. Note that the nuclear H densities appear as "holes" in the maps because the H nucleus has a negative scattering factor.

Neither low nor high temperature neutron data indicate any disorder of the H1 nuclear density, as evident from the difference Fourier maps (Figure 3-8). The ADPs are slightly elongated in the direction of the HB path with a small increasing trend towards higher temperatures. However, this elongation is of no greater extent than that in the out of plane direction and is frequently observed in short HBs. Furthermore, the nuclear densities are of the same magnitude, if marginally smaller, than those for the other H atoms in the structure (see Figure 3-9), so that one cannot even observe a significant delocalisation of the H nucleus in the SSHB. On the contrary, the H1 appears to be well localised at low *and* high temperatures. Taken together with the shortening of the covalent bond at high T (see discussion below), this rules out both H migration and H disorder in the current system. This is seemingly in disagreement with the X-ray data which show a strong delocalisation of the electron population in this HB. It is furthermore in disagreement with some of the ab-initio calculations which will be described later.

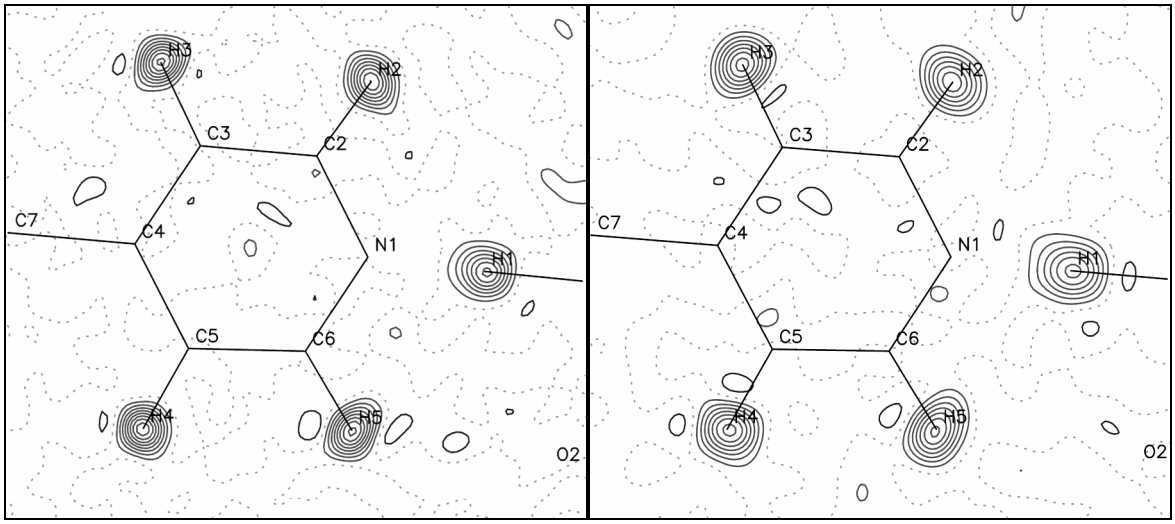

Figure 3-9: Difference Fourier maps for IN_2–OA Form I in the pyridine plane for all observed data ($F_{obs} > 4\sigma(F_{obs})$) after refinement without H1–H5; (left) 100 K , (right) RT structure; positive contours – solid black, zero levels – dotted, negative contours – solid grey, contour levels as in Figure 3-8.

Table 3-2 summarises the HB parameters as refined for the variable temperature neutron datasets. For all temperatures, H1 shows the shift towards the bond centre that is typical of strong HBs. At 30 K the covalent O1–H1 bond is lengthened to 1.165(3) Å with a short H1···N1 distance of 1.390(3) Å in a near linear geometry (O1–H1···N1 = 178.3(2)º). As the O1···N1 separation increases with temperature from D = 2.556(1) Å at 30 K to D = 2.582(2) Å at 350 K, the covalent bond length decreases to 1.148(5) Å and the actual hydrogen bond length increases to 1.434(4) Å in agreement with simple bond valence arguments.[68]

Table 3-2: HB parameters for IN_2–OA Form I (neutron data).

	T	HB	D–H / Å	H···A / Å	D···A / Å	∠DHA / °
Form I	30K	O1–H1···N1	1.165(3)	1.390(3)	2.5555(11)	178.3(2)
		N2–H6···O3*	1.0289(19)	1.889(2)	2.9138(11)	173.4(2)
		N2–H7···O2*	1.015(2)	1.988(2)	2.9957(11)	171.81(19)
	100K	O1–H1···N1	1.161(3)	1.398(3)	2.5587(16)	178.2(3)
		N2–H6···O3*	1.027(2)	1.894(2)	2.9165(16)	173.3(2)
		N2–H7···O2*	1.013(2)	1.997(3)	3.0024(17)	171.8(2)
	200K	O1–H1···N1	1.152(4)	1.415(4)	2.5666(17)	178.2(4)
		N2–H6···O3*	1.030(3)	1.897(3)	2.9209(17)	172.7(3)
		N2–H7···O2*	1.009(3)	2.013(3)	3.0151(19)	171.6(3)
	300K	O1–H1···N1	1.148(4)	1.430(4)	2.5768(17)	178.2(4)
		N2–H6···O3*	1.025(3)	1.911(3)	2.9311(17)	173.2(3)
		N2–H7···O2*	1.011(3)	2.027(4)	3.030(2)	171.3(3)
	350K	O1–H1···N1	1.148(5)	1.434(4)	2.5821(19)	178.0(4)
		N2–H6···O3*	1.028(3)	1.918(3)	2.9397(18)	172.5(4)
		N2–H7···O2*	1.015(3)	2.029(4)	3.036(2)	170.8(3)

* Atoms generated by symmetry.

A comparison of the neutron HB parameters with the corresponding X-ray data obtained at 100 K is also of interest, of course. The heteroatom distance refines to D = 2.559(2) Å and is thereby 0.01 Å longer than that determined by X-rays (D = 2.549(1) Å). This deviation between the positional parameters refined from the nuclear and electronic densities is of the magnitude which has been observed for elements like C, N, and O in earlier studies (see for example reference [38]). The covalent and hydrogen bond lengths are 1.161(3) and 1.398(3) Å respectively, which are close to those determined from X-rays (1.19(1) and 1.36(1) Å), and demonstrate that the refinement model used for the low temperature X-ray data yields approximately correct positional parameters for H1. Of the heavy atom parameters, which are indicative of the protonation states of OA and IN, the C–O(H) distance shows the largest discrepancy. The neutron and X-ray bond lengths for C1–O1 are 1.2897(16) and 1.2944(8) Å respectively; and the shorter neutron distance partially accounts for the longer O···N separation. A full description of the variation of bond lengths upon different diffraction techniques is presented later in 3.1.3 *Charge Density Studies* (Figure 3-14). A comparison of the RT data is less instructive, because of the higher experimental errors, especially those associated with the X-ray determined H parameters. With respect to the SSHB, the observations from the analysis of X-ray and neutron data on Form I can now be summarised as:

- a high electron density delocalisation with a small accumulation towards the O site
- a low absolute electron density
- a well localised nuclear density of H1 close to the O site
- no H transfer reaction in this complex

The apparent inconsistency in the description of the SSHBs provided by nuclear and electronic densities requires explanation. In particular the question needs to be answered as to where the significant "amount" of electron density near the N site originates from, if not from the H. One seemingly obvious explanation is that N lone pair density is observed, which is not accounted for by the aspherical atom model. But such high density levels for lone pairs have, to the knowledge of the author, not been reported before; in any case not from standard X-ray diffraction experiments within the resolution range used here – high resolution charge density studies on the other hand, do reveal and actually model lone pair densities, see 2.1.4 *X-ray Charge Density Analysis*. Especially in comparison with the lone pair densities observed for the O atoms, the N lone pair density should not be pronounced to the degree it is in Figure 3-4 and Figure 3-5. The current explanation for the phenomenon of the high electron density near the N atom is a superposition of N lone pair density with bonding density that originates from the H1···N1 interaction which is known to have partly covalent character for SSHBs (see 1.2 *Strong Hydrogen Bonds*). The lone pair is also likely to be strongly polarised in this strong HB interaction giving rise to a further concentration of charge at this point. Furthermore, the low absolute electron density for the well localised H nucleus can now be explained by the additional charge transfer from H1 into the H···N interaction. This is supported by population analysis of the ground state wave function calculated for the 100 K neutron geometry (described later in 3.1.4 *Ab Initio Studies*). O1–H1 and H1···N1 Mulliken bond populations of 0.18 and 0.12e respectively, and a total H1 Mulliken population of 0.54e confirm the enhanced covalence of the SSHB and the experimentally observed charge transfer into the hydrogen bonding interaction. For comparison, the N2–H6, H2···O3 and H6 populations in the longer amide–amide HB are 0.28, 0.06 and 0.66e respectively.

To support this idea, X–(X+N) and X–N deformation densities have been calculated according to the description in 2.1.4 *Deformation Densities*. For the X–(X+N) map in Figure 3-10, top, the H parameters are taken from the neutron refinement, and all others from the X-ray refinement. The H ADPs were additionally scaled to the X-ray data with the program UIJXN.[44] The X–(X+N) map differs from the X–X difference map in Figure 3-4, top, insofar as atom H1 and the information on accurate H parameters is included. It shows a few additional features. First, bonding density becomes apparent in all X–H bonds, including the O1–H1 covalent bond. Second, the electron density near the N site now "looks" like N lone pair density, i.e. the maximum is closer to the pyridyl N atom and has a lower absolute value – if still much stronger than the O lone pair densities. Imaging the X–(X+N) deformation densities thus reveals valuable information otherwise missed, especially with respect to the SSHB. This statement seems a bit unfair since the above X–(X+N) map can be qualitatively reproduced from X-ray only data by including the atom H1 in the refinement (as it was modelled in the end). But in view of the high electron density delocalisation, the H1 parameters could not be determined reliably prior to the neutron diffraction experiment, and strongly depended on the refinement model used (see *X-ray Studies* above). For the X–N map (Figure 3-10, bottom) all atomic parameters are taken from the neutron refinement without imposing a scaling model. It emphasises both bonding and lone pair densities, and the absolute peak heights have now quantitatively representative values, especially those of the O lone pairs. This arises from the fact that the spherical densities which are subtracted from the molecular density are based on the neutron determined ADPs, that is they reflect the nuclear densities and are therefore considerably smaller than the electronic volumes determined by X-ray diffraction. Hence

electron densities are imaged here which are located outside the core regions, and correspond qualitatively to the valence shells. The X–(X+N) and X–N deformation densities are in good agreement with previous charge density studies on oxalic acid dihydrate and an analogue of isonicotinamide, nicotinamide.[69, 70]

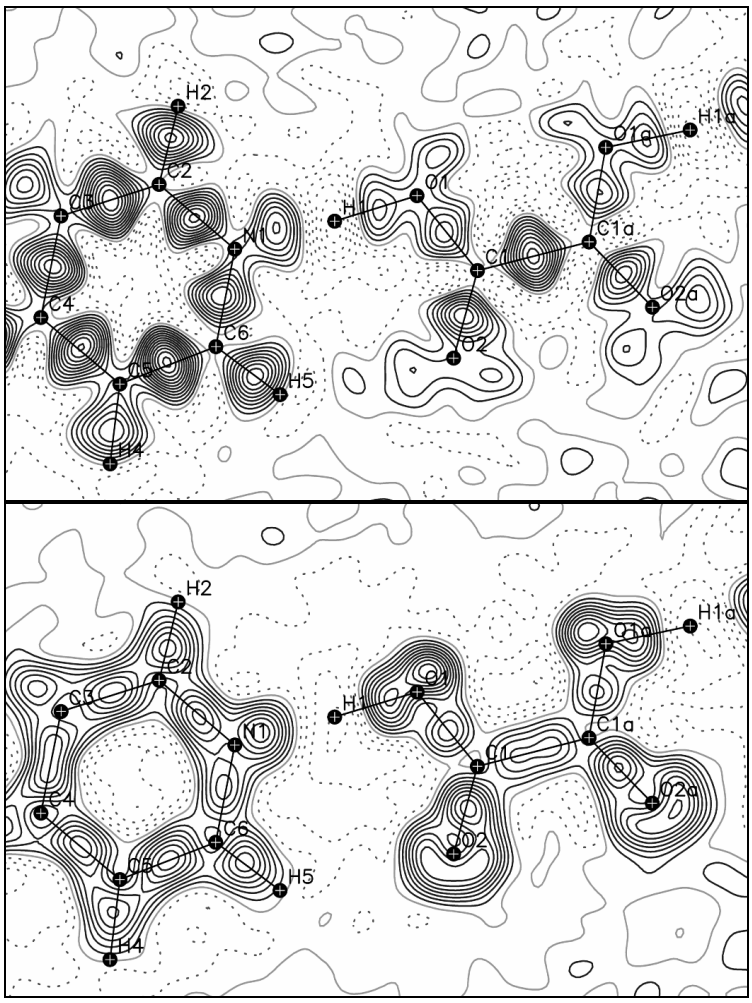

Figure 3-10: Deformation density maps for IN_2–OA (100 K data) in the C1–O1–N1 plane; (top) experimental X–(X+N) map with contours at 0.05 eÅ^{-3}; (bottom) experimental X–N map with contours at 0.1 eÅ^{-3}; maps for $F_{obs} > 4\sigma(F_{obs})$, $\sin\theta/\lambda < 0.78$ Å^{-1}; positive contours – solid black, zero levels – solid grey, negative – dotted; for details about construction of the maps see text.

Form II

The variable temperature experiment on IN_2–OA Form II was performed on the VIVALDI instrument at the ILL reactor source in Grenoble. Form II crystallises with needle or stick shaped morphology and does not readily yield single crystals with the required size for neutron experiments. It was necessary to seed a saturated solution of IN and OA with a small specimen to grow a large, several centimetres long, but multi-domain crystal of which a block shaped fragment (crystal 1, $1.5 \times 0.8 \times 0.6$ mm^3) was separated and used for data collection. Although analysis of the reflection profiles showed that crystal 1 had a very high mosaicity and consisted of several single domains (see Figure 3-11, top), the reflections were distinct enough for integration and a dataset was measured at RT. Upon cooling to 100 K however, crystal 1 cracked and was no longer suitable for a structure determination. Subsequent datasets on a smaller but better quality fragment

(crystal 2, 0.8 × 0.6 × 0.4 mm^3) were measured for temperatures of 200 K, and 100 K. However, crystal 2 proved also to be sensitive to the process of (this time very slow) cooling to 100 K and split into two domains – the previously well defined reflections at 200 K showed splitting into pairs constituting a major and a minor component at 100 K (see Figure 3-11, bottom). The orientation matrices of the crystals were determined with the program LAUEGEN.[71] The reflections were integrated with ARGONNE_BOXES,[72] normalised to a common wavelength and scaled and merged with LAUENORM.[73] As usual, the structure refinements were performed with SHELXL. Despite the experimental difficulties arising from the crystal qualities described above, the datasets thus obtained are of a sufficient quality to allow the refinement of all atomic parameters (the crystal data are summarised in Table B-2 in Appendix B). Figure 3-12, left, shows the ellipsoid plots of the refined structures at the different temperatures. While the atomic displacement parameters, as a measure of the quality of a dataset, look reasonable for the RT structure, they show a preferential orientation for the two low T datasets (both obtained from crystal 2). For the 100 K data this can be rationalised by the fact that the crystal had split, but for the 200 K structure this is slightly surprising in view of the very nice diffraction pattern obtained at this temperature (Figure 3-11, bottom), pointing to systematic errors during either the data collection or data treatment. There might be scope for improving the data processing, but in the end, the current neutron structure refinements produced the information aimed for, that is reasonable positional and displacement parameters for the H atoms, in particular for the H atom involved in the SSHB. They confirm the previous estimation from the X-ray structure determination and the later ab-initio studies (described below) that also the H atom in IN_2–OA Form II is not disordered but occupies a single site close to the centre of the SSHB.

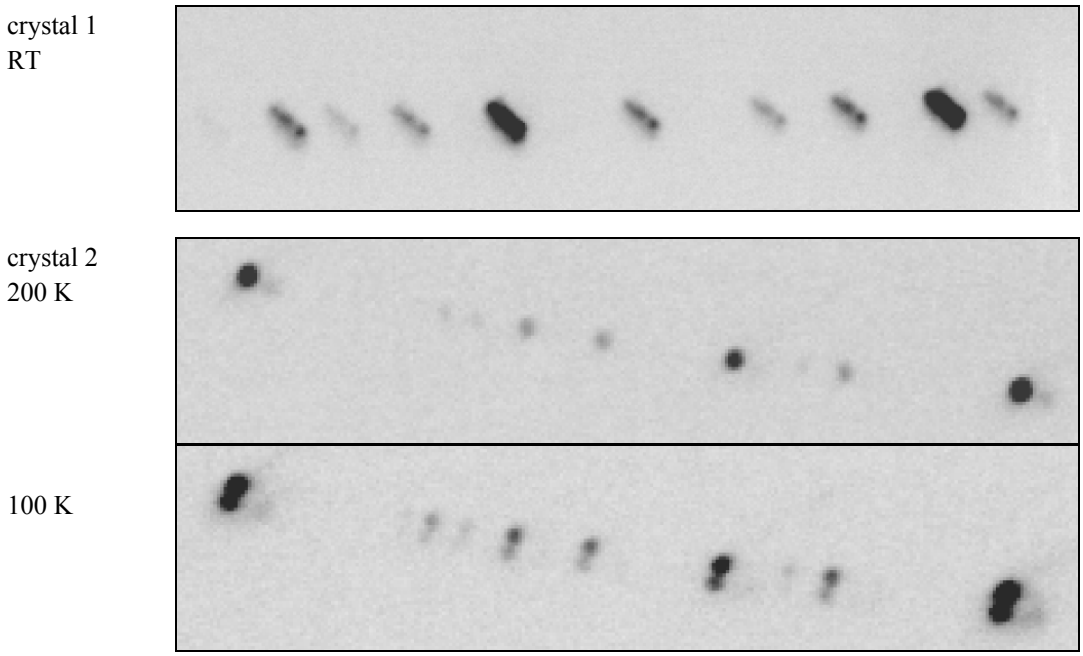

Figure 3-11: Neutron Laue diffraction patterns for IN_2–OA Form II collected on VIVALDI. (top) crystal 1 at RT shows a high mosaicity; (bottom) crystal 2 at 200 K and 100 K split upon cooling.

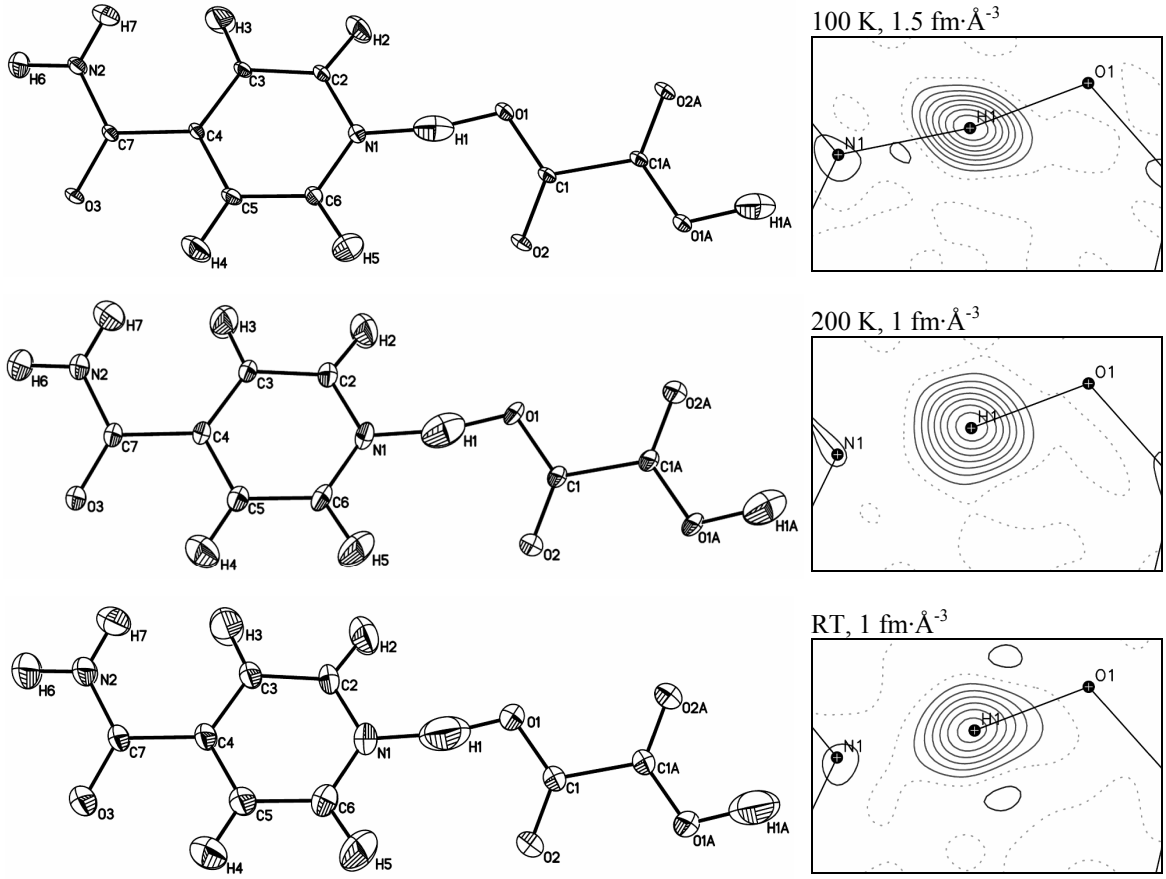

Figure 3-12: (Left) ellipsoid plots at the 50 % level for the neutron data of IN_2–OA Form II. (Right) difference Fourier maps in the C1–O1–N1; for details see Figure 3-8.

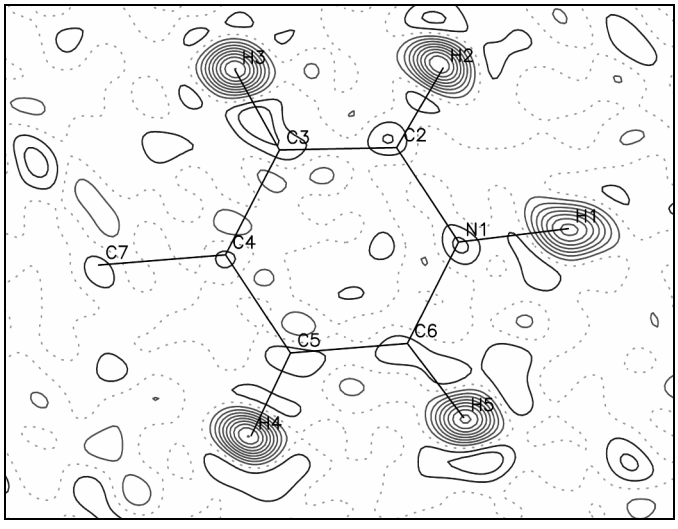

Figure 3-13: Difference Fourier map for the 100 K structure of IN_2–OA Form II in the pyridine plane after refinement without H1–H5; contours at 1.5 fm·Å^{-3}.

Similar to the situation found in Form I, the nuclear densities for H1 shown in Figure 3-12, right, bear no evidence for disorder in the examined temperature range, although the apparent systematic errors in the low T data certainly affect the difference densities. The thermal ellipsoids for H1 are elongated in the general direction of the HB, as expected, but

the overall displacement parameters of the H atoms involved in the SSHB are not significantly larger than those determined for the other H atoms in the structures. This becomes apparent in Figure 3-13 which compares the nuclear density for H1 to those for the pyridine H atoms in the 100 K structure; the preferential orientation of the ADPs appears also in these H densities.

The refined neutron HB parameters for IN_2–OA Form II, listed in Table 3-3, reveal a few general trends in comparison to Form I. First of all, the shift of the H atom towards the centre of the SSHB is further enhanced. Comparing the O1–H1 bond lengths in the two polymorphic structures at 100 K (1.161(3) and 1.235(5)Å in Form I and Form II respectively), shows that the H atom is shifted by another 0.07 – 0.08 Å towards the centre of the HB. Bearing in mind that covalent O–H bonds are systematically shorter than N–H bonds, it can be reasoned that at 100 K the H1 atom occupies a quasi central position in this heteronuclear SSHB with O1–H1 and H1···N1 distances of 1.235(5) Å and 1.313(6) Å respectively. The differentiation between a covalent and a hydrogen bonding interaction in this case is of course not applicable and has only formal character – the SSHB is more appropriately described as O··H··N or O–H–N. In addition to the appearance of the centred HB at 100 K, the lengthening of the O–H bond, caused by the temperature induced shortening of the O···N heteroatom distance, is enhanced. In the series of RT, 200 K, and 100 K structures, the O1–H1 bond distance increases continuously from 1.194(9), to 1.226(5), and to 1.235(5) Å respectively, amounting to an increase of ~0.04 Å; for comparison, the corresponding O–H distance in Form I is only lengthened by ~0.015 Å in the same temperature range. It is possibly this pronounced shift of the H atom which leads to a transfer of charge sufficient to cause the crystals to crack upon cooling. However, this has not been observed for the previously carried out X-ray experiments on smaller specimens.

In view of the moderate quality of the current experimental data, a detailed analysis of the neutron data is not advisable at this point. The standard uncertainties of the refined atomic parameters are on average twice as high as the corresponding uncertainties obtained in the neutron structure of Form I. The systematic errors leading to the bias in the ADPs for the low T data presumably add further to the mathematically determined uncertainties. In particular, a comparison of the neutron and X-ray determined atomic parameters is not helpful due to the inaccurately determined neutron ADPs. For example, an X–N deformation density map (not presented here) which proved to give an insightful image of the charge transfer effects in Form I, did not provide any useful information in this case.

With respect to the nature of the SSHB however, the neutron data give a reasonably clear picture that the H atom occupies a single site with a considerable shift towards the centre of the HB, and that this shift exceeds that observed for Form I. This leads to the same inconsistency between a well localised nuclear density and a highly delocalised electron density as in Form I (compare the corresponding densities for Form II in Figure 3-12 and Figure 3-7). The explanation is consequently similar to that found for Form I: the high electron density level in the vicinity of the N atom is caused by an overlap of N lone pair density with bonding density originating from the covalent H··N interaction. Since in this case the H nucleus occupies such a central position in the SSHB there is likely to be an increased contribution to the density from the H atom itself because of its proximity to the pyridine N. In any case, the covalent character of the SSHB is assumed to be enhanced in Form II which is supported by the Mulliken population analysis of the calculated ground

state wave function (see 3.1.4 *Ab Initio Studies*) with O1··H1, H1··N1 and H1 populations of 0.16, 0.13 and 0.54e respectively (the corresponding values found for Form I were 0.18, 0.12 and 0.54e respectively).

Table 3-3: HB parameters for IN_2–OA Form II (neutron data).

	T	HB	D–H / Å	H···A / Å	D···A / Å	∠DHA / °
Form II	100K	O1–H1···N1	1.235(5)	1.313(6)	2.539(3)	170.5(4)
		N2–H6···O3*	1.036(4)	1.871(5)	2.906(3)	177.3(5)
		N2–H7···O2*	1.015(3)	1.904(4)	2.903(3)	167.6(4)
	200K	O1–H1···N1	1.226(5)	1.332(5)	2.549(4)	170.3(4)
		N2–H6···O3*	1.026(4)	1.882(5)	2.908(4)	179.2(4)
		N2–H7···O2*	1.013(3)	1.919(4)	2.916(3)	167.1(4)
	RT	O1–H1···N1	1.194(9)	1.369(9)	2.553(5)	170.0(6)
		N2–H6···O3*	1.017(5)	1.895(6)	2.912(6)	177.7(5)
		N2–H7···O2*	1.010(5)	1.935(6)	2.929(7)	167.3(5)

* Atoms generated by symmetry.

3.1.3. Charge Density Studies

The discrepancy between electronic and nuclear density in the SSHBs demands a better description of the electron density as the nuclear positions for the H atoms are well determined by neutron diffraction. For this reason, charge density studies were carried out on both forms of IN_2–OA in order to account for the charge transfer effects observed above with the aspherical atom model and subsequently obtain a clearer picture of the electronic structure in the SSHBs. Furthermore the topological analysis of the total electron density becomes possible and allows a quantification of the hydrogen bonding interactions present.

Form I

The charge density experiment on IN_2–OA Form I was carried out on the in-house Bruker AXS Apex II diffractometer at T = 100 K. The data were integrated with SAINT[74] to $2\theta = 120º$, and scaled and corrected for absorption with SADABS.[75] The 62005 reflections thus obtained were subsequently merged with SORTAV[76] to generate a set of 9393 independent reflections for use with XD[40] (for details see Appendix B, Table B-1). The initial model for the multipole refinement with XD was taken from the spherical atom refinement with SHELXL.[39] The H parameters were taken from the neutron experiment at 100 K and fixed during the refinement; the H ADPs were additionally compared to the heavy atom ADPs obtained from the SHELXL refinement, and scaled accordingly with the program UIJXN.[44] In the XD refinement, multipole expansions up to the octupolar level ($l = 3$) were included for the heavy elements (C, N, O); and to the quadrupolar ($l = 2$) for H, but here only the bond directed quadrupole has been included as suggested by Volkov *et al*.[77] No chemical constraints have been employed on the refinement model, other than that the contraction–expansion parameters (kappas) of chemically similar atoms were set equal, resulting in 9 kappa sets for the 19 independent atoms (H1 was assigned a unique kappa set). The kappas for the spherical monopole terms were refined independently from those for the multipolar terms, and the latter were set to

be equal within each kappa set. Although the dataset is not complete in the very high resolution shells to the maximum $\sin\theta/\lambda$ = 1.21 Å^{-1}, all observed reflections (F_{obs} > 4σ(F_{obs})) were used for the structure refinement. A total of 354 parameters were refined to R_1 = 0.0159 for the 7817 observed, independent data. The two strongest reflections (3 1 1, 6 0 2) had unfortunately to be omitted from the dataset because their experimental intensities were significantly underestimated – probably due to strong extinction despite the use of an isotropic extinction correction (type 2). The inclusion of the above reflections heavily biases the difference Fouriers resulting in large negative residual densities in the molecular planes (F_{obs} – F_{calc}). In addition, an XD refinement has been performed on theoretical structure factors which were calculated from the ground state wave function for the 100 K neutron geometry. A comparison of the refinements on experimental and theoretical data will be presented following the discussion of the experimental charge density analysis.

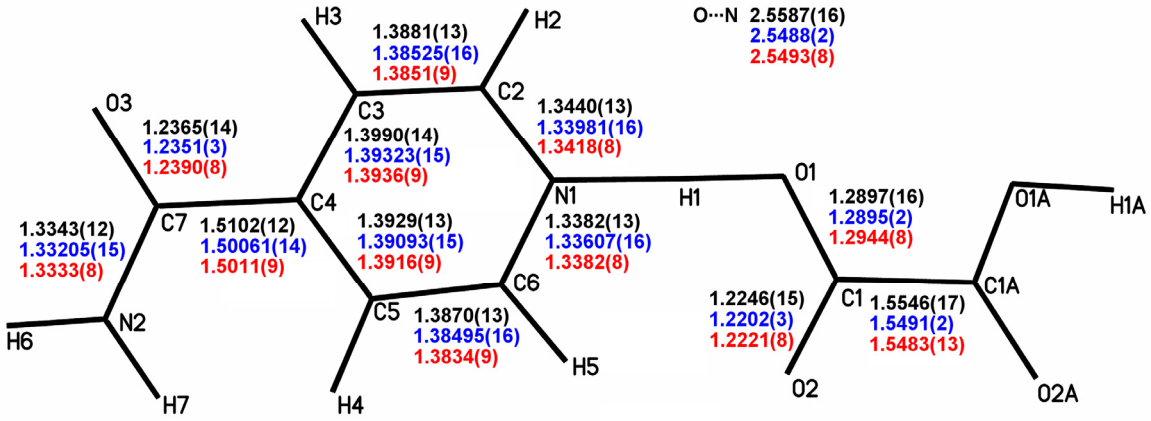

Figure 3-14: Comparison of the bond length in IN_2–OA Form I as refined from the neutron (black), the current charge density (blue), and the standard X-ray dataset (red), all 100 K data; units in Å.

Figure 3-14 compares the bond lengths between the non hydrogen atoms as refined from the various datasets and refinement models. The neutron data have to be regarded as the most accurate with respect to the internuclear distances, even though the standard uncertainties on the bond lengths are higher than for both the standard X-ray and the charge density study. The neutron distances, however, are systematically longer, with a maximum Δd of 0.01 Å for C4–C7, arising from various experimental factors differing in the X-ray and neutron experiments (larger crystal, less absorption, different cooling device, etc). Correspondingly, the unit cell volume is highest for the neutron data at 1395.3(12) Å^3, compared to 1378.9(1) and 1382.2(2) Å^3 for the charge density and standard X-ray data respectively, leading to the observed increase of interatomic distances. Refining the neutron data with the X-ray determined unit cell parameters yields interatomic distances in good agreement with the X-ray experiments (e.g. C4–C7 = 1.5046(11) Å, O1···N1 = 2.5492(11) Å). Comparing the X-ray data only shows that with the exception of the C1–O1 and to a lesser extent the C7=O3 distances, the spherical atom refinement yields no inferior results compared to the multipole refinement. The above discrepancies manifest in a small (~0.005 Å for C1–O1) but significant bond lengthening, caused by a shift of the O atom in the direction of the lone pairs. This effect for first row atoms in an asymmetric environment has been documented by Coppens and a list of typical shifts is presented in reference [38].

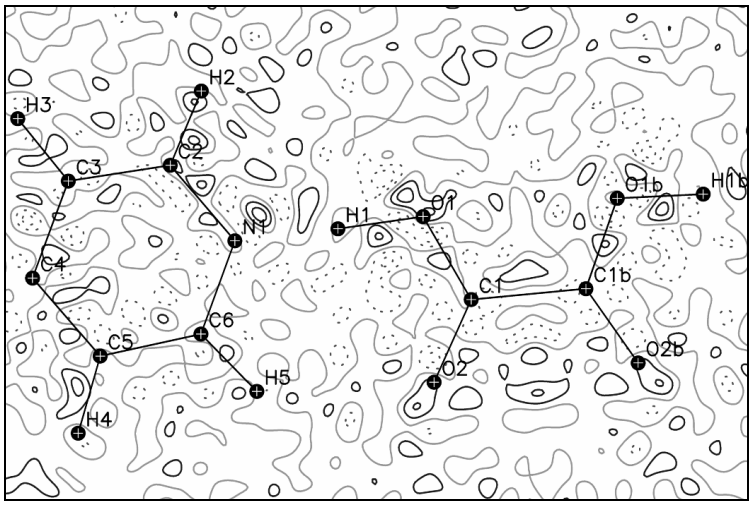

Figure 3-15: Residual density map (X–(X+N)) of IN_2–OA Form I in the C1–O1–N1 plane, map for $F_{obs} > 4\sigma(F_{obs})$, $\sin\theta/\lambda < 1.21$ Å^{-1}; positive contours – solid black, zero levels – solid grey, negative – dotted, contours at 0.05 eÅ^{-3}.

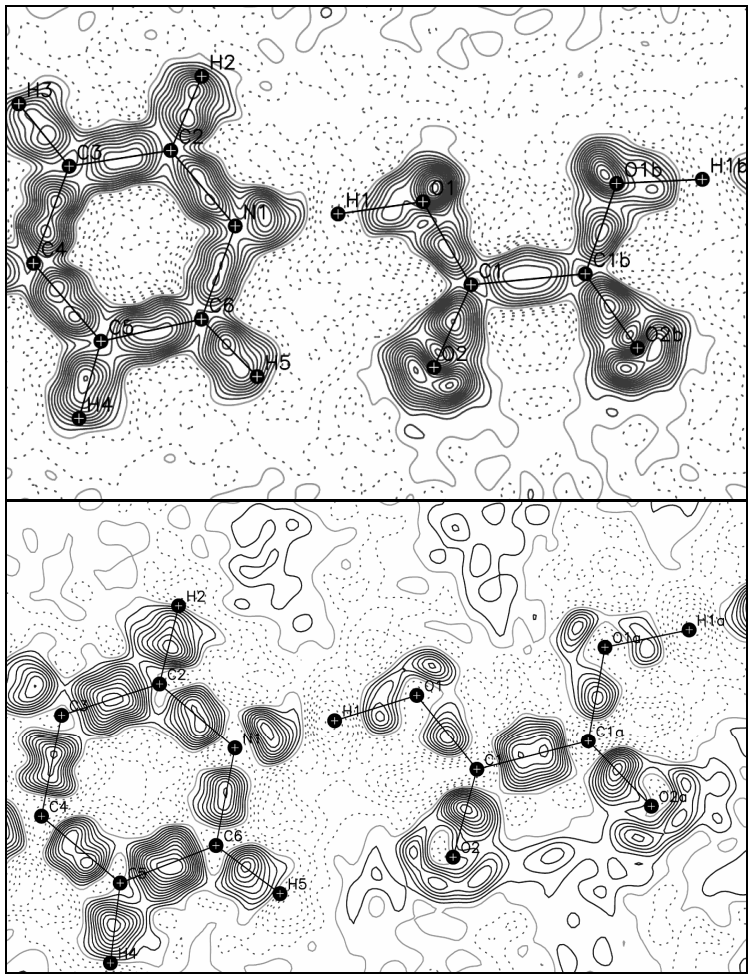

Figure 3-16: Experimental deformation density map after multipole refinement (top) and after spherical atom refinement (bottom) of the same dataset; $\sin\theta/\lambda < 1.21$ Å^{-1}, for details see Figure 3-15.

The residual density map in Figure 3-15 shows that the deformation densities unaccounted for in the previous spherical atom refinement (Figure 3-4, top) have now been

modelled properly. It is noisy in parts but featureless, and the maximum and minimum residual densities are reduced to 0.139 and -0.136 eÅ^{-3} respectively, compared to 0.593 and -0.413 eÅ^{-3} for the standard X-ray refinement.

The experimental deformation density in Figure 3-16, top, shows the expected charge accumulations in the bonding and lone pair regions. Again, the experimental map is slightly noisy in places because all observed reflections to $\sin\theta/\lambda < 1.21$ Å^{-1} have been included in order to present here the unbiased results.[a] In comparison with the experimental X–(X+N) deformation density obtained for the standard X-ray dataset in Figure 3-10, top, the charge transfer effects are qualitatively the same. However, while the densities in the centres of bonds are of comparable magnitude, the lone pair densities are now enhanced, particularly for the O atoms. This is mainly caused by the improved determination of the ADPs and, to a smaller extent, of the positional parameters, because the multipole formalism allows a deconvolution of charge transfer densities and the thermal motion of atoms, resulting in more realistic, smaller ADPs. In order to highlight the importance of accurate atomic parameters for the analysis of charge transfer effects, the charge density dataset has been additionally refined with SHELXL and the resulting experimental deformation density map is included in Figure 3-16 for comparison. Although the absolute differences in the ADPs are very small and well below 5 % in the current case, the effect for the visualisation and quantification of the lone pair densities, especially for the O atoms, is striking. Finally, the dynamic and static model deformation density maps in Figure 3-17 and Figure 3-18 have been included here for completeness. They are noiseless as no experimental data are used for their generation, and they agree very well with the previously discussed deformation densities. The static density, calculated directly from the refined multipole populations, emphasises the density accumulations particularly in the lone pair regions because they are not obscured by thermal motion.

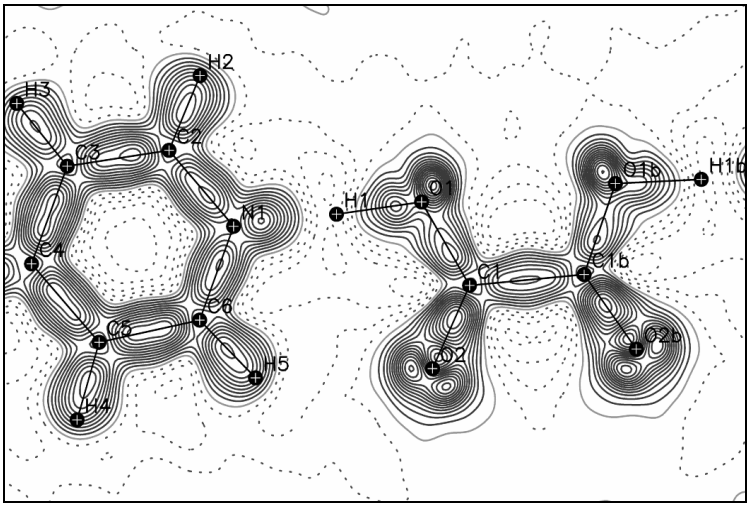

Figure 3-17: Dynamic model deformation density map; $\sin\theta/\lambda <$ 1.21 Å^{-1}, for details see Figure 3-15.

[a] The experimental deformation map looks much clearer and in closer resemblance to the dynamic model density if only reflections to $\sin\theta/\lambda < 1.08$ Å^{-1} are included

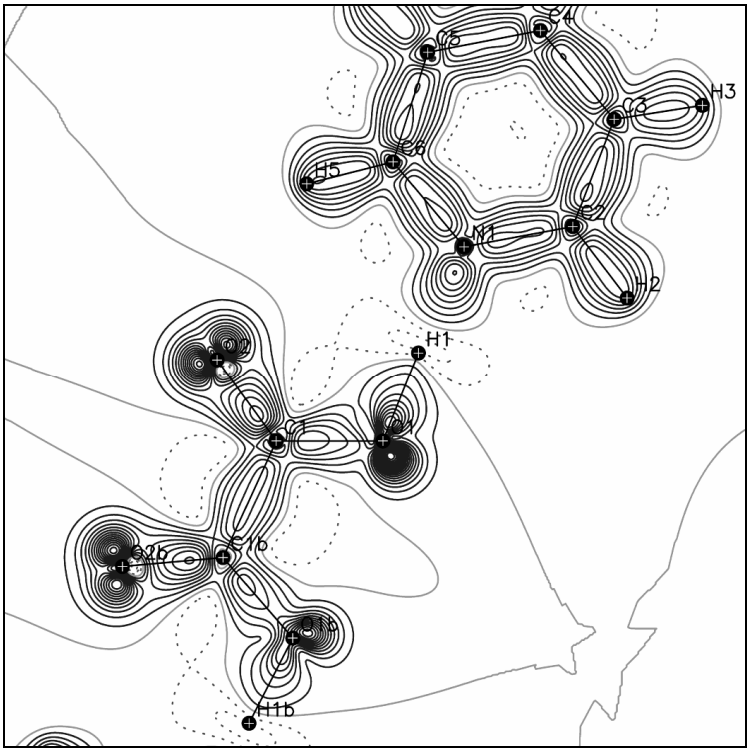

Figure 3-18: Static model deformation density in the C1–O1–N1 plane; contours at 0.1 eÅ^{-3}.

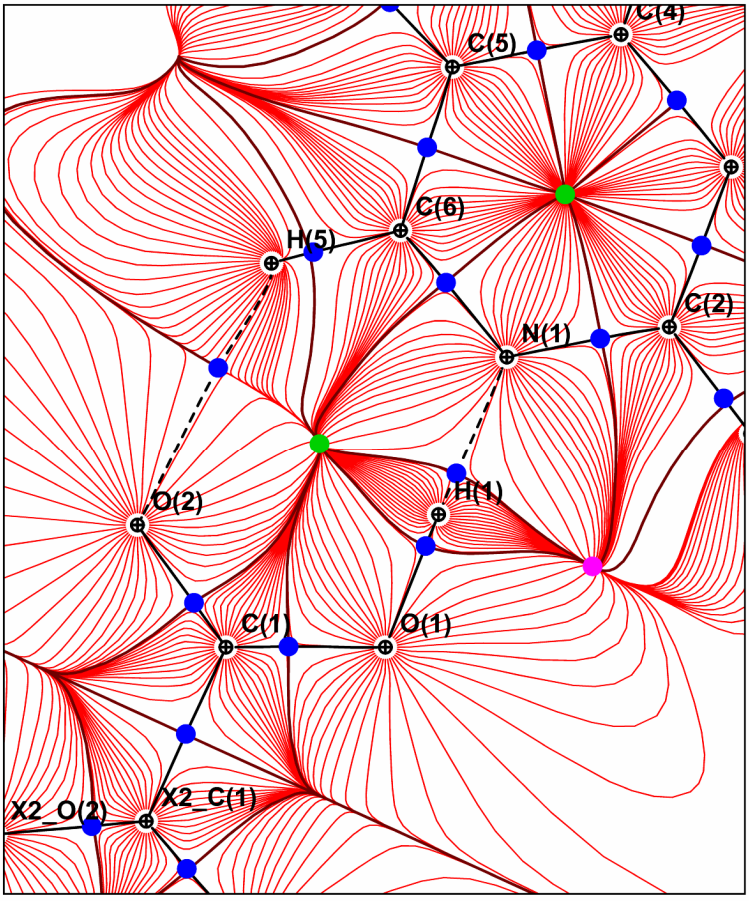

Figure 3-19: Gradient vector field map in the C1–O1–N1 plane of IN_2–OA Form I; BCP (blue), RCP (green), CCP (magenta), IAS (brown), BP (black).

The accurate determination of the total electron density, $\rho(\mathbf{r})$, within the multipolar model allows the topological analysis of the same, following the theory of atoms in molecules (AIM) by Bader and co-workers.[53] Figure 3-19 shows the gradient vector field map in the plane of the SSHB. The bond paths (BPs) are projected onto the map as black solid lines (dashed for HBs), and the positions of the bond critical points (BCPs) are marked by blue circles. Unsurprisingly, the topological analysis confirms the bonding interaction for H1···N1 by the very existence of a bond path, and the mandatory BCP, between the two atoms. Less self-evident is the existence of a BP between H5···O2, separated by 2.3835(2) Å, which completes the circular carboxylic acid – pyridine synthon. Consequently, there is a ring critical point (RCP, green circle) in the centre of this circular arrangement of BPs.

Table 3-4: Topological properties at the BCPs of the HBs in IN_2–OA Form I.

	refinement on experimental structure factors					refinement on theoretical structure factors				
HB	ρ_{BCP} / eÅ^{-3}	$\nabla^2\rho_{BCP}$ / eÅ^{-5}	λ_1	λ_2	λ_3	ρ_{BCP} / eÅ^{-3}	$\nabla^2\rho_{BCP}$ / eÅ^{-5}	λ_1	λ_2	λ_3
O1–H1	1.37	–17.2	-18.4	-18.4	19.6	1.37	–12.3	-16.9	-16.8	21.4
H1···N1	0.769	–3.31	-8.27	-7.97	12.9	0.795	–1.94	-7.55	-7.27	12.9
N2–H6	2.19	–35.7	-30.9	-29.3	24.6	2.17	–32.1	-28.6	-27.2	23.7
H6···O3	0.157	2.07	-1.09	-1.07	4.22	0.209	1.65	-1.26	-1.24	4.15
N2–H7	2.23	–32.7	-30.8	-29.2	27.4	2.27	–33.6	-29.8	-28.1	24.3
H7···O2	0.129	1.81	-0.77	-0.76	3.34	0.150	1.35	-0.83	-0.81	2.99
C6–H5	1.97	–22.1	-20.0	-18.8	16.7	1.96	–23.1	-18.9	-17.8	13.7
H5···O2	0.043	1.10	-0.21	-0.16	1.46	0.064	0.97	-0.26	-0.20	1.43

Table 3-4 lists the electronic properties evaluated at the BCPs of the HBs present in IN_2–OA Form I: The previously discussed SSHB O1–H1···N1, the moderate diamide and amide–carbonyl HBs, N2–H6···O3 and N2–H7···O2 respectively, and the weak C6–H5···O2 HB. For comparison, the BCP properties which have been derived from the multipole refinement on a theoretical dataset are included. The high value for the electron density of 0.77 eÅ^{-3} at the H1···N1 BCP and the negative value for the Laplacian ($\nabla^2\rho_{BCP}$ = –3.3 eÅ^{-5}), as a measure of local charge concentration at this point, readily classify this interaction as a shared one and confirms the covalent character of the SSHB. Also, the previously observed high electron density delocalisation in the SSHB can now be quantified. First, by the above increased electron density in the H···A interaction; second, by a reduced density in the D–H bond; and third, by the charge depletion on H1. The reduced electron density in the covalent O1–H1 bond manifests in a lowered ρ_{BCP} = 1.37 eÅ^{-3} and a less negative value for the charge concentration $\nabla^2\rho_{BCP}$ = –17.2 eÅ^{-5}; comparable BCP properties for the two covalent N–H bonds in the structure are in average ρ_{BCP} ~ 2.2 eÅ^{-3} and $\nabla^2\rho_{BCP}$ ~ –34.5 eÅ^{-5}. The extent of charge depletion on H1 is reflected by the refined monopole population of 0.64e for H1, giving rise to a formal "monopole" charge of +0.34e on H1. For comparison, the monopole populations for the pyridine H atoms are on average ~0.94e; and for the amide H atoms, which are involved in moderate hydrogen bonding, ~0.83e. This highlights the significant degree of charge transfer from H1 to the carboxylic acid group and also the pyridyl N (the monopole charges on O1, O2 and N1 are -0.24, -0.44, and -0.28e respectively). Regarding the weaker HBs, there is a clear trend of a decreasing ρ_{BCP} with increasing H···A lengths, accompanied by an

increased ρ_{BCP} in the corresponding covalent X–H bonds. Unlike for the SSHB, these HBs show positive values for the Laplacian and low electron densities at the H···A BCPs. By the definition of AIM they are therefore classified as closed shell interactions, and are hence of mainly electrostatic nature.

Figure 3-20 shows the plots of the negative Laplacian, $L(\mathbf{r})$, in the plane of the SSHB after refinement against the experimental and theoretical data (the latter will be discussed later). They highlight the regions of local charge concentration and depletion, of which especially the valence shell charge concentration (VSCC) is of interest from the chemical point of view. It visualises the direction of bonding interactions and the orientation of lone pairs. In Figure 3-20 for example and as a proof of concept, it shows that the O1–H1 HB donor group is indeed directed towards the N lone pair. With respect to the electronic structure (experimental) in the SSHB, the charge concentration around H1 spans nearly the whole range between the VSCC of the hydrogen bonded heteroatoms. Surprisingly, it is continuous between H1 and N1, whereas there is a small region of charge depletion in the formally covalent interaction O1–H1. Intuitively, one would expect the opposite. In order to put this observation into the right perspective, a couple of general remarks should be made here: first, the contours in the plots of $L(\mathbf{r})$ are on an exponential scale, implying that the outer contours mark very low absolute values of $\nabla^2\rho$. Second, the error on $\nabla^2\rho$ is large, and small variations in the total electron density can change the sign of $\nabla^2\rho$. Despite this, the analysis of the Laplacian shows that H1 is strongly polarised towards the N lone pair, and supports the previous explanation that the high electron density in the vicinity of the N atom is caused partially by charge originating from the covalent H1···N1 interaction. The discontinuity of charge concentration in O1–H1 is atypical of a covalent X–H bond and suggests that this bond has experienced a considerable weakening upon formation of the SSHB. It is thus justified to argue that IN_2–OA Form I can be seen as an incipient H transfer complex.

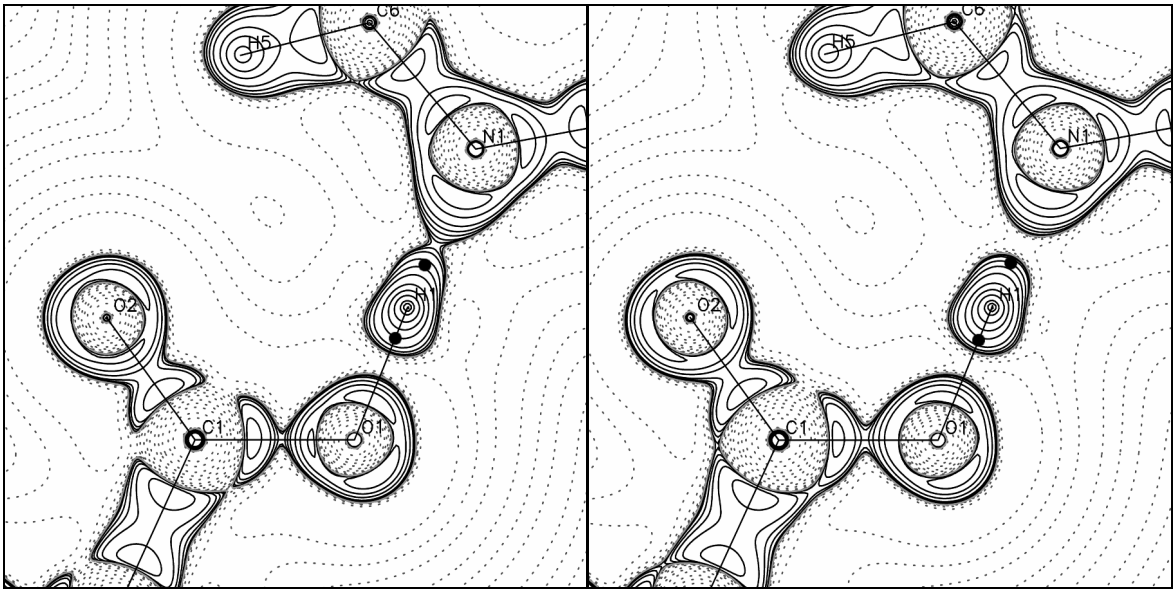

Figure 3-20: Plots of the negative Laplacian, $L(\mathbf{r})$, in the C1–O1–N1 plane of the SSHB in IN_2–OA Form I after refinement on the experimental (left) and theoretical data (right); BCPs in the SSHB – black circles, positive contours – solid black, zero levels – solid grey, negative – dotted.

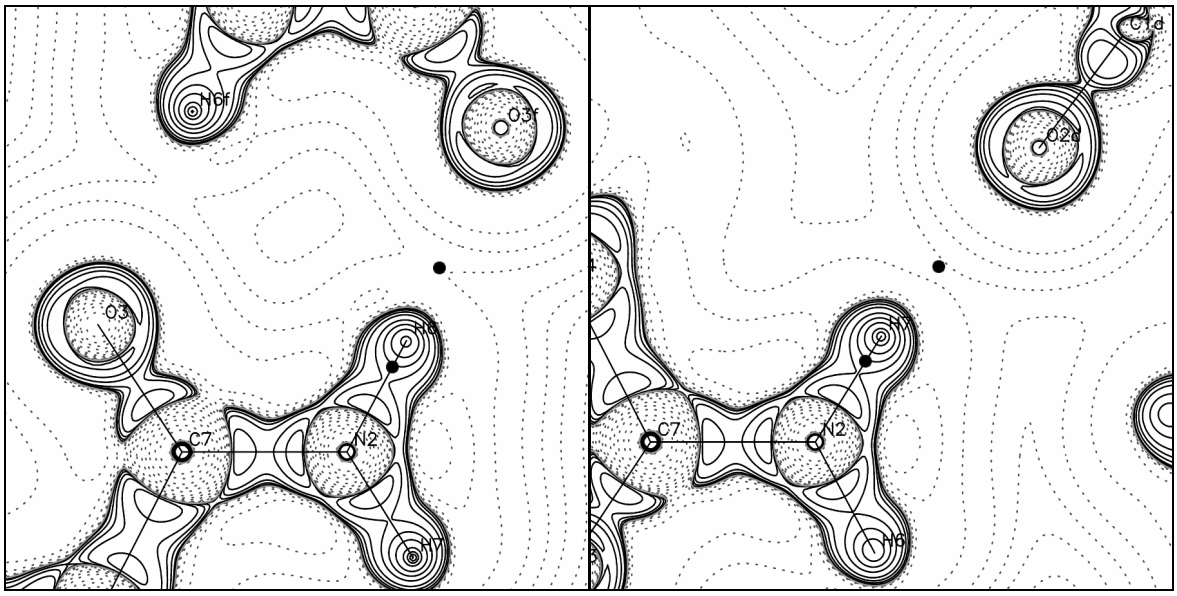

Figure 3-21: Plots of $L(\mathbf{r})$ in the planes of the diamide HB C7–N2–O3 (left), and the amide–carbonyl HB C7–N2–O2 (right); experimental data; BCPs in the HBs – black circles, contours as in Figure 3-20.

The plots of $L(\mathbf{r})$ in the planes of the moderate HBs in IN_2–OA (Figure 3-21) show some general differences regarding the electronic structure, when compared to the SSHB. First, the BCPs for the hydrogen bonding interactions fall in a large region of charge depletion. The Laplacians at the BCPs for the HBs H6···O3 and H7···O2 consequently have positive values, +2.1 and +1.8 $eÅ^{-5}$; and the electron densities are much lower at 0.16 and 0.13 $eÅ^{-3}$ respectively. Second, and unlike for the SSHB, the covalent interactions now show a continuous charge concentration as one would expect of covalent bonds. This is quantified by higher electron densities and more negative values for the Laplacians (Table 3-4). As a consequence there is now a clear distinction between H donor and H acceptor, which is much more ambiguous in the above SSHB when looking at plots of the negative Laplacian only. Comparing the two moderate HBs with each other, one can see that in the diamide HB the N2–H6 donor points directly to the O3 lone pair, while this is clearly not the case for the amide–carbonyl HB N2–H7···O2. This adds to the previous findings, following from the initial geometrical analysis in 3.1.1 *X-ray Studies* and from the BCP properties, that the diamide HB is the stronger of the two moderate HBs present.

The nature of the HBs in IN_2–OA is also reflected by the source function. Despite its potential use in describing bonding interactions, little application of the source function has appeared in the literature – the few on hydrogen bonding have all been carried out on theoretical charge densities.[78, 79, 80, 81] Gatti, Cargnoni and Bertini have shown that the HB classification by Gilli and Gilli[18] is reflected by characteristic features in the source function, in particular by the contribution of the H atom to the density at the H···A BCP.[79] From the reference material available to date, the following trend has emerged: in strong covalent HBs, S(H) is high and amounts to ~ 30 % to ρ_{BCP}; in borderline cases between strong and moderate HBs, S(H) is small but positive; in moderate electrostatic HBs, S(H) is negative and acts thus as a sink of electron density (with respect to ρ_{BCP}). Reduction in HB strength also decreases the contribution of the HB acceptor, S(A), and increases the contribution of the HB donor, S(D). Strong HBs are furthermore characterised by a pronounced "localisation" of the source function, meaning the sum of source contributions

of the atoms involved in the HB, S(D+H+A) is high, typically ~90% for strong covalent HBs. Moderate HBs show a more "delocalised" source function with S(D+H+A) ~ 30% and comparably high source contributions from atoms further away from the H···A BCP, reflecting the long range nature of electrostatic interactions.

Table 3-5: Source contributions in % to the HB BCPs in IN_2–OA Form I, S(molD) refers to the sum of the source contributions from the donor molecule. The values for the H1···N1 BCP in Form II have been included for comparison. Table analogous to those in reference [79]

HB	H···O / Å	ρ_{BCP} / eÅ^{-3}	S(H)	S(A)	S(D)	S(H+A)	S(D+H)	S(D+H+A)	S(molD)
H1···N1*	1.313	0.966	30.8	43.6	7.9	74.4	38.7	82.3	43.3
H1···N1	1.398	0.769	26.2	40.1	11.4	66.3	37.6	77.7	44.6
H6···O3	1.894	0.157	-33.4	19.8	51.0	-13.6	17.6	37.4	44.4
H7···O2	1.997	0.129	-44.0	5.7	58.6	-38.3	14.6	20.3	45.0
H5···O2	2.392	0.043	-127	-51.7	53.1	-178	-73.6	-125	44.3

* IN_2–OA Form II

For the current study, the source function has been calculated from the experimental charge density for the HBs present in IN_2–OA. The definition of the source function given in Chapter 2.3 on *The Source Function* implies that it may be obtained from experimental charge densities without any approximations, but to date all reported studies have dealt with theoretical densities. The work reported here represents the first example of the use of the source function derived from experimental densities. The results are listed in Table 3-5 and the individual source contributions to the electron density at the H···A BCPs are visualised in Figure 3-22. For the O1–H1···N1 SSHB, the characteristic features reported by Gatti *et al* for strong covalent HBs are found: a high positive source contribution of H (S(H1) = 26.2 %), and also a high combined source contribution from the atoms forming the HB (S(O1+H1+N1) = 77.7 %). The source function appears localised at the HB (see Figure 3-22, top). In contrast to the SSHB, the N2–H6···O3A diamide and N2–H7···O2A amide–carbonyl HBs show features in the source function typical of moderately strong HBs of electrostatic nature: the source contributions of the H atoms are negative (-33.4 and -44.0 %) and the combined source contribution of D, H, A is significantly smaller (37.4 and 20.3 %) than in strong covalent HBs. This trend is continued in the source function for the weak C6–H6···O2 interaction: the source contribution of H is highly negative (-127 %), as is the combined contribution of D, H, A (-125 %). Consequently, the source function appears highly delocalised in Figure 3-22, bottom). For all HBs, the sum of the source contributions originating from the HB donor molecule appears to adopt a constant value of ~45 % as previously observed by Gatti *et al*. This seems rather surprising in view of the very different HBs studied.

For the strong and moderate HBs, the trends found by Gatti *et al*[79] have been reproduced, that is with decreasing HB strengths decrease also the relative source contributions of H, A, D+H and D+H+A while only that of D shows an increase. In contrast to the findings by Gatti *et al*, however, the current source function calculations show that the same trend is followed by the weak C–H···O HB. However, the errors associated to relative source contributions increase significantly with decreasing reference densities, and whether the results for C–H···O interactions ($\rho_{BCP(H\cdots O)}$ typically < 0.05 eÅ^{-3}) are significant at all remains to be seen. Overall, the previous applications of the source function to HBs, which have all been performed on theoretical charge densities, have

largely been confirmed by the current source function calculations on an experimental charge density.

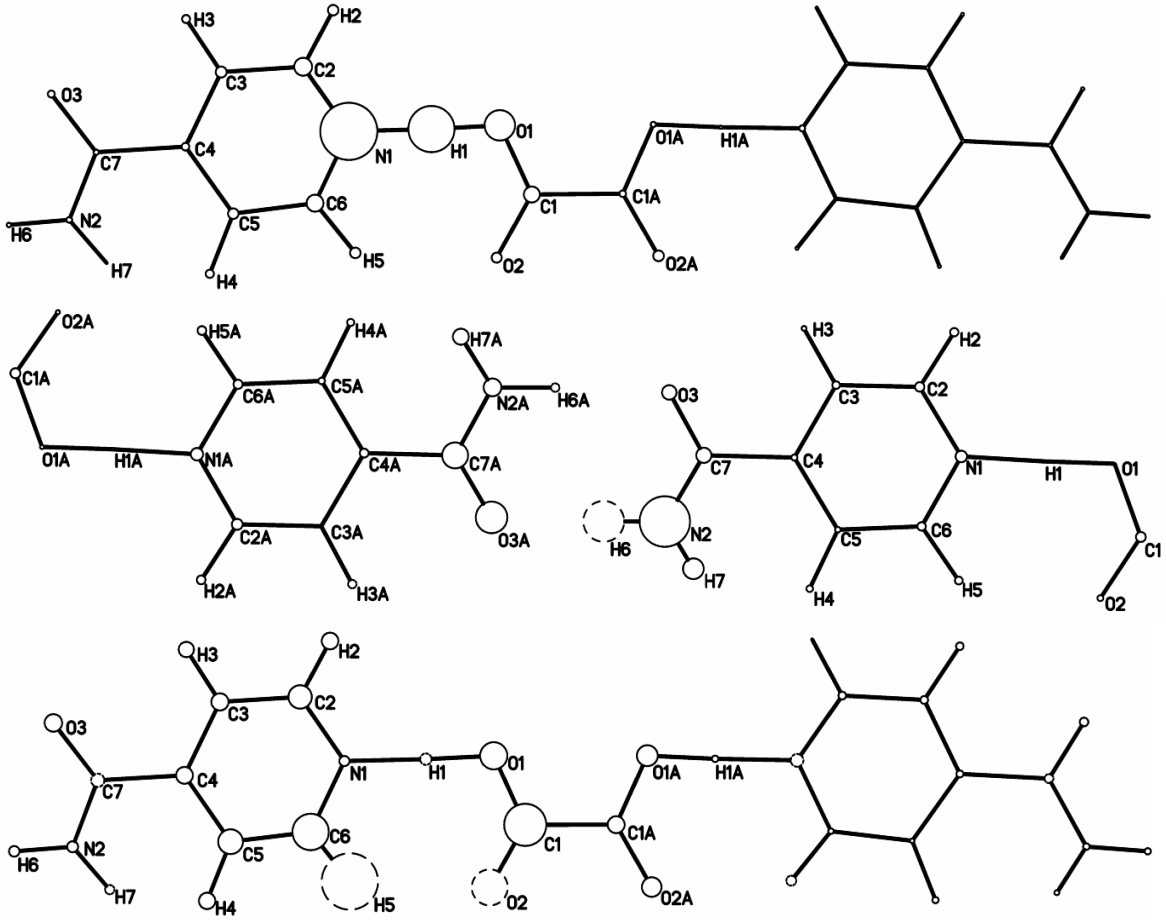

Figure 3-22: Source contribution to the H1···N1 (top), H6···O3A (centre), and H5···O2A (bottom) BCPs in IN_2–OA Form I. The sizes of the circles representing the atoms are proportional to the source contributions, positive source contributions as solid circles, negative as dashed. The qualitative differences by going from the strong O1–H1···N1, to the moderate N2–H6···O3, to the weak C6–H5···O2 HB are apparent.

As mentioned earlier, a multipole refinement has been performed on theoretical static structure factors, which have been calculated from a ground state wave function up to the experimental resolution of $\sin\theta/\lambda$ = 1.21 Å^{-1}. The wave function was obtained from a single point energy calculation on the 100 K neutron geometry with CRYSTAL03[51] at the B3PW/6-31g** level of theory (for details see 3.1.4 *Ab Initio Studies*). The refinement on theoretical data serves two purposes; first, the aspherical atom formalism and the applied model are tested, for the theoretical structure factors are free of any experimental noise and should in principle yield residuals of zero. Second, the parameters refined against the experimental structure factors can be evaluated. However, the fact that no thermal motion was included in the calculation of the theoretical structure factors implies that the ADPs will be zero. This fundamental difference to the experiment has to be considered for any comparative interpretation.

For the multipole refinement the same multipole model has been used as for the refinement against the experimental data in order to keep the two refinements consistent where possible. The atomic coordinates, however, have been fixed to the values used for the ground state wave function calculation with ADPs set to zero. The multipole

refinement of the theoretical dataset yields a residual value of R_1 = 0.0056 for 10324 independent reflections (unit weights have been applied in the absence of meaningful standard uncertainties). This reflects the error associated with the multipole model used, and furthermore points out the inherent limits of the Hansen–Coppens formalism as the theoretical structure factors are free of noise, as mentioned before. One source of error in the theoretical data does, however, originate from the fact that the current set of structure factors was calculated only to a limited resolution, giving rise to the same Fourier truncation effects present in the experiment (see 2.1.1 on *Structure Factors*).

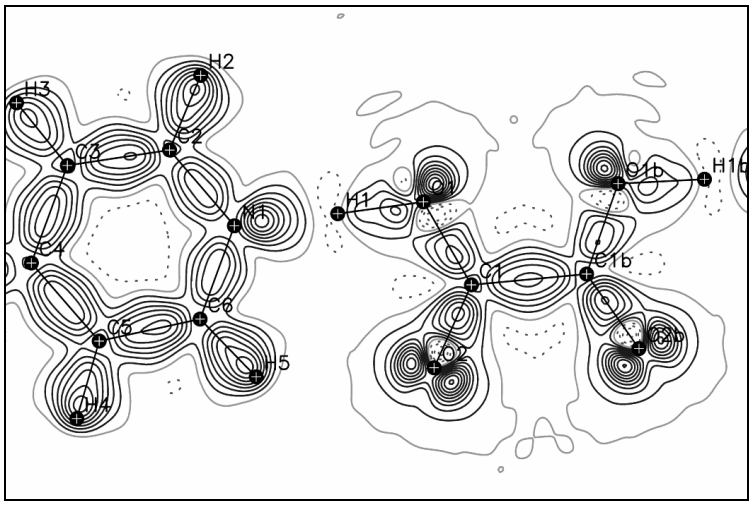

Figure 3-23: Model deformation density after the multipole refinement on the theoretical structure factors; contours at 1.0 eÅ^{-3}.

Figure 3-23 shows the model deformation density obtained by Fourier synthesis ($F_{\text{calc, multipole}} - F_{\text{calc, spherical}}$) after XD refinement with the multipolar model. It resembles the static model deformation density in Figure 3-18, bottom, because thermal motion is neither involved for the calculation of the theoretical structure factors nor in the refinement model. Consequently the features are very similar to those in the above static deformation density.

The topological analysis of the total electron density, ρ, has also been carried out for the refinement of the theoretical dataset. The results have been included in the previous plots of $L(\mathbf{r})$ (Figure 3-20) and the table containing the BCP properties (Table 3-4). They are compared in the following with the results obtained from the refinement of the experimental dataset. For the SSHB, the electron densities at the BCPs of the covalent O1–H1 bonds and the H1···N1 interaction can be considered to be the same within the error of the method. The Laplacian of the electron density, on the other hand, reveals some differences. The N lone pair of the pyridyl group is less polarised towards H1 for the theoretical data, and the continuous region of charge concentration between H1 and N1, as observed for the experiment, is disrupted (Figure 3-20, right). This is reflected in a less negative value for $\nabla^2\rho_{\text{BCP}}$ of –1.9 eÅ^{-5} compared to –3.3 eÅ^{-5}. Analysis of the principal curvatures at the BCPs (Table 3-4) shows that the pronounced charge concentration at the H1···N1 BCP determined from the experimental data originates from enhanced negative curvatures for λ_1 and λ_2, both of which are perpendicular to the bonding interaction, whereas the values for the positive curvature λ_3 along the HB are equal for both datasets. Also, the charge at the covalent O1–H1 BCP is significantly less concentrated with $\nabla^2\rho_{\text{BCP}}$ = –12.3 eÅ^{-5} in comparison to –17.2 eÅ^{-5}, here due to a contribution of all three principal

curvatures. Despite the difference in absolute values, the ratios of the Laplacians at the O1–H1 and H1···N1 BCPs derived from the experimental and theoretical charge densities are comparable. As far as the moderate and weak HBs are concerned, the BCP properties for the covalent bonds all agree very well with the experiment. In the non covalent HB interactions, the theoretical dataset shows a trend of slightly higher values for the electron densities and of less pronounced charge depletions at the BCPs. These differences are small and in the end a good agreement with the experiment is found. As expected, the main discrepancies arise for the properties which involve H1. They can at least partially be rationalised by the enhanced thermal motion the H1 atom experiences in the real system in the direction of the O1···N1 HB path.

Form II

The charge density dataset for IN_2–OA Form II has been measured on a Bruker AXS Apex II diffractometer at T = 100 K. The data reduction was carried out according to the experimental procedure described for Form I yielding a charge density dataset of comparable quality: 64585 measured reflections were merged to yield a set of 8857 independent reflections to a maximum $\sin\theta/\lambda$ = 1.19 Å^{-1} of which 7501 reflections are observed ($F_{obs} > 4\sigma(F_{obs})$). The refinement procedure was carried out in an analogous manner to Form I; it deviates only insofar that for H1 (the H atom involved in the strong hydrogen bonding) the multipolar terms for the contraction–expansion parameters had to be fixed to a standard value of 1.20 – they refined to unrealistically high values of ~2.0. There are missing reflections in the very high resolution ranges; nevertheless all observed reflections to $\sin\theta/\lambda$ = 1.19 Å^{-1} have been used for the multipole refinement of 353 parameters resulting in R_1 = 0.0150 for the observed data. As for Form I, theoretical structure factors have been calculated up to the experimental resolution ($\sin\theta/\lambda$ = 1.19 Å^{-1}) from the ground state wave function obtained from a single point energy calculation on the 100 K neutron geometry. The multipole refinement on the theoretical data, resulting in R_1 = 0.0054 for 9975 data with $F_{obs} > 4\sigma(F_{obs})$, will be compared with the refinement on the experimental data.

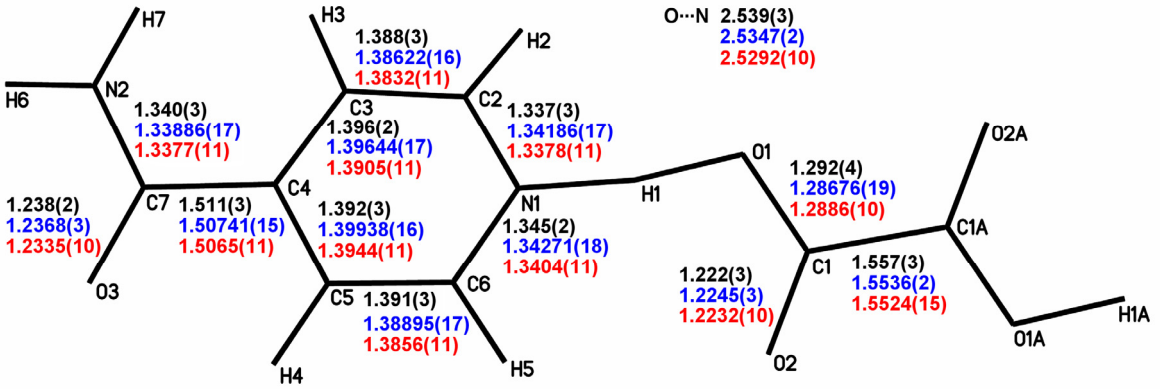

Figure 3-24: Comparison of the bond length in IN_2–OA Form II as refined from the neutron (black), the current charge density (blue), and the standard X-ray dataset (red), all 100 K data; units in Å.

Figure 3-24 gives an overview of the bond distances (not involving H) obtained from the multipole refinement (blue) and the spherical atom refinements of both the standard X-ray (red) and the neutron datasets (black). It has been mentioned previously in *Neutron Studies* that the neutron refined distances (usually the source of the most accurate nuclear

position) are less reliable in this case than the corresponding distances determined for Form I, making a comparison difficult and more tentative in this case. In Form I the neutron distances were observed to be systematically longer than the X-ray distances which was explained by the systematic differences in the experiments leading to small but significant difference in unit cell volumes. In Form II, the unit cell volumes show no significant deviations (345.31(6) and 346.5(5) $Å^3$ for the charge density and neutron data respectively), which might be rationalised by the fact that the crystal used for the neutron experiment on Form II was considerably smaller than that of Form I. Correspondingly, no trend towards longer neutron bond lengths is observed in Form II.

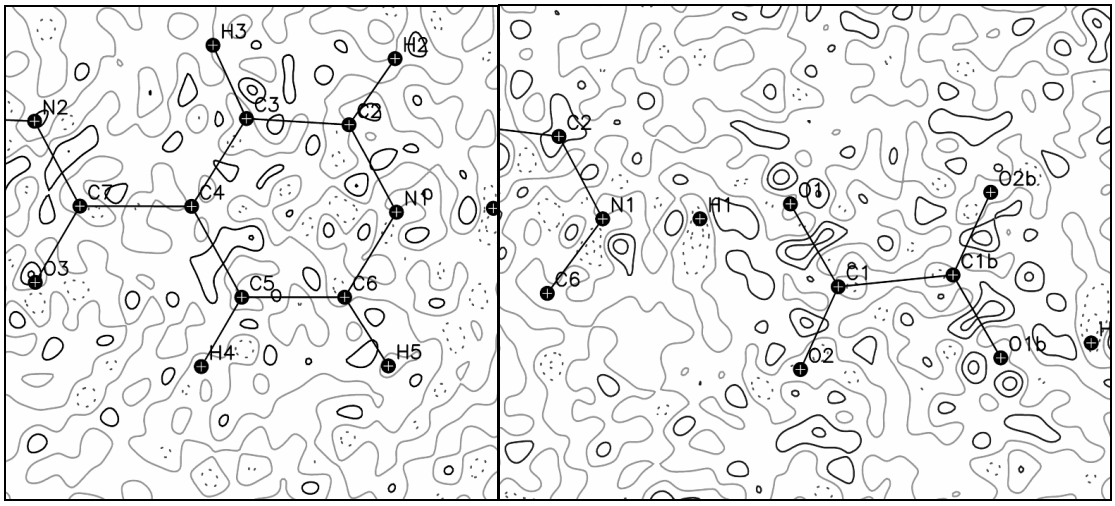

Figure 3-25: Residual density maps (X–(X+N)) of IN_2–OA Form II in the pyridine (left) and the C1–O1–N1 plane (right); $\sin\theta/\lambda < 1.19$ $Å^{-1}$, for details see Figure 3-15.

Figure 3-25 shows the residual density maps after multipole refinement in the pyridine plane and in the plane of the SSHB. Since the pyridine ring is rotated out of the oxalic acid plane in this polymorph two separate maps were generated. The maximum and minimum difference densities amount to 0.139 and -0.126 $eÅ^{-3}$ respectively, and are considerably reduced in comparison to the spherical atom refinement on the standard X-ray dataset where difference densities of 0.633 and -0.510 $eÅ^{-3}$ were obtained. The residual density maps are featureless showing no evidence for an improper model of the charge density. Figure 3-26 shows the experimental (top) and dynamic model (bottom) deformation densities. They both show the charge transfer effects which arise upon the formation of chemical bonds. As expected, density accumulations are observed in the regions of chemical bonds and also in the regions of the N and O lone pairs. A comparison of the experimental with the model deformation density shows no significant differences, highlighting the very good quality of the current charge density dataset which appears to be slightly improved compared to that obtained for Form I.

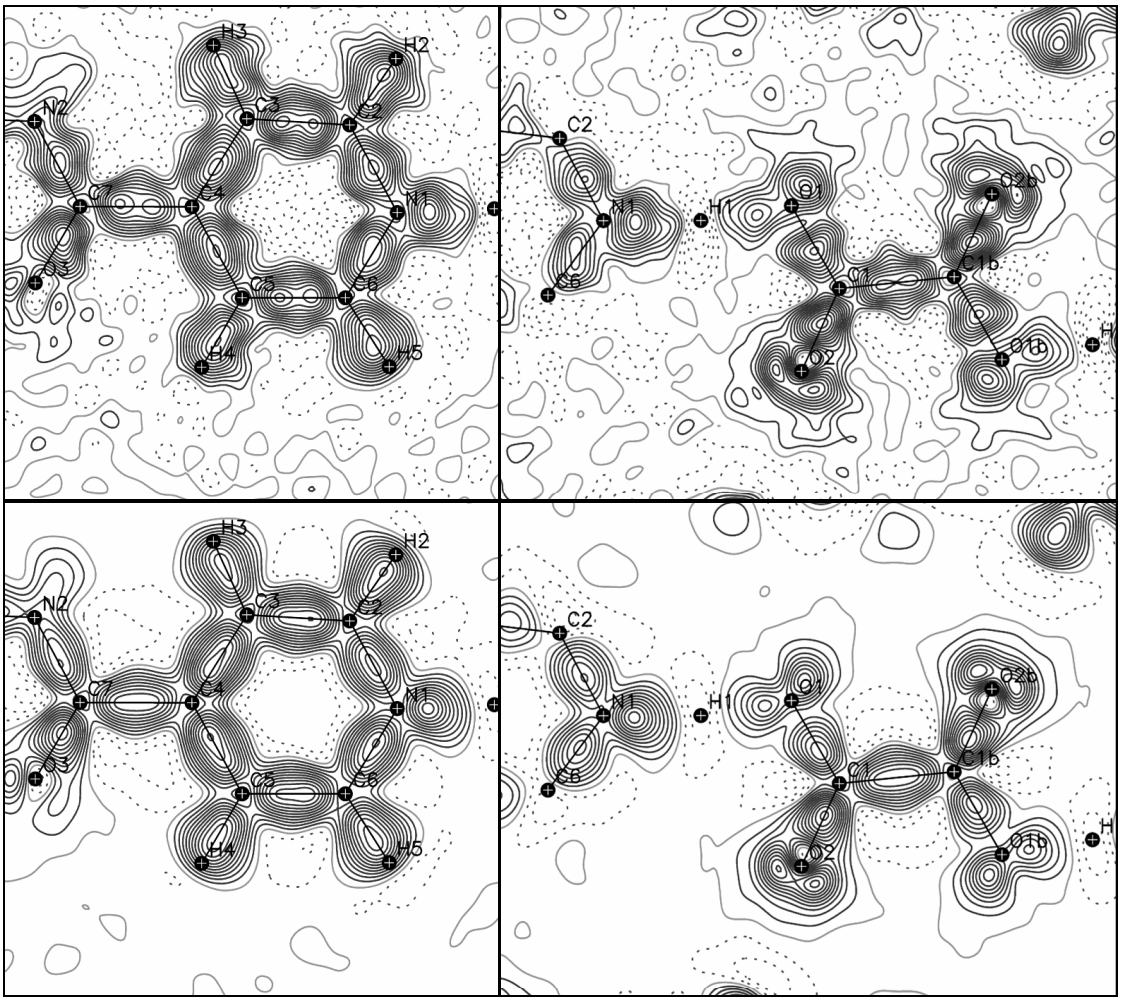

Figure 3-26: (Top) experimental deformation density maps in the pyridine plane (left) and in the C1–O1–N1 plane (right). (Bottom) dynamic model deformation density maps in the same planes; $\sin\theta/\lambda < 1.19$ Å^{-1}, for details see Figure 3-15.

The topological analysis of the total electron density according to AIM has been performed on the multipolar charge density model obtained from the refinement of the experimental and also of the theoretical data. The results will be summarised briefly.

Figure 3-27 shows the gradient vector field, determined from the experimental density, in the C1–O1–N1 plane of the SSHB and the associated critical points. It differs from the map obtained for Form I (Figure 3-19) in that there is no bond path for a C6–H5···O2 hydrogen bonding interaction, and consequentially there is no ring critical point in the hydrogen bonded cyclic synthon previously observed in Form I. This is intuitively explained by the increased separation of H5 and O2 to 2.996 Å in this polymorph (compared to 2.384 Å in Form I) because the pyridine ring is considerably rotated out of the oxalic acid plane, but AIM now rationalises the absence of the weak C–H···O HB on the basis of a physically meaningful property, i.e. the electron density.

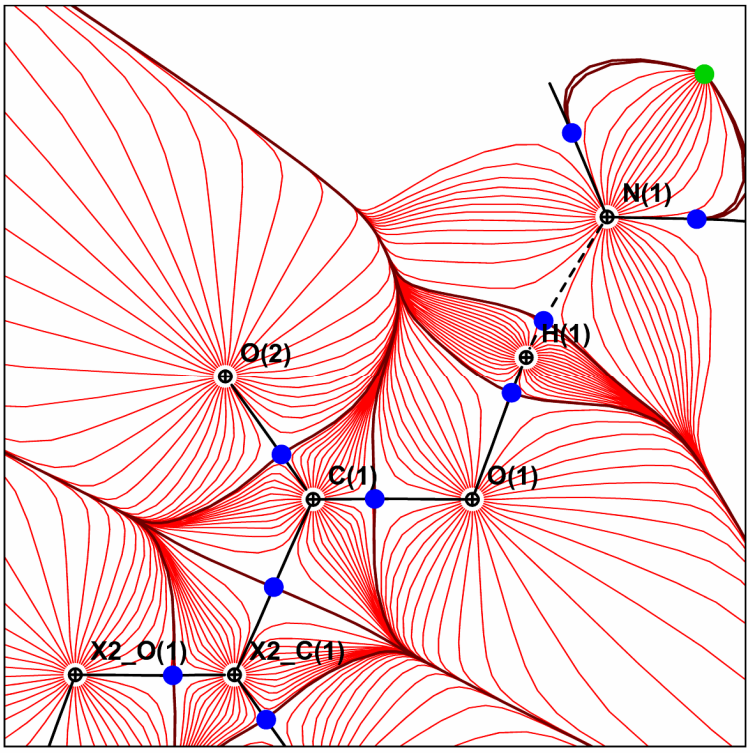

Figure 3-27: Gradient vector field map in the C1–O1–N1 plane of IN_2–OA Form II; for details see Figure 3-19.

Table 3-6: Topological properties at the BCPs of the HBs in IN_2–OA Form II.

	refinement on experimental structure factors					refinement on theoretical structure factors				
HB	ρ_{BCP} / eÅ^{-3}	$\nabla^2\rho_{BCP}$ / eÅ^{-5}	λ_1	λ_2	λ_3	ρ_{BCP} / eÅ^{-3}	$\nabla^2\rho_{BCP}$ / eÅ^{-5}	λ_1	λ_2	λ_3
O1··H1	1.08	–8.35	-12.2	-12.1	15.9	1.10	–4.88	-11.7	-11.7	18.5
H1··N1	0.966	–6.87	-10.3	-10.0	13,4	0.969	–3.76	-9.91	-9.45	15.5
N2–H6	2.14	–34.1	-29.7	-28.3	23.9	2.13	–30.8	-27.9	-26.6	23.7
H6···O3	0.205	1.61	-1.15	-1.14	3.90	0.228	1.63	-1.41	-1.39	4.43
N2–H7	2.34	–38.2	-32.3	-30.8	24.9	2.26	–33.0	-29.6	-28.0	24.6
H7···O2	0.192	1.50	-1.04	-1.02	3.57	0.183	1.77	-1.05	-1.02	3.84

Table 3-6 summarises the properties evaluated at the BCPs of the HBs present in IN_2–OA Form II: the short, strong HB (O1··H1··N1), and the two moderate diamide (N2–H6···O3) and amide–carbonyl (N2–H7···O2) HBs. Again, the BCP properties which have been derived from the multipole refinement on the experimental and theoretical datasets are compared. The centred position of the H atom in the SSHB is reflected by the AIM analysis indicating similar values for the electron densities and charge concentrations at the BCPs for the formally covalent and hydrogen bonding interactions: the enhanced covalence in H1··N1 manifests in a high electron density of ρ_{BCP} = 0.97 eÅ^{-3} and a highly negative Laplacian $\nabla^2\rho_{BCP}$ = –6.9 eÅ^{-5}. The reduced covalence in O1··H1 on the other hand, manifests in (for covalent O–H bonds) a low electron density of ρ_{BCP} = 1.08 eÅ^{-3} and a small negative value for the Laplacian of $\nabla^2\rho_{BCP}$ = –8.4 eÅ^{-5}. The corresponding values obtained from the theoretical data confirm this trend: the experimental electron densities

are very well reproduced, and the Laplacians at the O··H and the H··N BCPs show a similar ratio, if the absolute values are considerably less negative. The increased covalent character of the SSHB in this polymorph is highlighted when the BCP properties are compared to those obtained for the SSHB in Form I (Table 3-4).

Figure 3-28 compares the plots of the negative Laplacian, $L(\mathbf{r})$, shown in the planes of the SSHB as calculated after refinement against the experimental (left) and the theoretical (right) structure factors. The experimentally determined $L(\mathbf{r})$ exhibits very similar features to the situation observed previously in Form I: a) the charge in the SSHB is locally concentrated in nearly the complete region spanned by the O1 and N1 VSCC; b) the region of charge concentration is continuous between the H1 atom and the HB acceptor N1, while it is c) disrupted between H1 and the actual HB donor atom O1. Unlike for Form I however, the continuity of the positive $L(\mathbf{r})$ between H1 and N1 is reproduced by the topological analysis of the theoretical electron density (Figure 3-28, right) in this case. This supports the previous experimental findings that the SSHB in Form II is stronger than that in Form I. In an analogous argument to that made for IN_2–OA Form I, IN_2–OA Form II can be described as an incipient H transfer complex.

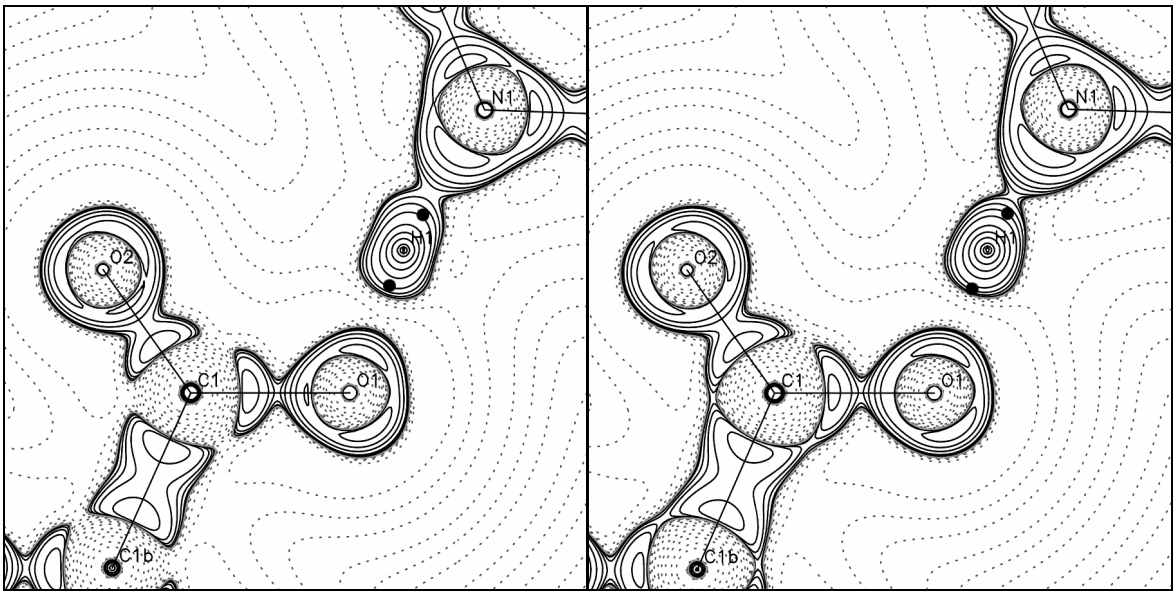

Figure 3-28: Plot of the negative Laplacian, $L(\mathbf{r})$, in the C1–O1–N1 plane of the SSHB in IN_2–OA Form II after refinement on the experimental (left) and theoretical data (right); BCPs in the SSHB – black circles, contours as in Figure 3-20.

The increased covalency of the SSHB is also reflected by the source function, which, as for Form I, has been calculated from the experimental charge density. The source contributions to the electron density at the H1··N1 BCP are visualised in Figure 3-29. Both the source contributions of the H atom (S(H1) = 30.8 %) and the combined contribution of the hydrogen bonded atoms (S(O1+H1+N1) = 82.3 %) are increased with respect to the values found in Form II (26.2 and 77.7 % respectively). The source contributions of O1, H1, and N1, and the sums thereof (included in Table 3-5) also fit the trends of HB strengths observed by Gatti *et al* and described earlier for Form I, adding to the evidence that the SSHB is stronger in this polymorph.

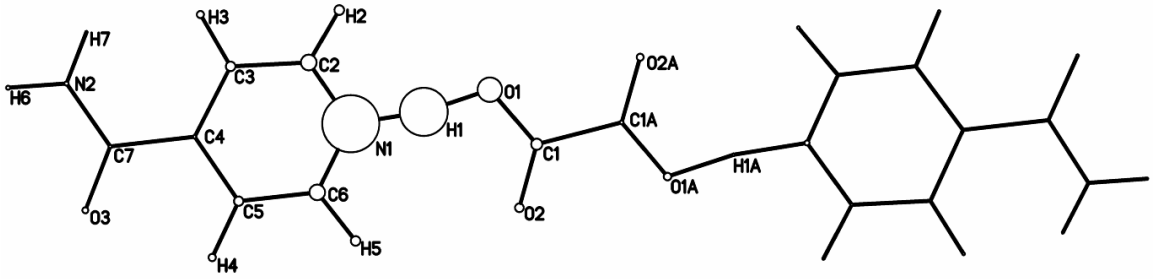

Figure 3-29: Source contribution to the H1··N1 BCPs in IN_2–OA Form II; for details see Figure 3-22.

With respect to the two moderate HBs in IN_2–OA Form II, the AIM analysis of the experimental and theoretical charge densities yields very similar ρ_{BCP} values for both the covalent N–H and the hydrogen bonding H···O interactions. Also the $\nabla^2\rho_{BCP}$ values for the H···O interactions agree well, whereas they are slightly pronounced in the experimental density for the covalent N–H bonds. In contrast to Form I, where the diamide HB is the stronger of the two moderate HBs, in Form II both HBs are assumed to have similar strengths as previously deduced from simple H···O distance considerations. This is supported by the properties at the H6···O3 and H7···O2 BCPs, where the electron densities amount to 0.21 and 0.19 eÅ^{-3}, and the Laplacians to +1.6 and +1.5 eÅ^{-5} respectively (the HB energies which are derived from the BCP properties are listed in 3.1.5 *Hydrogen Bond Energies*, Table 3-10). Figure 3-30 shows the plots of the experimentally determined $L(\mathbf{r})$ in the planes of the two moderate HBs. They are very similar to those obtained for Form I (Figure 3-21). There are subtle differences in the regions of the HB acceptor VSCC, where the "lone pair" VSCC appear to be pronounced in comparison to those for Form I, adding to the findings that the amide–carbonyl HB is strengthened in this case.

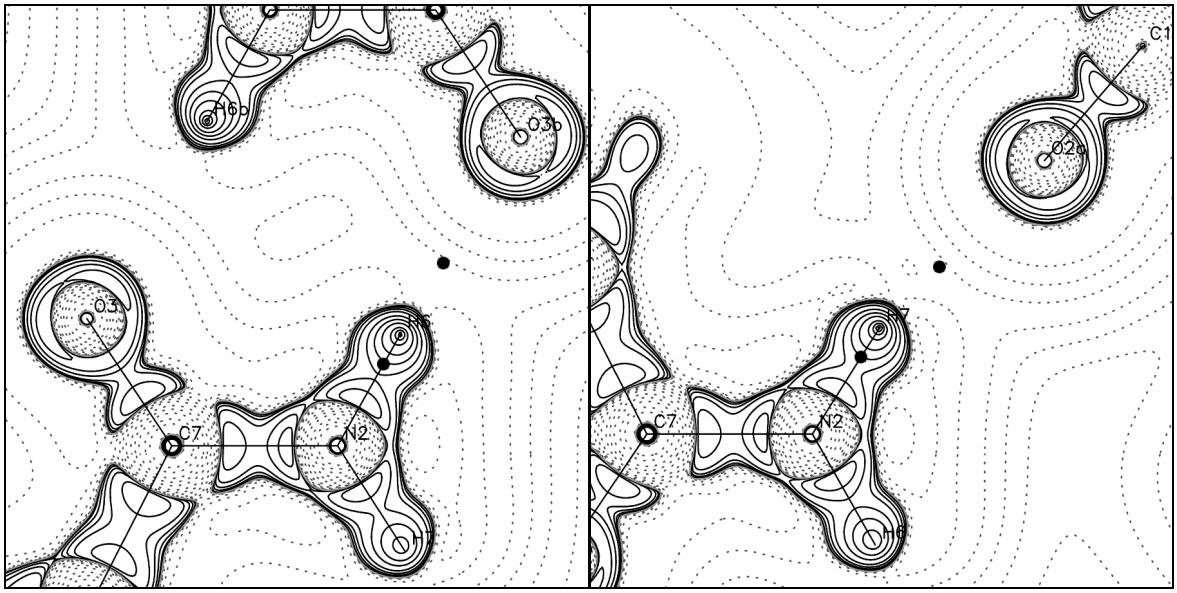

Figure 3-30: Plots of $L(\mathbf{r})$ in the planes of the diamide HB C7–N2–O3 (left), and the amide–carboxyl HB C7–N2–O2 (right); experimental data; BCPs in the HBs – black circles, contours as in Figure 3-20.

3.1.4. Ab Initio Studies

Quantum mechanical calculations have been performed on the two hydrogenous forms of IN_2–OA with the aim of obtaining further insight into the energies involved in both the hydrogen bonding and the occurrence of polymorphism. The energy scale for polymorphism has been established for this material by geometry optimisations in the periodic environment. The energy barriers for H transfer in the SSHB are estimated by the calculation of potential energy curves (PECs) along the HB path. Also, guidance for the problematic localisation of the actual H atom in the SSHB was looked for by finding the energetically favoured HB configuration, i.e. OH···N or NH···O. All calculations were carried out in the full periodic environment using both the plane wave (PW) approach as implemented in the CASTEP code,[50] and the atomic orbital (AO) approach as implemented in CRYSTAL03.[51] Furthermore, quantum molecular dynamic (QMD) studies with CASTEP have been carried out on both forms in order to simulate potential H transfer processes on a finite timescale. The results obtained from the various methodologies are compared against the experimental findings and evaluated accordingly.

Geometry Optimisations

The geometries for IN_2–OA Form I and Form II have been optimised in various ways. The starting geometries were taken from the low T X-ray structure determinations and the lattice parameters fixed to the experimental values for all calculations. At the time the computational studies were initiated, only standard X-ray data were available and for both forms the actual configuration of the SSHB was ambiguous. Hence a few assumptions had to be made regarding the applied symmetry of the system and also the starting geometries. The crystallographic symmetry, a 2-fold axis in the case of Form I and an inversion centre in the case of Form II, renders the two SSHBs formed by OA equivalent in both polymorphs. Thus, the optimised structures can only result in either fully protonated or fully deprotonated OA when the crystallographic symmetry is used. In order to allow for the H disorder model described in *X-ray Studies*, the symmetry needs breaking in a way that OA can adopt the mixed protonated state, i.e. HOOC–COO^-. In practical terms this means that the symmetry is reduced from C2/c to Cc in the case of Form I, and from $P\bar{1}$ to P1 in the case of Form II, with the consequence that for each polymorph one formula unit IN_2–OA is computed independently. Since energy minimisations are always vulnerable to finding a local, rather than the global minimum, the geometries were in addition optimised by starting from the OH···N and the NH···O HB configuration. Of course, the energies of the local minima are also of interest for the estimation of the energies involved in the potential H transfer reaction. The consequential starting geometries for the high and low symmetry setups are depicted in Scheme 3-1 and Scheme 3-2 respectively.

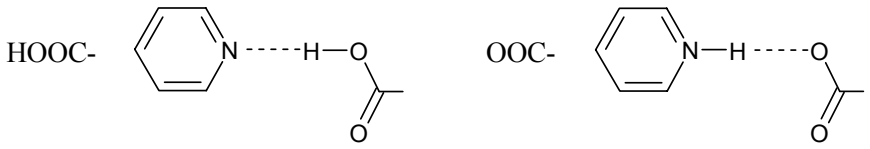

Scheme 3-1: Starting configurations for the optimisation in the crystallographic symmetry.

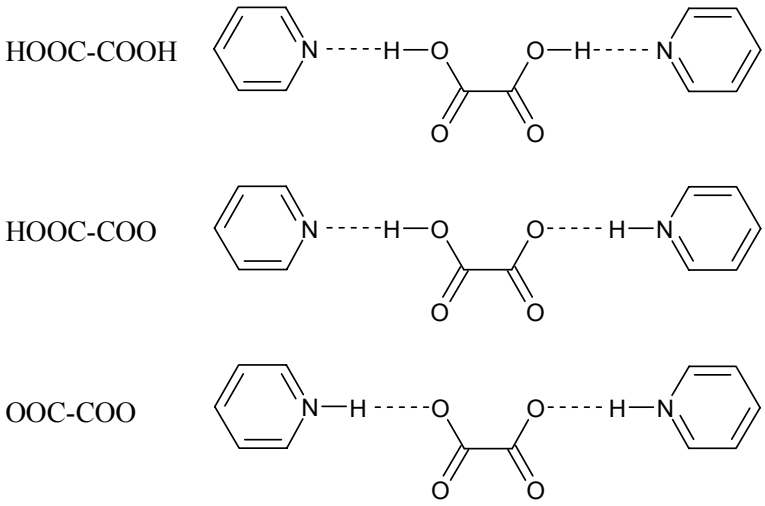

Scheme 3-2: Starting configurations for the low symmetry setup, shown for Form I as an example.

The PW (CASTEP) calculations were carried out using the exchange–correlation functional of Perdew, Burke and Ernzerhof (PBE)[82] with PBE consistent pseudopotentials. The kinetic energy cut-off for the plane wave basis set was set to 450 eV, at which previous performed tests showed that the total energies converge to approximately 1 meV/atom. It varies by much less than this amount for any increase in the shrinking factors of the Monkhorst-Pack mesh beyond the used values of 3×3×2 and 5×3×2 for Form I and Form II respectively. The AO (CRYSTAL) calculations were carried out at the B3PW/6-31g** level of theory. Becke's 3 parameter exchange functional with 20 % HF exchange was combined with Perdew–Wang correlation, yielding the B3PW functional.[48, 83] For the description of the AOs, the Gaussian type basis set 6-31g** was used; it includes polarisation functions on all atoms (*p* basis function for H, and *d* for C, N, and O). For the calculation on atoms or molecules in the gas phase this basis set might be considered incomplete, but for solid state calculations it provides a sufficiently complete description of the wave function, because the close packing of AOs makes the use of diffuse functions unnecessary. On the contrary, introducing more diffuse functions can lead to overcompleteness and numerical instability. The shrinking factors were set to similar values as used for the PW calculations, 3×3×3 and 5×3×2 for Form I and Form II respectively.

Table 3-7: Computed HB parameters for IN_2–OA Form I as obtained by starting from the different geometries shown in Scheme 3-1 and Scheme 3-2; if the geometry failed to converge into a (local) minimum the corresponding line is hyphenated, energies are per formula IN_2–OA and relative to the lowest energy structure, values in parentheses are estimated from the potential energy curves discussed below.

Form I	Starting config.	N···O	N··H	H··OOC	COO··H	H··N	O···N / Å	ΔE / kJ·mol^{-1}	
CASTEP	HOOC–	–	–	–				–	
	OOC–	2.549	1.155	1.394				0	
	HOOC–COOH	–	–	–	–	–	–	–	(+6.0)
	HOOC–COO	2.543	1.420	1.124	1.441	1.130	2.570	+0.9	(0)
	OOC–COO	2.547	1.159	1.389	1.389	1.159	2.547	0	(0)
CRYSTAL	HOOC–	2.550	1.470	1.080				0	(+0.1)
	OOC–	–	–	–				–	(+9.0)
	HOOC–COOH	2.551	1.473	1.078	1.079	1.473	2.551	+0.2	(0)
	HOOC–COO	2.598	1.551	1.048	1.407	1.128	2.535	+0.1	(+0.1)
	OOC–COO	–	–	–	–	–	–	–	(+9.1)

The data obtained from the geometry optimisation runs on Form I are summarised in Table 3-7. Even though the same starting geometries were used for the CASTEP and CRYSTAL calculations, the results could not be more different. For the high symmetry setup, the PW calculations only relaxed into the NH···O minimum, independent of whether the calculation started from the NH···O or OH···N configuration. Correspondingly for the low symmetry setup, no minimum was found for the neutral OA molecule. The optimisations only relaxed into minima for the singly and doubly deprotonated OA, for which the energy difference is ~1 kJ/mol in favour of the latter. The AO calculations on the other hand, resulted in the opposite. For the high symmetry case, only the OH···N minimum was found, and for the low symmetry no minimum was found for the doubly deprotonated OA. Here, the structures relaxed into the HOOC–COOH and the HOOC–COO^- configurations, for which the energy difference is negligible. In short, the PW calculations favour the NH···O, and the AO the OH···N configuration for the SSHB between IN and OA. Optimisations with both approaches relax into geometries for the mixed protonated HOOC–COO^- molecules which are in addition energetically very close to the global minimum. This would justify the calculations in the low symmetry setup, and does indeed support the idea of H disorder in Form I of IN_2–OA. In view of the experimental results showing no H disorder however, CASTEP fails to reproduce, while CRYSTAL successfully reproduces, the correct SSHB configuration, but unequivocally so only when the crystallographic symmetry is used.

As far as the O···N distances are concerned, the computed HB parameters for Form I are reasonably well reproduced by all solid state calculations. The calculated O···N distances agree very well with the experimental value of 2.55 Å, with the exception of the geometry relaxing into the mixed protonated HOOC–COO^-. Here, small asymmetries are observed which manifest in a longer N(H)···O distance (2.57 Å) for the PW calculations and a longer O(H)···N (2.60 Å) for the AO. A comparison of the covalent O–H bond lengths with the neutron data has to be limited to the CRYSTAL calculations since the CASTEP failed to reproduce the correct HB configuration. The calculated O–H distance of 1.08 Å only qualitatively reproduces the experimental elongation to 1.165 Å (at 30 K)

upon formation of the SSHB. For comparison, O–H groups which are involved in moderate or weaker hydrogen bonding have bond lengths of 0.95 – 1.00 Å.

Table 3-8: Computed HB parameters for IN_2–OA Form II; for details see Table 3-7.

Form II	Starting config.	N···O	N··H	H··OOC	COO··H	H··N	O···N / Å	ΔE / kJ·mol^{-1}	
CASTEP	HOOC–	N/A	N/A	N/A				N/A	
	OOC–	N/A	N/A	N/A				N/A	
	HOOC–COOH	–	–	–	–	–	–	–	(+10)
	HOOC–COO	–	–	–	–	–	–	–	(+3.2)
	OOC–COO	2.548	1.142	1.417	1.417	1.142	2.548	0	(0)
CRYSTAL	HOOC–	2.500	1.384	1.125				+0.6	(+1.0)
	OOC–	–	–	–				–	(+4.3)
	HOOC–COOH	2.499	1.363	1.143	1.143	1.363	2.499	+1.5	(+2.6)
	HOOC–COO	2.539	1.468	1.079	1.387	1.139	2.516	0	(0)
	OOC–COO	2.502	1.179	1.331	1.336	1.177	2.504	+2.9	(+4.8)

Table 3-8 lists the results for Form II. The discussion for the PW optimisation runs can be kept short, because these calculations exclusively relaxed into the doubly deprotonated OA, $^{-}$OOC–COO^{-}, independent of the starting geometry. This clearly contradicts the experimental findings. In addition, applying the crystallographic symmetry leads to numerical instabilities. The results for the AO calculations are more versatile and are in much better agreement with the experimental findings. Using the crystallographic symmetry yields, like for Form I, an optimised geometry in the neutral OH···N configuration only. When using the lowered symmetry on the other hand, local minima are found for all starting configurations. Here, the mixed protonated HOOC–COO^{-} geometry is the energetically most favoured, while the HOOC–COOH and $^{-}$OOC–COO^{-} configurations have ~1.5 and ~3.0 kJ/mol higher energies respectively. Thus, the global minimum as determined from the CRYSTAL geometry optimisations is found for HOOC–COO^{-} which would be unattainable when applying the crystallographic symmetry. In this respect, the low symmetry model is also justified for Form II. With respect to the experimental findings on the other hand, showing a nearly centred HB, this is only helpful insofar that the partial H transfer is reproduced as a matter of principle. In general, the CRYSTAL-computed O···N heteroatom distances are about 2.50 Å and therefore too short in comparison with the experimental value of 2.53 Å. The exception is found for the energetically favoured HOOC–COO^{-} geometry for which N···O and O···N are well reproduced, at 2.54 and 2.52 Å respectively. The computed lengthening of the covalent O–H bond (1.125 Å in the high symmetry calculation) is pronounced for Form II, which on the whole agrees with the experimentally observed centred HB (O–H = 1.235 Å), but as for Form I the bond lengthening is underestimated by ~0.1 Å.

An examination of the energies involved in the formation of the IN_2–OA polymorphs is also of interest, for the combination of intermolecular forces driving the formation of such materials is often subtle, with total energy differences usually of the order of only a few kJ/mol. The relative energies are listed in Table 3-9, and are derived from the geometry yielding the global energy minimum for the various optimisation runs. Again, the PW and AO calculations show contradictory results: according to CASTEP, Form II is the

energetically stable polymorph, and according to CRYSTAL it is Form I. The computed absolute energy differences are small, as expected for polymorphic materials; and it is of particular note, that they are on the same scale as the energy differences obtained for the different SSHB configurations. Yet again, it is the CRYSTAL calculations that confirm the tentative experimental observations that Form I is the energetically stable form.

Table 3-9: Energy scale for polymorphism in IN_2–OA.

		optimal OA geometry	ΔE / kJ·mol^{-1}
CASTEP	Form I	OOC–COO	+1.7
	Form II	OOC–COO	0
CRYSTAL	Form I	HOOC–COOH	0
	Form II	HOOC–COO	+2.4

In summary of the geometry optimisations performed, the PW and AO calculations show a trend towards an increased preference for the NH···O configuration when moving from Form I to Form II. Since the neutron data show that in fact the H atom "moves" towards the centre of the SSHB by going from Form I to Form II, the calculations are consistent within each approach in this respect. The PW approach with CASTEP shows, in contradiction to the experimental evidence, a strong preference towards the NH···O configurations, and has consequently to be considered less suitable for reproducing the protonation states in the present strongly hydrogen bonded molecular complexes. The results from the AO calculations with CRYSTAL agree better with the experiment. However, they are misleading in that they do not contradict H disorder in Form I and suggest an increased likelihood for H disorder in Form II. Both these findings are in disagreement with the neutron diffraction experiments. In contrast to the CASTEP calculations however, which determine the energy minima for both forms for the doubly deprotonated OA, CRYSTAL determines the energy minima for Form I and Form II to be those corresponding to the neutral OA, and the singly deprotonated OA molecule respectively. CRYSTAL also seems to better reflect the energy ranking for the two polymorphs.

HB Potentials

In order to reveal more details about the nature of the SSHB, potential energy curves for H transfer along the HB path have been calculated. For this purpose a series of geometry optimisation steps has been performed for variable H positions at O···N distances fixed to the experimental values (2.555 and 2.535 Å for Form I and Form II respectively). The O···N separation has been fixed because it would otherwise adapt to the H position as it is moved across the HB pathway. So it will shorten for a H position close to the centre of the SSHB and lengthen for one close to one of the hydrogen bonded atoms, in accordance to considerations from the bond valence model.[68] Such a shortening/lengthening of the intermolecular distances would involve whole molecule vibrations, accompanied by anisotropic lattice contraction/expansion which is difficult to model reliably. All other atoms, on the other hand, are allowed to relax for each H transfer step because secondary parameters like the previously discussed carboxylic acid C–O bond distances and the pyridine CNC bond angle depend to a small degree on the protonation state of the corresponding species. The correlation between such parameters and the H

transfer coordinate will be documented following the discussion of the PECs (Figure 3-35). Single point energy calculations would run into unfavoured geometries when the H is moved, thereby raising artificially the total energy, and result in biased PECs which do not reflect the correct energy for the H transfer complex. It seems contradictory that the overall geometry is allowed to relax to the varying H position with the exception of the O···N distance only. The current approach has been used for practical reasons and as a compromise between the determination of diabatic and adiabatic HB potentials. The *diabatic* potential assumes that the H transfer occurs at high frequencies to which the heavy atoms *cannot* adapt, whereas the *adiabatic* potential assumes low H transfer frequencies to which the heavy atoms *can* adapt. Because SSHBs are characterised by a shift towards lower X–H stretching frequencies, which are now in the range of the internal (C~O) vibrations, but still much higher than the external (whole molecule) vibrations, the approach used to determine semi adiabatic HB potentials for the current system is considered to be appropriate. In a manner analogous to that used in the geometry optimisations, the PECs have been calculated using both the crystallographic and the reduced symmetry. For the calculations in the reduced symmetry setup, both PW (CASTEP) and AO (CRYSTAL) approaches were employed, while the calculations in the crystallographic symmetry were limited to the AO approach.

In a first step, the symmetry has been reduced in order to allow for the mixed protonated HOOC–COO$^-$ geometry. For this purpose one SSHB formed by OA was kept fixed in either the N···HOOC or the NH···OOC configuration, while for the other the H transfer reaction COOH···N → COO···HN was simulated by stepwise moving the H atom.

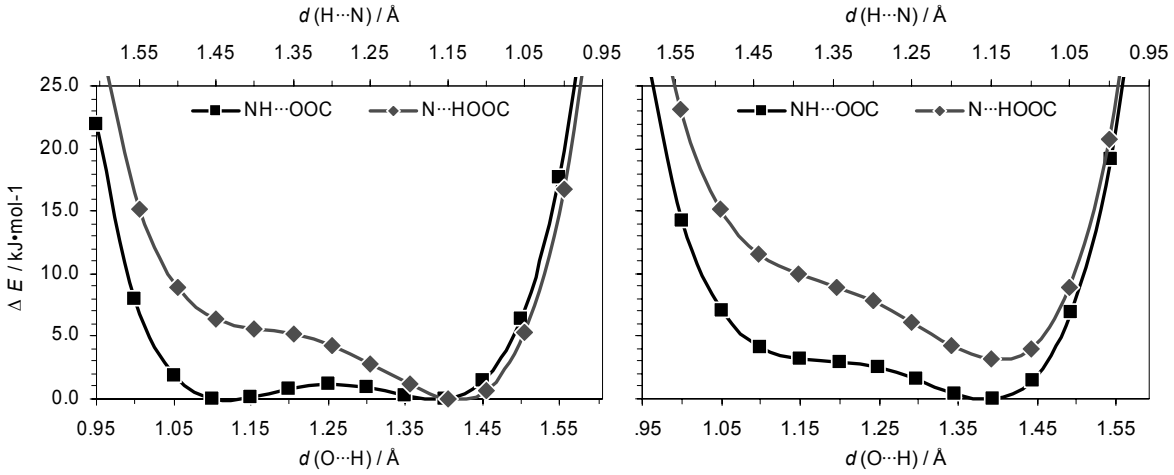

Figure 3-31: Adiabatic HB potentials calculated with CASTEP in the low symmetry setup, IN_2–OA Form I (left), Form II (right), second carboxylic group of OA fixed in NH···O (black squares) and OH···N (grey diamonds). Relative energies are per formula unit IN_2–OA.

The potentials obtained with CASTEP (Figure 3-31) reflect what the geometry optimisations have shown previously: the NH···O configuration is energetically favoured over the OH···N for nearly all potentials. The only minimum for a H position at the O site is found for Form I, and only when the second SSHB formed by OA is fixed in the NH···OOC configuration. This situation corresponds to the local minimum obtained for the mixed protonated HOOC–COO$^-$ geometry. The corresponding potential (black squares in Figure 3-31 left) shows the nearly symmetrical double well profile with a low barrier of ~1.2 kJ/mol for H transfer, which is typical of a low barrier hydrogen bond (LBHB). The

associated H transfer reaction can be illustrated as NH···OOC–COOH···N → NH···OOC–COO···HN. The other HB potential (grey diamonds in Figure 3-31 left), has been obtained by fixing the second SSHB formed by OA in the N···HOOC configuration. It shows an asymmetric single well profile with the minimum for NH···O, and the HB can consequently be classified as a single well hydrogen bond (SWHB). For Form II (Figure 3-31, right), the analogous HB potentials show only the profiles characteristic of SWHBs, both with the energy minima corresponding to H occupying the N sites.

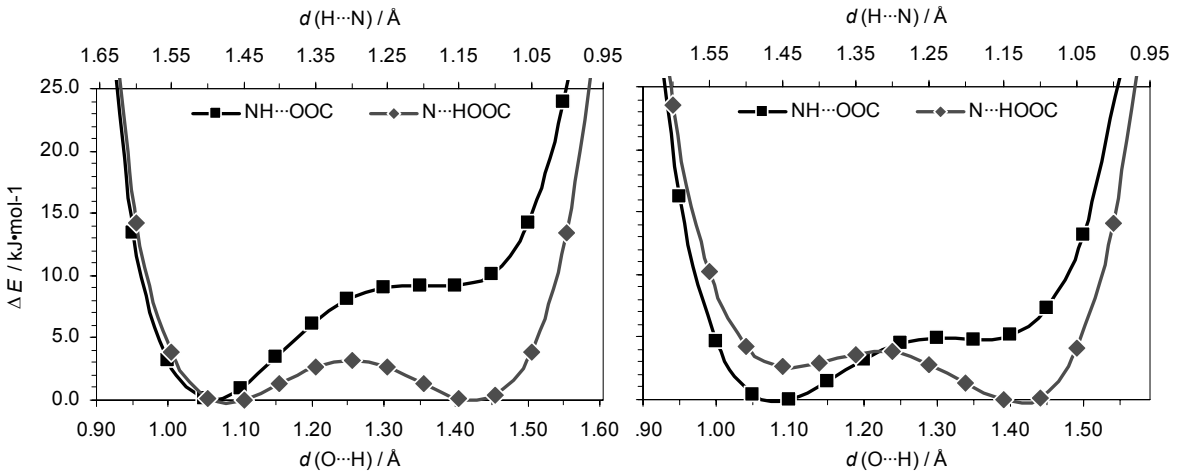

Figure 3-32: Adiabatic HB potentials calculated with CRYSTAL in the low symmetry setup, IN_2–OA Form I (left), Form II (right); for details see Figure 3-31.

The PECs calculated with CRYSTAL (Figure 3-32) also reflect the results from the geometry optimisations as expected: pronounced minima are found for H occupying the O site for Form I, and minima for all HB configurations in Form II. In Form I, the HB potentials also show a LBHB and a SWHB profile. The H transfer reaction which corresponds to the LBHB (grey diamonds in Figure 3-32 left), N···HOOC–COOH···N → N···HOOC–COO···HN, differs from the CASTEP calculation in the configuration of the second OA HB. The energy barrier for H transfer is calculated here to a higher value of ~3.1 kJ/mol compared to the above ~1.2 kJ/mol. The SWHB profile (black squares in Figure 3-32 left), obtained with the second OA HB fixed as NH···OOC, shows now the minimum energy for the OH···N configuration. In Form II the PECs have the shapes of asymmetric LBHB profiles; the two minima in the double well profiles have slightly different energy levels. The lower energy level in each case is obtained for the HB configuration which opposes that of the second OA HB. In other words, when one HB is in the N···HOOC configuration, the low energy minimum for the other HB will be found for COO···HN, and vice versa.

As mentioned previously, in a second step PECs have been calculated with CRYSTAL also using the crystallographic symmetry. This implies that the H atoms are moved simultaneously across the two SSHBs, and that the N···HOOC–COO···HN geometry is symmetry forbidden. This is maybe the more appropriate approach in view of the neutron data, which show no evidence for H disorder and thus none for the occurrence of the above forbidden configuration. In addition to adiabatic HB potentials (determined in an analogous fashion to the low symmetry setups above), in this case also diabatic HB potentials were calculated. For this purpose single point energy calculations were performed for each H step on a previously optimised geometry (with the O···N distance

fixed to the experimental value), which relaxed for both forms into the OH···N configuration. Furthermore, the 1-dimensional Schrödinger equation was solved for each potential thus obtained with the program 1D_SCHRODINGER.[84] The calculated wave functions serve two purposes: first, the zero point energy and the energy levels for the excited states are determined; and second, the probability density distribution (reflected by ψ^2) for the H atom in the SSHB returns an expectation value for the O–H distance.

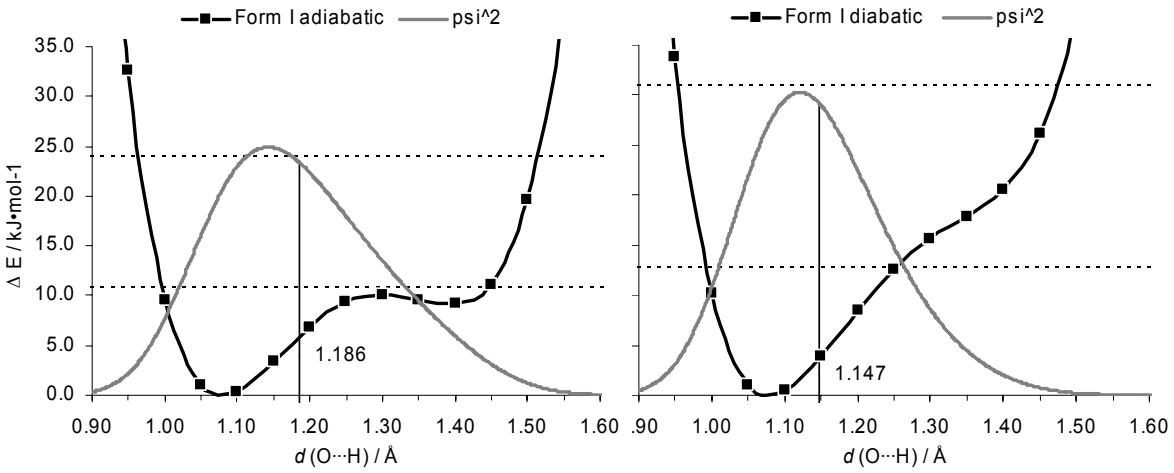

Figure 3-33: Adiabatic (left) and diabatic (right) HB potentials in IN_2–OA Form I calculated with CRYSTAL using the crystallographic symmetry, probability density distribution (ψ^2) in grey, zero point energy and first excited state as dashed lines, vertical lines mark the expectation values for *d*(O···H).

The adiabatic and diabatic PECs for Form I are shown in Figure 3-33. They both have in common the global energy minimum for the OH···N configuration as previously established from the geometry optimisation runs. The difference is found in the evolution of the potential shapes when moving the H atom across the HB path. The adiabatic potential shows a second, high energy minimum for the NH···O configuration, separated by an energy barrier for H transfer of approximately 10 kJ/mol. This NH···O minimum is absent in the diabatic potential because the geometry of the hydrogen bonded molecules was not allowed to adapt to the changed HB configuration. The consequence is an asymmetric single well profile in comparison to the broader double well profile in the adiabatic case. The difference in the profile shape is reflected by the energy levels which are consequently lower in the adiabatic potential: 10.7 and 23.8 kJ/mol compared to 12.8 and 31.0 kJ/mol in the diabatic case for the zero point energy and first excited state respectively. The difference is furthermore reflected by the probability density distribution and the expectation value for the H position which offers a useful tool to evaluate the approach used to determine the profile. The O–H distance of 1.165 Å found in the experimental low T structure at 30 K lies midway between those found for the ground state expectation values of 1.186 and 1.147 Å in the adiabatic and diabatic potential respectively. In view of the observed trend towards longer O–H distances with decreasing T, the adiabatic HB profile seems to better reflect the true nature of this SSHB. It is worth mentioning that the NH···O minimum in the adiabatic double well potential cannot be populated by thermal excitation alone since the energy difference between the first excited state and the zero point energy (ΔE = 13.1 kJ/mol) corresponds to T = ~1600 K ($E = k_B \cdot T$).

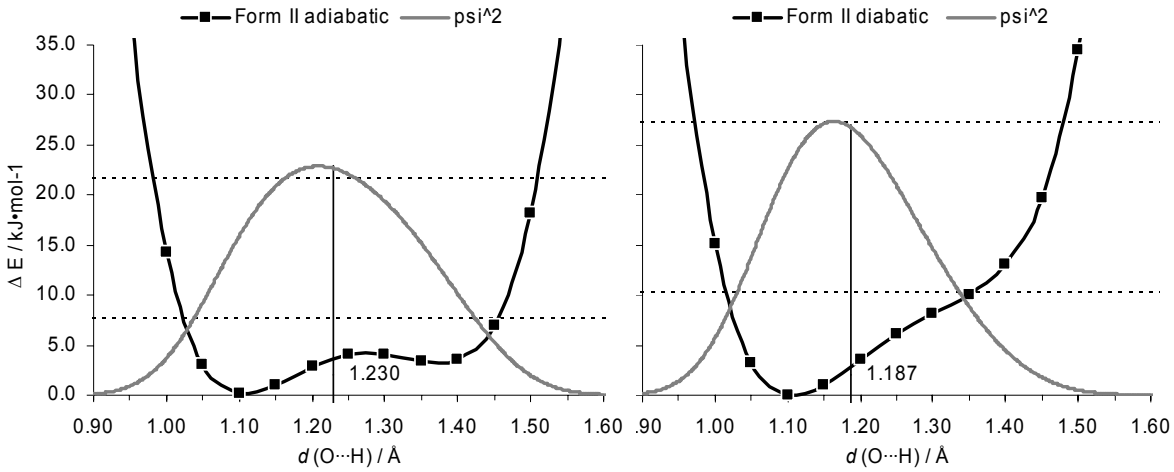

Figure 3-34: Adiabatic (left) and diabatic (right) HB potentials in IN_2–OA Form II in the crystallographic symmetry; for details see Figure 3-33.

The PECs calculated for Form II (in Figure 3-34) show similar profile shapes: a double well profile in case of the adiabatic, and an asymmetric single well profile in the case of the diabatic potential. The HB potentials in Form II are flatter than those in Form I, as observed previously for the potentials determined in the reduced symmetry. The H transfer barrier in the adiabatic potential is reduced to ~4 kJ/mol and the two energy minima found for the OH···N and the NH···O configurations are separated by ~3 kJ/mol only, giving rise to a LBHB profile. The zero point energy levels are also reduced to 7.7 and 10.1 kJ/mol in the adiabatic and the diabatic case respectively. As far as the expectation values are concerned, the experimental O–H distance of 1.235 Å at 100 K is very well reflected by 1.230 Å in the adiabatic HB potential, showing that the approach used is indeed appropriate. For comparison, the expectation value of 1.187 Å in the diabatic potential is significantly underestimated.

As a result of the HB potential calculations, the relative energies for those geometries which did not relax into a local minimum in the previous geometry optimisations, can now be estimated from the PECs, and are listed for Form I and Form II in Table 3-7 and Table 3-8 respectively (energy values in brackets). They have higher values than those obtained by full optimisations, because for the calculations of the PECs, the O···N separations were fixed to the experimental, time averaged distances, and were consequently not allowed to relax into optimal (from the computational point of view) geometries.

Finally, the dependence of carboxylic acid C–O bond lengths and pyridine CNC bond angles on the protonation states has been established/reproduced on the basis of the computational studies carried out here. Figure 3-35 shows the evolution of these heavy atom parameters upon stepwise moving the H atom from the carboxylic acid towards the pyridine base. The data have been taken from the geometry optimisation steps for the determination of the adiabatic HB potential for Form I[a] in Figure 3-33. Starting from the carboxylic acid, the distance between C and the hydroxyl O continuously shortens upon abstraction of the H atom, while the carbonyl C=O lengthens by almost the same amount until they reach equal values for the completely deprotonated carboxylate ion. The

[a] The corresponding parameters for Form II are essentially the same and have therefore not been included in this work.

pyridine CNC bond angle increases in a similarly continuous manner upon the stepwise protonation; in this case from ~118º to ~122º for isonicotinamide.

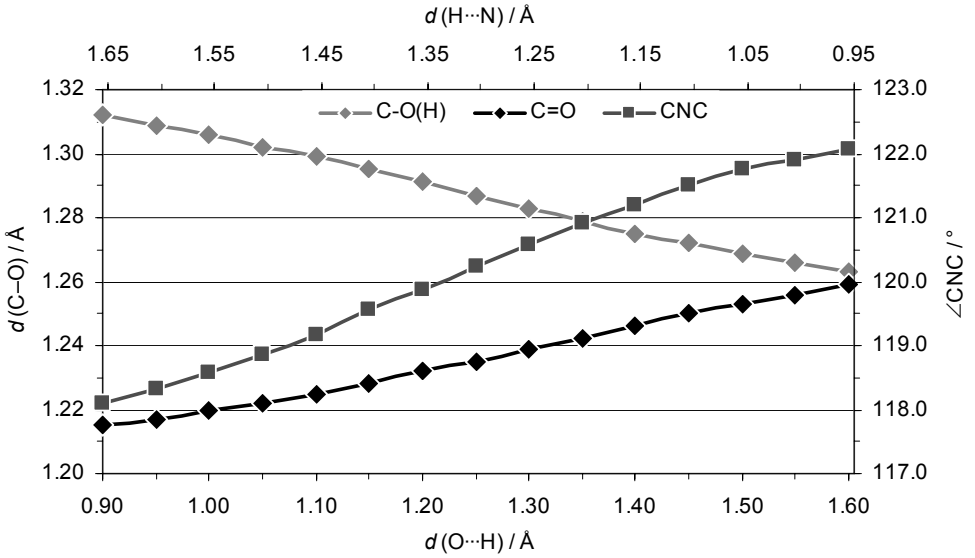

Figure 3-35: Correlation between carboxylic acid C–O bond lengths (black and grey diamonds) and pyridine CNC angle (grey squares) and the H transfer coordinate.

In summary, the results obtained with CRYSTAL seem to better reproduce the experimental data. In particular the energy barriers for H transfer are more realistic – energy barriers which are essentially absent from the CASTEP PW calculations. It has been shown by Poater *et al* that an increase in the weight of HF exchange leads to progressively higher energy barriers.[85] Since no HF exchange is included in the PW approach, compared to 20 % HF exchange in the AO approach, the difference in PW and AO determined energy barriers is mainly due to the use of different functionals. Furthermore, the barrier crossing events are liable to be strongly coupled to the heavy atom distances, i.e. the hydrogen bonded atoms contract prior to an H transfer event. Hence, the energy barriers calculated with fixed heavy atom distances are likely to be overestimated.

Both forms IN_2–OA show energy minima for the singly deprotonated OA, which are clearly not occupied as evident from the neutron diffraction experiment. In spite of a potentially wrong determination of the energy minima, especially with the PW calculations, the HB potentials show the broad and flat shape typical of SSHBs. The energy levels in most PECs span less than 5 kJ/mol for a large range on the H transfer path. The energy differences are small, and the actual potential shapes depend on the applied model. Once again it is worth mentioning the symmetry and the geometry constraints imposed on the structure – in this case the O···N distances and the configuration of one of the two SSHBs. All PECs obtained in the low symmetry situation show a cooperative effect with respect to the protonation state of the second OA SSHB, a result which does not agree with the experimental evidence. The PECs obtained in the crystallographic symmetry on the other hand, perfectly reflect the time averaged, experimental H positions at O–H distances of 1.165 and 1.235 Å for Form I and Form II respectively. Comparing the results from the PW and AO calculations, they give opposite answers to the same questions, as previously observed for the geometry optimisations. So far, the AO approach within CRYSTAL has to be considered superior over the PW within CASTEP for the calculations carried out here.

Molecular Dynamics

Quantum molecular dynamic (QMD) simulations have been carried out on the two hydrogenous forms of IN_2–OA with the PW approach as implemented in CASTEP. The motivation was to simulate the H transfer behaviour, or in other words, the H mobility in the SSHBs at finite temperatures. The previous ab-initio calculations are all based on ground state energy calculations at a temperature of zero Kelvin, while the experimental data are obtained at finite temperatures (100 K for the X-ray, and a minimum of 30 K for the neutron diffraction studies). Thus, QMD might better simulate the material for the experimental conditions, as the previously observed discrepancy between PW calculations and experiment might be due to kinetic effects. For this purpose, QMD calculations have been performed for Form I at three different temperatures, 50 K, 100 K, and 200 K; and for Form II at 100 K. The NVT ensemble has been used which fixes the crystal volume and keeps the temperature at a constant level via thermostat control by the *Nosé–Hoover* algorithm.[86, 87] For Form I, the crystallographic lattice parameters of the C centred monoclinic cell were used as lattice parameters for a symmetry deprived P1 supercell, containing now 4 formula units of IN_2–OA to be calculated independently. For Form II, a similar 4 formula unit containing supercell was constructed from the crystallographic triclinic cell. The QMD simulations were run for a duration of ~2 ps each, in steps of 0.4 fs. The first 500 time steps, corresponding to 0.2 ps, have been excluded from the analysis to assure that the kinetic and potential energies have reached an equilibrium state. The data thus obtained data are discussed here briefly.

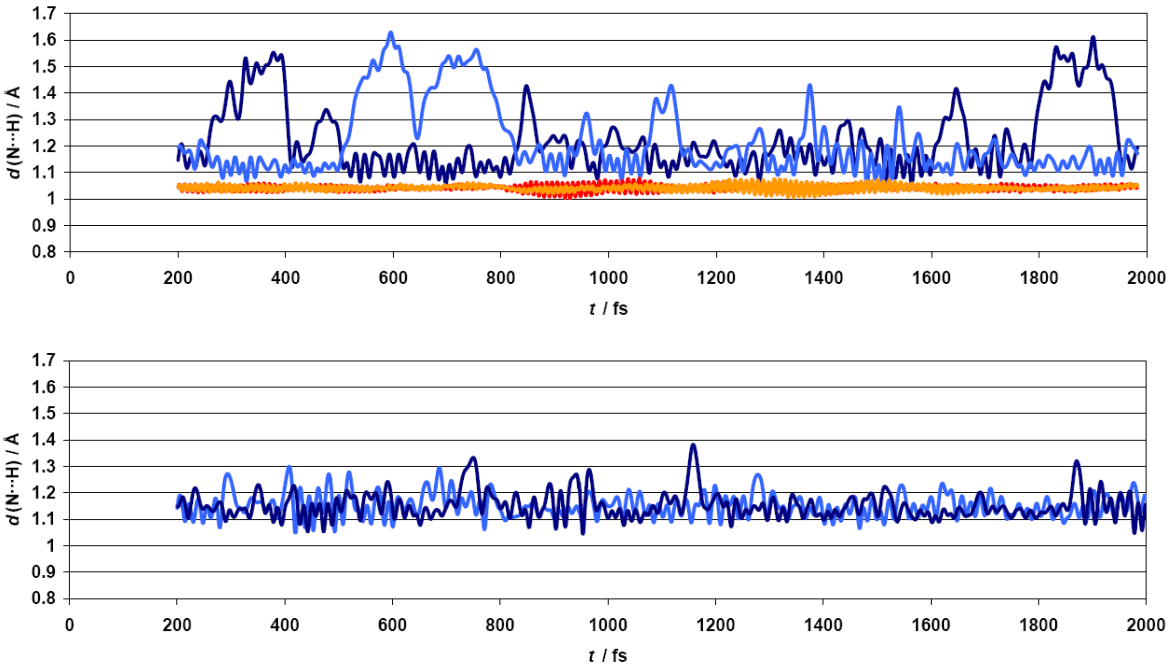

Figure 3-36: 100 K MD simulations on IN_2–OA Form I (top) and Form II (bottom); the configurations of the two SSHBs formed by one exemplary OA unit are shown by means of N–H bond lengths (blue/light blue); for comparison N–H bond lengths in the amide–amide HB are also presented (red/orange).

Figure 3-36 presents the evolution of the H positions in the SSHBs at 100 K for one exemplary IN_2–OA moiety in each of the polymorphs. The two N–H distances in N··H··OOC–COO··H··N are plotted versus the simulation time in blue and light blue respectively. In Form I, the H atoms occupy mostly the N sites in the SSHBs, and are

occasionally transferred towards the O (reflected by long N–H distances in Figure 3-36, top). At no time however, are the two H atoms simultaneously located in the OH···N configuration which would give rise to the molecular configuration of the complex IN_2–OA, N···HOOC–COOH···N. Instead, only the N···HOOC–COO···HN and the NH···OOC–COO···HN configurations are observed. This is true not only for the exemplary IN_2–OA unit in the above figure, but for all of the 4 independently simulated units; and at all simulated temperatures. Only the ground state energy minima in the HB potentials are occupied at finite temperatures on a finite time scale, and in this respect the QMD simulations confirm the previous PW results. On the other hand, the QMD calculations nicely point out the difference between SSHBs and common HBs. Figure 3-36, top, includes the evolution of the N–H bond lengths taken from an arbitrary diamide HB (red/orange). The different H behaviour is evident: while the amide N–H vibrations occur at small amplitude and high frequencies, the oxalic acid H atoms experience large positional shifts, but at lower frequencies. This observation agrees well with the observed redshift in IR for SSHBs, and is qualitatively reproduced by the frequency analysis of the 100 K QMD runs (Figure 3-37). In Form II (Figure 3-36, bottom), the H atoms almost exclusively occupy the N sites, and move only on few occasions halfway across the HB path to a central position in the SSHBs.

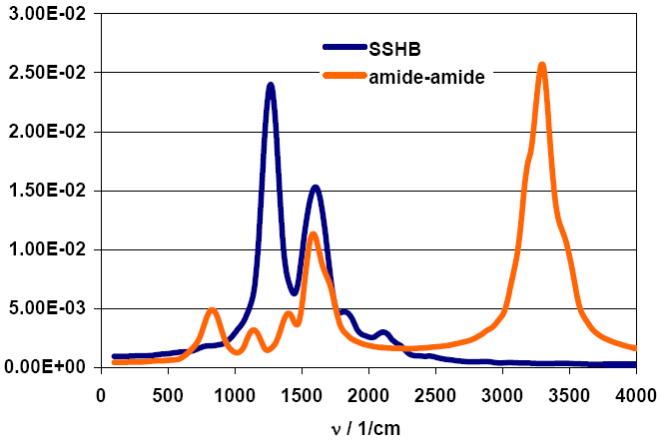

Figure 3-37: Frequency analysis of the 100 K QMD run for Form I by Fourier transformation of the force autocorrelation function.

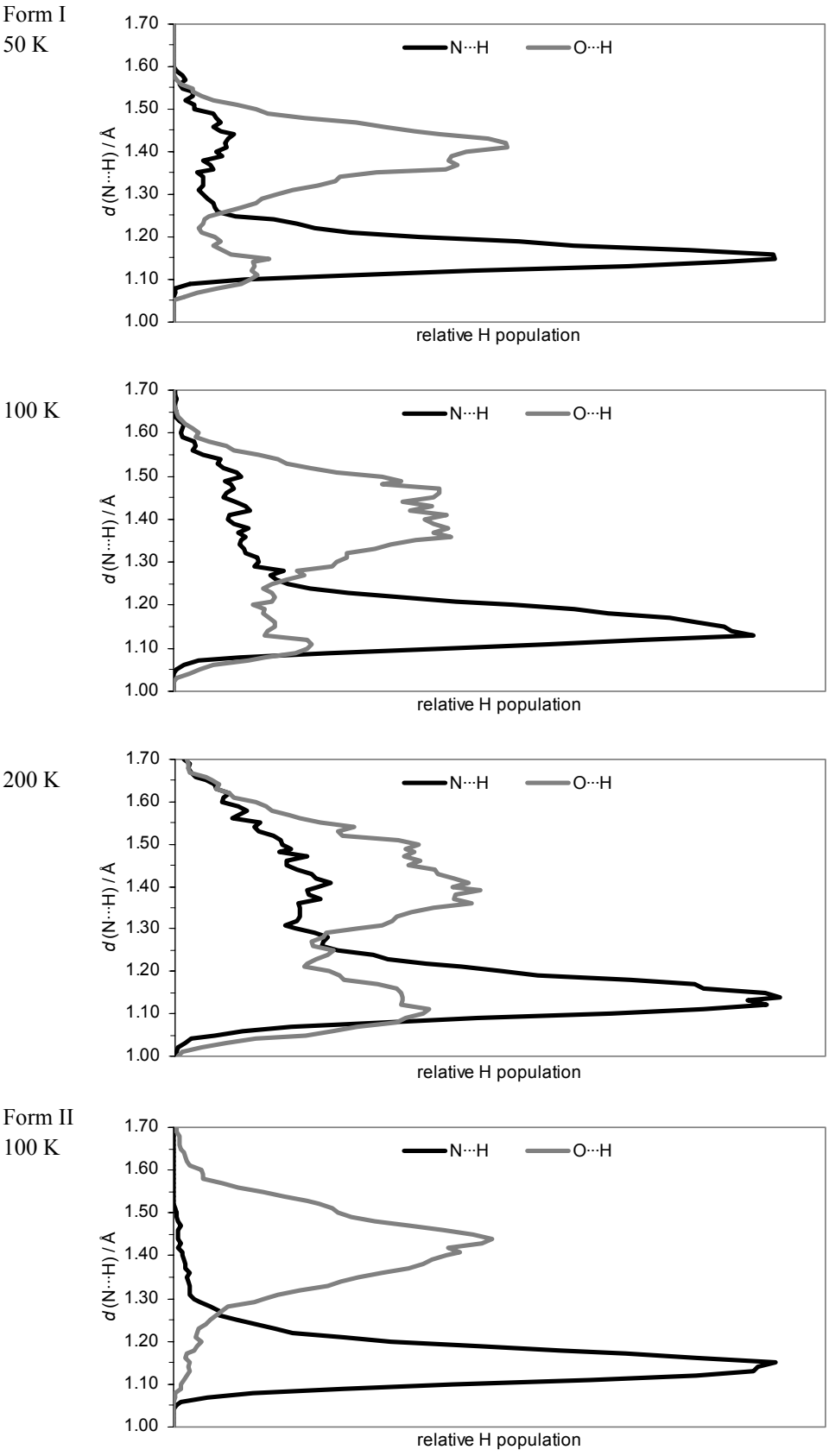

Figure 3-38: Relative H population frequencies in the SSHBs as obtained from the MD simulations on IN_2–OA, determined over the 8 independent SSHBs, distances in Å.

Another way of analysing the H behaviour is demonstrated in Figure 3-38. It shows the population frequencies of the H atoms in the SSHB potential by means of the O–H and N–H distances. The relative population levels are averaged over all independent H atoms involved in the strong hydrogen bonding, and over the complete period of the simulation time (omitting the first 0.2 ps). In the series of the variable temperature QMD simulations for Form I at 50 K, 100 K, and 200 K, the preference of the NH···O configuration manifests in the sharp peak for the N site minimum (black curves, in the population distributions). It broadens slightly with increasing T but maintains the maximal H population level at a constant ~1.15 Å away from the N nucleus. The O site minimum (grey curves) in the HB potential only gets significantly populated when the thermal energy of the system is increased; with a population maximum closer to the covalently bonded atom than for the N site minimum. The broad peaks in the H population distributions at distances around 1.4 Å correspond to the hydrogen bonding H···O and H···N interactions. They considerably broaden at higher temperatures as the fluctuations of the O···N distances increase. For Form II, the population analysis confirms that, according to the PW calculations, H exclusively populates the N site (Figure 3-38, bottom). This is in good agreement with the previous geometry optimisations and PEC calculations, but again contradicts the experimental findings.

In summary, the QMD studies using the PW approach nicely point out the qualitative difference between moderate and strong HBs, and they show at least qualitatively correct trends upon variation of the thermal energy in the system. They are consistent with the results from the previous PW ground state energy calculations, and thus do not improve the strong disagreement with the experiment. For this reason the QMD studies can not improve the understanding with respect to the SSHB in the current system.

3.1.5. Hydrogen Bond Energies

The HB energies in the two polymorphic forms of IN_2–OA have been subject to discussion in the previous parts of this chapter. They have been estimated for the present work from the topological analyses and also by separate energy calculations for the solid state structures and the individual (hydrogen bonded) moieties constituting the solid state.

The topological analysis of the total electron density, determined by the previous charge density studies, allows a "quantification" of the HB energies according to the approximation proposed by Espinosa *et al* (see 2.3 on Energy Densities).[17] The required BCP properties have been taken from the multipole refinements on both the experimental and theoretical structure factors. The HB energies thus obtained are listed in Table 3-10; unfortunately they are unrealistic and highly overestimated for the SSHBs (H1···O1), because the condition for this approach that the BCP to nuclei distances are in the range of ~ 0.5 – 2.1 Å is not fulfilled in this case as d(BCP···H1) < 0.4 Å (more realistic HB energies have been obtained from the solid state calculations described below). The calculated HB energies for the moderate and weak HBs on the other hand, can be assumed to reflect realistic values; at least they fall in the expected energy range for such interactions. In any case, the relative HB strengths of the two moderate HBs as present in the two polymorphs can now be compared. They reflect the previous observations that in Form I the diamide HB (H6···O3) is stronger than the amide-carbonyl HB (H7···O2), and that in Form II the two moderate HBs are more similar in strength. The largest deviations between the HB energies derived from the AIM analysis of experimental and theoretical

data appear for the diamide HB whereas all applied methods for the amide–carbonyl HB yield very consistent values.

Table 3-10: HB energies (kJ·mol^{-1}) in IN_2–OA, calculated according to Espinosa *et al* from the BCP properties of the experimental and theoretical (in parenthesis) charge densities, H1···N1 HB energies are unrealistic and given in italics; calculated also from neutron H···O distances (100 K) using the approximation $E_{HB} \sim 25300 \cdot \exp(-3.6 \cdot d(H\cdots O))$.[17]

	HB	d(H···O) / Å	ρ_{BCP} / eÅ^{-3}	$\nabla^2\rho_{BCP}$ / eÅ^{-5}	E_{HB} from BCP	E_{HB} (H···O)
Form I	H1···N1	1.398	0.769 (0.795)	–3.31 (–1.94)	*187 (205)*	–
	H6···O3	1.894	0.157 (0.209)	2.07 (1.65)	23.7 (30.5)	27.7
	H7···O2	1.997	0.129 (0.150)	1.81 (1.35)	18.5 (19.4)	19.1
	H5···O2	2.392	0.043 (0.064)	1.10 (0.97)	6.6 (7.6)	4.6
Form II	H1···N1	1.313	0.966 (0.969)	–6.87 (–3.76)	*264 (280)*	–
	H6···O3	1.871	0.205 (0.228)	1.61 (1.63)	29.6 (34.0)	30.1
	H7···O2	1.904	0.192 (0.183)	1.50 (1.77)	26.8 (26.5)	26.7

HB energies have also been determined by means of separate energy calculations on the hydrogen bonded molecular fragments and their constituting individual molecules. For this purpose, solid state calculation have been performed with CRYSTAL according to the following procedure: in a first step, the crystallographic geometry has been optimised in order to retrieve a) the total energy of the periodic structure as a reference energy, and b) the optimised geometries which the molecular fragment IN–OA–IN and the molecules IN and OA adopt in the solid state. In a second step, the individual fragments have been isolated from the crystalline environment in order to model the breaking of the HB interactions, and their ground state energies have subsequently been determined by single point energy calculations. The counterpoise correction has been applied which corrects for the fact that the close packing of AOs – as it is present in the crystal – is lost upon isolation of a molecular fragment.[88] In a periodic calculation, an atom/molecule can, driven by basis set incompleteness, use basis functions of neighbouring AOs yielding more variational freedom and a reduction in total energy. This of course is not possible for a molecular calculation in the absence of such AOs. In other words, not correcting for the missing AOs would result in systematically higher energies which cannot be compared with the reference energy obtained from the periodic calculation. The effect is known as basis set superposition error (BSSE). The counterpoise correction places fixed "ghost atoms", which are effectively empty AOs, around the molecular fragment at positions where the real atoms would have been in the crystalline environment. The radius around the fragment within which such ghost atoms are generated has been set to 4 Å. The HB energies are determined by taking the difference of the total energy of the periodic structure and the corresponding molecular fragments and individual molecules respectively. Thus calculated HB energies and the mathematical operations to obtain these are listed in Table 3-11.

Table 3-11: Calculation of HB energies, N = number of HBs present in the crystal moiety, for details about the energy calculations see text.

	moiety	E_{moiety} / au	HB	N	E_{HB} / kJ·mol^{-1}	energy calculation
Form I	Crystal	-1211.9233				
	IN-OA-IN	-1211.9033	moderate HB	4	13.1	(IN-OA-IN – Crystal)/4
	IN	-416.8406				
	OA	-378.1675	SSHB	2	71.6	(2×IN + OA – IN-OA-IN)/2
Form II	Crystal	-1211.9220				
	IN-OA-IN	-1211.8911	moderate HB	4	20.3	(IN-OA-IN – Crystal)/4
	IN	-416.8400				
	OA	-378.1521	SSHB	2	77.5	(2×IN + OA – IN-OA-IN)/2

One formula unit IN_2–OA forms 8 moderate HBs to neighbouring molecules as can be seen from Figure 3-1. Because the energy gain on formation of each such HB is equally shared with another molecule, the energy loss upon removing one unit IN_2–OA corresponds to that of 4 moderate HBs. Dividing the energy difference between IN_2–OA in the full crystalline environment and the isolated IN_2–OA by 4, thus yields the approximate average energy for one moderate HB, which is ~13 kJ/mol in Form I. This energy unfortunately also includes all other intermolecular interactions (attractive as well as repulsive) which cannot be quantified separately. Fortunately, they are weak in comparison to the HB energies and ignoring them is a tolerable approximation. Similar considerations lead to the estimation of the SSHB energy as ~72 kJ/mol, although here the contribution of the weak CH···O HB to the interaction energy between IN and OA is ignored. In Form II, the HB and SSHB energies are calculated as ~20 and ~78 kJ/mol respectively. The HB energies for the moderate HBs are systematically smaller in comparison to those derived from the topological analysis (see Table 3-10).

3.2. DEUTERATED POLYMORPHS

3.2.1. X-ray Studies

The isotopic substitution of H for D in the molecular complex IN_2–OA was motivated by the possibility to obtain additional, valuable information about the nature of the SSHB. Any observation of the H/D isotope effects, the intrinsic as well as the equilibrium H/D isotope effect as described in 1.2 *Strong Hydrogen Bonds*, should help in determining the "true" potential energy surface for H transfer in this material. Aside from the structural information obtained by diffraction experiments, the hydron motion in HBs becomes observable by solid state NMR studies for D atoms.

Deuteration in this system was easily achieved by co-crystallising IN and OA from D_2O instead of H_2O. Aside from the acidic oxalic acid H atoms, the amide H atoms were also almost completely exchanged (see absence of the N–H stretch in Figure A-3, Appendix A). Like the non deuterated complexes, IN_2–d-OA crystallises in two polymorphic forms of which crystals could be isolated and their structures determined by X-ray diffraction. Surprisingly none of the structures proved to be isostructural to any of

the non deuterated forms (rendering the envisaged solid state NMR studies obsolete). Such behaviour of structural change upon isotopic replacement is known as isotopomeric polymorphism.[32] The two deuterated structures are formulated as:

IN_2–d-OA Form I $\equiv 2[DC_6H_4D_2N_2O]^+ [C_2O_4]^{2-}$

IN_2–d-OA Form II $\equiv C_6H_4D_2N_2O \cdot [DC_6H_4D_2N_2O]^+ [DC_2O_4]^-$

Both forms of IN_2–d-OA co-crystallise from the same solution, Form I with stick shaped morphology and Form II with plate shaped, and both in the space group $P\bar{1}$. Form I is by far the dominant species in the deuterated system, whereas only a few crystals of Form II could be obtained from the present crystallisation conditions (crystallising from a mixture of D_2O and EtOD has no effect in this respect). The crystals of Form II furthermore dissolve on a timescale of a few days if they are not isolated from the solution. It seems to be evident that Form I is both the energetically and kinetically favoured polymorph under the present experimental conditions. Interestingly, when IN and OA are co-crystallised from a mixture of H_2O and D_2O, crystals isostructural to both IN_2–OA and IN_2–d-OA (Form I in each case) are obtained with the deuterated structure forming prior to the non deuterated.

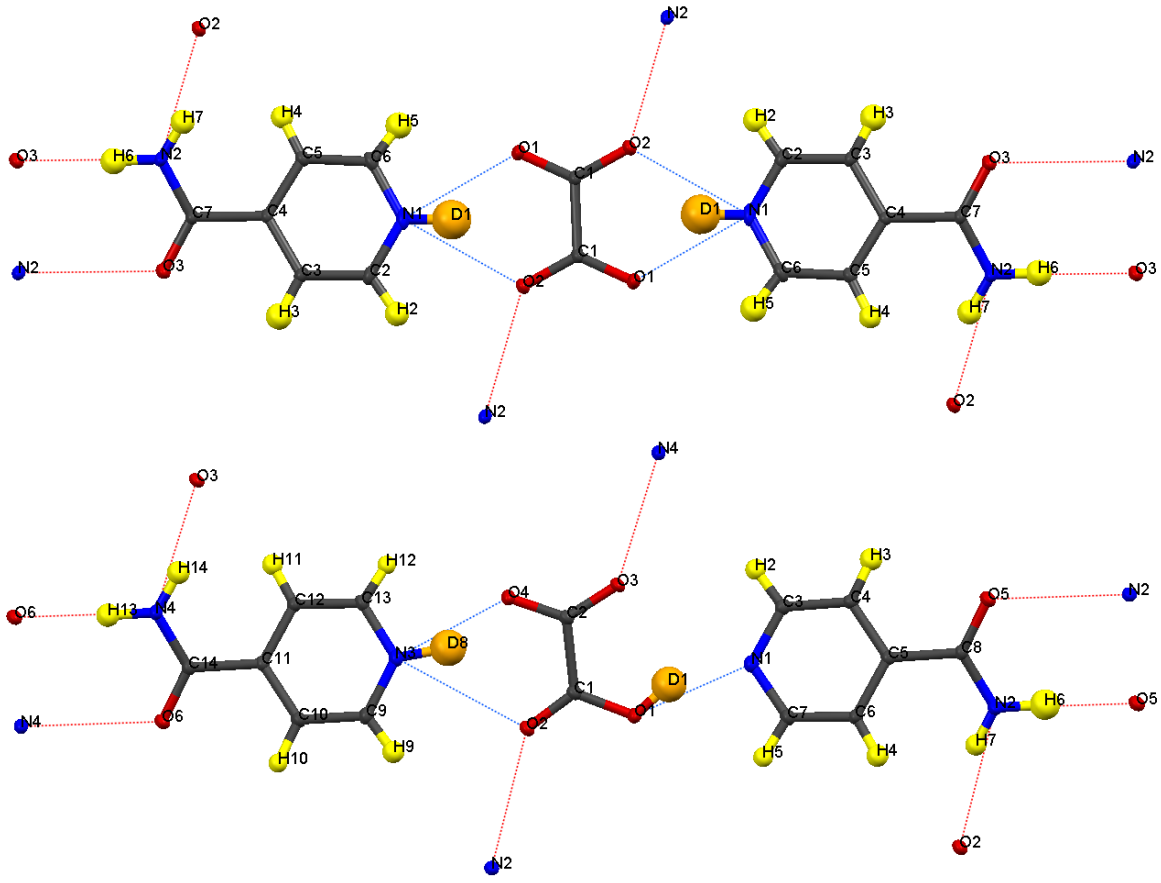

Figure 3-39: Formula units of IN_2–d-OA including the HB schemes, (top) Form I, (bottom) Form II, the amide H are largely exchanged by D.

Figure 3-39 shows the formula units of the two IN_2–d-OA polymorphs. They share the $(–IN–OA–IN–)_n$ chain motif known from the non deuterated analogues. The main structural difference manifests in the way OA is hydrogen bonded to the IN molecules. The OA units in both forms are rotated about 90º in the IN–OA–IN plane with respect to

OA in the non deuterated forms, and as a consequence now form surprisingly bifurcated HBs to IN. The "secondary" hydrogen bonded motif, on the other hand, is common with the non deuterated system. This includes the amide–amide HBs as well as the interchain amide–carbonyl HBs, of which the latter are responsible for the formation of the hydrogen bonded extended networks (Figure 3-40). Both Form I and Form II of the deuterated complexes show 2-dimensional layered structures and are in this respect comparable to the non deuterated Form II. In fact, the crystal packing schemes of IN_2–d-OA Form I and IN_2–OA Form II are very similar; this is also reflected by very similar lattice parameters (see Appendix B, Table B-1). The structural difference between the two deuterated forms arises from the stacking of the tape-like –IN–OA–IN– chains. In Form I, the OA as well as the IN units are stacked upon each other in a parallel fashion (as they do in IN_2–OA Form II), whereas in Form II the amide groups of IN alternatively point in opposite directions with the consequence that the OA units are situated above the centres of the amide–amide HBs.

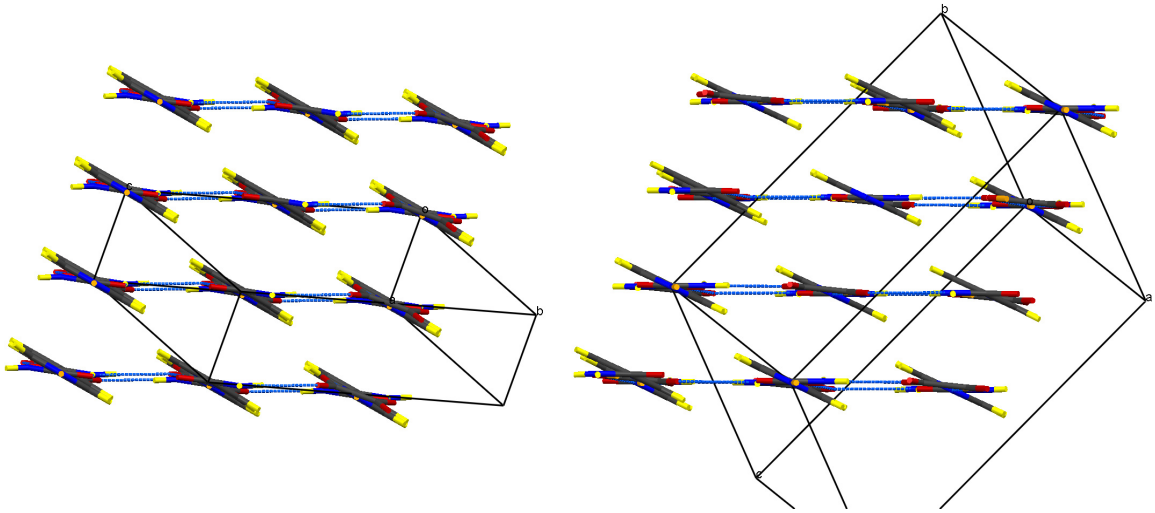

Figure 3-40: Packing schemes of IN_2–d-OA, viewed along the –IN–OA–IN– chains; (left) Form I, (right) Form II, HBs are shown in blue dotted lines.

As far as the SSHBs in the non deuterated forms are concerned, one can conclude that deuteration did not result in the desired information gain. For one, the occurrence of isotopomeric polymorphism alone challenges a direct comparison because it can be argued that any potential H/D isotope effect in the SSHB is caused by a change in the crystalline environment. A deduction from the deuterated to the non deuterated system is eventually rendered obsolete by the dramatic change of the HBs between OA and IN. They are bifurcated in the deuterated forms and have thus changed from strong interactions in IN_2–OA to rather moderate HBs in IN_2–d-OA. The isotopic substitution has failed in this respect. On the other hand, the deuterated system is of course of great interest on its own. Also, an investigation of the driving forces behind the "structural" H/D isotope effect, meaning the isotopomeric polymorphism, is highly desirable, if not part of this work.

Form I

The structure of IN_2–d-OA Form I was determined by means of a high quality X-ray dataset at 100 K. All positional parameters and ADPs including those for the H and D atoms were refined to R_1 = 3.73 % for all data and to a resolution of $\sin\theta/\lambda$ = 0.78 Å^{-1}.

Figure 3-41 shows the ellipsoid plot of the asymmetric unit (the OA molecule has been completed for clarity). As in the non deuterated forms, OA is situated on a symmetry element (an inversion center in this case), and consequently only one bifurcated HB formed by OA is independent. As mentioned previously, the HB can no longer be considered a SSHB, with heteroatom distances of N1···O1 = 2.708(1) and N1···O2a = 2.773(1) Å. They are of only moderate strength, rather comparable to the other intermolecular HBs in this structure. The HB parameters for both forms of IN_2–d-OA are summarised in Table 3-12. The high quality of the X-ray dataset is indicated by the difference Fourier map in Figure 3-42 which has been obtained after refinement without the inclusion of the hydrogen bonding atom D1. It shows the regions around the bifurcated HB in the O1–N1–O2a plane where the distinct features of bonding and even O lone pair densities can be observed. It is evident from Figure 3-42 that the D atoms have been completely transferred from d-OA towards the IN molecules. This is also reflected by the C–O bond lengths of 1.247(1) and 1.263(1) Å which are characteristic of carboxylate anions, and the CNC bond angle of 122.40(6)° which agrees very well with those found for the fully protonated IN cations in references [64, 65] (the C–O and CNC parameters are listed in Table 3-13).

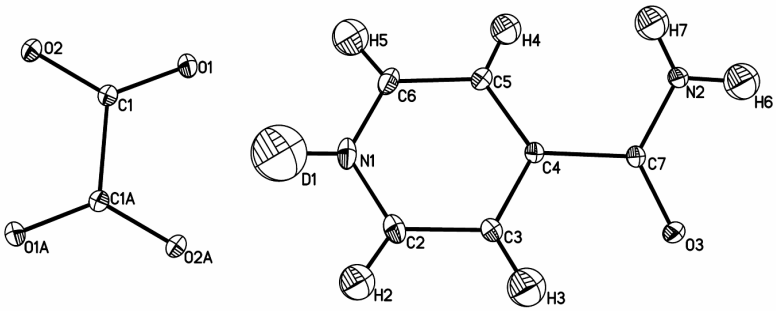

Figure 3-41: Ellipsoid plot of IN_2–d-OA Form I, the amide H are largely exchanged by D; for details see Figure 3-3.

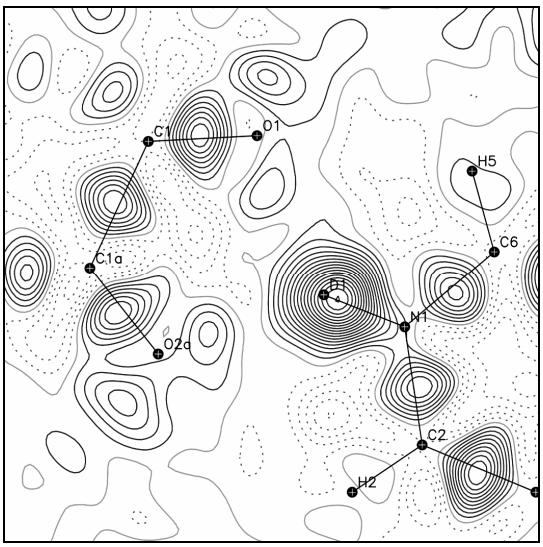

Figure 3-42: Difference Fourier map in the O1–N1–O2a plane of IN_2–d-OA Form I; $\sin\theta/\lambda < 0.78$ Å^{-1}, for details see Figure 3-4.

Form II

The crystal structure of IN_2–d-OA Form II, determined by X-ray diffraction at 100 K, displays a superstructure. It can be solved and refined in two different unit cell settings which are referred to as "supercell" and "small cell" from hereon, of which the correct structure is determined in the supercell as we will see below. The supercell can be transformed into the small cell by applying the transformation matrix (1 0 0, 0.5 0 0.5, 0 -1 0). The small cell can be visualised as the primitive setting of a B centred supercell, and has consequently half the volume of supercell (see Appendix B, Table B-1). The intensities of reflections contributing to the supercell (h + l = odd) are on average lower by a factor ~25. In the small cell, half a formula unit IN_2–d-OA is independent with the OA unit lying on a symmetry element ($\bar{1}$) as known from the previous structures. In the supercell, for the first time in this system, one complete formula unit is independent. Individual datasets have been integrated for the two unit cell settings from the same experiment, and the resolution was set in both cases to $\sin\theta/\lambda = 0.78$ Å^{-1}. As for Form I, all positional and displacement parameters have been fully refined; in the small cell to R_1 = 3.99 and 5.12 %, and in the supercell to R_1 = 4.62 and 8.60 % for the observed ($F_{obs} > 4\sigma(F_{obs})$) and all data respectively. The higher residuals after the supercell refinement are naturally caused by the inclusion of the low intensity supercell reflections.

The ellipsoid plots and difference Fourier maps in Figure 3-43 and Figure 3-44 respectively, reveal the reason for the occurrence of the superstructure: apparently only one D atom is transferred from d-OA to IN. Refining the structure in the small cell results in an "artificial" D disorder with a 50 : 50 ratio, because here only one of the two O··D··N HBs is crystallographically independent. The "disorder" is resolved by refinement in the supercell. The HB configurations with respect to d-OA can be denoted as N–D···OOC–COO–D···N, where the orientation of the covalent X–D bonds alternate in the –IN–OA–IN– chains with each IN_2–OA unit from right to left. This can be visualised by means of the inversion centres in the centres of the diamide HBs common to all co-crystals of IN with OA. The HBs between OA and IN have separation distances of O1···N1 = 2.623(1) Å and O4···N3 = 2.614(1) Å (see Table 3-12) and are hence borderline cases regarding a classification as strong or moderate, if significantly stronger than the HBs in Form I. An indication for the potentially covalent character of these HBs is presented below by interpretation of the deformation densities. But let us first discuss the ellipsoid plots of Form II in Figure 3-43.

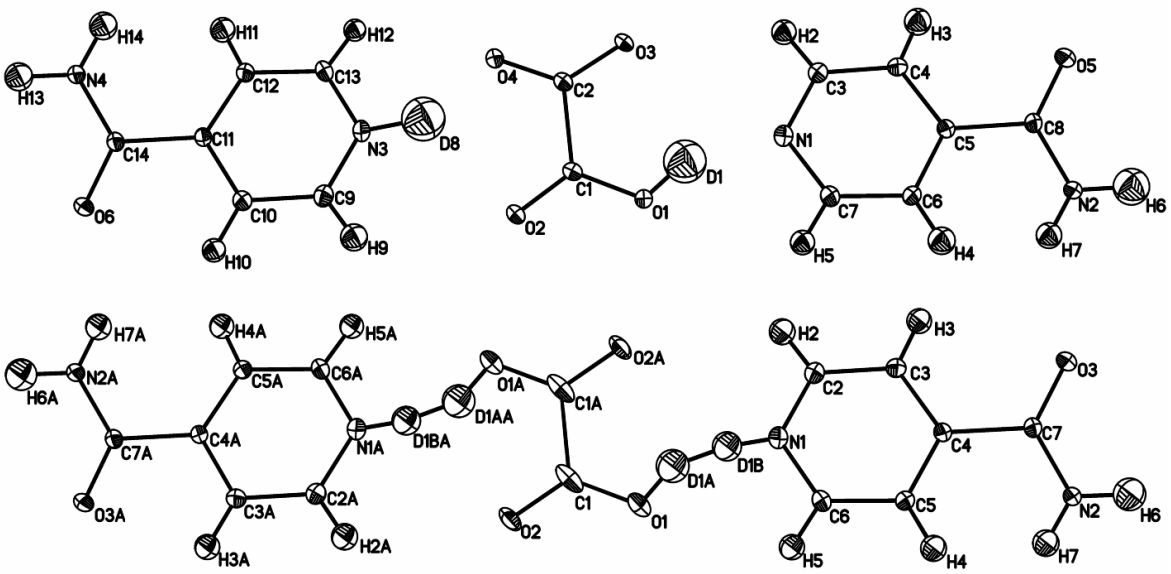

Figure 3-43: Ellipsoid plots of IN_2–d-OA Form II at the 50 % probability level as refined in the supercell (top) and the small cell (bottom), the amide H are largely exchanged by D.

Figure 3-43, top shows the ADPs as refined in the supercell which is the correct unit cell setting; and Figure 3-43, bottom, shows the ADPs as refined in the small cell. In the small cell, the structure shows disorder with respect to the O··D··N HB, and the D atom has been refined correspondingly on a split site with the ratio of occupancies fixed to 50 : 50. The disorder manifests not only in the split site but also in suspiciously elongated ADPs for the C and O atoms constituting the OA molecule, whereas the ADPs for all other atoms in the structure look reasonable. The determination of H/D atoms from X-ray diffraction is always ambiguous but the determination of the "heavy" atoms should result in reasonable and accurate positional and displacement parameters, which is apparently not the case for the OA molecule. Hence, it is the suspicious ADPs above which primarily indicate that the structure is not modelled properly; the structure is eventually modelled properly in the supercell setting. In this case the D disorder is resolved and also the ADPs of the OA atoms now look reasonable. From this it can be deduced that (in this structure) the apparent disorder of the O··D··N HB in the small cell not just affects the D atom itself but the complete OA unit which links the two IN molecules. This is an encouraging result because the reverse conclusion is that in the absence of suspicious heavy atom ADPs, H/D disorder can more confidently be ruled out, even in cases of high electron density delocalisation for the H/D atoms. This conclusion is supported by the findings for the non deuterated forms which both show reasonable looking heavy atom ADPs.

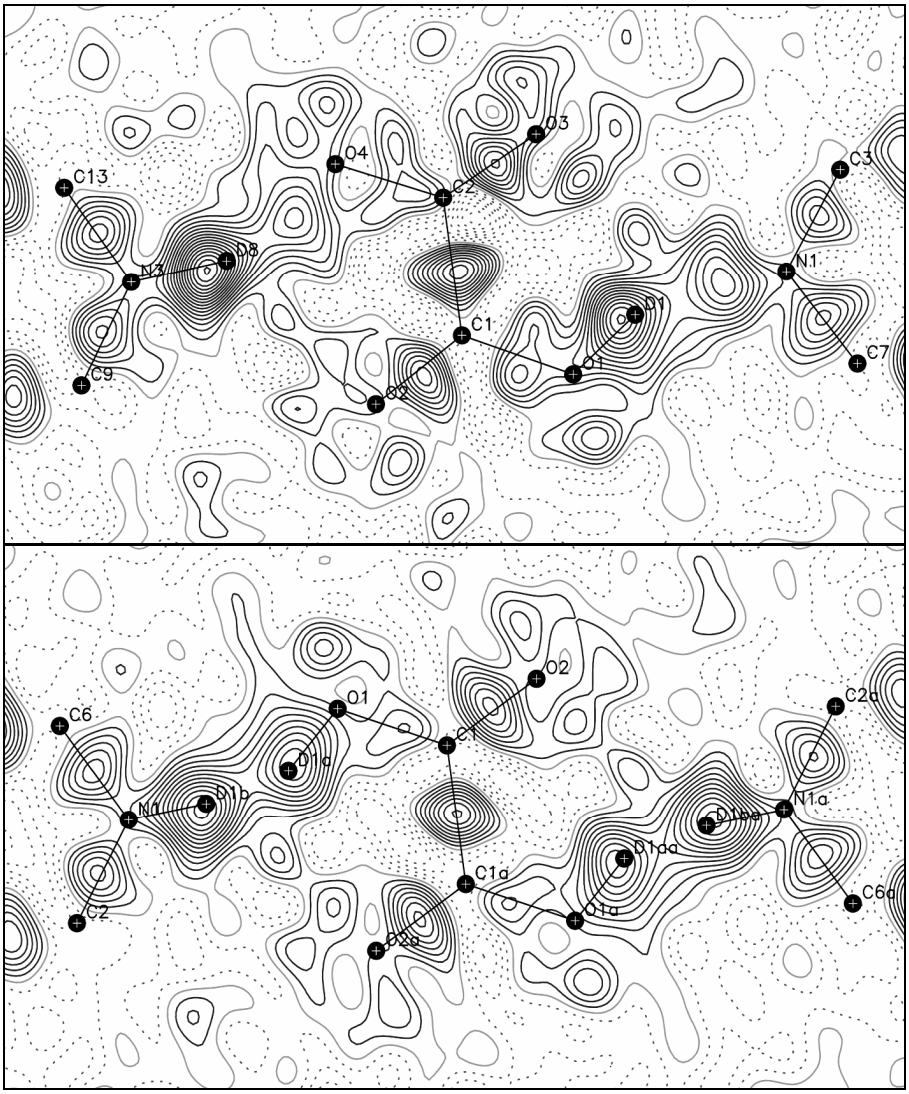

Figure 3-44: Difference Fourier maps of N_2–d-OA Form II in the OA planes after refinement in the supercell (top) and the small cell (bottom); $\sin\theta/\lambda < 0.78$ Å^{-1}, for details see Figure 3-4.

The interpretation of the electron difference Fourier maps obtained after refinement in the supercell (Figure 3-44, top) and the small cell (Figure 3-44, bottom) follows a similar argument. Knowing that D is disordered in the small cell but ordered in the supercell, offers the opportunity to visualise and describe the electron density for a truly disordered H/D atom in such an acid – pyridine base system; and from there, to make conclusions about systems with unknown HB configuration. The first observation is that the two density peaks for the disordered D atoms in Figure 3-44, bottom, are distinctively separable – in contrast to the situation to be recalled for the non deuterated, not disordered structures. Second, the relative densities for the D atoms which correspond to the O–D···N and N–D···O configurations can now directly be compared. For the small cell refinement, the density maxima for the disordered (O1)D1a and (N1)D1b are ~0.5 and ~0.6 eÅ^{-3} respectively. For the supercell refinement, the corresponding densities for the ordered (O1)D1 and (N3)D8 are ~0.7 and ~0.8 eÅ^{-3} respectively (for comparison the (N1)D1 density in Form I is also ~0.8 eÅ^{-3}). As a result, the D atoms located at the N sites have persistently higher electron densities by ~0.1 eÅ^{-3}. This can be explained by the previously observed contribution of the N lone pair density which is higher compared to that of the O

lone pairs – that is when they are determined by difference Fourier synthesis after spherical atom refinement (see Chapter 4 *Imaging the Electron Density of Hydrogen in Strong Hydrogen Bonds*). Third, the electron densities in the H···N and H···O interactions can be estimated from the difference Fouriers of the ordered system (Figure 3-44, top). For D1···N1 and D8···O4 they are ~0.45 and ~0.35 eÅ^{-3} respectively, and have thus comparable magnitudes. The density for D8···O4 can be furthermore compared with the O lone pair densities in this structure, which have average values of 0.20 – 0.25 eÅ^{-3}, and are thus lower by 0.10 – 0.15 eÅ^{-3}. This difference indicates that the densities in the HB interactions D1···N1 and D8···O4 do not exclusively originate from lone pairs, but have an additional contribution from H···A bonding densities. As a result, the current HBs can be considered to have partial covalent character as observed for the SSHBs in the non deuterated structures.

Table 3-12: HB parameters for IN_2–d-OA.

	HB	D–H / Å	H···A / Å	D···A / Å	∠DHA / °
Form I	N1–D1···O1	0.98(2)	1.94(2)	2.7077(8)	133.1(15)
	N1–D1···O2*	0.98(2)	1.970(19)	2.7727(8)	137.5(15)
	N2–H6···O3*	0.954(14)	1.947(14)	2.8999(8)	176.9(12)
	N2–H7···O2*	0.899(13)	1.963(13)	2.8252(8)	160.1(12)
Form II	O1–D1···N1	0.95(2)	1.74(2)	2.6231(14)	152.1(18)
	N3–D8···O4	1.08(2)	1.61(2)	2.6137(14)	150.7(17)
	N3–D8···O2	1.08(2)	2.30(2)	3.0307(13)	123.3(14)
	N2–H6···O5*	1.02(2)	1.87(2)	2.8847(14)	175.3(16)
	N2–H7···O2*	0.875(17)	2.161(16)	3.0041(13)	161.6(15)
	N4–H13···O6*	0.978(18)	1.914(18)	2.8868(13)	172.6(14)
	N4–H14···O3*	0.954(17)	1.954(16)	2.8767(12)	162.0(14)

* Atoms generated by symmetry.

Table 3-13: C–O bond lengths and CNC bond angles in IN_2–d-OA.

			C~O / Å		∠CNC / °
Form I		C1–O1	1.2468(8)	C2–N1–C6	122.40(6)
		C1–O2	1.2626(8)		
Form II	supercell	C1–O1	1.3056(14)	C3–N1–C7	117.65(10)
		C1–O2	1.2181(14)		
		C2–O3	1.2463(14)	C9–N3–C13	122.12(10)
		C2–O4	1.2506(14)		
	small cell	C1–O1	1.2761(13)	C2–N1–C6	119.99(8)
		C1–O2	1.2331(11)		

It has been discussed previously that the protonation states of OA and IN influence the carboxylic acid C–O bond lengths and the pyridine CNC angles. It is now of interest to see how these parameters (in Table 3-13) compare after refinement in the supercell and the small cell where the HBs and hence the protonation states are ordered and disordered respectively. In the supercell, the C–O bond lengths of the COOD group refine to 1.306(1)

and 1.218(1) Å, and those of the COO^- group to 1.251(1) and 1.246(1) Å. They agree perfectly with the expected values for neutral and deprotonated carboxylic acids. In the small cell on the other hand, the C–O bond lengths refine to intermediate values of 1.276(1) and 1.233(1) Å, confirming the previous observation from the analysis of the ADPs that the disorder of the HB is also manifest in the heavy atom parameters of OA. The pyridine CNC bond angles show a similar behaviour. While in the supercell the CNC bond angles refine to expected values of 117.7(1) and 122.1(1)° for neutral and protonated IN respectively, an intermediate value of 120.0(1)° is found for refinement in the small cell. Thus, the disorder is also reflected here even though the ADPs of the heavy atoms constituting the IN molecules do not appear unusual.

In the end, the occurrence of the superstructure with the possibility of refinement with artificial disorder provides great insight into the current system, IN_2–OA. It points out characteristic features which help interpreting the results for such ambiguously hydrogen bonded acid – pyridine base complexes. The importance of a careful examination is highlighted for the localisation of H/D atoms in such disordered and ordered SSHBs.

3.2.2. Ab Initio Studies

The determination of the energies involved in the formation of the polymorphic forms in IN_2–OA has been extended to the deuterated forms, IN_2–d-OA. For this purpose ab-initio studies have been carried out in the periodic environment in an analogous way to the non deuterated forms. The ground state energies have been determined by means of geometry optimisations with the PW and AO approaches using the CASTEP and CRYSTAL03 codes. The isotopic substitution in this case has no effect on the ground state energy calculations because the electronic configuration is the same for H and D, and the atomic masses are ignored, in contrast to molecular dynamics studies. For this reason, the calculated total energies are directly comparable. The starting geometries for the optimisation runs have been taken from the X-ray diffraction experiments, in the case of Form II from the refinement in the supercell. For both forms the crystallographic symmetry has been employed. For further computational details see 3.1.4 *Ab Initio Studies* on *Geometry Optimisations*.

The computed parameters for the HBs between OA and IN are shown in Table 3-14. First of all, the experimental HB configurations are reproduced by the AO and also the PW calculations. In this respect, the PW calculations in this case work better than for the non deuterated system where the optimisation runs relaxed into incorrect HB configurations. In the absence of accurate neutron H parameters, the computed HB geometries can only be compared with the experimental by means of the O···N heteroatom distances. For Form I, the overall intermolecular HB lengths are well reproduced by the CASTEP calculations. During the optimisation run with CRYSTAL however, the OA unit rotates slightly in the IN–OA–IN plane with the consequence that the previously nearly symmetrically bifurcated HB (O···N = 2.708, 2.773 Å) becomes more asymmetric (O···N = 2.590, 2.902 Å) and adopts a geometry similar to that of Form II. For Form II on the other hand, it is the optimisation with CASTEP where the OA unit experiences a small rotation, resulting in a shortened O1···N1 distance of 2.529 Å compared to the experimental 2.623 Å. In this case, the CRYSTAL geometry agrees very well with the experimental. Each computational approach fails to accurately reproduce one form of IN_2–d-OA, with calculated HB lengths

deviating by more than 0.1 Å. Consequently, the experimental structures cannot be regarded as reproduced with a satisfactory reliability by either the PW or the AO approach.

Table 3-14: Computed HB parameters for IN_2–d-OA; the experimental D···A distances are given in parentheses for easier comparison.

		HB	D–H / Å	H···A / Å	D···A / Å
CASTEP	Form I	N1–D1···O1	1.065	1.849	2.698 (2.708(1))
		N1–D1···O2	1.065	1.960	2.821 (2.773(1))
	Form II	O1–D1···N1	1.088	1.506	2.529 (2.623(1))
		N3–D8···O4	1.085	1.600	2.590 (2.614(1))
		N3–D8···O2	1.085	2.359	3.128 (3.031(1))
CRYSTAL	Form I	N1–D1···O1	1.067	1.641	2.590 (2.708(1))
		N1–D1···O2	1.067	2.151	2.902 (2.773(1))
	Form II	O1–D1···N1	1.030	1.641	2.589 (2.623(1))
		N3–D8···O4	1.068	1.617	2.591 (2.614(1))
		N3–D8···O2	1.068	2.322	3.075 (3.031(1))

The energies involved in the formation of the hydrogenous IN_2–OA complexes in Table 3-9 have been completed in Table 3-15 by those of the two deuterated polymorphs. Both PW and AO calculations see the deuterated forms as energetically unfavoured by ~5 kJ/mol when compared to the non deuterated; and for the two deuterated forms, both assign the lower energy to IN_2–d-OA Form II. This appears to contradict the experimental observations that the crystals of Form II not only precipitate in much lower quantities, but also redissolve after time to leave only crystals of Form I. As said previously, the ground state energies of deuterated and non deuterated materials are directly comparable. The reason the deuterated complexes adopt structures that are likely to be less favoured should therefore be attributed to kinetic effects which indeed play an important role during crystallisation processes. The solubilities of the co-crystals also have to be considered an important factor in this respect.

Table 3-15: Energy scale for polymorphism in IN_2–OA and IN_2–d-OA.

			optimal OA geometry	ΔE / kJ·mol^{-1}
CASTEP	IN_2–OA	Form I	OOC–COO	+1.7
		Form II	OOC–COO	0
	IN_2–d-OA	Form I	OOC–COO	+5.6
		Form II	DOOC–COO	+5.0
CRYSTAL	IN_2–OA	Form I	HOOC–COOH	0
		Form II	HOOC–COO	+2.4
	IN_2–d-OA	Form I	OOC–COO	+5.9
		Form II	DOOC–COO	+4.4

3.3. CONCLUSION

SSHBs in the Hydrogenous Forms

It has been shown by X-ray charge density studies and subsequent topological analyses of the resulting total electron densities that the SSHBs in the hydrogenous complexes of IN_2–OA have a covalent nature. This manifests in a considerable charge transfer into the hydrogen bonding H···N interaction which partially overlaps with the pyridine N lone pair. As a consequence, the occurrence of strong hydrogen bonding in IN_2–OA leads to a considerable charge concentration in the region of the N lone pair – to the extent that it becomes easily observed by standard X-ray diffraction experiments, and might be confused with a disordered H atom. This finding is likely to be transferable to other acid – pyridine base systems which exhibit such strong hydrogen bonding.

It is of interest to ask whether similar observations have been indicated in previous studies. A number of X-ray structures show strong hydrogen bonding between carboxylic acids and pyridine bases, describing disordered or centred H positions; examples can be found in references [89, 90, 91, 92, 93, 94]. These may well exhibit a similar electron density distribution in the SSHB. However, difference Fourier maps from which the H atoms are determined are unfortunately rarely published these days. Closest to our observations is the case of the SSHBs which are formed between 3,5-dimethylpyridine and 3,5-dinitrobenzoic acid (O···N = 2.529 and 2.531 Å for the hydrogenous and deuterated complex respectively).[89] The SSHBs show the high electron delocalisation observed for the current IN_2–OA complexes; and also the heavy atom parameters for the carboxylic acid and pyridine groups are remarkably similar to those in IN_2–OA. The H/D atoms in the SSHBs have been refined with a 50 : 50 disorder, which in view of our findings might be reconsidered. Also, the complex of IN with squaric acid (reference [94]) is of interest as it is almost isostructural to IN_2–OA Form I. The electron density in the SSHB (O···N = 2.532 Å) is highly delocalised but shows a clear density maximum near the pyridyl N, suggesting that H transfer has taken place or, more likely, that, in view of the findings discussed in this and the following chapter, the H atom is located in the centre of the SSHB. The material is documented formally as a H transfer complex with a doubly deprotonated squaric acid, but the ambiguity arising from the electron delocalisation has been noted by the authors.

Hydron Transfer and Polymorphism

In the hydrogenous forms, IN_2–OA, formally no H transfer is observed. However, the covalent O–H bonds are considerably elongated, as known to be common for SSHBs, to an extent that in Form II the H atom occupies a near central position in the SSHB. It can thus be argued that in Form II partial H transfer has taken place, in agreement with the chemical pK_a values. The charge density analyses reveal that the regions of charge concentration in the formally covalent O–H bonds is disrupted, indicating that the H atoms are not bonded very strongly to O, and that both IN_2–OA polymorphs can be seen as incipient H transfer complexes. The deuterated forms, IN_2–d-OA, remarkably do clearly show D transfer. In case of Form I, both D atoms of d-OA are transferred to IN resulting in an ionic complex; and in case of Form II, only one D is transferred. In the end, all levels of hydron transfer are observed (0 %, 50 % and 100 %) in this system, notably of what are chemically identical materials prior to the co-crystal formation.

The occurrence of isotopomeric polymorphism in itself is rarely observed in molecular materials,[32] and the formation of more than one isotopomeric polymorph in this case is unprecedented to the knowledge of the author. This system should be of great interest to the crystal structure prediction community as an investigation of kinetic effects is mandatory to explain the present H/D isotope effects. Furthermore, the fact that all four forms in this system show a variable degree of hydron transfer, accompanied in the various cases by a significant change in the nature of the HB, renders this material an ideal model system to study the influence of crystal field effects upon the hydron transfer behaviour.

Ab Initio Studies

The PW calculations (static and dynamic) on the hydrogenous forms do not reproduce the experimental findings with respect to the SSHB configuration. The AO calculations do a much better job, although when lowering the crystallographic symmetry, for both forms energy minima are found for the experimentally unobserved mixed protonated N···HOOC–COO^{-}···HN^{+} complexes. Using the crystallographic symmetry on the other hand, yields improved ground state geometries but with computed O–H distances underestimated by ~0.1 Å. Determining the adiabatic HB potentials and including the zero point energy contribution results eventually in O–H expectation values which in fact agree very well with the experimental findings. On the deuterated forms, the PW and AO calculations perform equally well – or equally poorly – depending on the point of view. The correct HB configurations are reproduced but the computed HB parameters deviate in places too much from the experiment.

The energy ranking for polymorphism determined with the AO calculations has been established to be IN_2–OA Form I < IN_2–OA Form II (+2.4 kJ/mol) < IN_2–d-OA Form II (+4.4 kJ/mol) < IN_2–d-OA Form I (+5.9 kJ/mol).

As a final comment, the present solid state codes cannot be regarded as capable of reliably reproducing the intermolecular interactions present in these molecular complexes. They show trends and help interpreting experimental results, but great care has to be taken and constant feedback from the experiment is required – in the absence of this, it is easily possible to be pointed into the wrong direction by such ab-initio studies.

4. IMAGING THE ELECTRON DENSITY OF HYDROGEN IN STRONG HYDROGEN BONDS

This chapter addresses a few aspects regarding the localisation of H atoms from Fourier maps when they are involved in strong hydrogen bonding. The majority of structure determinations are carried out by standard X-ray diffraction experiments, where "standard" refers here to a spherical atom refinement on a limited experimental resolution dataset of typically $\sin\theta/\lambda = 0.6 - 0.8$ Å^{-1} ($2\theta = 50 - 70$º for $Mo_{K\alpha 1}$ radiation). The previous discussion in Chapter 3 showed that the H atom in the SSHB of the type O··H(acid)··N(pyridine) could not be localised unambiguously from such a standard X-ray structure analysis alone. However, the electron density maps could be rationalised in retrospect with the knowledge of neutron data. The purpose of this chapter is therefore to compare the electron density distribution in some SSHBs with neutron data, and use these electron densities as reference points for the interpretation of the strongly hydrogen bonded materials for which neither neutron nor high resolution X-ray data are available.

In a first step, the question will be answered as to which experimental resolution yields a deconvolution of the H atom electron density from that originating from charge transfer effects (i.e. bonding and lone pair densities). In other words, which experimental resolution is required to reliably determine approximate H positional parameters and hence the correct SSHB configuration. This is performed on the basis of the system IN_2–OA (Chapter 3) where the availability of high resolution X-ray and neutron datasets allows a systematic study.

In a second step, the reproducibility of centred SSHBs and temperature dependent H transfer from standard X-ray data will be investigated. For this purpose, X-ray datasets have been collected on two well documented materials which exhibit the strongest O··H(acid)··N(pyridine) HBs observed to date: the previously mentioned complex of pentachlorophenol with 4-methylpyridine and pyridine-3,5-dicarboxylic acid.[95, 96] Both materials show temperature dependent H transfer, and for both materials neutron data are available in the literature.[25, 28]

4.1. RESOLUTION DEPENDENCE OF ELECTRON DENSITY MAPS IN ISONICOTINAMIDE – OXALIC ACID

Figure 4-1 and Figure 4-2 show a series of difference Fourier maps for IN_2–OA Form I and Form II respectively, calculated for data at different experimental resolution. They have been obtained after spherical atom refinements on both the charge density and the standard X-ray datasets, after omitting H1 from the refinement model. The resolutions have been cut off at values typical of standard X-ray experiments, and for each such obtained dataset an individual SHELXL refinement has been performed prior to the calculation of the map. At the bottom in each figure, additional difference Fourier maps are shown for a refinement of the charge density dataset at a high resolution cut-off using the spherical atom and multipolar formalism.

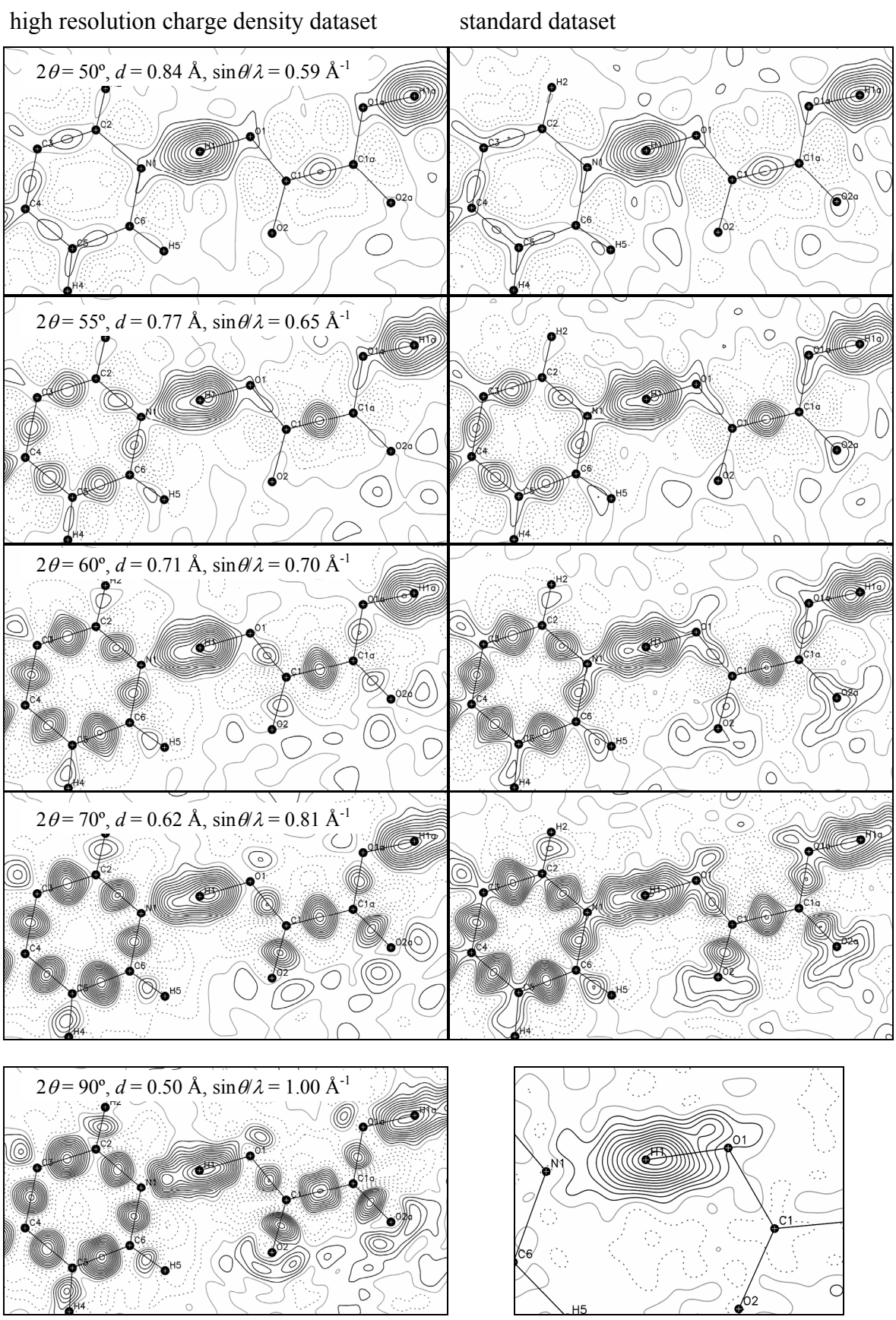

Figure 4-1: (Top) Difference Fourier maps of IN_2–OA Form I after spherical atom refinement (omitting H1) of the charge density (left) and the standard X-ray dataset (right) showing the resolution dependence of these maps (λ = 0.71073 Å). (Bottom) maps after spherical atom (left) and multipole refinement (right) of the charge density dataset at a high resolution cut-off; maps for $F_{obs} > 4\sigma(F_{obs})$, contours at 0.05 eÅ^{-3}.

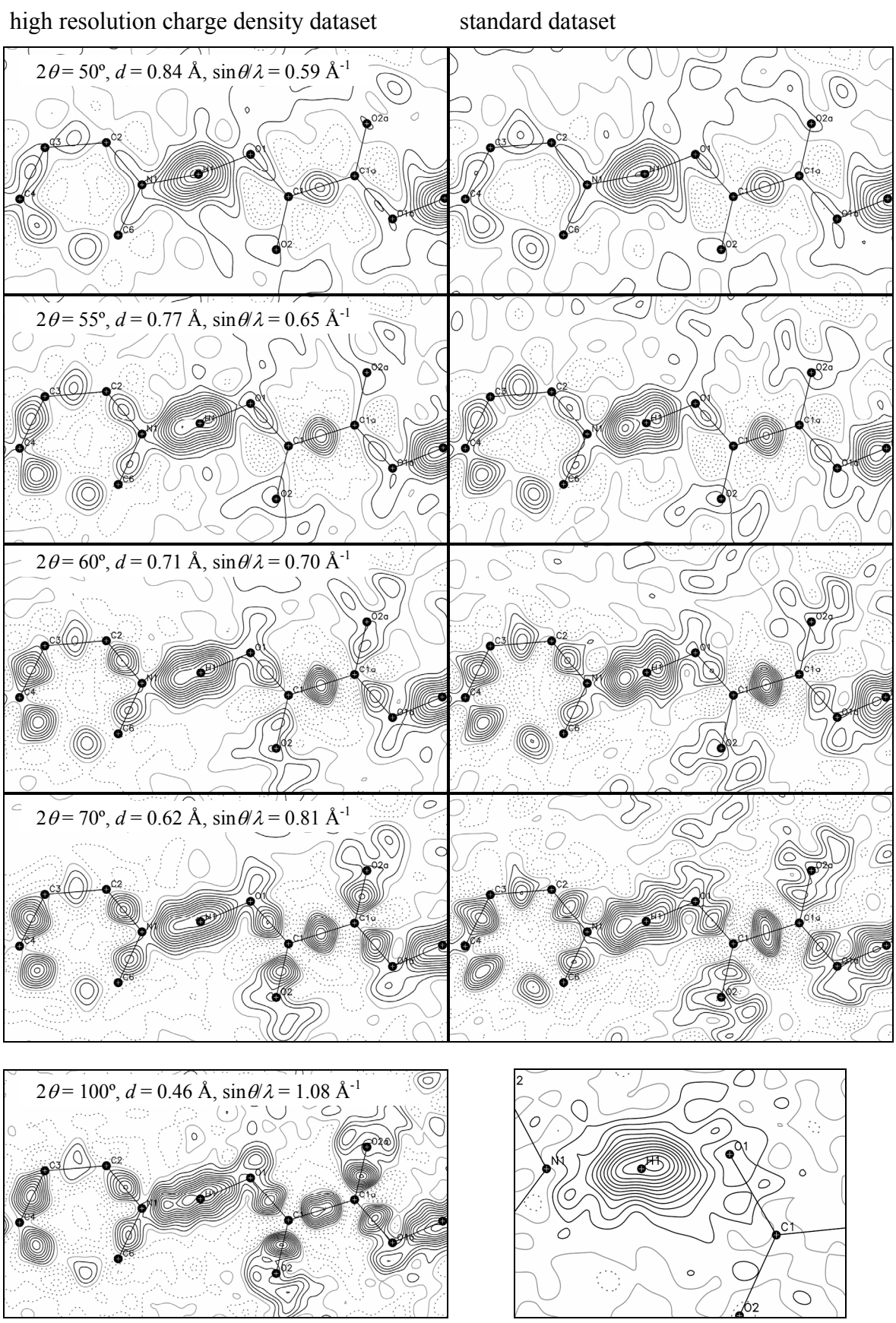

Figure 4-2: Difference Fourier maps of IN_2–OA Form II; for details see Figure 4-1.

The qualitative difference between the standard and the high resolution datasets is reflected in the experimental effort: the standard X-ray data were measured in a day yielding 10080 and 8196 reflections for Form I and Form II respectively – to a resolution of $\sin\theta/\lambda = 0.78$ Å^{-1}; the charge density data were measured in 5 and 7 days respectively, yielding 62005 and 64585 reflections to $\sin\theta/\lambda = 1.21$ Å^{-1}; for details see Table B-1 in Appendix B. In the following evaluation of the observed difference densities it is important to bear in mind that in fact only difference densities are observed which do not necessarily coincide with the true total electron densities. The height of a difference density peak observed at a point strongly depends on the amount of spherical density subtracted from the total density at that point.[42] This manifests in generally smaller deformation density levels observed in short bonds when determined from low resolution datasets – see the evolution of the bonding densities in the oxalic acid C–O and C=O bonds in Figure 4-1 and Figure 4-2, for example.

A comparison of the standard with the high resolution datasets shows that they yield very similar difference Fourier densities when moderate resolution cut-offs are applied.[a] The high resolution data give only a slightly clearer picture around the carboxylic O atoms. The extent to which charge transfer effects are observed in the difference Fourier map depends on the resolution of the dataset: at $\sin\theta/\lambda \sim 0.6$ Å^{-1}, hardly any charge transfer effects are observed aside from small charge accumulations on the C–C bonds. At $\sin\theta/\lambda \sim 0.65$ Å^{-1}, bonding densities become distinctly observable on the C–C and C–N bonds, for which the absolute electron densities increase with increasing resolution until the average peak maxima reach values of ~0.55 and ~0.45 eÅ^{-3} respectively, at a resolution of $\sin\theta/\lambda \sim 0.8$ Å^{-1}. For the C–O bonds, density accumulations start to appear at $\sin\theta/\lambda \sim 0.7$ Å^{-1}, and for the O lone pairs at $\sin\theta/\lambda \sim 0.8$ Å^{-1}. The density peaks on the C1–O1 and C1=O2 bonds level off at 0.35 and 0.50 eÅ^{-3} at resolutions of $\sin\theta/\lambda \sim 1.0$ Å^{-1} and ~ 1.1 Å^{-1} respectively, available only for the charge density datasets. The lone pair densities keep increasing beyond the experimental resolution limit of $\sin\theta/\lambda \sim 1.2$ Å^{-1} where values of ~0.35 eÅ^{-3} are observed (Figure 3-16, bottom).

With respect to visualising the electron density in the SSHB, which includes the density for H1 as well as the additional contributions caused by charge transfer effects, all difference Fourier maps show the high delocalisation spanning the whole region between O1 and N1. The electron density maxima for H1 are remarkably constant, they range from 0.60 – 0.65 eÅ^{-3} and 0.55 – 0.60 eÅ^{-3} for Form I and Form II respectively, across all resolutions for all datasets. They thus have the same magnitude as the strongest bonding density peaks. The resolution dependence manifests in the appearance of features in the density distribution between O1 and N1. For the lowest resolution datasets in this series ($\sin\theta/\lambda = 0.6$ Å^{-1}), no statement can be made regarding the position of the H atoms, other than that it is somewhere near the centre for the HBs. With increasing resolution (from $\sin\theta/\lambda = 0.65 – 0.8$ Å^{-1}), the electron density successively splits into two sites: the O site, which, as known from the previous studies, points to the actual H1 position; and the N site, which is assumed to be the overlap of N lone pair with H1···N1 bonding density. In Form II this separation is more ambiguous since the H atom occupies a near central position in the SSHB. In any case, the difference density maps in this resolution range ($\sin\theta/\lambda = 0.65 – 0.8$ Å^{-1}) are susceptible to misinterpretation towards H disorder, in particular the maps obtained for Form II from the standard X-ray data.

[a] The current standard datasets are admittedly of good quality.

The N lone pair densities become finally separable between $\sin\theta/\lambda \sim 1.0 - 1.1$ eÅ^{-1} in Form I and Form II respectively, at resolutions which are undoubtedly beyond those of standard diffraction experiments. The H densities as modelled at these resolutions by the multipolar formalism are included in Figure 4-1 and Figure 4-2, bottom right, for comparison. Notably, for Form II the high resolution X-ray data show, in addition to the distinct N lone pair, two distinct density maxima for the H atom. This effect is evident when refined with the spherical atom model (Figure 4-2, bottom left) – refining the same dataset with the aspherical atom model, reassuringly, yields a difference density exhibiting a single density maximum only (Figure 4-2, bottom right). This is rationalised, of course, by the fact that the aspherical atom model accounts for charge transfer effects and that consequently the O··H and H··N bonding densities do not – unlike within the spherical atom model –contribute to the difference density.

The reason that a higher experimental resolution is required to distinctively observe the N lone pair in Form II can be rationalised by the fact that it is in closer proximity to the H atom. The N lone pair density peaks can also at these resolutions be quantified to ~0.50 eÅ^{-3}, a value which does not increase with higher resolution.[a] For comparison, the O lone pair densities have maximum values of ~0.25 eÅ^{-3} at $\sin\theta/\lambda = 1.0 - 1.1$ Å^{-1}. It is important to note that the N lone pair peak height is not much smaller than that for the actual H atom, which suggests that pyridyl N lone pairs can already be observed at much lower resolutions and strongly contribute to the difference densities there. A separation of a formal O "lone pair" density in the centred SSHB in Form II on the other hand, is not observed for the current high resolution datasets when refined with the spherical atom model.

4.2. CENTRED HYDROGEN BOND IN PENTACHLOROPHENOL – 4-METHYLPYRIDINE

Pentachlorophenol and 4-methylpyridine form a hydrogen bonded dimer (PCP–4-methylpyridine) which is linked via a strong O··H(acid)··N(pyridine) HB. The HB is the strongest[b] of this type observed to date and shows furthermore a temperature induced H migration as referred to earlier in Chapter 1.3 *Hydrogen Transfer in the Solid State*. At around 90 K the H atom occupies a central position in the SSHB, equidistant to the O and N atoms (for the temperature dependent evolution of the H position see Figure 1-3.[25] For the purpose of visualising the electron density in this SSHB, a standard X-ray dataset has been collected at 100 K to a resolution of $\sin\theta/\lambda = 0.70$ Å^{-1}, and was refined to $R_1 = 3.11$ % for all data.

Figure 4-3 shows the difference Fourier density map in the plane of the SSHB O1··H1··N1 obtained after refinement without the hydrogen bonding atom H1 for which the isotropic displacement and the positional parameters have been refined. For comparison, the neutron and X-ray determined HB parameters are included at the bottom of the map (both 100 K data). The O1··H1 and H1··N1 distances refine to 1.34(3) and 1.18(3) Å against the X-ray data, and to 1.258(8) and 1.265(8) Å against the neutron data

[a] The relevant high resolution maps are not included in Figure 4-1 but a similar value can be estimated from the dynamic model deformation density maps after multipole refinement of the complete datasets (Figure 3-17 and Figure 3-26 bottom for Form I and Form II, respectively).

[b] Based on the O···N distance criterion.

respectively. The X-ray refined H position deviates thus by ~0.08 Å from the average nuclear position, shifted in the direction of the pyridine N atom, which appears to be significant. On an absolute scale, however, (both positions are marked in Figure 4-3) the difference diminishes, in particular in view of the magnitude of the neutron determined ADPs.

With respect to the electron density distribution in this centred SSHB, Figure 4-3 reveals the expected electron delocalisation but also shows that the density maximum is clearly located near the pyridine N and not in the centre of the HB. This is caused by the additional contribution of the N lone pair to the total difference density as has been observed previously in the IN_2–OA complexes. As a result the X-ray H parameters are biased in that they refine to a position too close to the N atom in relation to the true position of the H nucleus as found in the current structure refinement. For this reason, also the approach of fixing the thermal parameter to that of a bonded heavy atom (O1 or N1) in order to locate the region of maximum electron density (as applied for the IN_2–OA complexes) is counter-productive in this case and will result in an even stronger shift towards the N atom as one would expect by visual inspection of the difference density map. To conclude, X-ray difference densities for H atoms in strong, centred O··H··N(pyridine) HBs exhibit a strong electron density delocalisation with a density maximum always at the site of the pyridine base.

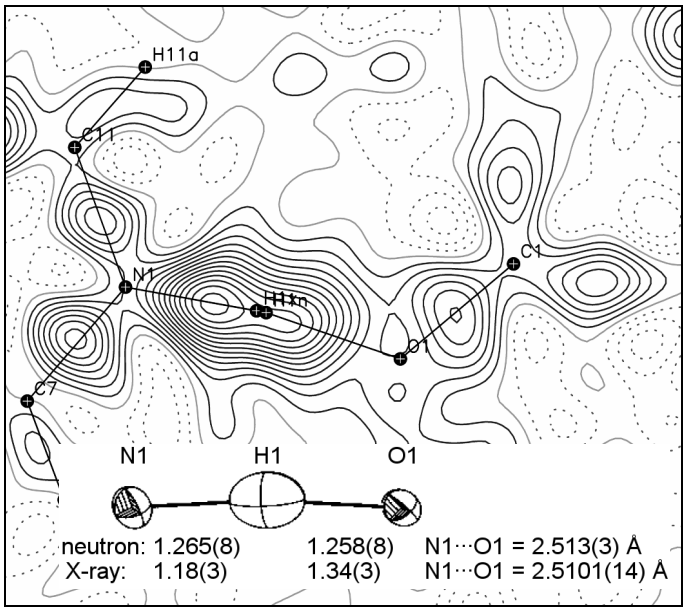

Figure 4-3: Comparison of the X-ray difference Fourier map and the neutron ADPs (50 % probability level) in the plane of the SSHB in PCP–4-methylpyridine at 100 K. Fourier maps as in Figure 4-1 for $\sin\theta/\lambda <$ 0.70 $Å^{-1}$, the two H positions in the centre of the HB point to the X-ray (H1x, the left one) and neutron refined (H1n, right) positions. Neutron data from reference [25].

4.3. HYDROGEN TRANSFER IN PYRIDINE-3,5-DICARBOXYLIC ACID

Pyridine-3,5-dicarboxylic acid (in short dinicotinic acid) forms in the solid state a 2-dimensional hydrogen bonded network. Each molecule of dinicotinic acid is linked to four neighbouring molecules of dinicotinic acid via moderate O–H(acid)···$^{-}$OOC HBs and strong centred SSHBs of the type O··H(acid)··N(pyridine); for a full structural description

see the original reference [96]. A later variable temperature neutron study revealed that the H is transferred from a position closer to the carboxylic acid O to one closer to the pyridine N; the SSHB changes its configuration from (formally) O–H···N to O···H–N, see reference [28]. X-ray datasets have been collected at 100 K and at room temperature in order to visualise the previously observed H transfer reaction by means of electron difference Fourier maps. The resolutions of the datasets were cut off at $\sin\theta/\lambda = 0.70$ Å^{-1}; the 100 K structure was refined to $R_1 = 3.86$ % for the observed ($F_{obs} > 4\sigma(F_{obs})$) and to $R_1 = 4.70$ % for all data; and the RT structure to $R_1 = 4.17$ % and 5.98 % respectively.

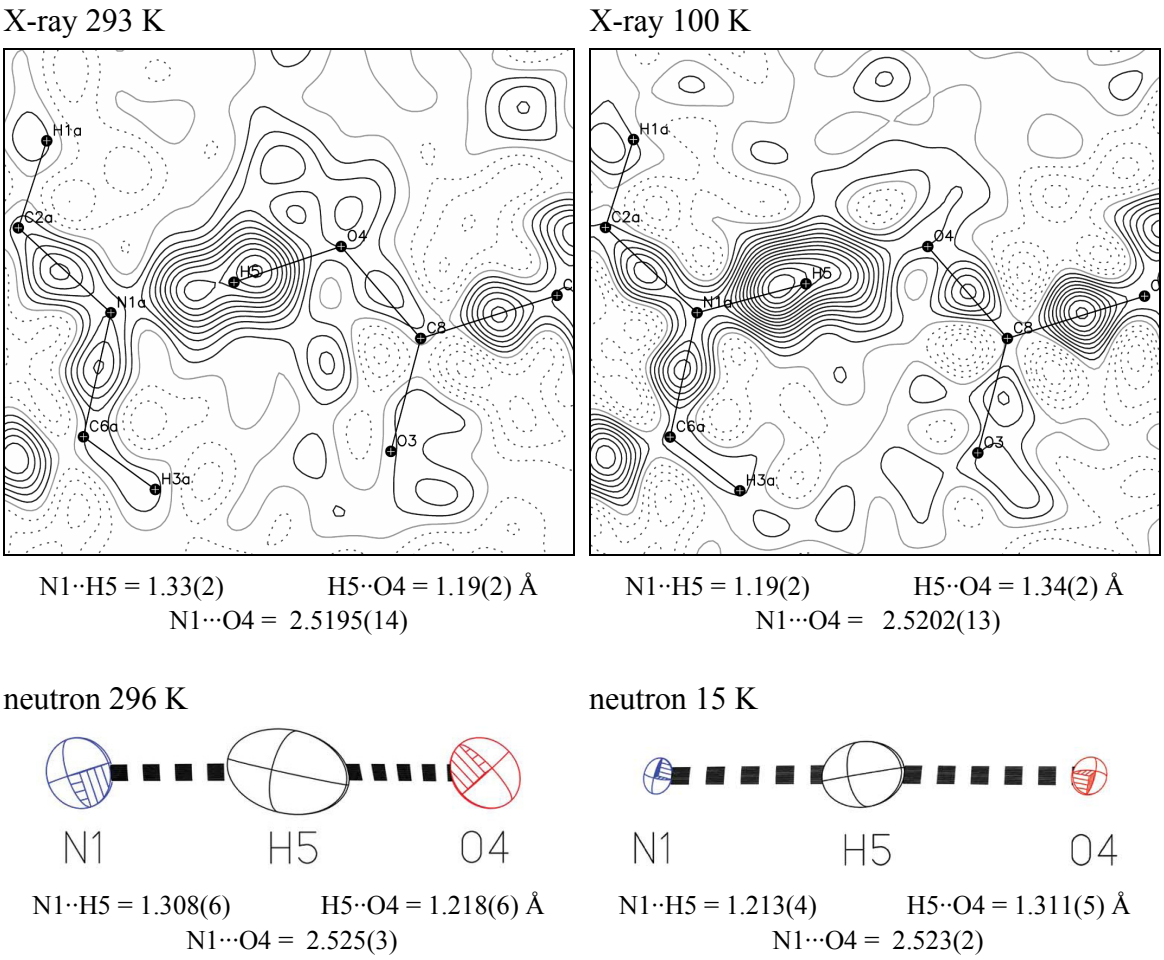

Figure 4-4: Comparison of X-ray and neutron refinement of dinicotinic acid at RT (left) and low T (right). (Top) X-ray difference Fourier maps and X-ray refined HB parameters, Fourier maps as in Figure 4-1 for $\sin\theta/\lambda < 0.70$ Å^{-1}. (Bottom) neutron ADPs (50 % probability) and neutron refined HB parameters. Neutron data and figures from reference [28].

Figure 4-4 compares the electron density distribution in the O4··H5··N1 SSHBs with the ADPs determined by neutron diffraction, as well as the X-ray and neutron refined HB parameters. As in the previous example the parameters for H5 have been fully refined from the X-ray data without imposing any restraints. A quick comparison of the O4··H5 and H5··N1 distances shows that the time averaged positions of the H nuclei are well reproduced by the X-ray refinements and agree within the refined standard uncertainties with those determined from the neutron data – for both the RT and low T data. This implies that the subtle H migration effect, a ~0.1 Å shift towards the N base by going from RT to 15 K, has been reproduced by the variable temperature X-ray diffraction experiment. Although the low T data are not directly comparable – they have been determined at

100 K and 15 K in case of the X-ray and neutron experiment respectively – the quantitative observation of H transfer is quite remarkable in itself, in particular in view of the quality of the current datasets which cannot be regarded as exceptionally good. More importantly, however, is perhaps the fact that the electron density distribution in the SSHB experiences a considerable change by moving from the (formally) O–H···N configuration to the O···H–N. At RT (O–H···N), the density shows a split site, comparable to that obtained from the standard X-ray data on IN_2–OA Form II (Figure 4-2). At 100 K (O···H–N), the density shows a single site with the maximum density near the pyridine N. The two maps simply "look" qualitatively different. It appears that the change in the electronic structure in this SSHB is stronger than the shift of the H nucleus by a mere 0.1 Å would suggest (0.1 Å is about the distance between the two H positions marked in Figure 4-3). This effect has also been seen in X-ray and neutron maps of the short HBs in urea – phosphoric acid.[27]

4.4. CONCLUSION

It has been shown that charge transfer effects strongly contribute to the difference densities in SSHBs obtained from X-ray diffraction experiments. In particular the N lone pair densities in O··H··N(pyridine) SSHBs are observed to low experimental resolutions, and almost certainly in the resolution ranges typical of standard X-ray diffraction experiments. From this it follows that an unbiased localisation of H atoms which are involved in such strong HBs is generally not achieved in a reliable manner by refinement of the H positional parameters (there are exceptions, of course, as seen above). However, the examples discussed here have shown that the difference Fourier maps provide valuable information. Once the fact is acknowledged that the N lone pair density is always observed, a visual inspection of the density maps aids the localisation of H atoms in these SSHBs. It furthermore allows a differentiation of O–H···N from centred O··H··N and O···H–N HBs. Subtle H transfer reactions can thus be reproduced by standard X-ray diffraction even if the absolute differences in the positions of the H nuclei are small.

5. DESIGN OF STRONGLY HYDROGEN BONDED MATERIALS

5.1. PENTACHLOROPHENOL – DIMETHYLPYRIDINE COMPLEXES

The majority of the work presented in this chapter on the pentachlorophenol – lutidine complexes has formed the basis of a publication.[97] The co-crystallisation of pentachlorophenol (PCP) with the series of dimethylpyridines (lutidines) results in the formation of molecular complexes, many of which show strong hydrogen bonding in the solid state. Competition for the H atom in these short, strong hydrogen bonds (SSHBs) by the pK_a matched molecules leads to a variable degree of H transfer from PCP towards the lutidine, dependent on the ΔpK_a value in a particular complex. The influence of weak C–H···O interactions in the vicinity of the strong O··H··N HB on the H transfer is also discussed.

It has been said previously in 1.2 *Strong Hydrogen Bonds* that one important condition for the formation of intermolecular SSHBs is a similar proton affinity of the hydrogen bonded molecules, reflected for systems in solution by a sufficiently small ΔpK_a = pK_a(acceptor) – pK_a(donor). $\Delta pK_a^{50\%}$ values mark the point at which 50 % H transfer has taken place, and the H atom is equally shared between donor and acceptor. Albrecht and Zundel, for example, have determined a $\Delta pK_a^{50\%}$ value of ~1.6 for PCP – pyridine base adducts in CCl_4 (including some of the PCP – lutidine complexes discussed here).[98] In the solid state such pK_a dependences are no longer strictly valid, as the proton affinities are now also affected by the combination of intermolecular forces in the crystalline environment. This is particularly the case in the SSHBs, where HB configurations can be altered by small changes in crystal packing, a fact which becomes especially noticeable when chemically equivalent HBs adopt different HB configurations in the same or in polymorphic materials.[33] On the other hand it has been pointed out by Steiner[8] that HBs, when isolated from strong polar interactions, can exhibit a very similar behaviour to that in solution, i.e. the H transfer follows the trend of ΔpK_a values, see for example Malarski *et al* on PCP – amine adducts.[14]

The present work establishes such a correlation between solution ΔpK_a values and H transfer in the solid state on the basis of the hydrogen bonded PCP – lutidine (1 : 1) complexes (Scheme 5-1). Depending on the proton affinity of the relevant lutidine, the PCP hydroxyl H is transferred to the lutidine, or not, or some sort of intermediate form is generated. The varying pK_a values for the different lutidines in combination with the constant pK_a for PCP allow a systematic investigation in the resulting ΔpK_a range from 1.45 – 2.29. The complex of PCP–2,4-lutidine (ΔpK_a = 2.29) was already reported by Majerz *et al* to show a H transfer reaction.[99] The only HB which can and will form in this system is of the type O··H(pcp)··N(pyridine), and is anticipated to be of strong nature due to the similar proton affinities of the participating species. All other interactions will be weak because no further HB donors and acceptors are present (aside from C–H); the HB of interest is thus embedded in an apolar environment. This is true for the dimeric 1 : 1 complexes. Some PCP – lutidine complexes, however, prefer to crystallise in a 2 : 1 ratio and introduce thereby an additional H donor (and potential H acceptor). These structures are also presented for comparison and documentation of the effect of a polarity change in the vicinity of the strong HB.

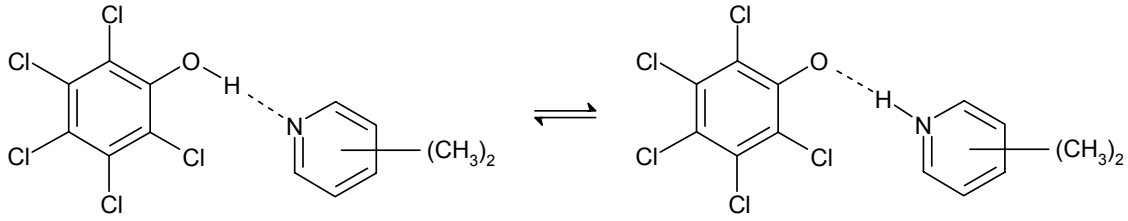

Scheme 5-1: H transfer scheme in the PCP – lutidine complexes.

5.1.1. Dimeric 1:1 Structures

Crystals of the dimeric 1 : 1 PCP – lutidine complexes were grown by the method of isothermal slow evaporation of the solvent. The complexes crystallise from various solvents; usually ethanol or chloroform was used, but solvents like carbon tetrachloride, acetone, methanol, or mixtures thereof also yield the same structures. No particular influence of the solvent on the experimental outcome has been observed other than the resulting crystal size and crystal quality which can also be attributed to the evaporation rates of the various solvents. The experimental details which yielded the single crystals for this work are given in Appendix A *Experimental*. All structures were determined by X-ray diffraction at 100 K for which the crystallographic details are summarised in Table B-4 in Appendix B. Ordered by increasing pK_a values with respect to the lutidines, they can be formulated as:

PCP–3,5-lutidine ≡ $C_6Cl_5OH \cdot C_7H_9N$ ($\Delta pK_a = 1.45$)

PCP–2,5-lutidine ≡ $[C_6Cl_5O]^- [HC_7H_9N]^+$ ($\Delta pK_a = 1.70$)

PCP–3,4-lutidine ≡ $C_6Cl_5OH \cdot C_7H_9N$ ($\Delta pK_a = 1.76$)

PCP–2,3-lutidine ≡ $C_6Cl_5OH \cdot C_7H_9N$ ($\Delta pK_a = 1.87$)

PCP–2,6-lutidine Form I ≡ $C_6Cl_5OH \cdot C_7H_9N$ ($\Delta pK_a = 1.90$)

PCP–2,6-lutidine Form II ≡ $[C_6Cl_5O]^- [HC_7H_9N]^+ \cdot C_6Cl_5OH \cdot C_7H_9N$ ($\Delta pK_a = 1.90$)

PCP–2,4-lutidine ≡ $[C_6Cl_5O]^- [HC_7H_9N]^+$ ($\Delta pK_a = 2.29$) [99]

With the exception of PCP–2,5-lutidine, all structures have been published in reference [97]. The ellipsoid plots of the asymmetric units, containing usually one PCP – lutidine dimer, are shown in Figure 5-1. As predicted, the crystal structures are comprised of dimers which are linked by the O··H(pcp)··N(pyridine) HBs. Aside from PCP–3,4-lutidine all these HBs can be regarded as strong as the O···N heteroatom distances, D, in these complexes cluster around 2.6 Å; D(O···N) will reach a minimum value of about 2.50 Å for a H atom positioned in the centre of the HB – in the centred HB in the pentachlorophenol – 4-methylpyridine complex, for example, D = 2.506(2) Å at 20 K.[25] Table 5-1 lists the HB parameters for the strong O··H··N HBs, and also details of the weak C–H···O interactions in the environment of the SSHBs because they might influence the SSHB configurations as discussed later. Table 5-2 finally rationalises the ΔpK_a – H transfer relationship and includes geometrical parameters that are, aside from the HB parameters, indicative of the protonation states of PCP and lutidines. The pK_a data for the lutidines are taken from Perrin[100] and that for PCP from Cessna and Grover.[101]

Before giving a detailed description of the structural work, a few general remarks are made regarding the H treatment. The H atoms have been refined in a slightly different approach to that of the IN_2–OA complexes in Chapter 3 since they cannot be determined with the same accuracy for two main reasons. First, the lack of an extended hydrogen bonded structure leaves the PCP – lutidine dimers in a flexible environment which results in an enhanced rigid motion of the molecules, naturally also affecting the H atoms. Second, the presence of strong scatterers, chlorine in this case, generally reduces the sensitivity to the low electron density regions. Unless stated otherwise, the H atoms were all located from the difference Fourier densities but for the above reasons subsequently fixed using the riding model; the methyl H atoms were additionally allowed to rotate around the C–C bond. For the H atoms involved in the hydrogen bonding between PCP and lutidine, on the other hand, all positional and displacement parameters were fully refined.

PCP–3,5-lutidine

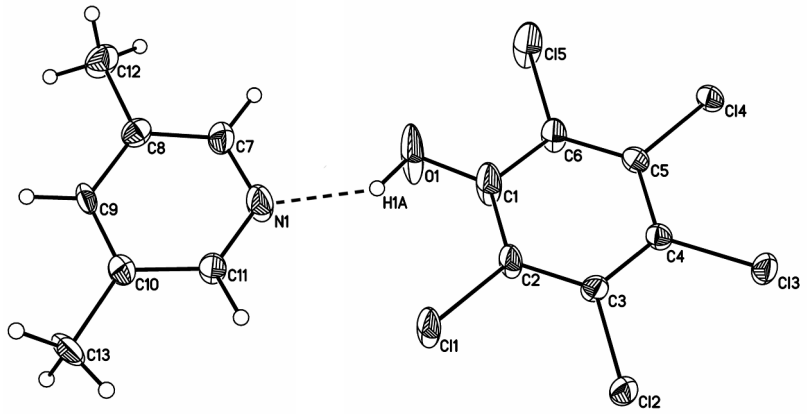

PCP–2,5-lutidine

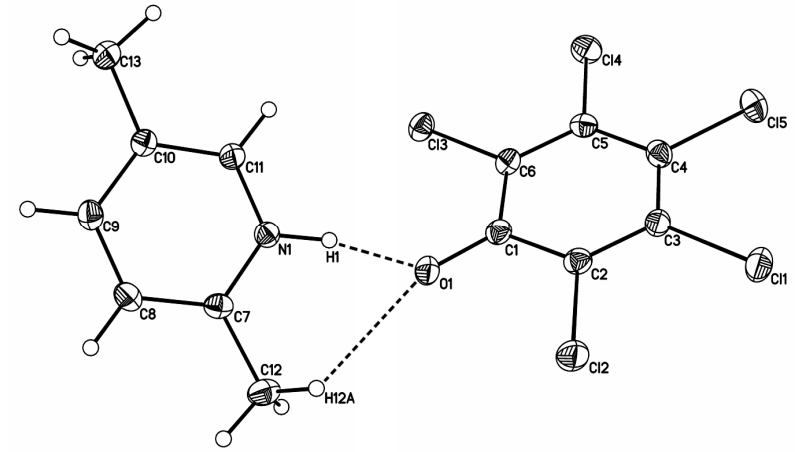

PCP–3,4-lutidine

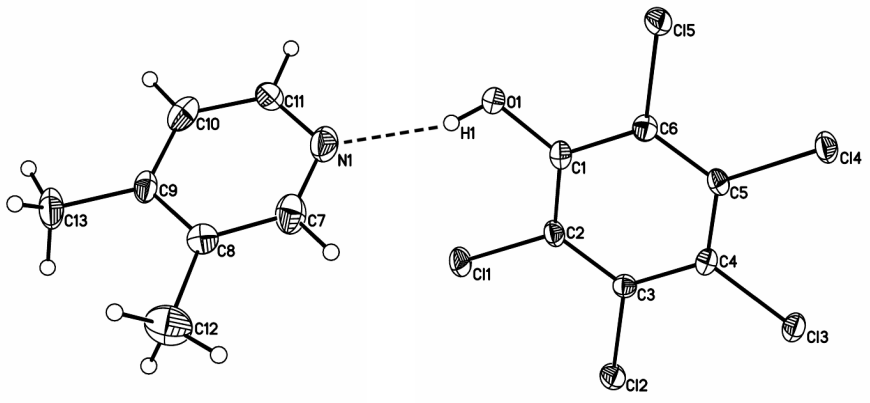

PCP–2,3-lutidine

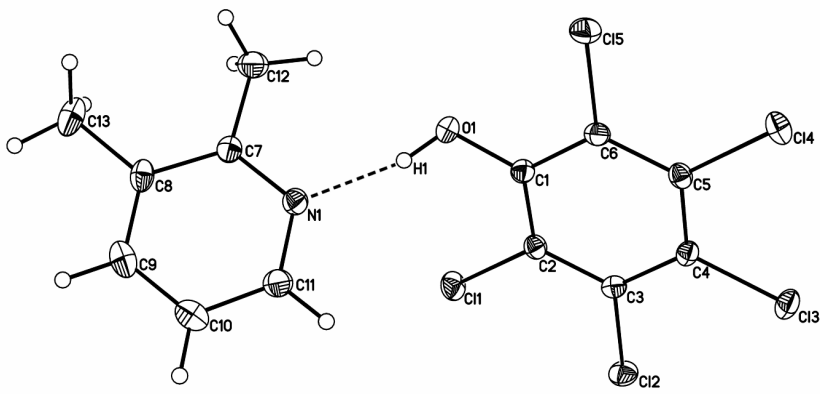

PCP–2,6-lutidine

Form I

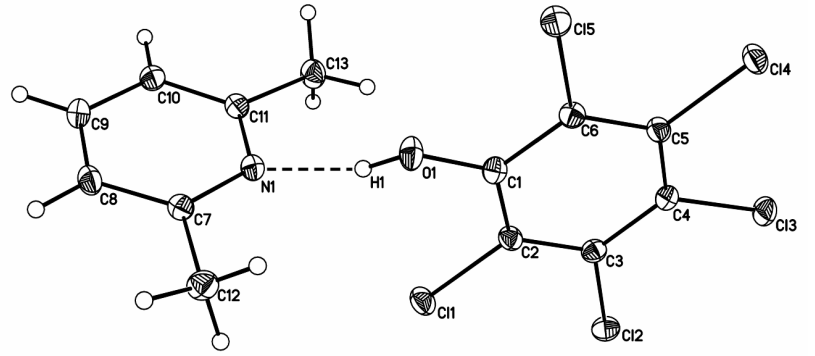

Form II

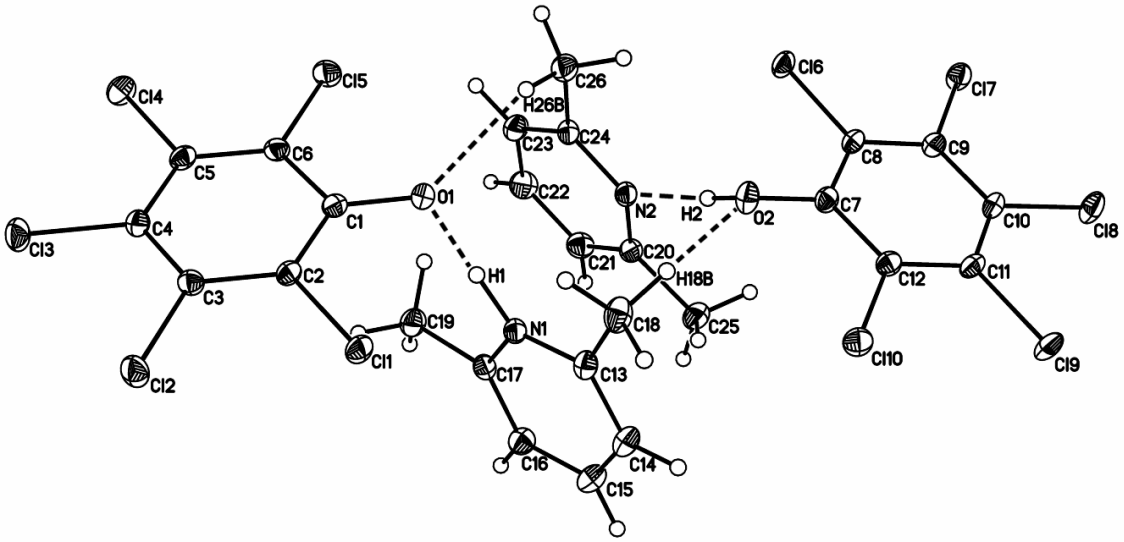

PCP–2,4-lutidine

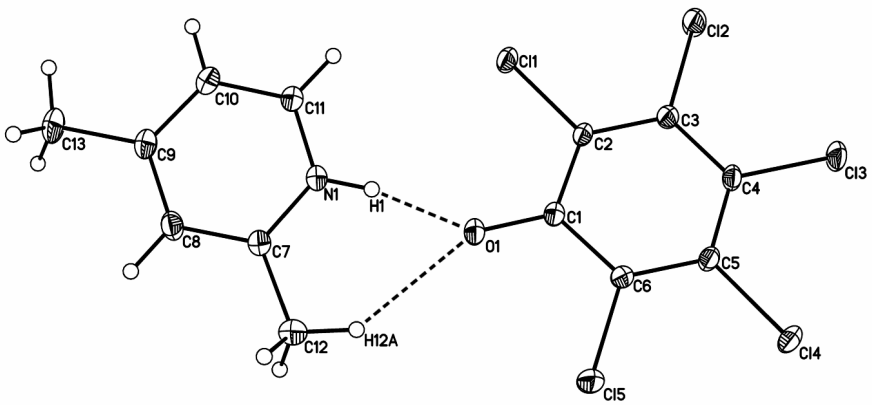

Figure 5-1: Ellipsoid plots of the dimeric (1 : 1) PCP – lutidine structures, ellipsoids at 50 % probability level, H atom representation at fixed sizes, HBs as dashed lines.

PCP – 3,5-Lutidine

Obtaining the crystal structure PCP–3,5-lutidine ($\Delta pK_a = 1.45$) presented something of a challenge. PCP–3,5-lutidine crystallises in small *very* thin platelets, which tend not to form good single crystals. Compared to the other dimeric PCP – lutidine complexes discussed in this chapter, the plate shaped crystals of PCP–3,5-lutidine precipitate very rapidly (but in pure form) and show by far the lowest solubility in the variety of solvents used. Attempts to obtain a reasonable X-ray structure either by trying to find a twin matrix or measuring the thinnest of the thin plates have been unsuccessful so far. The structure as published in reference [97] was processed in a small triclinic unit cell (a = 6.908, b = 8.663, c = 12.910 Å, α = 77.43, β = 82.55, γ = 88.70º, V = 748 Å^3, space group P$\bar{1}$) which in view of our later findings (see discussion below) merely describes the average structure. However, the X-ray structure has been solved and the heavy atom parameters refined; all H atoms were fixed using the riding model and were included for decorative, rather than crystallographic purposes. The structure refines to R_1 = 11.85 % and 14.45 % for the observed ($F_{obs} > 4\sigma(F_{obs})$) and all data respectively, at a resolution of $\sin\theta/\lambda$ = 0.64 Å^{-1}. The poor quality of the current structure determination is reflected by the atomic displacement parameters for this complex (see Figure 5-1 and Figure 5-3 right). The atoms in the vicinity of the HB show a large displacement perpendicular to the aromatic ring planes, of which the PCP unit is affected most and in particular the phenol O atom.

The O1···N1 distance in the SSHB refines to D = 2.586(11) Å, but in view of the pronounced ADPs of both the O1 and N1 atoms, this value has to be treated with a significantly larger error than the mathematically determined standard uncertainty. Unlike in the other complexes discussed, no statement regarding the H transfer can be made by direct observation of electron density for the H atom because of the poor quality of the data and the refinement model used. However, the structure has been included here because the protonation state in the O··H··N HB can be indirectly deduced from geometrical parameters which are determined only by heavy atom positions (Table 5-2). The relation of the protonation state of a pyridine group with its CNC bond angle has already been exploited in Chapter 3. The phenol parameters vary in similar fashion, but to a lesser extent – with increasing degree of protonation the CC(O)C bond angle increases from ~114 to 118º, and similar to carboxylic acids the C–O(H) distance varies from ~1.26 to 1.34 Å as documented by Wozniak *et al*.[102] The corresponding C1–O1 distance and the C2–C1–C6 bond angle in PCP of 1.33 Å and 117º respectively, and also the C7–N1–C11 bond angle of 119º in the lutidine indicate that PCP–3,5-lutidine exists in its neutral, molecular form. This becomes particularly noticeable in comparison with the corresponding parameters in Table 5-2 and Table 5-5 for the other PCP – lutidine complexes for which the protonation states are clearly observed by means of electron difference densities.

A reinvestigation of this system on an image plate diffractometer has revealed that this material shows some strong diffuse scattering which passed unnoticed previously. Also, the previous observed pairs of reflections, which gave rise to the suspicion that this material is intrinsically twinned, are always present. The pairs of reflections are consistently separated by a reciprocal space distance corresponding to a unit cell repeat of ~26–28 Å, but indexing results either in the above unit cell or in larger cells which are not easy to reproduce and that yield a large number of absent or very weak reflections. These are indeed signs for non-merohedral twinning but no reasonable set of domains could yet be indexed. Promising but tentative results of a recent data collection with a subsequent

data treatment in a large unit cell setting are presented below. They reveal the origin of the poor ADPs of the original structure determination, and help in understanding the presence of diffuse scattering.

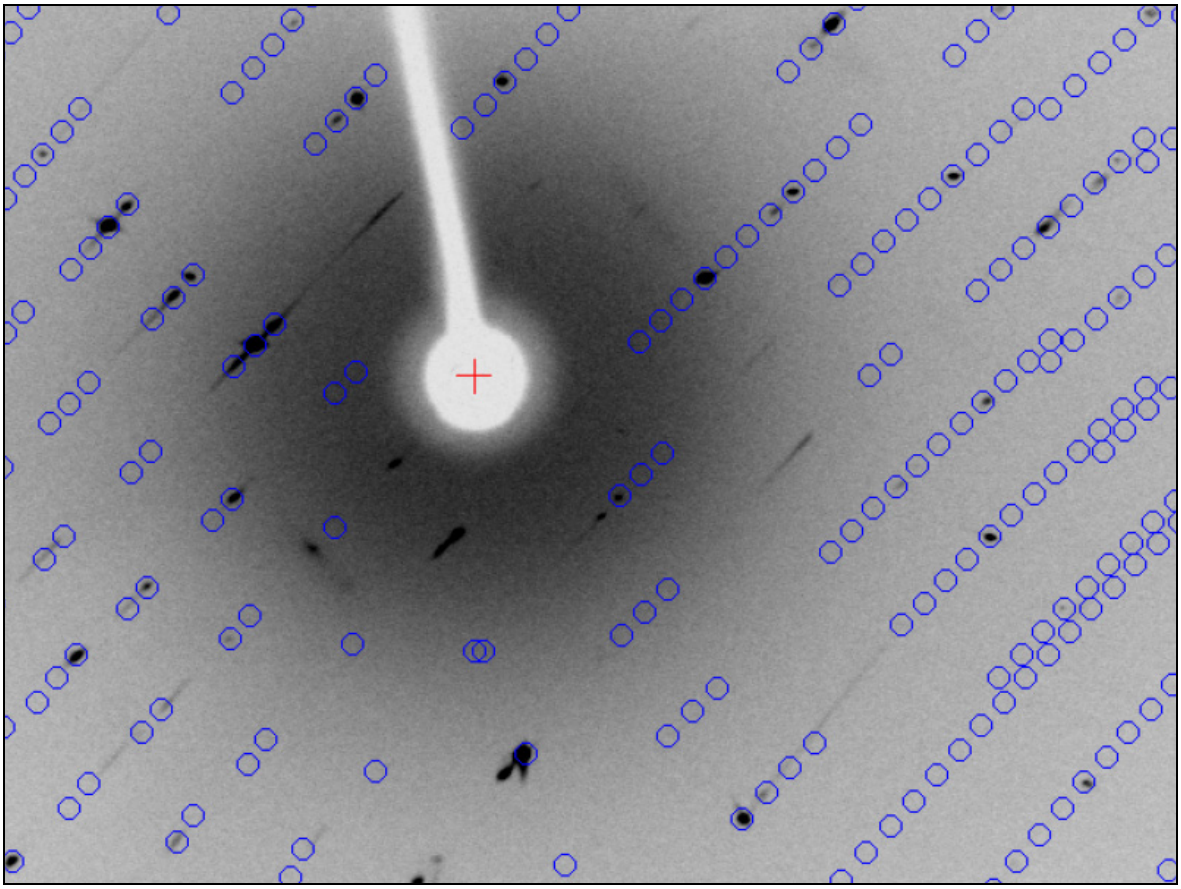

Figure 5-2: Diffraction pattern of PCP–3,5-lutidine on an image plate detector shows diffuse scattering and the absence of many reflections (predictions from the larger unit cell as blue circles).

The dataset obtained from the image plate system was collected on a small platelet with the approximate crystal dimensions 0.20 × 0.10 × 0.02 mm^3 for which the exposure time was set to 25 minutes per 2.5º sweep in omega. Figure 5-2, showing an exemplary image obtained during this data collection, indicates the streaks of diffuse scattering and the large number of absent or weak reflections for the unit cell setting given below, which was used to process the data. The data have been integrated in a triclinic cell (space group $P\bar{1}$) with the lattice parameters a = 8.688, b = 12.943, c = 26.789 Å, α = 99.38, β = 97.13, γ = 102.56º, V = 2861 $Å^3$. To avoid confusion, this unit cell is referred to as "large" and the previously discussed original as "small". Both have in common two similar unit cell vectors: a and b in the large cell correspond to b and c in the small cell respectively (see Appendix B, Table B-4). However, it is important to note that the large cell does not correspond to a supercell setting of the small, as for example observed for IN_2–d-OA Form II (3.2 *Deuterated Polymorphs*), and the ratio of the unit cell volumes is a non integer 3.83 : 1. It is also important to note that there is no confirmation as yet that either of the two settings is correct. The structure as presented here, was refined in the space group $P\bar{1}$ to R_1 = 10.54 % and 19.43 % for the observed ($F_{obs} > 4\sigma(F_{obs})$) and all data respectively. The resolution cut-off was set to $\sin\theta/\lambda$ = 0.70 $Å^{-1}$, at which ~50 % of the reflections are unobserved.

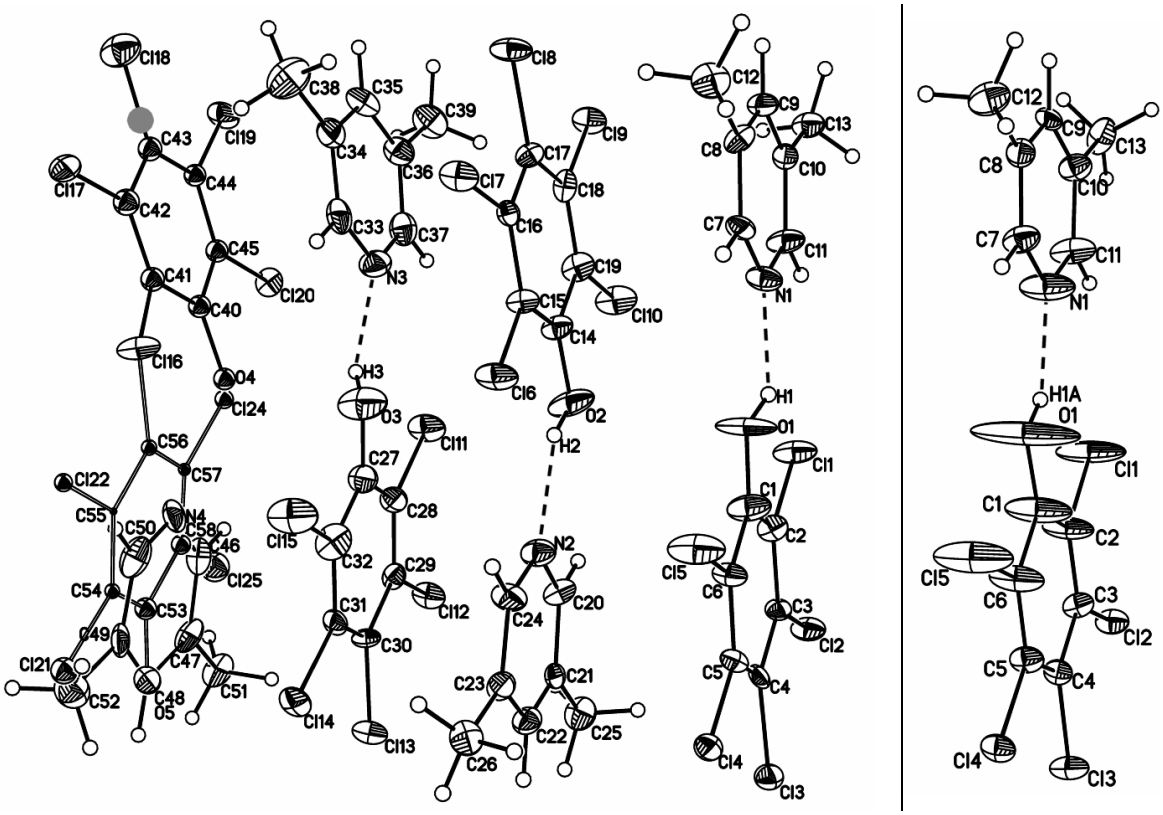

Figure 5-3: Comparison of the asymmetric units of PCP–3,5-lutidine in the large (left) and the original small cell (right), grey circle on the C43–Cl18 bond marks the inversion centre resulting in disorder of the PCP unit, ellipsoids at 50 % probability level, H atom representation at fixed sizes, HBs as dashed lines.

The structures as obtained from the refinements in the two unit cell settings can be compared by means of Figure 5-3 and Figure 5-4, which show the ellipsoid plots of the asymmetric units and the resulting arrangement of the PCP–3,5-lutidine dimers in the crystal respectively. First however, a description of a few details concerning the refinement in the large unit cell is helpful for a better understanding of the structure. While the three dimers on the right side in Figure 5-3, left, are ordered and calculated with 100 % occupancy, the "unit" on the very left is strongly disordered and is hence termed "disordered unit" from heron. In this unit, the PCP molecule which is comprised of the carbon atoms C40 – C45 is disordered over two sites, by symmetry (the corresponding inversion centre is marked as a grey circle), and is consequently calculated with site occupancy factors of 50 %. The rest of the disordered unit is comprised of another molecule of PCP (C53 – C58) disordered with a lutidine (C46 – C52). Guided by rationalising the 3-dimensional packing (see below), these PCP and 3,5-lutidine units are refined with 25 % and 75 % occupancy respectively. The isotropic displacement parameters for the PCP unit refine to small values at this site occupancy level; but this way, the overall ratio of PCP to lutidine remains 1 : 1 in agreement with the elemental CHN analysis (see Appendix A *Experimental*). Summed up, the complete disordered unit yields another 0.75 formula unit of PCP–3,5-lutidine, resulting in 3.75 dimers per asymmetric unit or 7.5 per unit cell volume. It is worth noting that the 3.83 : 1 ratio for large cell volume to small cell volume fits well with the corresponding 7.5 : 2 for formula units per unit cell.

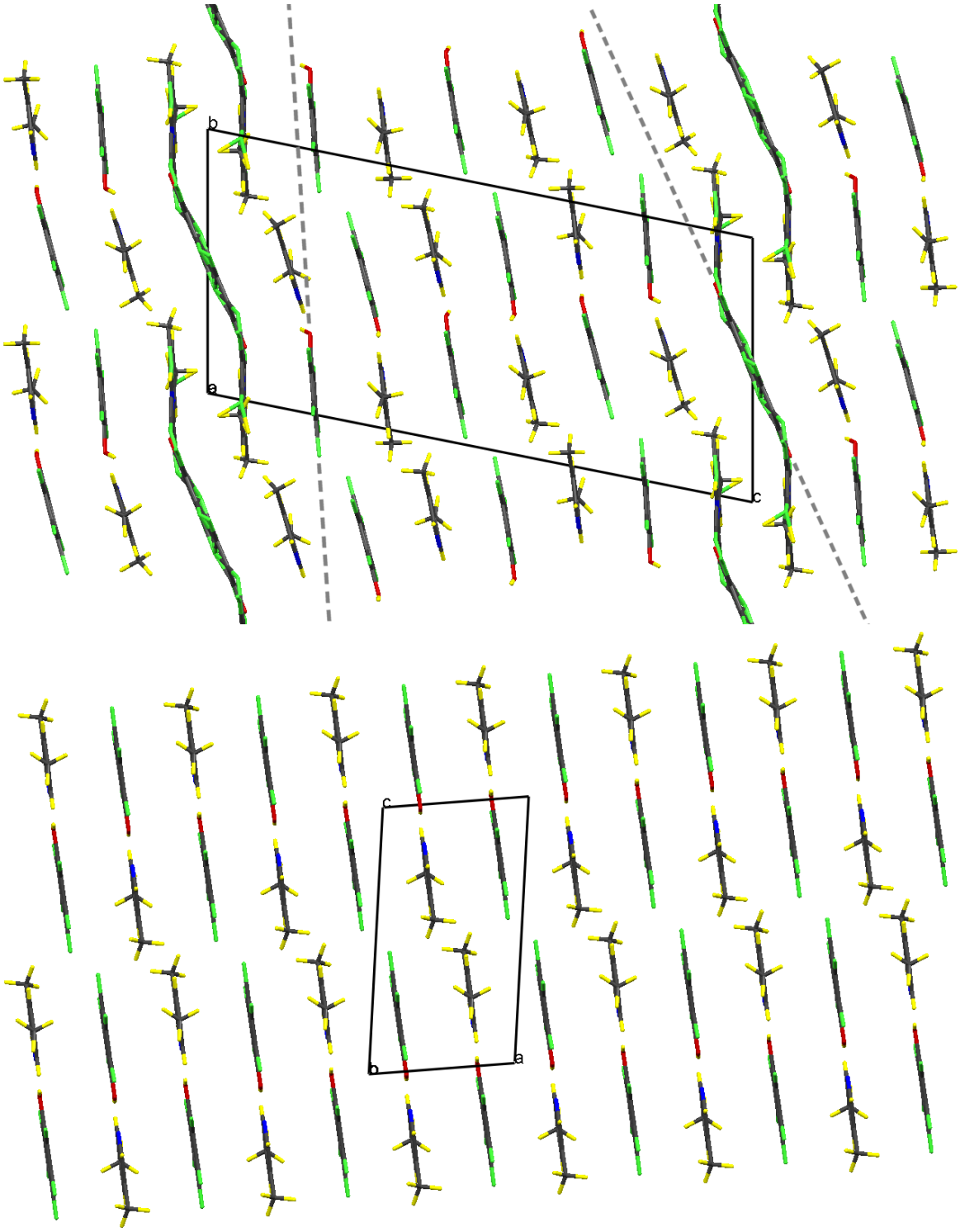

Figure 5-4: Slices through the 3-dimensional crystal structure showing the packing of PCP and 3,5-lutidine molecules; (top) large cell model, view along the *a* axis (8.688 Å); (bottom) original small cell model, view along the *b* axis (8.663 Å).

From Figure 5-3 it is evident that the strongly anisotropic displacement parameters observed in the small cell refinement model, adopt much more reasonable dimensions in the large cell model. This leaves us confident that the employed refinement model in the current cell setting is appropriate, particularly in view of the poor quality of the dataset and the high level of disorder. Furthermore, and rather surprisingly, the electron densities for

the H atoms (including the H atoms involved in the SSHBs!) of the non disordered PCP–3,5-lutidine dimers can be directly located from the difference Fourier synthesis – they have been fixed subsequently using the riding model in accordance with the procedure for the other PCP – lutidine complexes, including the phenol H atoms. The H atoms in the SSHBs are all located at the O sides, and confirm thereby directly the previous indirect determination of the SSHB configuration. No H transfer has occurred in this material, and the PCP and 3,5-lutidine molecules in the 3 independent ordered dimers are neutral. The HB parameters and the heavy atom parameters indicating the protonation states of PCP and lutidines are included in Table 5-1 and Table 5-2.[a]

Figure 5-4 shows slices through the 3-dimensional structures as modelled in the large (top) and the small (bottom) unit cell for which all represented PCP and lutidine molecules are situated in a plane. The packing scheme for the large cell refinement reveals the inadequacy of the original refinement model and contains valuable information regarding a rationalisation of the observed diffraction pattern.

First, the origin of the high anisotropy of the displacement parameters in the original determination is illustrated: the PCP–3,5-lutidine dimers do not stack in a parallel fashion as simulated in the small cell refinement (Figure 5-4, bottom) but they are tilted against each other. The angle spanned between the mean planes of the PCP units (marked by the grey dashed lines in Figure 5-4 top) amounts to ~16.1º by going from the first ordered PCP unit to the first disordered; the corresponding tilt angle between the pyridine planes of the lutidine molecules amounts to ~14.6º.

Second, the origin of disorder becomes evident by closer inspection of the molecular arrangement at the crystallographic unit cell vertices: there is a frustration in the apparent stacking preference of alternating PCP and 3,5-lutidine molecules. Two fragments of the disordered unit (denoted as "?") sit between two molecules of PCP, schematically expressed as (PCP | ? | ? | PCP), one of which should be a lutidine resulting in either (PCP | Lut | ? | PCP) or (PCP | ? | Lut | PCP). The remaining disordered fragment can then either be a PCP or a lutidine molecule, leading to the applied site occupancy factors of 0.25 : 0.75 (PCP : lutidine) in the above structure refinement. The disorder of the lutidine causes further disorder of the PCP unit (C40 – C45, see Figure 5-3 left) to which the lutidine is hydrogen bonded; the PCP unit is situated on the centre of the crystallographic *b* axis (hence the centre of inversion) and is located between two lutidines. The structure can also be refined in the acentric space group P1 which removes the inversion centres. The disorder is in this case slightly reduced from (PCP | ? | ? | PCP) to (PCP | Lut | ? | PCP) with respect to the situation at the vertices of the unit cell. Removing the centre of inversion in the PCP unit (C40 – C45) however, results in the same level of disorder with the difference that the two disordered PCP fragments have to be calculated independently. In view of the small fraction of electron density that is affected by a reduction of the symmetry by going from $P\bar{1}$ to P1, and the fact that a refinement in P1 leads to considerable higher standard uncertainties and a large number of undefined ADPs, the final refinement has been performed in the space group $P\bar{1}$.

Third, the inadequacy of modelling the X-ray structure in the small cell becomes most apparent when looking at the orientation of the dimers in the extended structure. Viewing

[a] The corresponding data for the SSHB in the disordered unit also indicate a neutral adduct, but have been excluded from the further discussion.

perpendicular to the molecular pyridine and phenol planes (roughly from left to right in Figure 5-4), the dimers in the small cell model are stacked in a parallel way throughout the whole structure. This implies that the SSHBs are situated on top of each other throughout the whole structure, and consequently that the hydrophobic regions of the molecules in *para* position to the SSHB are situated on top of each other. In the large cell model, on the other hand, the stacking of SSHBs alternates with that of the hydrophobic contacts with each translation along the unit cell vector *c*.

In the end it should be emphasised again that there is no confirmation that the large unit cell setting is correct, and that the applied disorder model, although appearing reasonable, may not be completely definitive. However, the current refinement model reveals many features of this material which passed unrecognised previously. The large number of absent and very weak reflections can be explained by the fact that a comparatively large fraction of the electron density, i.e. the 3 ordered dimers, can be modelled in a smaller unit cell. The high degree of disorder certainly contributes to the occurrence of diffuse scattering, but there are probably additional origins for the diffuse scattering that are still not revealed. PCP–3,5-lutidine may be an incommensurate solid and better be modelled by a modulated structure, or by a still larger unit cell setting. Future work has to be done in order to understand the "true" structure of this material. In any case, PCP–3,5-lutidine offers a great vehicle for the study of diffuse scattering as it is easily reproducible in large quantities with well defined crystal morphology.

PCP – 2,5-Lutidine

PCP and 2,5-lutidine co-crystallise preferentially in the trimeric 2 : 1 complex PCP_2–2,5-lutidine with a block shaped habitus (discussed in 5.1.3 *Trimeric 2:1 Structures*), and the needle shaped crystals of the dimeric complex only form with an excess of the lutidine (for experimental details see Appendix A *Experimental*). The X-ray structure of the dimeric PCP–2,5-lutidine (ΔpK_a = 1.70) was only obtained after the original paper was accepted for publication.[97] It crystallises in tiny needles for which previous attempts to determine the structure on a conventional CCD system failed even to produce the unit cell parameters. In the end, an X-ray dataset was measured on an image plate system from a specimen with the approximate crystal dimensions 0.15 × 0.02 × 0.02 mm^3. This was only possible exploiting the high dynamic range of the image plate detector – for the current experiment the exposure time per frame was set to 16 minutes per 2.5 degree sweep. A reasonably good quality dataset of PCP–2,5-lutidine, crystallising in the monoclinic space group $P2_1/c$, was obtained to a resolution of $\sin\theta/\lambda$ = 0.70 $Å^{-1}$. The X-ray structure was refined to R_1 = 3.23 % and 4.51 % for the observed ($F_{obs} > 4\sigma(F_{obs})$) and all data respectively.

The SSHB formed between PCP and 2,5-lutidine belongs to the strongest observed for the PCP – lutidine complexes, the heteroatom distance O1···N1 refines to D = 2.559(2) Å. The H atom has clearly been transferred in this complex from PCP to the lutidine as evident from the difference Fourier map in Figure 5-5. The H transfer surprisingly occurs against the trend of ΔpK_a values as observed for all other dimeric PCP – lutidine complexes presented in this chapter (see Table 5-2). It is difficult to rationalise why the current structure deviates from the ΔpK_a rule established in reference [97]. One can argue that the weak C12–H12A···O1 interaction with d(H···O) = 2.56 Å, which originates from the lutidine *ortho*–methyl group (see Figure 5-1), stabilises the pentachlorophenolate ion,

thereby triggering the H transfer. However, such C–H···O HBs are also present in some of the other dimeric structures (discussed below) which do not show H transfer even though they have higher ΔpK_a values.

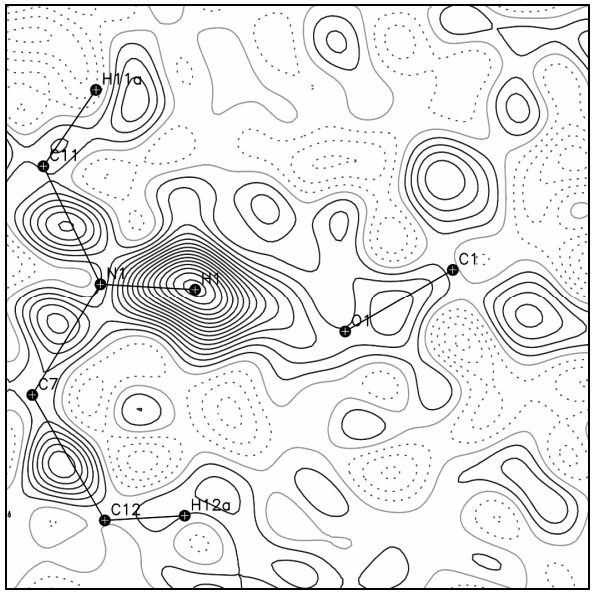

Figure 5-5: Difference Fourier map in the C1–O1–N1 plane of PCP–2,5-lutidine, obtained after omitting H1 from the refinement, H1 points to the previously refined position, map for $F_{obs} > 4\sigma(F_{obs})$, $\sin\theta/\lambda < 0.70$ Å^{-1}; positive contours – solid black, zero levels – solid grey, negative – dotted, contours at 0.05 eÅ^{-3}.

PCP – 3,4-Lutidine

PCP and 3,4-lutidine also prefer to co-crystallise in a trimeric 2 : 1 complex (plate shaped crystals). The same approach as for obtaining crystals of PCP–2,5-lutidine (i.e. excess of the lutidine) has been used to grow crystals of the dimeric structure, PCP–3,4-lutidine (ΔpK_a = 1.76). It crystallises with plate like morphology in the triclinic space group $P\bar{1}$. All crystals examined so far show non-merohedral twinning: a 180º rotation about the reciprocal 0 0 1 axis. However, data collection and appropriate data processing yielded a reasonable dataset for this complex. The data published in reference [97] have been reprocessed using an improved version of TWINABS[103] which resulted in better statistics for the dataset. The resolution has also been cut off at a higher value of $\sin\theta/\lambda$ = 0.70 Å^{-1} compared to the previous cut-off for the published dataset at 0.64 Å^{-1}. The crystal was indexed with CELL_NOW,[104] where 188 out of 237 reflections were assigned to domain 1, 148 to domain 2, and 18 were left unindexed. TWINABS was used for absorption correction, scaling, and the generation of a twin component intensity file in which only reflections involved in domain 1 were included. The structure was eventually refined to R_1 = 3.91 % and 5.64 % for the observed and all reflections respectively. The contribution of domain 2 to the total scattering refined to ~22 % – potential contributions from additional *minor* domains (18 unindexed reflections) have been ignored for the current structure determination.

The position of the H atom in the intermolecular HB was determined from a difference Fourier map and found to be located at the O side of the HB (Figure 5-6). Thus no H transfer has taken place upon the formation of the co-crystal. The O1–H1···N1 HB, with a heteroatom distance of D = 2.682(3) Å, is the weakest in the series of 1 : 1 adducts studied

here, and cannot be regarded as a SSHB. This is also reflected in the pyridyl and PCP heavy atom geometries, which are representative of those for the neutral species, whereas those in the complexes in which there is stronger hydrogen bonding tend to show more intermediate values (see Table 5-2). As a side note, PCP and 3,4-lutidine show stronger hydrogen bonding in the preferentially crystallising 2 : 1 complex, PCP_2–3,4-lutidine, than in this complex. Aside from the HB formed between PCP and the lutidine, the structure exhibits an additional weak C–H···O HB between an aromatic pyridine H atom from a neighbouring dimer and the phenol O. This C11–H11A···O1 interaction with d(H···O) = 2.64 Å leads to the formation of a "tetrameric" unit, comprised of two weakly linked PCP–3,4-lutidine dimers (Figure 5-7). Similar tetramers are also observed for the PCP–2,6-lutidine complexes discussed later.

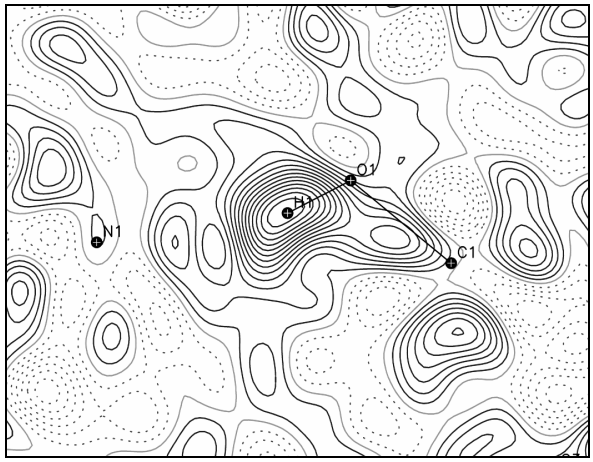

Figure 5-6: Difference Fourier map in the C1–O1–N1 plane of PCP–2,5-lutidine; $\sin\theta/\lambda < 0.70$ Å^{-1}, for details see Figure 5-5.

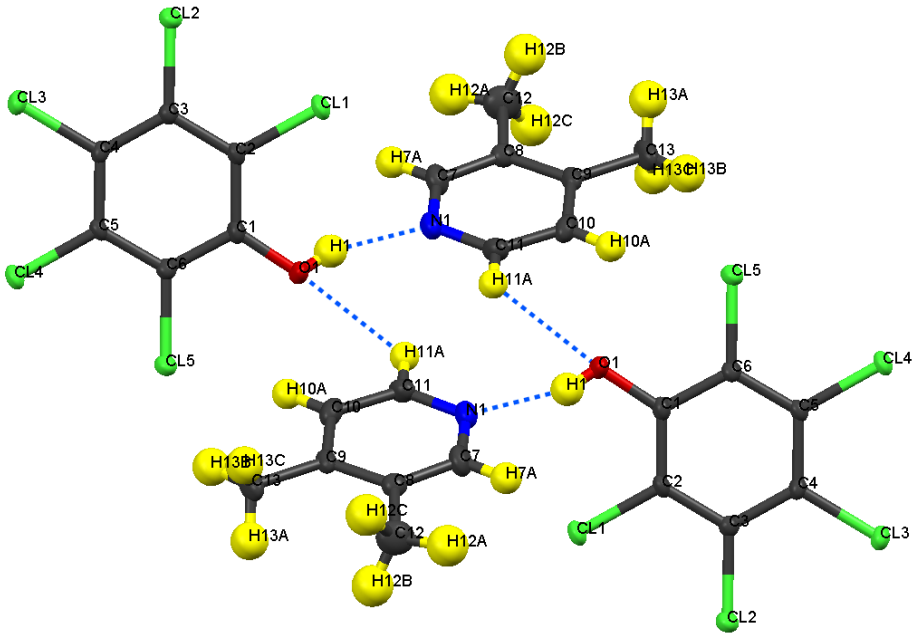

Figure 5-7: Tetrameric unit of PCP–3,4-lutidine, HBs are shown in blue dotted lines.

PCP – 2,3-Lutidine

In contrast to the systems discussed above, no difficulties were involved in the determination of the X-ray structure of PCP–2,3-lutidine ($\Delta pK_a = 1.87$). PCP–2,3-lutidine crystallises nicely with block shaped morphology in the space groups C2/c, for which a good quality dataset ($R_1 = 3.38$ % for all data to $\sin\theta/\lambda = 0.78$ Å^{-1}) was obtained.

No H transfer has occurred upon formation of the SSHB between PCP and the lutidine (see difference Fourier in Figure 5-8), hence this complex also exists in its molecular form. The O1···N1 distance in the SSHB refines to D = 2.605(1) Å. Besides the localisation of the H atom, the good quality dataset in this case also allows the observation of deformation density caused by molecular bonding effects. Electron density is clearly visible on the centres of the covalent bonds and for the first time in the lone pair region of the aromatic pyridine N atom. The previous findings on the electron density delocalisation in strongly hydrogen bonded acid – pyridine base systems in Chapter 3, leaves us confident that in fact N lone pair density (potentially with a contribution of H···N bonding density) is observed rather than density for a disordered second H site. The heavy atom parameters in Table 5-2 also confirm the absence of a H transfer reaction in this complex. The difference Fourier map in the plane perpendicular to the pyridine ring in Figure 5-8, right, has been included to show the orientation of the lone pair towards the H atom, and to document the covalent nature of these SSHBs (see the discussion below of the complexes of PCP with 2,6-lutidine). PCP–2,3-lutidine also exhibits a weak C–H···O interaction originating from the lutidine methyl groups in *ortho* position (see Figure 5-1). However, C12–H12A···O1 (d(H···O) = 2.52 Å) should not be regarded as a HB, because the HB path intersects the space occupied by the phenol H atom at an geometrically unfavourable H12A–O1–H1 angle of ~64°.

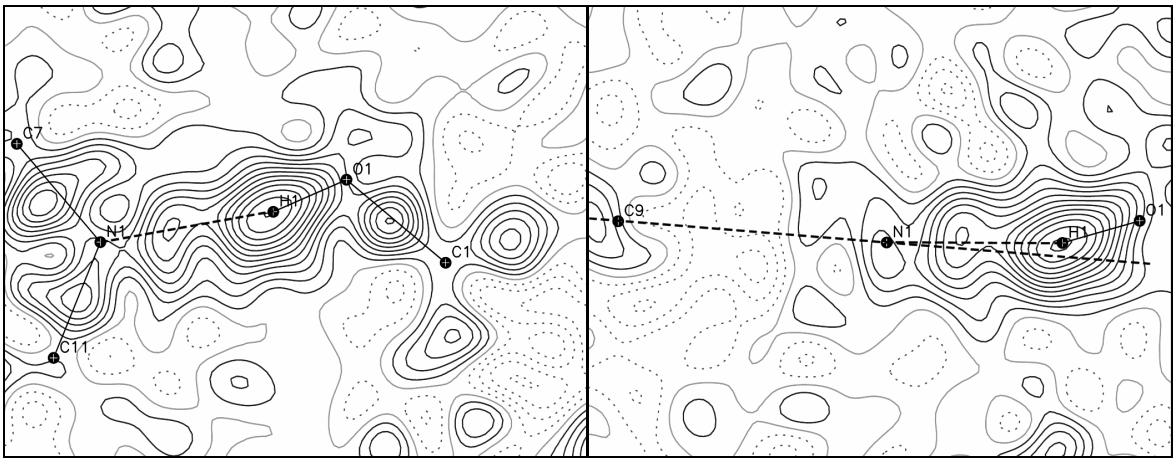

Figure 5-8: (Left) difference Fourier map in the C1–O1–N1 plane of PCP–2,3-lutidine; (right) in the C9–N1–O1 plane approximately perpendicular to the pyridine ring, dashed lines indicate the SSHBs and the pyridine planes; $\sin\theta/\lambda < 0.78$ Å^{-1}, for details see Figure 5-5.

PCP – 2,6-Lutidine

The system of PCP–2,6-lutidine ($\Delta pK_a = 1.90$) is of great interest as it shows a variable degree of H transfer and crystallises in two polymorphic forms: a triclinic Form I (space group $P\bar{1}$) and a monoclinic Form II ($P2_1/n$). Both polymorphs co-crystallise from the same solution, unfortunately with the same morphology which can be described as sticks

or long plates. The crystals are macroscopically undistinguishable other than that those of Form I often appear of better quality (visually and crystallographically). A tentative observation is that the crystals of Form II precipitate preferably under fast growing conditions, i.e. fast evaporation of the solvent, while Form I starts to appear later. There is evidence that a phase transition occurs from Form II to Form I under certain conditions (upon grinding, see powder patterns in Figure A-4 in Appendix A, or when the crystals are kept in solution for a long time). Furthermore, crystals of Form II deteriorate at RT when exposed to air, which might also imply a phase transition. Unlike all other 1 : 1 adducts reported here, PCP–2,6-lutidine Form II crystallises with two PCP – lutidine dimers in the asymmetric unit. Figure 5-9 compares their relative orientation with that of two dimers in Form I, one of which is generated by the inversion centre. The two dimers constitute tetrameric units, weakly linked in each polymorph by two C–H···O HBs which are formed between the phenol O atoms and the methyl H of a neighbouring lutidine.

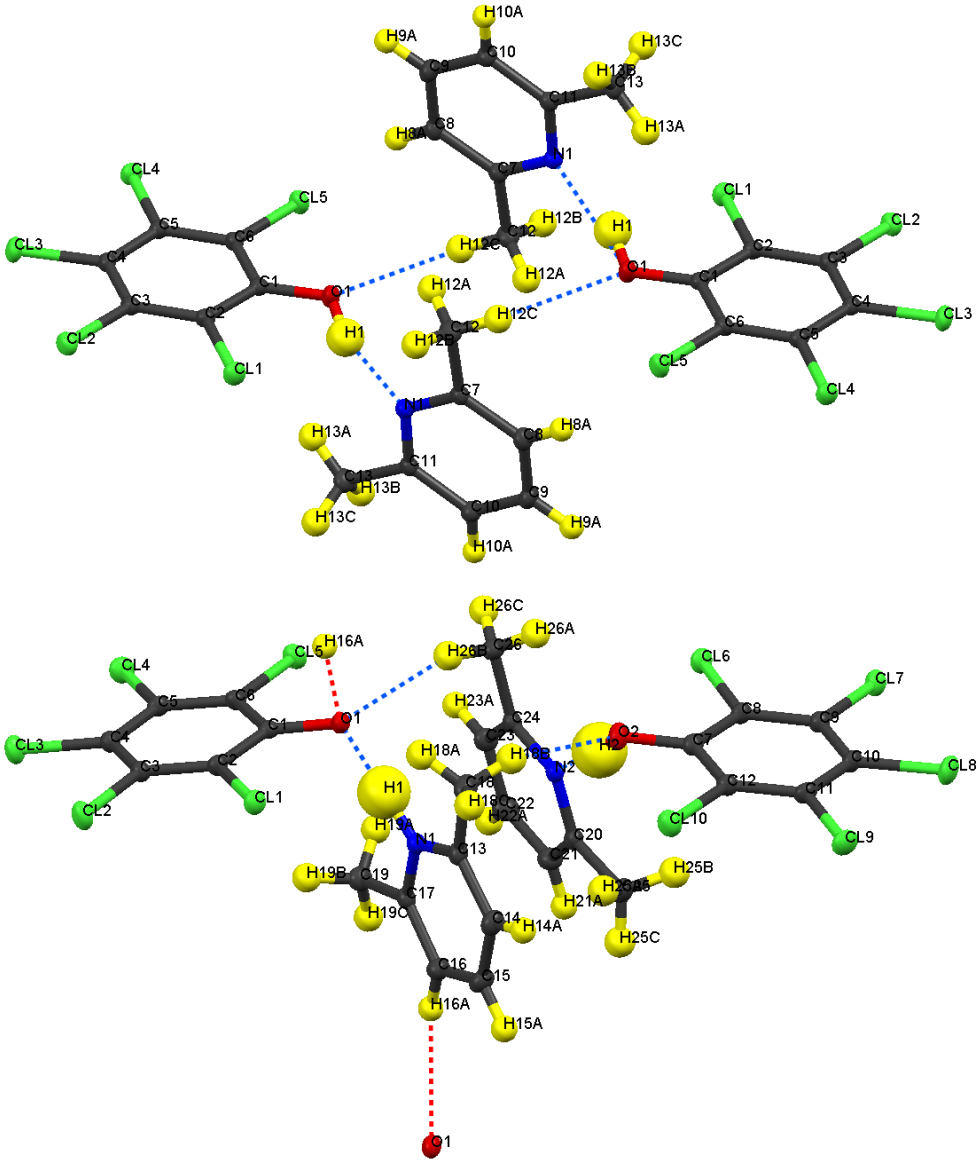

Figure 5-9: Tetrameric units of PCP–2,6-lutidine Form I (top) and Form II (bottom), for Form I the second dimer has been generated by symmetry ($\bar{1}$), HBs are shown in blue dotted lines and the CH···O HBs linking the "tetramers" of Form II are shown in red.

For both polymorphs good quality datasets were measured, and the X-ray structures were refined to R_1 = 3.62 % and 4.35 % respectively, for all data to a resolution of $\sin\theta/\lambda$ = 0.78 Å^{-1}. In Form I there is still no evidence for H transfer, neither from the difference Fourier maps in Figure 5-10, nor from the heavy atom parameters. The difference Fouriers show the electron densities in the plane of the HB and perpendicular to the pyridine plane, and similar to the situation in PCP–2,3-lutidine, lone pair density is visible for N1. However, in this case it is considerably shifted out of the pyridyl plane and oriented towards the H1–O1 group, roughly on the center of the H1···N1 vector. This suggests a polarisation of the lone pair towards the electropositive H atom, or an observation of H1···N1 bonding density in superposition with that of the lone pair, or a combination of both. This observation is thus possibly reflective of some covalent character in the SSHB. In any case, the out of plane orientation indicates strong hydrogen bonding in this O1–H1···N1 HB with D = 2.588(1) Å. These considerations are of course also valid for the other strong O–H···N(pyridine) HBs discussed here, but in those structures the H atoms happen to be in plane with the pyridine rings. For comparison, see the difference density map perpendicular to the pyridine plane in PCP–2,3-lutidine (Figure 5-8).

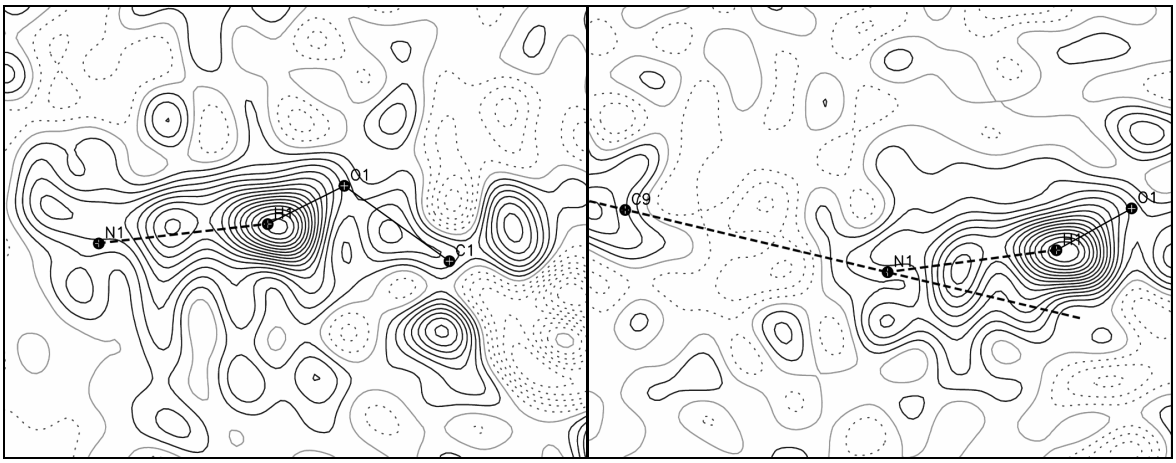

Figure 5-10: (Left) difference Fourier map in the C1–O1–N1 plane of PCP–2,6-lutidine Form I, (right) in the C9–N1–O1 plane perpendicular to the pyridine ring, dashed lines indicate the SSHBs and the pyridine planes; $\sin\theta/\lambda$ < 0.78 Å^{-1}, for details see Figure 5-5.

As mentioned previously, Form II of PCP–2,6-lutidine crystallises with two dimers in the asymmetric unit. The two independent O··H··N HBs show different HB configurations as evident from the difference Fourier maps (Figure 5-11). While the dimer linked by the O2–H2···N2 HB still exists in molecular form, in the other dimer the PCP hydrogen is transferred to the lutidine to form the O1···H1–N1 HB and thus a (formally) ionic adduct $[C_6Cl_5O]^-$ $[HC_7H_9N]^+$. The two SSHBs are the strongest in this family of dimeric PCP–lutidine complexes (comparable to that found for PCP–2,5-lutidine above) which manifests in a) short heteroatom distances of O2···N2 = 2.563(1) and O1···N1 = 2.555(1) Å, and b) the high linearity of the HBs with ∠O2–H2···N2 = 175(3)º and ∠O1···H1–N1 = 179(3)°. For a detailed comparison with the other SSHBs discussed here, the reader is referred to the HB geometries summarised in Table 5-1. The fact that the two PCP–2,6-lutidine dimers occupy different protonation states is quite remarkable, because they, and also that in Form I, are chemically equivalent. Crystal packing effects must therefore account for the occurrence or absence of H transfer in this material. Because of the unequal

protonation states the formula unit now contains one molecular and one ionic adduct, formally keeping $Z' = 1$: $C_6Cl_5OH \cdot C_7H_9N \cdot [C_6Cl_5O]^- [HC_7H_9N]^+$.

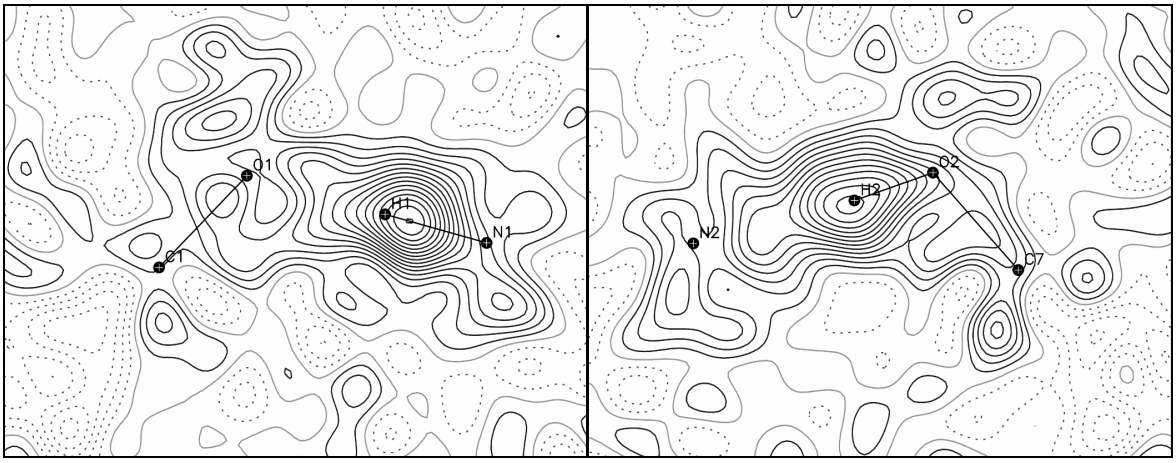

Figure 5-11: Difference Fourier maps for the two independent SSHBs in PCP–2,6-lutidine Form II, (left) in the C1–O1–N1 plane of the ionic H transfer adduct, (right) in the C7–O2–N2 plane of the molecular adduct; $\sin\theta/\lambda < 0.78$ Å^{-1}, for details see Figure 5-5.

The question naturally arises as to why H transfer happens only for one dimer in Form II, and not at all in Form I. A possible answer might lie with the weak C–H···O interactions present in the two polymorphs. As seen in Figure 5-9 both forms of PCP–2,6-lutidine have in common that two PCP – lutidine dimers are weakly linked by intermolecular C–H(methyl)···O(PCP) HBs to form tetrameric units. They have different geometries but the C–H···O HB strengths are comparable, which is indicated by similar H···O distances. They range from 2.60 Å (H12C···O1) in Form I to 2.50 (H18B···O2) and 2.47 Å (H26B···O1) for the molecular and ionic adduct in Form II respectively. What distinguishes the ionic adduct from the molecular is the existence of a further C–H···O HB between an aromatic pyridyl C–H and the deprotonated phenol O with H16A···O1 = 2.46 Å. The phenol O thereby is the acceptor of two instead of one such weak interactions. It may be that is sufficient to trigger H transfer by stabilising the phenolate ion. Strictly speaking, one cannot refer to tetrameric units in Form II anymore, because they are linked by these additional C–H···O interactions to "chains of tetramers" oriented along the crystallographic *b* axis. Regardless of the underlying physical meaning, the classification of these materials into weakly bonded aggregates (tetramers, or chains thereof) helps in visualising the arrangement of the otherwise isolated PCP – lutidine dimers in the 3-dimensional space.

For both polymorphs variable temperature X-ray diffraction experiments were also performed. The PCP–2,6-lutidine complexes can be thought of as borderline cases regarding the H transfer reaction and therefore as ideal candidates for showing temperature dependent H migration effects in the SSHBs. In addition to the 100 K data reported above, datasets have been obtained for temperatures of 200 K and RT, for Form I on the same crystal and for Form II on a different crystal. The results are presented only briefly for completeness, because no evidence was found for H migration. For Form II deterioration of the crystal was observed at RT, resulting in a poor quality dataset (R_1 = 8.85 % for all data at a low resolution, $\sin\theta/\lambda = 0.64$ Å^{-1}). The configurations of the two SSHBs can only tentatively be determined not to have changed upon increasing the temperature, on the basis of the heavy atom parameters rather than from the ambiguous difference density

maps (not shown here). The O···N distance in the SSHB comprising the ionic dimer seems interestingly to be unaffected by the temperature (within the experimental error), while that of the molecular dimer increases slightly from 2.563(1) at 100 K to 2.589(3) Å at RT. However, the temperature behaviour certainly needs reinvestigation in view of the poor quality data. For Form I, the collected high T datasets are of much better quality and refine to R_1 = 5.24 % and 6.77 % at 200 K and RT respectively, for all data to $\sin\theta/\lambda$ = 0.78 Å^{-1}. The HB configurations for the high T structures can clearly be determined from the difference Fourier maps in Figure 5-12, they confirm that PCP–2,6-lutidine Form I exists in molecular form in the probed temperature range. Also, the heavy atom parameters (not shown here) show no evidence for H transfer or H migration. The O1···N1 separation in the SSHB lengthens as expected with increasing temperature; in the series 100 K, 200 K, and RT from 2.588(1), to 2.604(2), to 2.622(2) Å.

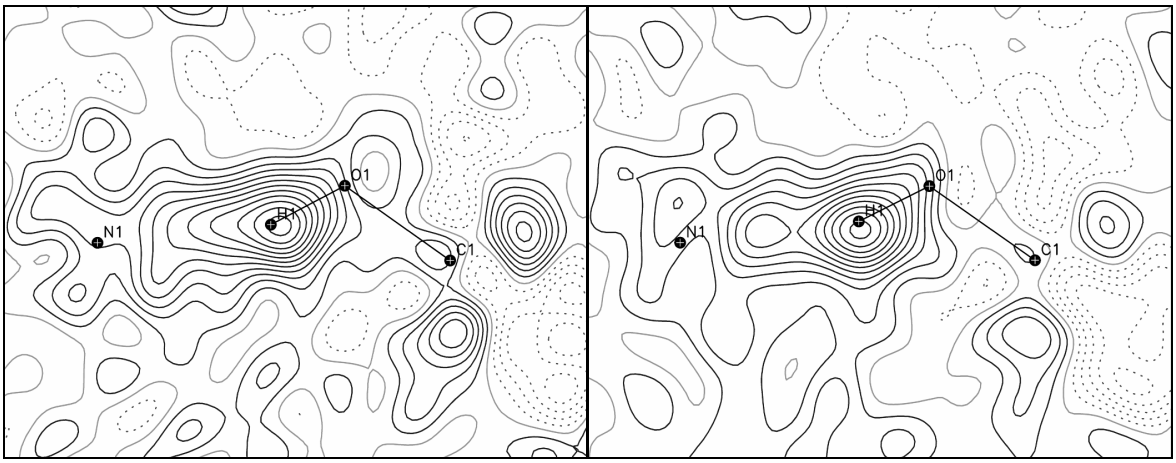

Figure 5-12: Difference Fourier maps in the C1–O1–N1 plane of PCP–2,6-lutidine Form I at 200 K (left) and RT (right); $\sin\theta/\lambda$ < 0.78 Å^{-1}, for details see Figure 5-5.

PCP – 2,4-Lutidine

The room temperature structure of PCP–2,4-lutidine (ΔpK_a = 2.29) has previously been published by Majerz *et al*.[99] For comparison and completeness the structure of this complex, measured at low temperature, has been included here. PCP–2,4-lutidine crystallises in nice block shaped morphology in the space group $P2_1/n$, and the structure was redetermined and refined to R_1 = 3.92 % for all data to $\sin\theta/\lambda$ = 0.78 Å^{-1}.

As already determined in the previous study,[99] in this material the H atom is completely transferred from PCP to the lutidine and an ionic complex, $[C_6Cl_5O]^-$ $[HC_7H_9N]^+$, is formed. Comparison of high and low T data shows that the O···H–N HB is pretty much unaffected in this temperature range. No shortening of the SSHB is observed at low temperature, the O1···N1 distances of 2.614(1) and 2.604(3) Å for the 100 K and RT data respectively, are comparable. It is difficult to judge on the basis of the heteroatom distance whether the HB between the PCP and the lutidine constitutes a SSHB. The difference Fourier map in Figure 5-13 shows density accumulations in the lone pair regions of the pentachlorophenolate O atom (pointing out the high quality of the X-ray data), but it does not show a polarisation of the H1 density towards the O lone pair which accepts the HB. Such a polarisation (or delocalisation) of electron density would be typical of SSHBs, and is observed for the other SSHBs described in this chapter. As for PCP–2,5-lutidine,

there is an "interdimer" C–H···O HB originating from the methyl group in *ortho* position (Figure 5-1) with, for such interactions, a short H12A···O1 contact of 2.36 Å. In fact, the H···O distance is the shortest, by 0.1 Å, in comparison with the other C–H···O HBs found for the dimeric and trimeric structures (see Table 5-1 and Table 5-4). In addition, a weaker C13–H13C···O1 HB with d(H···O) = 2.65 Å links the dimers into chains oriented along the crystallographic *n* glide plane (see Figure 5-14).

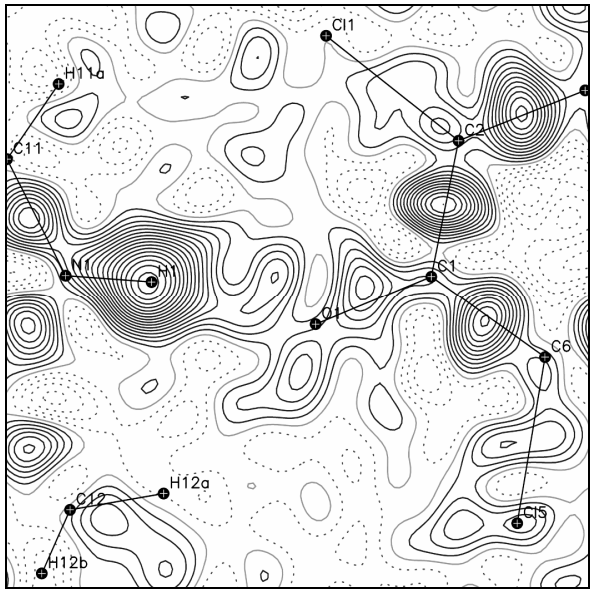

Figure 5-13: Difference Fourier map in the C1–O1–N1 plane of PCP–2,4-lutidine; $\sin\theta/\lambda < 0.78$ Å^{-1}, for details see Figure 5-5.

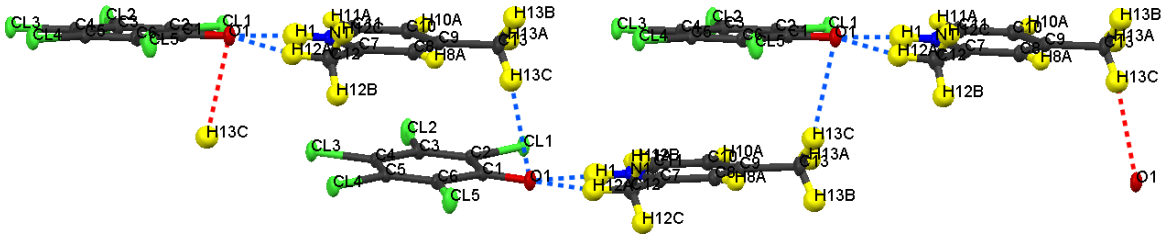

Figure 5-14: HB scheme of the weak CH···O interactions linking the PCP–2,4-lutidine dimers into chains.

Table 5-1: HB parameters for the dimeric (1 : 1) PCP – lutidine complexes; H positional and displacement parameters have been refined when errors are given, fixed using the riding model otherwise.

	HB	D–H / Å	H···A / Å	D···A / Å	∠DHA / °
PCP–3,5-lutidine small	O1–H1···N1	0.84	1.88	2.586(11)	141.1
large	O1–H1···N1	0.84	1.91	2.597(9)	137.9
	O2–H2···N2	0.84	1.94	2.639(10)	140.4
	O3–H3···N3	0.84	1.91	2.608(10)	139.3
PCP–2,5-lutidine	N1–H1···O1	0.97(2)	1.60(2)	2.559(2)	166(2)
	C12–H12A···O1	0.98	2.56	3.140(2)	117.9
PCP–3,4-lutidine	O1–H1···N1	0.73(4)	1.98(4)	2.682(3)	161(4)
	C11–H11A···O1*	0.95	2.64	3.337(3)	130.6
PCP–2,3-lutidine	O1–H1···N1	0.83(2)	1.80(2)	2.6054(12)	163(2)
	C12–H12A···O1	0.98	2.52	3.3245(14)	139.5
PCP–2,6-lutidine Form I	O1–H1···N1	0.88(2)	1.75(2)	2.5878(12)	158.0(19)
	C12–H12C···O1*	0.98	2.60	3.4098(13)	140.0
Form II	N1–H1···O1	1.08(3)	1.47(3)	2.5546(12)	179(3)
	O2–H2···N2	0.86(3)	1.71(3)	2.5629(13)	175(3)
	C16–H16A···O1*	0.95	2.46	3.2783(14)	144.3
	C26–H26B···O1	0.98	2.47	3.3990(15)	157.4
	C18–H18B···O2	0.98	2.50	3.3804(16)	148.6
PCP–2,4-lutidine	N1–H1···O1	0.89(2)	1.74(2)	2.6142(12)	169.1(19)
	C12–H12A···O1	0.98	2.36	3.1924(16)	142.0
	C13–H13C···O1	0.98	2.65	3.5269(16)	148.9

* Atoms generated by symmetry.

Table 5-2: Hydrogen transfer – ΔpK_a dependence (pK_a for PCP = 4.70) in the dimeric (1 : 1) PCP – lutidine complexes. Geometrical parameters that indicate the protonation states of PCP and lutidines are also included.

	pK_a(lut)	ΔpK_a	% HT	∠CNC / °	C–O / Å	∠CC(O)C / °
PCP–3,5-lutidine small	6.15	1.45	0	119.0(8)	1.326(12)	117.0(8)
large			0	117.6(7)	1.351(11)	118.5(8)
				119.5(7)	1.301(10)	117.8(7)
				117.0(8)	1.341(11)	117.7(8)
PCP–2,5-lutidine	6.40	1.70	100	122.25(14)	1.276(2)	114.72(14)
PCP–3,4-lutidine	6.46	1.76	0	115.6(2)	1.339(3)	117.4(2)
PCP–2,3-lutidine	6.57	1.87	0	119.44(9)	1.3281(12)	117.05(8)
PCP–2,6-lutidine Form I	6.60	1.90	0	120.02(9)	1.3283(12)	117.32(9)
Form II			50	122.80(10)	1.3030(13)	115.11(10)*
				120.84(10)	1.3286(14)	116.89(10)†
PCP–2,4-lutidine	6.99	2.29	100	121.88(9)	1.2862(12)	114.29(9)

* N1–H1···O1; † O2–H2···N2

In summary, hydrogen transfer in the dimeric PCP – lutidine complexes follows largely the trend of increasing lutidine pK_a values. With the exception of PCP–2,5-lutidine – and the (unexpected) H transfer reaction observed there is regarded as the exception to the rule in the following interpretation – the first occurrence of (partial) H transfer from PCP to lutidine is observed for the 2,6-lutidine complex, which has a ΔpK_a of 1.90. No H transfer is observed for the lutidines with lower pK_a and complete H transfer for the one with the next higher value. It could be argued that Form II of the PCP–2,6-lutidine complex can be seen as marking the $\Delta pK_a^{50\%}$ value at 1.90 because in this material, averaged over the two independent O··H··N HBs, 50 % of the phenol H is transferred. On the other hand, Form I of this material (with the same ΔpK_a of course) shows 0 % H transfer and emphasises that such a $\Delta pK_a^{50\%}$ value cannot be pinpointed accurately and should be better and less strictly estimated to $\Delta pK_a^{50\%} \sim 2.0$ for this system (still ignoring the "anomalous" H transfer in PCP–2,5-lutidine at $\Delta pK_a = 1.70$ of course).

5.1.2. Ab Initio Studies

The quantum mechanical calculations described in this section have been performed on the two polymorphic forms of PCP–2,6-lutidine, as these structures mark the borderline cases for H transfer reactions. Furthermore, an establishment of the energy ranking for this polymorphic material is also of interest, in particular as the occurrence of polymorphism is accompanied by H transfer in this case. The computational demand is increased compared to the previous calculations on IN_2–OA described in Chapter 3 *Molecular Complexes of Isonicotinamide with Oxalic Acid*, for two reasons. First, the lack of an extended hydrogen bonded network in these materials results in only a weak embedding of the PCP – lutidine dimers into the crystal environment by C–H···O and van der Waals interactions. This leads to an increased degree of freedom for the external molecular modes, implying a reduced convergence during geometry optimisation. Second, the number of electrons, and hence the computational effort, is increased, in particular for the calculations on Form II where two dimers are to be calculated independently. Initial attempts to use the plane wave method with CASTEP[50] showed poor convergence during the geometry optimisation runs, and also the preference for the NH···O configuration of the SSHBs as previously observed for the familiar acid – pyridine base materials examined in Chapter 3. The computational studies have therefore subsequently been limited to atomic orbital calculations with CRYSTAL.[51] They encompass geometry optimisations in the full periodic environment and on Form I also the determination of the HB potential. All calculations have been carried out using the AO approach in an analogous way to the previous ab-initio calculations on IN_2–OA. The same exchange–correlation functionals and the same basis set have been used, i.e. the B3PW/6-31g** level of theory[48, 83] (for further details see 3.1.4 *Ab Initio Studies*). The starting geometries for the geometry optimisations were taken from the crystallographically determined structures, and the lattice parameters as well as the crystal symmetry were fixed to the experimental values. In addition, variable starting configurations with respect to the SSHB have been employed to probe the energy surface of the molecular and ionic adducts.

At first, the structures were allowed to relax by starting from the experimental geometry, i.e. the SSHB in OH···N configuration for the molecular complex of Form I, and in the two different OH···N and O···HN configurations for the molecular and ionic adducts of Form II respectively. Table 5-3 lists the HB parameters optimised this way ("free

optimisation") and the relative energies per PCP – 2,6-lutidine dimer. Firstly of note is that the geometries all relaxed into minima for the experimental HB configurations. Comparing the computed and the experimental O···N distances shows that the SSHBs are shortened for the molecular dimers by ~0.03 – 0.04 Å, whereas it is lengthened for the ionic dimer by ~0.03 Å. The covalent bonds involving the hydrogens and hydrogen bonding interactions are difficult to compare due to the inaccuracy of the X-ray determined H parameters. In any case, elongations of the O–H and N–H bonds are observed, in particular for O2–H2 in Form II, consistent with the model of strong HBs. Regarding the energy scale for polymorphism, the CRYSTAL calculations determine Form II to be the stable form. This is rather contrary to the experimental observations which suggest that Form I is the energetically and Form II the kinetically stable polymorph. The energy difference of 1.3 kJ/mol, however, is small and can be considered to lie within the error of the applied method.

In a second step, the geometry optimisations were repeated with the O···N distances fixed at the experimental values. The outcome is similar to the free optimisation runs: the covalent bond lengths relax to comparable values with a maximum deviation of 0.015 Å for O2–H2, and the computed energies are only slightly increased by 0.5 and 0.3 kJ/mol per PCP – lutidine dimer in Form I and Form II respectively (see Table 5-3). In order to check for possible energy minima for the SSHBs adopting the experimentally unobserved HB configurations, the starting geometries were changed correspondingly before allowing the structures to relax again. For both polymorphs, local minima were also found for these alternate HB configurations. In Form I, a change from the experimental OH···N configuration to the O···HN is accompanied by an energy increase of only 0.3 kJ/mol per formula unit. The energy difference is very small and suggests that this material can also exist as an ionic complex. In Form II on the other hand, the energy increases by ~6.5 kJ/mol per dimer when changing the HB configurations (Table 5-3).

Table 5-3: Computed HB parameters for Form I and Form II of PCP–2,6-lutidine, starting from variable HB configurations, relative energies for the optimised structures are also given; for details see text.

	HB	D–H / Å	H···A / Å	D···A / Å	ΔE / kJ·mol^{-1}
Form I					
free optimisation	O1–H1···N1	1.047	1.553	2.555	+1.3
O···N fixed	O1–H1···N1	1.038	1.596	2.588	+1.8
O···N fixed, HB config. changed	N1–H1···O1	1.086	1.550	2.588	+2.1
Form II					
free optimisation	N1–H1···O1	1.087	1.497	2.583	0
	O2–H2···N2	1.078	1.451	2.527	
O···N fixed	N1–H1···O1	1.095	1.461	2.555	+0.3
	O2–H2···N2	1.063	1.502	2.563	
O···N fixed, HB config. changed	O1–H1···N1	1.098	1.458	2.555	+6.8
	N2–H2···O2	1.123	1.441	2.563	

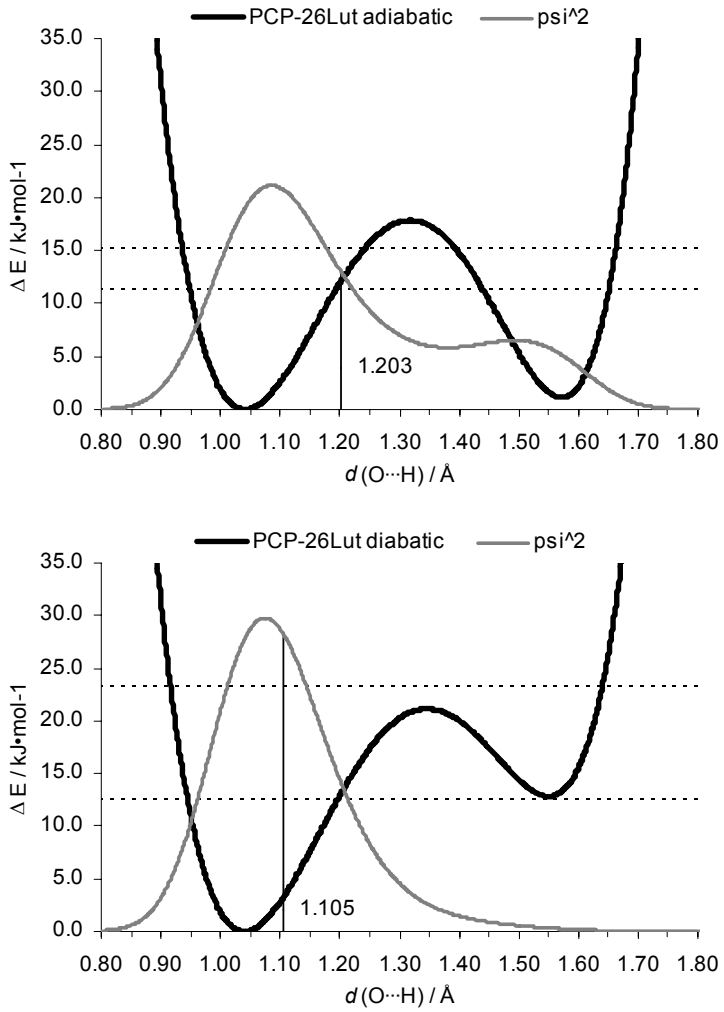

Figure 5-15: Adiabatic (top) and diabatic (bottom) HB potentials in PCP–2,6-lutidine Form I calculated with CRYSTAL, probability density distribution (ψ^2) in grey, zero point energy and first excited state as dashed lines, vertical lines mark the expectation values for *d*(O···H).

The determination of potential energy curves for H transfer had to be limited to Form I for the reason that the calculations on Form II are computationally very expensive.[a] The calculations have been performed in an analogous way to those on IN_2–OA, that is the O···N distance was fixed to the experimental, time averaged value, and the geometry was allowed to relax for each H position on the HB path. The resulting adiabatic HB potential is shown in Figure 5-15, top. As already indicated by the geometry optimisation runs, it shows a double well profile with a second minimum for the complex adopting the ionic O···HN configuration, $[C_6Cl_5O]^-$ $[HC_7H_9N]^+$, in addition to that found for the experimental molecular OH···N configuration, $C_6Cl_5OH \cdot C_7H_9N$. The energy difference estimated from the PEC between the molecular and ionic complex is small (< 1.0 kJ/mol) in favour of the molecular configuration although there is no experimental evidence for a population of the N site in the SSHB. The energy barrier for H transfer, however, is large and amounts to ~18 kJ/mol, and the SSHB can consequently not be classified as a LBHB although the two energy minima can be regarded as equivalent within the error of the method. Solving the

[a] Geometry optimisation on Form II for an average 50 optimisation steps takes about 8 – 10 days in parallel mode shared over 16 processors, compared to 1 – 2 days on 8 processors for Form I.

1-dimensional Schrödinger equation yields an expectation value for the H position at an O–H distance of 1.20 Å, which seems long when compared with the refined X-ray distance of 0.83 Å and the corresponding electron difference density for H1 in Figure 5-10. The energy difference between the zero point and the first excited energy level is small with 3.9 kJ/mol and close to being thermally accessible considering that $E = k_B \cdot T \sim 2.5$ kJ/mol for T = 300 K. In addition to the adiabatic HB potential, the diabatic potential (Figure 5-15, bottom) has been determined by means of single point energy calculations for each H step. It shows, like the adiabatic potential, a double well minimum, but in this case with a much higher energy of ~13 kJ/mol for the second minimum corresponding to the O···HN configuration, and a further increased H transfer barrier of ~21 kJ/mol. This is in better agreement with the experiment since no occupation of the second minimum is observed. Also, the difference between the first two energy levels is increased to 10.8 kJ/mol, but more importantly, the probability density distribution appears more realistic and the expectation value for the O–H bond length is reduced to 1.10 Å. It appears that, unlike for the molecular complexes IN_2–OA, calculating the diabatic rather than adiabatic HB potentials is the appropriate approach to model the SSHB in this material. This would also imply that the O–H stretching frequency occurs at higher frequencies and that consequently the SSHB in PCP–2,6-lutidine is weaker compared to those formed in IN_2–OA. This would agree with the geometrical HB parameters, i.e. an increased O···N distance and a reduced linearity in this case (corresponding HB parameters in Table 5-1 and Table 3-1).

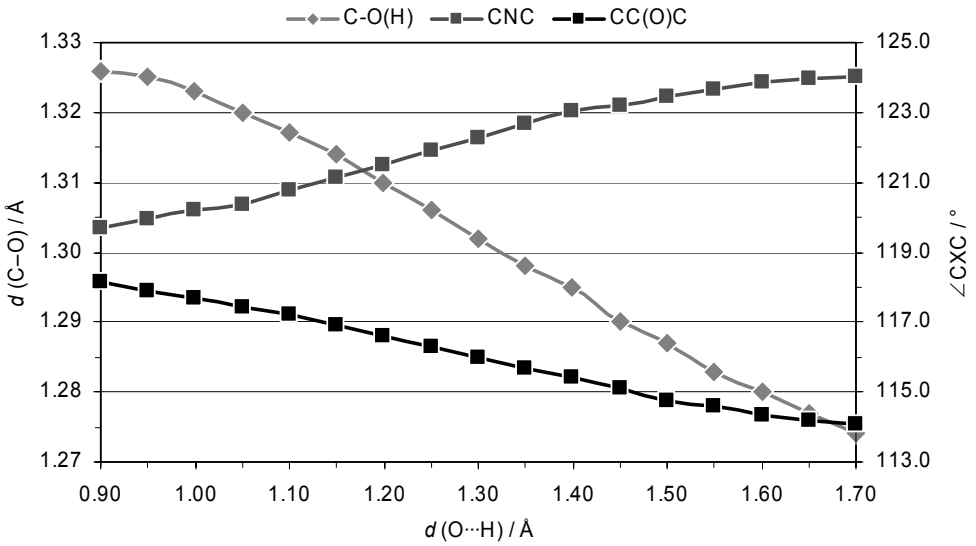

Figure 5-16: Correlation between the H transfer coordinate and phenol C–O bond length (grey diamonds), pyridine CNC and phenol CC(O)C angles (grey and black squares).

As mentioned in the previous discussion of the dimeric PCP – lutidine complexes, the phenol C–O bond length, the phenol CC(O)C and the pyridine CNC bond angles are indicative of the protonation states of the participating species. The correlation between H transfer and these heavy atom parameters is documented in Figure 5-16. The data have been extracted from the optimised geometries obtained from the determination of the adiabatic HB potential described above. The CNC dependence on the degree of protonation in pyridine derivatives has already been documented for IN_2–OA, where the CNC bond angle varied from 118º to 122º by going from unprotonated to fully protonated

isonicotinamide. In the present case of PCP–2,6-lutidine, the CNC bond angle for 2,6-lutidine is persistently higher by ~2º, but increases in the same continuous manner from 120º to 124º (compare with Figure 3-35). In addition, Figure 5-16 also points out a similar correlation of the PCP CC(O)C bond angle and the C–O(H) bond length, which decrease from ~118º to 114º and from 1.325 to 1.275 Å respectively upon step wise deprotonation.[102]

To conclude, the ab-initio calculations performed on PCP–2,6-lutidine largely reproduced the experimental geometries for both polymorphs. Furthermore, local minima were found for the complexes exhibiting alternate HB configurations. The energy difference for the formation of the two polymorphs is computed to be ~1 kJ/mol in favour of Form II, which, in view of the associated methodological error, can be considered negligible. The calculated HB potentials suggest that the SSHB in the current system is weaker than those found in the hydrogenous forms of IN_2–OA. However, comparative computational studies on other PCP–lutidine complexes, preferably on PCP–2,6-lutidine Form II, will be required to back up this conclusion.

5.1.3. Trimeric 2:1 Structures

During the process of co-crystallising the dimeric PCP – lutidine complexes, PCP was found to co-crystallise also as trimeric PCP_2 – lutidine complexes with some of the lutidines. In fact, these lutidines prefer to form the trimeric structures under experimental conditions which are essentially similar to those described in the above section *Dimeric 1:1 Structures*. To date, the following PCP_2 – lutidine structures have been obtained and characterised by X-ray diffraction:

PCP_2–3,5-lutidine–H_2O ≡ $C_6Cl_5OH \cdot [C_6Cl_5O]^- [HC_7H_9N]^+ \cdot H_2O$ ($\Delta pK_a = 1.45$)

PCP_2–2,5-lutidine ≡ $C_6Cl_5OH \cdot [C_6Cl_5O]^- [HC_7H_9N]^+$ ($\Delta pK_a = 1.70$)

PCP_2–3,4-lutidine ≡ $C_6Cl_5OH \cdot [C_6Cl_5O]^- [HC_7H_9N]^+$ ($\Delta pK_a = 1.76$)

These complexes have also been investigated since they offer an opportunity for investigating the effect of an extra molecule of PCP (and H_2O in the case of PCP_2–3,5-lutidine–H_2O), "co-crystallising" with an dimeric PCP – lutidine moiety. It is worthy of note that the three lutidines (3,5-lutidine, 3,4-lutidine and 2,5-lutidine) which have to date been found to form 2 : 1 complexes are exactly those which form the 1 : 1 structures, PCP–3,5-lutidine, PCP–2,5-lutidine and PCP–3,4-lutidine, for which either growing suitable single crystals or determining the structure proved to be difficult. In the chemical context of course, these complexes mark the lower end of the ΔpK_a range. The X-ray structures of the 2 : 1 complexes, all obtained at 100 K, were refined in accordance to the procedure described for the dimeric structures; and are presented here briefly as published in reference [97]. The ellipsoid plots of the asymmetric units are shown in Figure 5-17, the HB parameters in Table 5-4, and the ΔpK_a – H transfer relationship including the heavy atom parameters in Table 5-5.

PCP_2–3,5-lutidine–H_2O

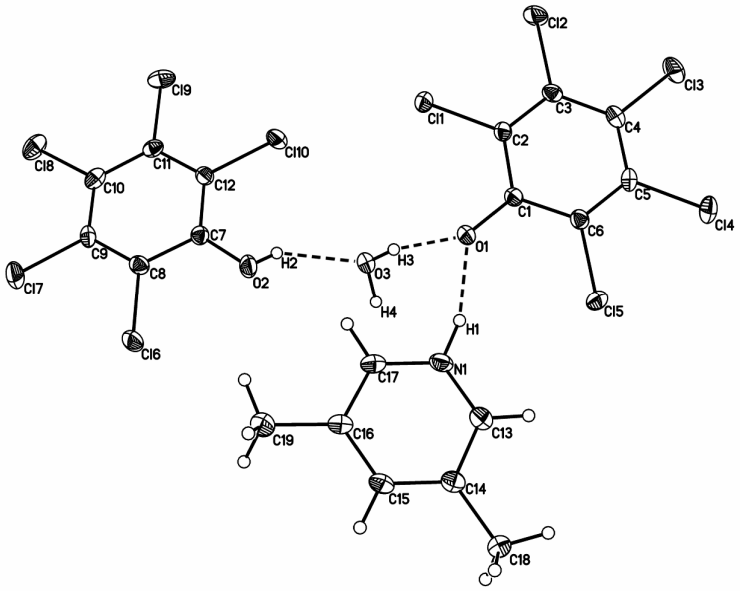

PCP_2–2,5-lutidine

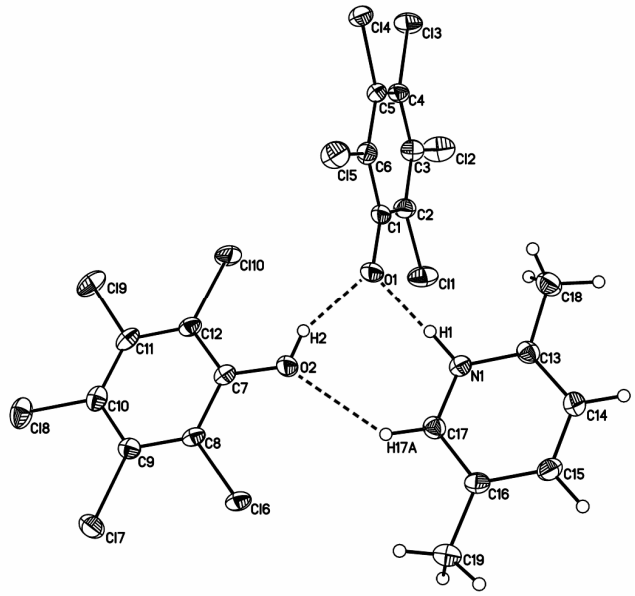

PCP_2–3,4-lutidine

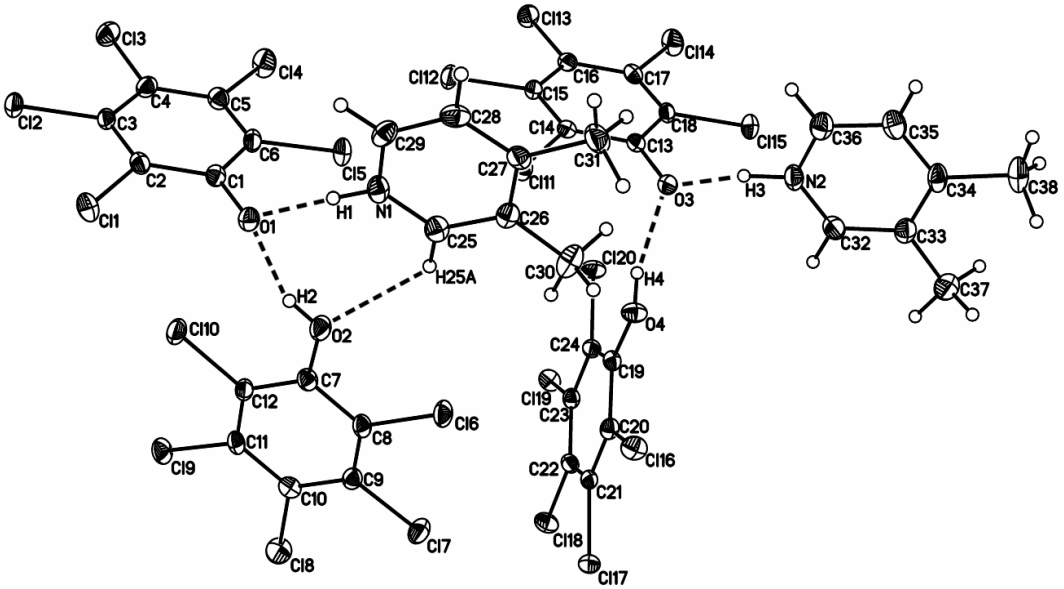

Figure 5-17: Ellipsoid plots of the dimeric (2 : 1) PCP_2 – lutidine structures; for details see Figure 5-1.

PCP_2 – 3,5-Lutidine – H_2O

In the presence of water, PCP and 3,5-lutidine co-crystallise as the trimeric hydrated complex, PCP_2–3,5-lutidine–H_2O, in addition to the previously described dimeric complex, PCP–3,5-lutidine. It crystallises with stick shaped morphology in the acentric space group $Pna2_1$. In contrast to the ambiguities involved in the determination of the dimeric structure, the crystals of PCP_2–3,5-lutidine–H_2O are of good quality and the X-ray structure was refined to R_1 = 3.80 % for all data to a resolution of $\sin\theta/\lambda$ = 0.70 Å^{-1}.

In this structure the hydrogen atom of one PCP unit is transferred to the lutidine accompanied by the formation of the weakest O(PCP)··H··N(pyridine) HB observed in the family of PCP – lutidine adducts (the heteroatom distance in O1···H1–N1 HB refines to D = 2.715(2) Å). The H transfer in this material is clearly observed in the difference Fourier map (Figure 5-18, left), and there is no sign of electron density delocalisation or polarisation of the H density towards the O lone pair in this moderate HB. The O1 atom of the resulting pentachlorophenolate ion itself accepts two moderate HBs from the co-crystallising water: O3W–H3···O1 and O3W–H4···O1 with D = 2.736(2) and 2.773(2) Å respectively. The water molecule in turn is the acceptor of the strongest HB in this structure, O2–H2···O3W (D = 2.570(2) Å), donated by the additional undissociated PCP molecule (see Figure 5-17 for the overall HB scheme). The electron density distribution in the plane of this HB is shown for completeness in Figure 5-18, right. The fact that H transfer occurs in this complex but not in the corresponding dimeric PCP–3,5-lutidine can be explained by the stabilisation of the phenolate anion by accepting the two moderately strong HBs from the co-crystallising water.

The presence of water leads to the formation of the only extended hydrogen bonded structure presented here, ignoring the weak linkage of the PCP – lutidine dimers by weak C–H···O interactions as discussed earlier. The extended structure manifests in chains which are made up of the ionic PCP–3,5-lutidine dimers, which alternate with the moieties made up of a water and a hydrogen bonded neutral PCP molecule (see Figure 5-19). Interestingly, only PCP and 3,5-lutidine co-crystallise with water; with all other lutidines PCP does not form hydrated structures.

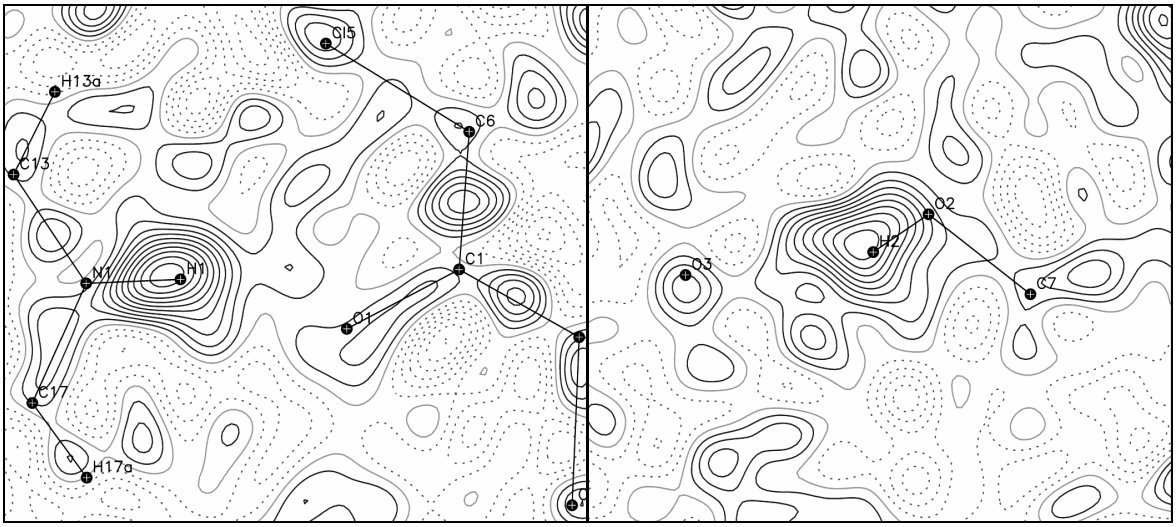

Figure 5-18: Difference Fourier maps for the HBs involving the two PCP molecules in PCP_2–3,5-lutidine–H_2O; (left) O(PCP)···H–N(pyridine); (right) O(PCP)–H···O(water); $\sin\theta/\lambda$ < 0.70 Å^{-1}, for details see Figure 5-5.

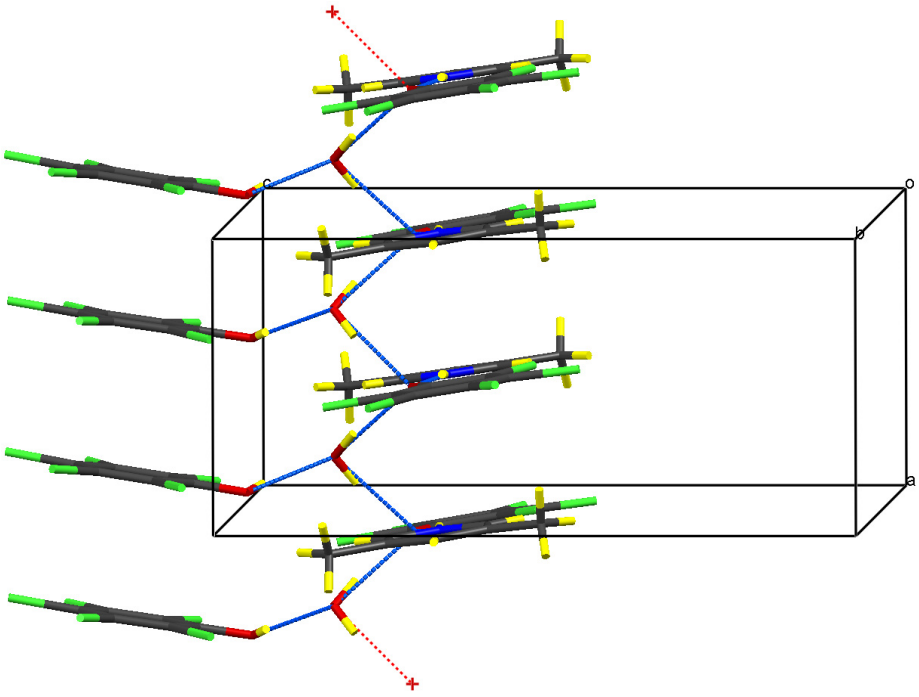

Figure 5-19: Extended hydrogen bonded structure of PCP_2–3,5-lutidine–H_2O.

PCP_2 – 2,5-Lutidine

As mentioned in the previous discussion of the dimeric structures, PCP and 2,5-lutidine co-crystallise preferentially as a trimeric complex with the ratio 2 : 1. This became apparent when stoichiometric ratios (1 : 1) of PCP and the lutidine were used in attempts to grow crystals of the dimeric PCP–2,5-lutidine complex, and the trimeric PCP_2–2,5-lutidine complex was formed instead. PCP_2–2,5-lutidine crystallises with block shaped crystals in the space group $P\bar{1}$, and unlike for PCP–2,5-lutidine (which crystallised in tiny needles), a good quality X-ray dataset was easily obtained for which the structure was refined to R_1 = 4.29 % for all data to $\sin\theta/\lambda = 0.70$ Å^{-1}.

The structure of PCP_2–2,5-lutidine comprises isolated hydrogen bonded trimers. As for PCP_2–3,5-lutidine–H_2O, one PCP hydrogen is transferred to the lutidine, resulting in the formation of an ionic adduct. In this case however, the O1···H1–N1 HB formed between PCP and the lutidine is considerably shorter with a heteroatom distance of D = 2.604(2) Å. The second PCP maintains its neutral form and stabilises the deprotonated PCP via the O2–H2···O1 HB (D = 2.536(2) Å). The two HBs can be considered to be of similar strength, because O··H··N HBs are usually about 0.1 Å longer than O··H··O HBs. Aside from these two strong HBs, an additional weak C–H···O interaction (H17A···O2 = 2.45 Å) is formed between the aromatic pyridine α-C–H and the hydroxyl group of the neutral PCP. The resulting HB scheme can be visualised as a "cyclic" synthon (see Figure 5-17) in which the aromatic ring systems of the undissociated PCP and the lutidine are approximately coplanar, with the deprotonated PCP oriented roughly perpendicular to this plane. The difference Fourier map in Figure 5-20, generated through the plane of the cyclic synthon, nicely points out the protonation states of the participating species in this complex.

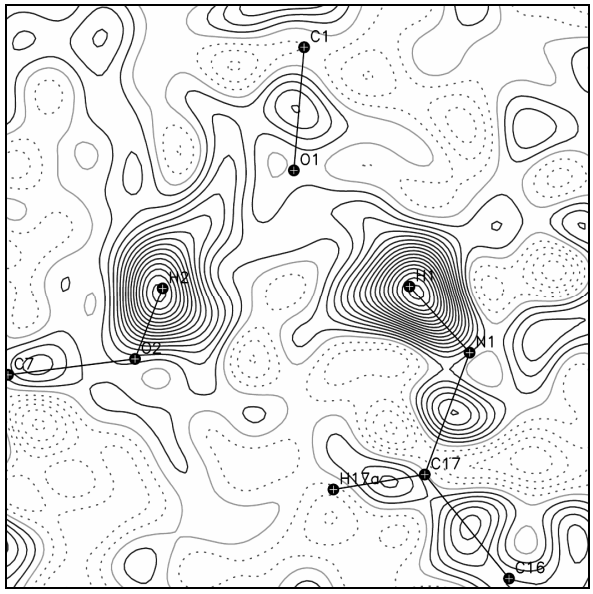

Figure 5-20: Difference Fourier map through the plane of the hydrogen bonded cyclic synthon in the O2–O1–N1 plane in PCP_2–2,5-lutidine; $\sin\theta/\lambda < 0.70$ Å^{-1}, for details see Figure 5-5.

PCP_2 – 3,4-Lutidine

PCP and 3,4-lutidine also co-crystallise preferentially in the 2 : 1 complex PCP_2–3,4-lutidine when a stoichiometric 1 : 1 ratio of the reactants is used. PCP_2–3,4-lutidine forms block shaped crystals (space group $P\bar{1}$) for which a good X-ray dataset was obtained and the structure was subsequently refined to $R_1 = 4.35$ % for all data to a resolution of $\sin\theta/\lambda = 0.70$ Å^{-1}.

In a similar fashion to PCP_2–2,5-lutidine, this complex forms hydrogen bonded trimers where one PCP H atom is transferred to the lutidine and the resulting pentachlorophenolate anion is stabilised by the second, neutral PCP molecule. To complicate this description, there are now two trimers in the asymmetric unit rendering $Z' = 2$. In addition, the two crystallographically independent trimeric units in this case differ slightly in their HB motifs (Figure 5-17). One trimer is very similar to that in PCP_2–2,5-lutidine, that is the cyclic synthon is present with comparable HB distances for O1···H1–N1 = 2.633(2), O2–H2···O1 = 2.555(2), and H25A···O2 = 2.48 Å respectively. The difference Fourier through the plane of this synthon, showing the protonation states of the participating molecules, is given in Figure 5-21, left. The necessary condition for the formation of the C–H···O HB, and thereby of the cyclic synthon, is that the lutidine and the neutral PCP molecules are roughly coplanar. The second trimer in PCP_2–3,4-lutidine differs in this respect in that the lutidine unit is rotated out of this plane and the C–H···O interaction is thus absent. The two strong O···H–N and O–H···O HBs, on the other hand, are still present. However, with O3···H3–N2 and O4–H4···O3 heteroatom distances of 2.556(2) and 2.627(2) Å respectively, the HB which is formed in the H transfer adduct, $[C_6Cl_5O]^-$ $[HC_7H_9N]^+$, is now for the first time the significantly stronger HB in the trimeric unit. The strength of the O3···H3–N2 HB in comparison to the other O···H–N HB formed in the trimeric units is emphasised by the difference density for H3 in Figure 5-21, right. In this case, the H3 density shows a considerable delocalisation in the HB and is polarised towards the O atom as typically found in SSHBs. In fact, there is evidence that the H atom occupies a centred

position in this HB: first, the electron density distribution exhibits some resemblance to that observed in centred SSHBs (Figure 4-3 and Figure 4-4, right, in Chapter 4 *Imaging the Electron Density of Hydrogen in Strong Hydrogen Bonds*); second, the heavy atom parameters, in particular the CNC bond angle and the C–O distance, adopt values typical of an intermediate protonation states (see Table 5-5). In any case the O3···H3–N2 HB is strong and potentially the only HB to be considered a SSHB in the family of trimeric PCP_2–lutidine complexes. The variation in HB strengths in the trimeric units might be accounted to weak C–H···O interactions. The lack of "stabilisation" the PCP hydroxyl group experiences by the absence of the weak C–H···O HB may prevent this PCP molecule from sharing its H atom to the same extent as is observed in the C–H···O stabilised synthons. In turn, the reduced stabilisation the $[C_6Cl_5O]^-$ anion experiences due to the weakened O–H···O HB might lead to an increased demand for charge balance by forming a stronger interaction to the N–H donor.

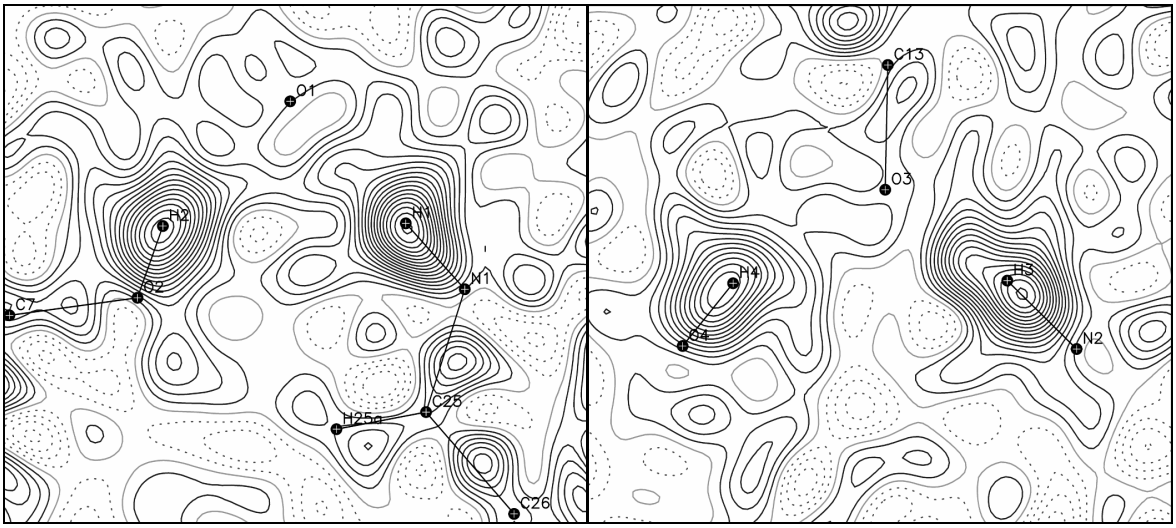

Figure 5-21: (Left) difference Fourier map through the plane of the hydrogen bonded cyclic synthon in the O2–O1–N1 plane of the first trimer, and (right) in the O4–O3–N2 plane of the second trimer in PCP_2–3,4-lutidine; $\sin\theta/\lambda < 0.70$ Å^{-1}, for details see Figure 5-5. The elongation/delocalisation of the density associated with H3 in the SSHB is notable.

Table 5-4: HB parameters for the trimeric (2 : 1) PCP_2 – lutidine complexes; for details see Table 5-1.

	HB	D–H / Å	H···A / Å	D···A / Å	∠DHA / °
PCP_2–3,5-lutidine–H_2O	N1–H1···O1	0.97(3)	1.78(3)	2.715(2)	160(3)
	O3W–H3···O1	0.86(4)	1.89(4)	2.736(2)	168(3)
	O3W–H4···O1*	0.91(3)	1.90(3)	2.773(2)	160(3)
	O2–H2···O3W	0.70(3)	1.94(3)	2.570(2)	149(3)
PCP_2–2,5-lutidine	N1–H1···O1	0.93(2)	1.68(2)	2.6036(18)	173.8(19)
	O2–H2···O1	0.79(3)	1.81(2)	2.5356(17)	152(2)
	C17–H17A···O2	0.95	2.45	3.207(2)	137.0
PCP_2–3,4-lutidine	N1–H1···O1	0.91(2)	1.73(2)	2.6334(19)	177(2)
	N2–H3···O3	1.00(3)	1.56(3)	2.5564(19)	172(2)
	O2–H2···O1	0.78(3)	1.83(3)	2.5554(17)	154(3)
	O4–H4···O3	0.83(3)	1.84(3)	2.6266(16)	158(3)
	C25–H25A···O2	0.95	2.48	3.193(2)	131.9

* Atoms generated by symmetry.

Table 5-5: Hydrogen transfer – ΔpK_a dependence in the trimeric (2 : 1) PCP_2 – lutidine complexes; averaged heavy atom parameters for the undissociated PCP molecules are included for comparison; for details see Table 5-2.

	pK_a(lut)	ΔpK_a	% HT	∠CNC / °	C–O / Å	∠CC(O)C / °
PCP_2–3,5-lutidine–H_2O	6.15	1.45	100	122.1(2)	1.305(3)	115.24(19)
PCP_2–2,5-lutidine	6.40	1.70	100	122.79(14)	1.3041(18)	115.22(14)
PCP_2–3,4-lutidine	6.46	1.76	100	121.71(16)	1.3096(19)	115.69(14)*
				120.90(16)	1.3148(19)	115.61(14)†
average for undissociated PCP in the trimeric complexes					1.333	117.593

* N1–H1···O1; † N2–H3···O3

In summary, all 2 : 1 complexes studied have in common the feature that a H atom is transferred from one PCP molecule to the lutidine, resulting in the formation of dimeric ionic adducts, $[C_6Cl_5O]^-$ $[HC_7H_9N]^+$. The pentachlorophenolate ion is stabilised by hydrogen bonding to either H_2O in case of PCP_2–3,5-lutidine–H_2O, or the second, neutral PCP molecule in the cases of PCP_2–2,5-lutidine and PCP_2–3,4-lutidine. Concerning the ΔpK_a – H transfer relationship it becomes evident that, in view of the ΔpK_a values for these compounds which range from 1.45 to 1.76, the empirical $\Delta pK_a^{50\%} \sim 2.0$ rule established for the dimeric complexes is no longer valid here, emphasising the influence of the solid state where a range of intermolecular interactions are present.

5.1.4. Conclusion

A strong correlation is found between H transfer and lutidine pK_a values in case of the dimeric (1 : 1) PCP – lutidine complexes. The reason for this is believed to be due to the fact that the O··H··N SSHBs are isolated from a polar environment. The two polymorphs of PCP–2,6-lutidine are borderline cases regarding H transfer and mark the $\Delta pK_a^{50\%}$ region

which can be quantified at ~2.0 in this case. The O··H··N SSHBs in the trimeric (2 : 1) PCP_2–lutidine complexes, on the other hand, are exposed to strong polar interactions. H transfer in these cases is facilitated by subsequent stabilisation of the pentachlorophenolate ion via moderate and strong hydrogen bonding. That is, the former neutral molecular complexes become ionic upon stoichiometric variation and/or solvation. The established ΔpK_a rule, derived from the dimeric structures, is consequently no longer applicable. These observations of course, are neither new nor unexpected, but seen in a wider context, for example to the pharmaceutical industry, they emphasise the importance of understanding the crystallisation behaviour of molecular compounds. Furthermore, in the related PCP–4-methylpyridine complex, with $\Delta pK_a = 1.30$, the H atom is situated in the centre of a O··H··N SSHB (at ~100 K) and marks literally the $\Delta pK_a^{50\%}$ point, which is also found to be temperature dependent.[25] Aside from weak C–H···O interactions, the SSHB in this previously studied material is very well isolated and should therefore be comparable to the dimeric PCP – lutidine complexes and obey the ΔpK_a rule established here, that is show no H transfer. The fact that it does, questions the transferability of ΔpK_a rules between even very similar solid state materials.

A few questions are deliberately raised regarding the effect of weak C–H···O HBs in some of the materials discussed, especially in the polymorphic PCP–2,6-lutidine. Although there is some structural evidence that these weak HBs influence the SSHB configuration, this influence is difficult to quantify, and other weak interactions such as van der Waals forces or simple steric effects can be equally accountable.

Although it is too early to draw conclusions on the performance of the ab-initio calculations (they have been carried out only on the two polymorphic PCP–2,6-lutidine complexes), the initial results are promising. First, the experimental geometries including the correct SSHB configurations are reproduced; second, the calculated (diabatic) HB potential with inclusion of the zero point energy results in a reasonable expectation value for the O–H distance in the SSHB. According to the calculations Form II is the energetically favoured polymorph by ~1.3 kJ/mol.

5.2. CARBOXYLIC ACID – DIMETHYLPYRIDINE COMPLEXES

The work presented in the previous section on the complexes of pentachlorophenol with the lutidines has been extended by variation of the acid moiety in the complex. The intention and the approach is the same: the design of strongly hydrogen bonded materials by varying the ΔpK_a of the hydrogen bonded molecules in a systematic manner whilst keeping them at reasonably small values. This is hoped to lead to the formation of SSHBs of the type O··H(acid)··N(pyridine) which show a variable degree of H transfer as observed previously. For this purpose, the acidic pentachlorophenol molecule (PCP) has been replaced by the carboxylic acids, oxalic acid (OA) and fumaric acid (FA). The lutidine pyridine bases have again been used as they are ideal HB acceptors, spanning a pK_a range from 6.15 to 6.99 without having significantly different chemical properties. Furthermore, they can, as discussed previously for the PCP – lutidine complexes, only form one strong or moderately strong HB, thereby allowing a systematic study as all other interactions involving the lutidine, such as C–H···A, C–H···π, or π–π, will inevitably be weak. The molecular, or in case of H transfer, ionic complexes which formed suitable co-crystals for a structure determination will be presented here. Lindemann and Zundel have established

ΔpK_a rules for the family of carboxylic acids and aromatic N bases based on IR studies on (solvent free) liquid systems. They differentiate between N bases with and without additional HB donor groups (N–H groups specifically), i.e. between N bases capable of facilitating H transfer by stabilising carboxylate anions and N bases not capable – the lutidines used for the present study belong to the latter group. Lindemann and Zundel also studied the influence of water molecules (as strong HB donors) on the H transfer behaviour, and determined $\Delta pK_a^{50\%}$ values of 4.0, 2.3, and 0.9 for N bases without HB donors, N bases with N–H donors, and hydrated systems respectively.[105]

5.2.1. Oxalic Acid – Dimethylpyridine Complexes

Oxalic acid is a diprotonic acid and a considerably stronger acid compared to PCP. The pK_a values for the removal of the two protons are 1.2 and 4.2 respectively, of which the latter is comparable to that of PCP (pK_a = 4.7). Therefore the idea is to generate hydrogen bonded 1 : 2 complexes of OA and lutidine, constituted of trimeric OA – $(lutidine)_2$ units where H transfer is expected to happen for the first deprotonation step of OA (ΔpK_a range = 4.95 – 5.79), and a variable degree of H transfer for the second deprotonation step, dependent on the lutidine pK_a. The formation of the second HB is assumed to result in strong hydrogen bonding as the corresponding ΔpK_a range of 1.95 – 2.79 is reasonably small. Crystals of the OA – lutidine complexes presented here have consequently been grown using stoichiometric (1 : 2) ratios of OA and the corresponding lutidines – by slow isothermal evaporation of the solvent. The range of suitable solvents is limited in this case since OA is soluble only in polar and the lutidines only in reasonably apolar solvents; ethanol appeared to be the obvious compromise in this respect and has been used for the co-crystallisation experiments. The OA – lutidine complexes which formed single crystals suitable for an X-ray structure determination are:

OA–3,5-lutidine ≡ $H_2C_2O_4 \cdot [HC_2O_4]^- [C_2O_4]^{2-} 3[HC_7H_9N]^+$

OA–2,5-lutidine ≡ $H_2C_2O_4 \cdot [C_2O_4]^{2-} 2[HC_7H_9N]^+$

OA–$(3,4\text{-lutidine})_2$–H_2O ≡ $[C_2O_4]^{2-} 2[HC_7H_9N]^+ \cdot 2H_2O$

OA–2,3-lutidine ≡ $[HC_2O_4]^- [HC_7H_9N]^+$

Notably, a structure determination of complexes of OA with 2,6- and 2,4-lutidine has not been successful to date. The co-crystallisation experiments of OA with 2,6-lutidine did not yield any precipitate at ambient conditions. After evaporation of the solvent (ethanol) the mixture of OA and the lutidine remained in a liquid state. Storing the solution at 4ºC for several weeks yielded small single crystals of ammonium hydrogenoxalate oxalic acid dihydrate, $[NH_4]^+ [HC_2O_4]^- \cdot H_2C_2O_4 \cdot 2H_2O$, isostructural to that reported in reference [106]. The origin of the ammonia remains unknown (decomposition of the aromatic amine lutidine might be a source). The co-crystallisation experiments of OA with 2,4-lutidine on the other hand yielded large block shaped crystals of which an X-ray dataset was collected. However, the diffraction pattern showed diffuse scattering and a strong intensity fall-off with increasing scattering angle. The lattice parameters were determined to be a = 6.577, b = 16.174, c = 8.752 Å, $\alpha = \beta = \gamma = 90º$, V = 931 Å^3, in a C-centred crystal system. A structure solution was possible in the monoclinic space group C2/c, showing the lutidine disordered on a 2-fold axis and a further disordered unit of unknown identity (presumably OA).

The asymmetric units of the OA – lutidine complexes for which the structure determination (all at 100 K) was successful are shown in Figure 5-22 represented in terms of the ADPs. The parameters of the strong or moderately strong HBs present in these materials are given in Table 5-6. For these HBs the H parameters have been refined during the structure determination. Those of the H atoms belonging to the lutidine molecules have been fixed using the riding model since not all structures presented here have been of sufficient quality to allow a free refinement resulting in reasonable H parameters, in particular for the methyl groups.

OA–3,5-lutidine

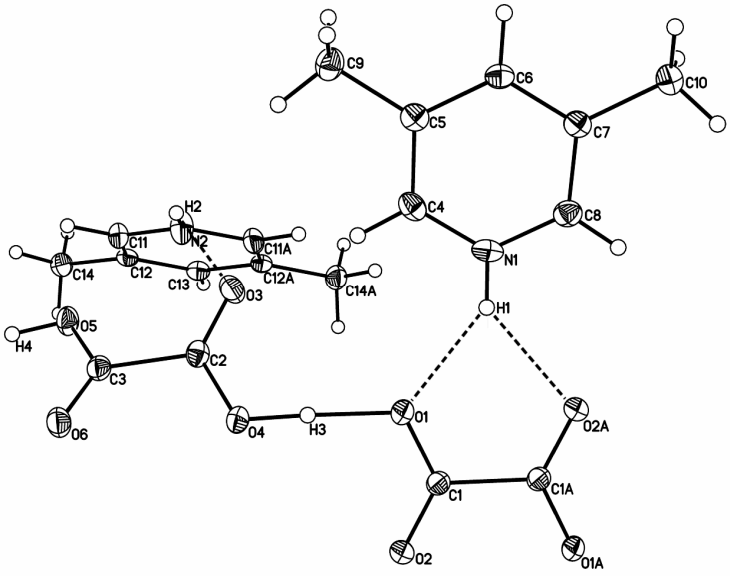

OA–2,5-lutidine

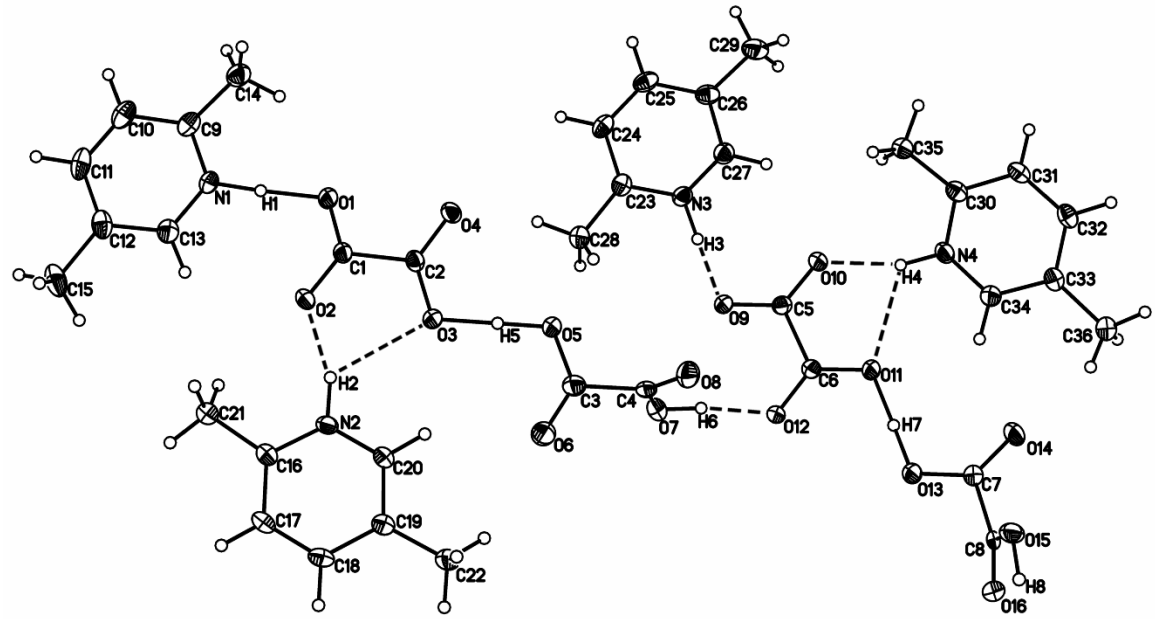

OA–3,4-lutidine–H_2O

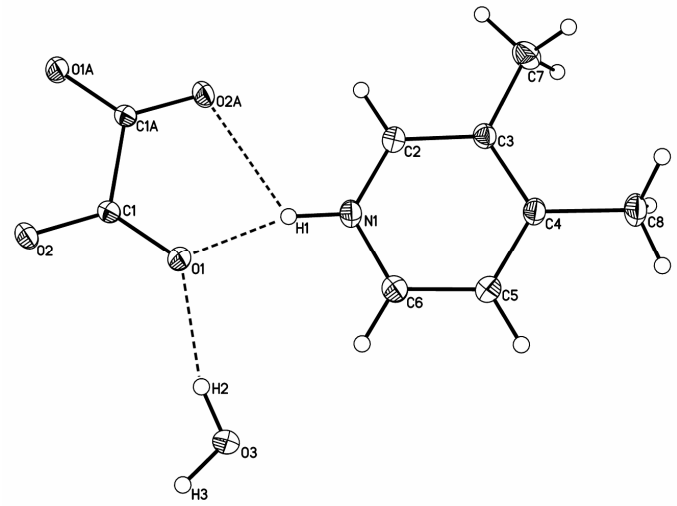

OA–2,3-lutidine

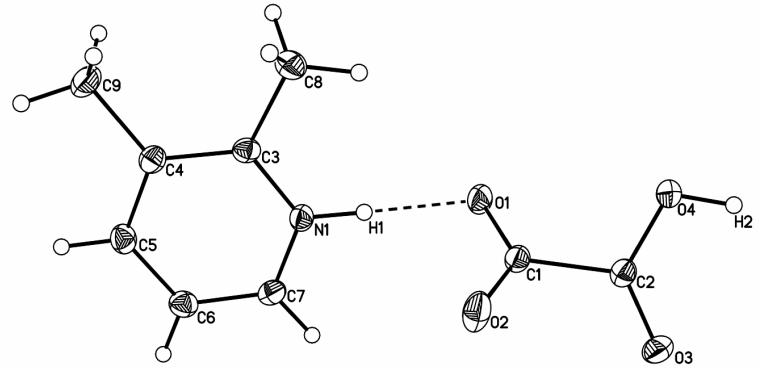

Figure 5-22: Asymmetric units of the OA – lutidine complexes, molecules situated on symmetry elements have been completed for clarity; for details see Figure 5-1.

OA – 3,5-Lutidine

OA and 3,5-lutidine ($\Delta pK_{a1,2}$ = 4.95, 1.95) co-crystallise in crystals with the shape of long plates (space group C2/c) and form a 1 : 1 complex which in view of the varying OA protonation states is more accurately formulated as a 3 : 3 complex, $H_2C_2O_4 \cdot [HC_2O_4]^- [C_2O_4]^{2-}$ $3[HC_7H_9N]^+$. The X-ray structure determined from this material is of moderate quality and refines to R_1 = 3.98 % and 6.24 % for the observed ($F_{obs} > 4\sigma(F_{obs})$) and all data respectively, to a resolution of $\sin\theta/\lambda$ = 0.64 Å^{-1}.

The structure of OA–3,5-lutidine is hard to visualise and is best described by breaking down the complete structure into two "building blocks": a 1 : 2 unit of OA–(3,5-lutidine)$_2$, $[C_2O_4]^{2-}$ $2[HC_7H_9N]^+$; and a 2 : 1 unit of OA_2–3,5-lutidine, $H_2C_2O_4 \cdot [HC_2O_4]^- [HC_7H_9N]^+$. Figure 5-23 shows the packing scheme containing two of these building blocks. From the difference Fourier map in Figure 5-24, left, it becomes evident that the OA molecule in the 1 : 2 unit (situated on an inversion centre) has both its H atoms transferred to two (symmetry equivalent) molecules of 3,5-lutidine to which it hydrogen bonds in a bifurcated manner (see also Figure 5-23). The two bifurcated HBs, N1–H1···O1 and N1–H1···O2, are nearly symmetrical and, as typical of such HBs, of only moderate strength with D = 2.800(2) and 2.829(2) Å respectively. The 1 : 2 unit (when isolated from the complete structure) constitutes the desired 1 : 2 adduct OA–(3,5-lutidine)$_2$, but, as opposed to what was hoped for, complete H transfer has taken place and no SSHB is formed. In any case,

the 1 : 2 units are linked to the 2 : 1 units via O–H···O HBs formed between oxalic acid and the oxalate anion thereby generating infinite chains of hydrogen bonded OA units. The O4–H3···O1 HB linking the two units is moderately strong (D = 2.527(2) Å); whether it constitutes a SSHB is difficult to evaluate based on this distance. In support of its strength, the H3 density shows a significant polarisation towards the HB acceptor (Figure 5-24, left). The 2 : 1 unit itself is comprised of two hydrogen bonded OA molecules – which are related by an inversion centre – and a molecule of 3,5-lutidine. The presence of the inversion centre leads to disordered or a centred H atom (Figure 5-24, right) in the strongest HB found in this material, O5–H4···O5A (D = 2.475(2) Å) and a mixture of $H_2C_2O_4$ and $[HC_2O_4]^-$. One oxalic acid H atom is transferred to the lutidine under formation of a comparably weak N2–H2···O3 HB (D = 2.894(2) Å), completing the 2 : 1 unit to $H_2C_2O_4 \cdot [HC_2O_4]^- [HC_7H_9N]^+$. Since the lutidine is situated on a 2-fold axis, it hydrogen bonds to two OA molecules and thereby links the present OA chains into a 2-dimensional arrangement. The HBs formed by the lutidine in this 2 : 1 unit are distinctive in that they are weak and show a very low directionality (∠N2–H2–O3 = 123°) where the HB acceptor O3 is significantly displaced from the pyridine plane (see Figure 5-22 and also Figure 5-23), opposing the expectation for hydrogen bonding between such strong HB donors and HB acceptors. It appears in this case that the lutidine merely acts a space filler. In this context is it worthy to note, that this material is the only OA – lutidine complex which does not exhibit any π–π stacking between the lutidine molecules.

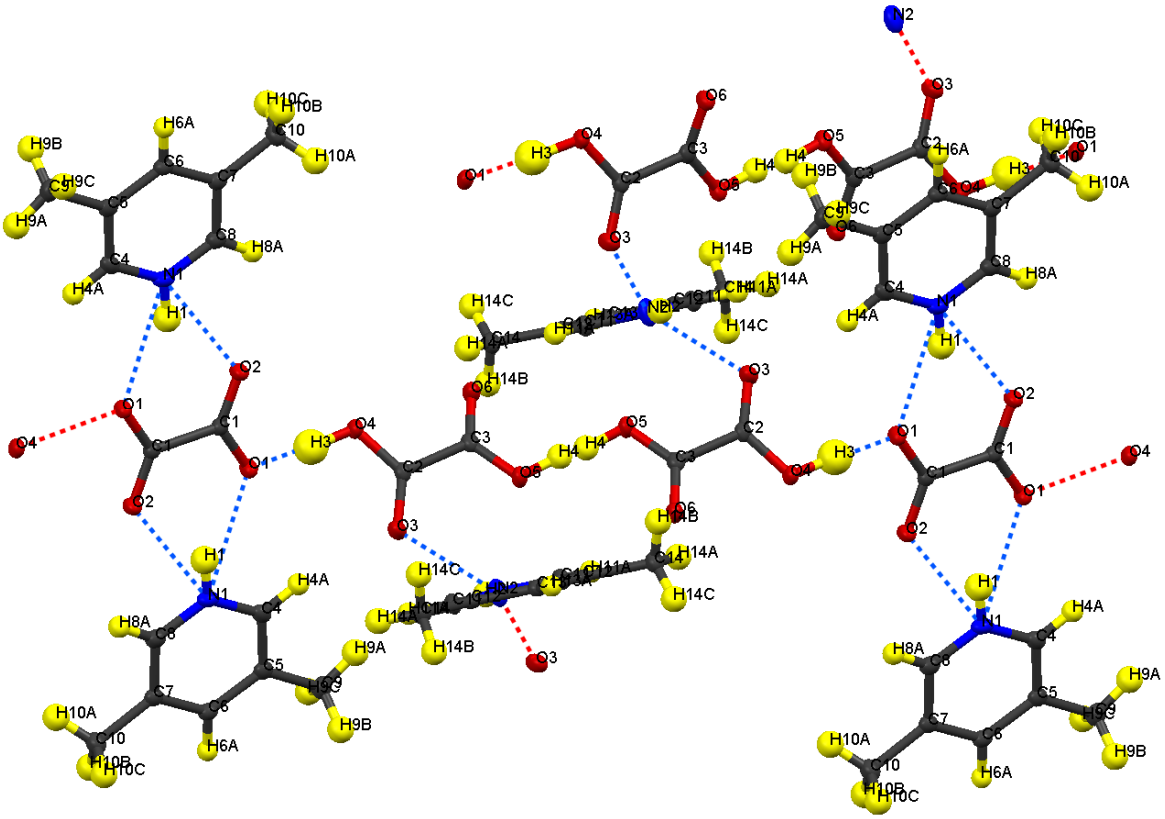

Figure 5-23: Packing scheme of OA–3,5-lutidine. Two 1 : 2 units OA–3,5-lutidine (left and right) and two 2 : 1 units (centre and top) are shown.

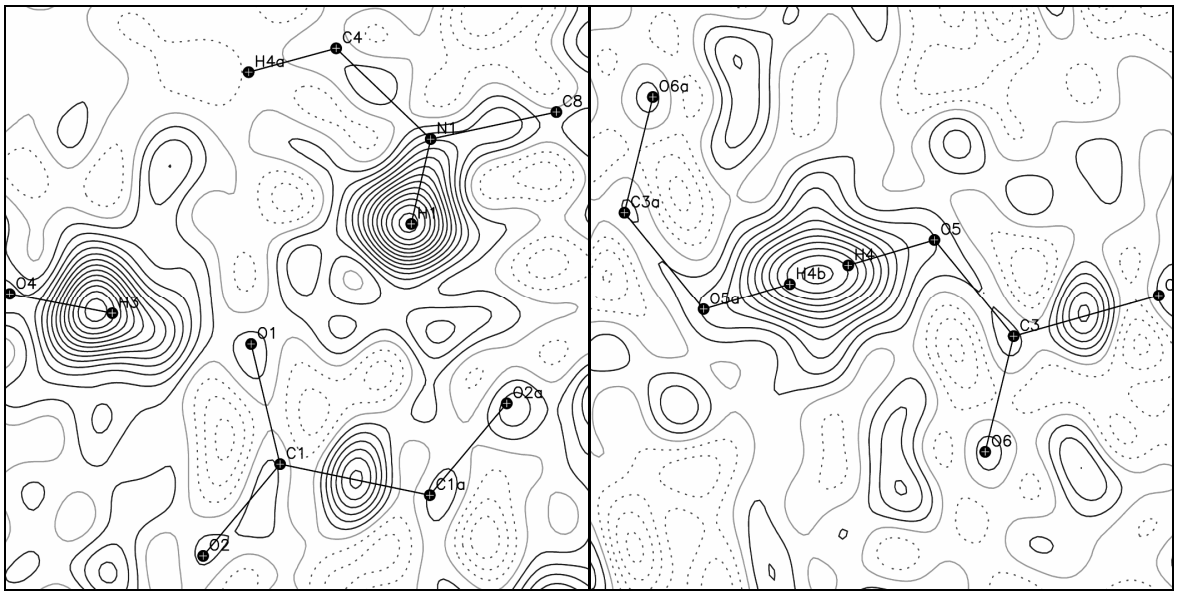

Figure 5-24: Difference Fourier maps in the planes of the HBs in OA–3,5-lutidine, O1–N1–O2A plane (left) and C3–O5–O5A plane (right); $\sin\theta/\lambda < 0.64$ Å^{-1}, for details see Figure 5-5.

OA – 2,5-Lutidine

OA–2,5-lutidine ($\Delta pK_{a1,2}$ = 5.20, 2.20) crystallises with a plate shaped morphology in the space group $P\bar{1}$. As for OA–3,5-lutidine the X-ray structure is of moderate quality and refines to R_1 = 4.43 % and 7.92 % for the observed and all data respectively, to $\sin\theta/\lambda$ = 0.64 Å^{-1}. The complex also constitutes a formal 1 : 1 adduct, but considering the different protonation states of the oxalic acid, it is more accurately formulated as a 2 : 2 complex of $H_2C_2O_4 \cdot [C_2O_4]^{2-}$ $2[HC_7H_9N]^+$ of which two formula units are located in the asymmetric unit (Figure 5-22), rendering Z' = 2.

Two of the four independent OA molecules in the structure are doubly deprotonated, having transferred both H atoms to lutidine molecules. Each $[C_2O_4]^{2-}$ anion thus formed hydrogen bonds to two 2,5-lutidinium cations – to one in a strong manner and to one in a weaker, semi-bifurcated manner. The $[C_2O_4]^{2-}$ $2[HC_7H_9N]^+$ moieties are interlinked by the two remaining oxalic acid molecules present in the structure, which (formally, see below) still exist in molecular form. The extended hydrogen bonded structure thus generated (shown in Figure 5-25) is characterised by chains of alternating $H_2C_2O_4$ and $[C_2O_4]^{2-}$ units to which the lutidines are hydrogen bonded.

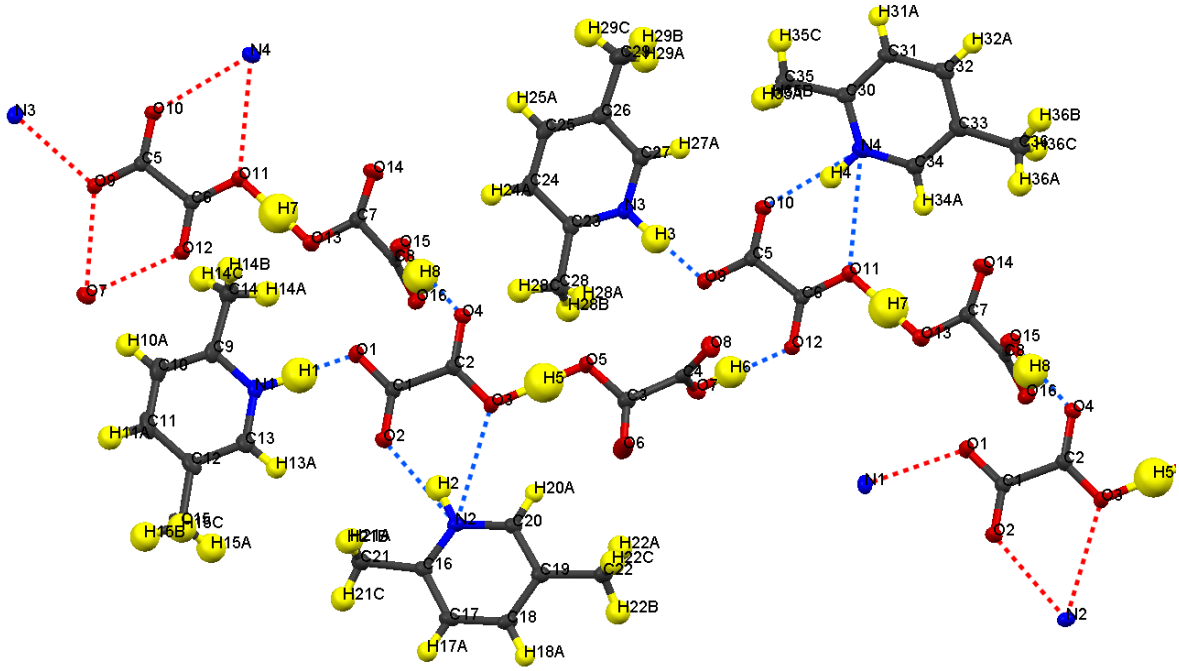

Figure 5-25: Packing scheme of OA–2,5-lutidine showing hydrogen bonded chains of OA units.

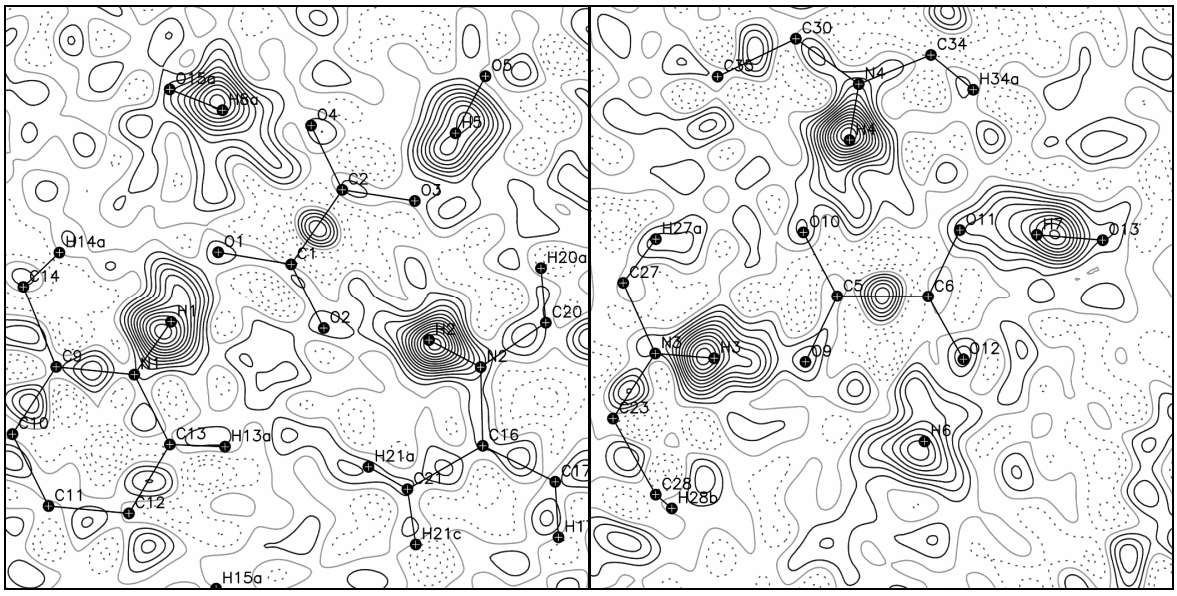

Figure 5-26: Difference Fourier maps in the planes of the two independent $[C_2O_4]^{2-}$ anions in OA–2,5-lutidine showing the four HBs formed by each oxalate anion; $\sin\theta/\lambda < 0.64$ Å^{-1}, for details see Figure 5-5.

Figure 5-26 shows the difference Fourier maps through the planes of the two independent $[C_2O_4]^{2-}$ anions for which the hydrogen bonding schemes are essentially the same and differ only in small variations in HB lengths. Each $[C_2O_4]^{2-}$ anion is the acceptor of two SSHBs and two moderate strength HBs. One SSHB is formed between $[C_2O_4]^{2-}$ and a lutidine in each case for which the heteroatom distances in the N1–H1···O1 and N3–H3···O9 HBs refine to D = 2.549(2) and D = 2.582(2) Å respectively. The second SSHB is of the homonuclear O–H···O type and formed between the second carboxylate group of $[C_2O_4]^{2-}$ and a neutral oxalic acid molecule in each case. The corresponding O5···O3 and O13···O11 distances refine to 2.456(2) and 2.463(2) Å respectively. These N–H···O as

well as O–H···O SSHBs are the strongest HBs observed in the family of OA – lutidine complexes, which manifests in the strong polarisation of the H densities towards the acceptor O atoms (see Figure 5-26). In case of the O5–H5···O3 SSHB the electron density for the H atom is particularly strongly delocalised between the donor and acceptor atoms, indicating H disorder. However, the C–O bond lengths of C3–O5 = 1.290(2) and C3–O6 = 1.206(2) Å in the (neutral) oxalic acid molecule, and of C2–O3 = 1.267(2) and C2–O4 = 1.243(2) Å in the oxalate anion, allow a confident differentiation as a carboxylic acid and a carboxylate group respectively. From the conclusion of the previous work on the system IN_2–OA (Chapter 3 *Molecular Complexes of Isonicotinamide with Oxalic Acid*), these heavy atom parameters in combination with the observation of the high electron density delocalisation suggest a well localised H nucleus which is considerably shifted towards the centre of the SSHB, rather than H disorder. In case of the O13–H7···O11 SSHB, with comparable heavy atom parameters, there is no evidence for a strong electron delocalisation. As mentioned previously, each $[C_2O_4]^{2-}$ anion accepts two additional moderate HBs. The carboxylate groups which are already hydrogen bonded to the lutidines upon formation of the N–H···O SSHBs, form additional moderate strength N–H···O HBs towards a second lutidine molecule. In this case, the HBs are asymmetrically bifurcated, with the shorter interactions N2–H2···O2 and N4–H4···O10 having heteroatom distances of D = 2.762(2) and D = 2.704(2) Å respectively. It is again the second carboxylate groups which hydrogen bond to the neutral oxalic acid molecules with O15···O4 and O7···O12 distances of 2.573(2) and 2.550(2) Å respectively. These HBs, being merely 0.1 Å longer than the corresponding O–H···O SSHBs, are still comparably strong even if they cannot be classified as SSHBs. Overall, the hydrogen bonding emerges particularly strongly in this material, not to mention the abundance of weak C–H···O interactions.

The structural complexity of this complex is further enhanced by the presence of π–π interactions. This becomes apparent when the molecules which constitute the asymmetric unit are presented in an alternative arrangement to that in Figure 5-22. Figure 5-27, showing the asymmetric unit in an orientation perpendicular to the planes spanned by the hydrogen bonded chains of OA and the pendant lutidines (as presented in Figure 5-22 and Figure 5-25), points to the nature of π–π stacking in which all four independent lutidine units are involved before the stacking becomes interrupted by the OA chains.

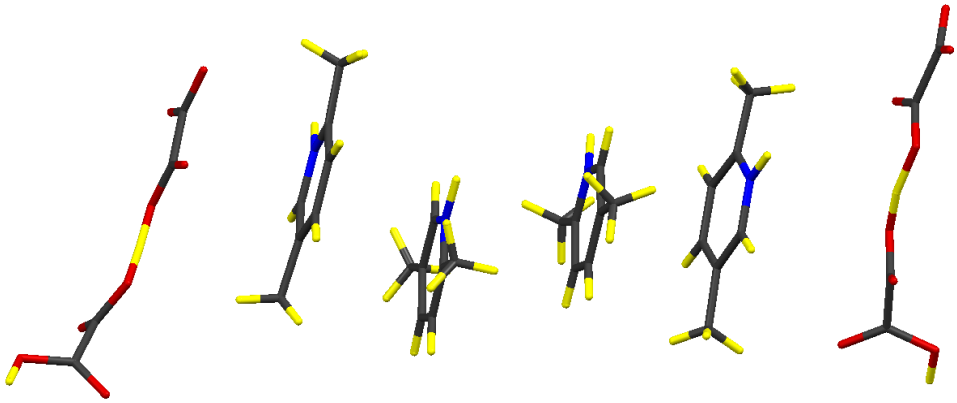

Figure 5-27: Alternate presentation of the asymmetric unit OA–2,5-lutidine showing π–π stacking.

OA – (3,4-Lutidine)$_2$ – H_2O

The structure of OA–(3,4-lutidine)$_2$–H_2O ($\Delta pK_{a1,2}$ = 5.26, 2.26) reported here is hydrated, containing two co-crystallising water molecules. Replacing oxalic acid dihydrate used in the original experiment by water free oxalic acid yielded crystals of the same composition – OA and 3,4-lutidine abstract water from the ethanol from which the present structure was crystallised. OA–(3,4-lutidine)$_2$–H_2O crystallises in block shaped crystals (space group $P\bar{1}$) of which a good quality X-ray dataset was measured at 100 K to a resolution of $\sin\theta/\lambda$ = 0.78 Å^{-1}. The X-ray structure was subsequently refined to R_1 = 4.41 % for all data.

OA–(3,4-lutidine)$_2$–H_2O is the only structure in this system that crystallises as a 1 : 2 complex of OA and lutidine. Both oxalic acid H atoms are transferred to the two molecules of 3,4-lutidine to which OA hydrogen bonds in a bifurcated manner – the OA unit is situated on an inversion centre, rendering the two bifurcated HBs symmetry equivalent. The hydrogen bonded motif of the ionic complex $[C_2O_4]^{2-}$ 2$[HC_7H_9N]^+$ thus formed is similar to that observed previously in OA–3,5-lutidine, although the bifurcated HB is less symmetrical with corresponding heteroatom distances of N1···O1 = 2.648(1) Å and N1···O2 = 2.968(1) Å. The OA–(3,4-lutidine)$_2$ moieties are interlinked by the two water molecules and form extended hydrogen bonded tapes as shown in Figure 5-28. These tapes stack as expected upon each other, resulting in π–π interactions between the pyridine rings and some weak C–H···O interactions between the lutidine methyl and carboxylate groups. Figure 5-29 shows the difference Fourier map in the plane of the bifurcated HB. Besides the localisation of the H atom, the high quality of the X-ray datas*et al*lows a visualisation of the deformation density showing charge accumulations on all covalent bonds and also in the lone pair regions of the oxalic acid O atoms.

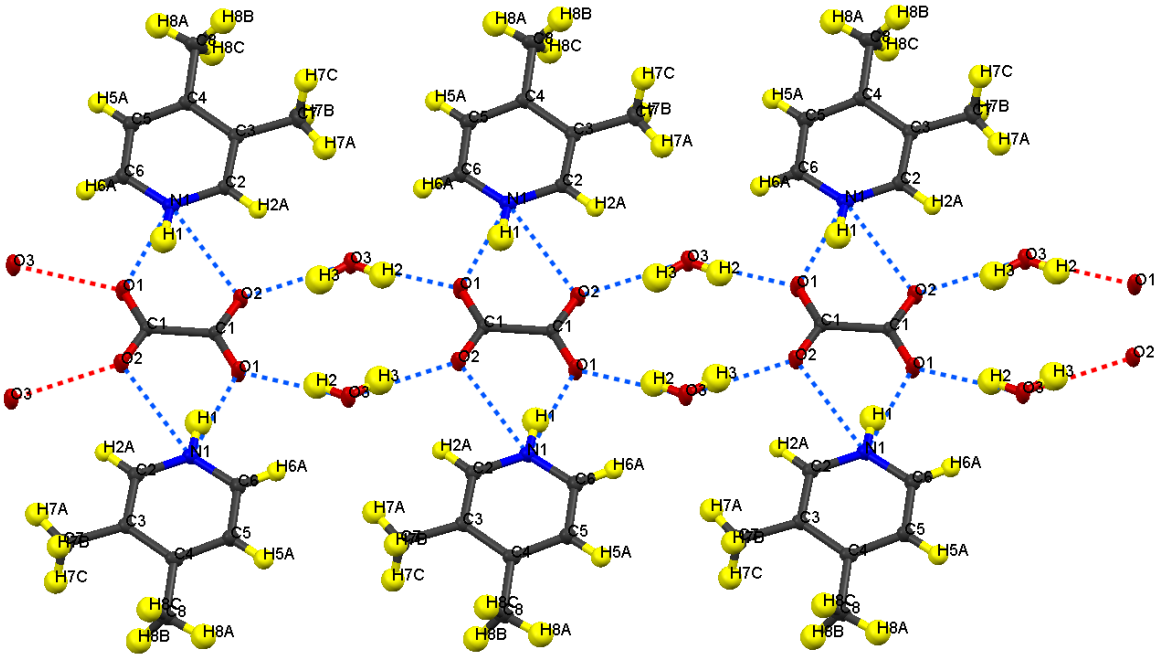

Figure 5-28: Extended hydrogen bonded structure in OA–(3,4-lutidine)$_2$–H_2O.

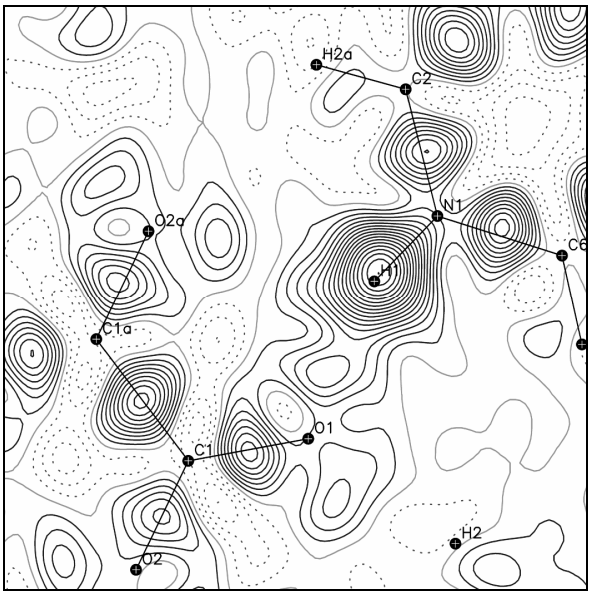

Figure 5-29: Difference Fourier map in the O1–N1–O2A plane in OA–(3,4-lutidine)$_2$–H_2O; $\sin\theta/\lambda < 0.78$ Å^{-1}, for details see Figure 5-5.

OA – 2,3-Lutidine

OA–2,3-lutidine ($\Delta pK_{a1,2}$ = 5.37, 2.37) is from the crystallographic point of view the most basic structure of all OA – lutidine complexes. The asymmetric unit contains one molecule of hydrogenoxalate and one molecule of 2,3-lutidinium. OA–2,3-lutidine can consequently be formulated as a 1 : 1 complex, $[HC_2O_4]^-$ $[HC_7H_9N]^+$. It crystallises in plates in the monoclinic space group C2/c; the X-ray structure determined at 100 K refines to R_1 = 4.81 % for all data to $\sin\theta/\lambda$ = 0.70 Å^{-1}. As in all previous OA – lutidine complexes, a H transfer reaction from OA to the lutidine is observed. The resulting N–H···O HB is of moderate strength with an N1···O1 distance of 2.662(1) Å; so is the O4–H2···O2 HB (D = 2.565(1) Å) which links the $[HC_2O_4]^-$ anions into hydrogen bonded zigzag chains of OA units with pendant lutidinium cations, as shown in Figure 5-30. Also shown in Figure 5-30 is the fact that the lutidines intercalate with lutidines of neighbouring chains to give perfect π–π stacking of parallel (by inversion) pyridine rings which are separated by 3.493 Å. The difference Fourier maps imaging the H densities are shown for completeness in Figure 5-31.

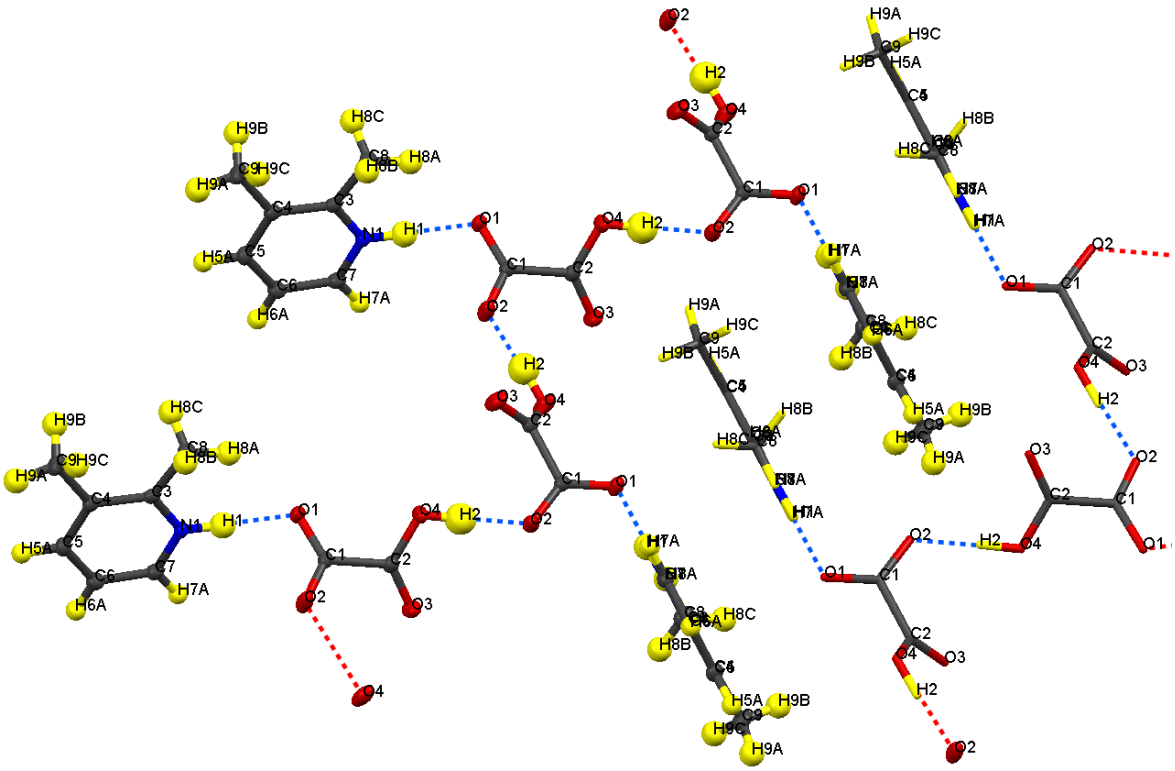

Figure 5-30: Packing scheme of OA–2,3-lutidine showing one extended chain of $[HC_2O_4]^-$ $[HC_7H_9N]^+$ (ellipsoid representation) and the intercalation of the lutidines with a second chain (stick representation).

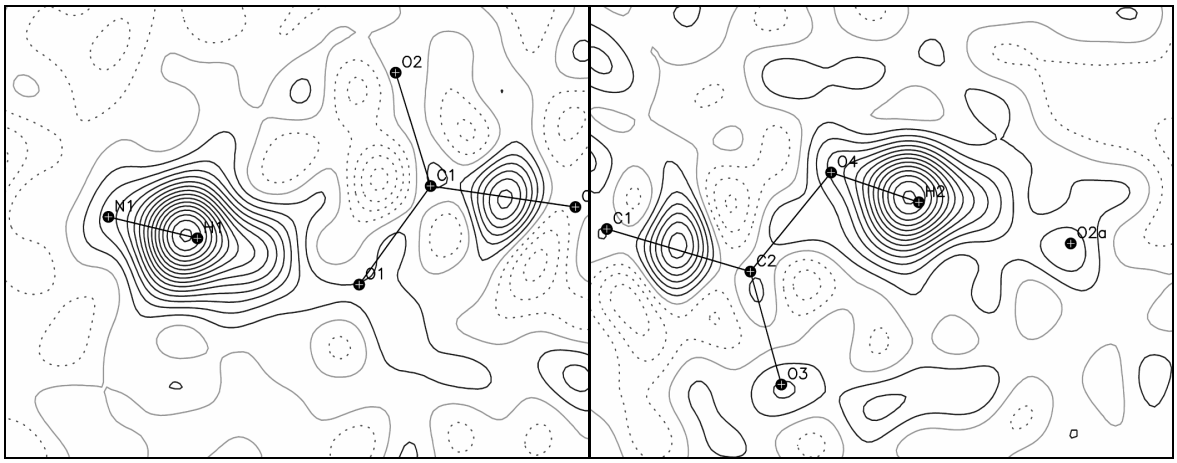

Figure 5-31: Difference Fourier maps in the planes of the HBs in OA–2,3-lutidine, C1–O1–N1 plane (left) and C2–O4–O2A plane (right); $\sin\theta/\lambda < 0.70$ Å^{-1}, for details see Figure 5-5.

Table 5-6: HB parameters for the OA – lutidine complexes.

	HB	D–H / Å	H···A / Å	D···A / Å	∠DHA / °
OA–3,5-lutidine	N1–H1···O1	0.90(2)	2.06(2)	2.8000(17)	139.1(17)
	N1–H1···O2*	0.90(2)	2.10(2)	2.8290(18)	138.0(16)
	N2–H2···O3	0.82(3)	2.364(16)	2.894(2)	122.7(6)
	N2–H2···O3*	0.82(3)	2.364(16)	2.894(2)	122.7(6)
	O4–H3···O1	1.07(2)	1.46(2)	2.5272(15)	176(2)
	O5–H4···O5*	0.93(4)	1.56(4)	2.475(2)	171(5)
OA–2,5-lutidine	N1–H1···O1	1.11(3)	1.45(3)	2.5494(19)	174(3)
	N2–H2···O2	1.00(2)	1.81(2)	2.7615(19)	159(2)
	N2–H2···O3	1.00(2)	2.41(2)	3.071(2)	123.3(16)
	N3–H3···O9	1.02(2)	1.57(2)	2.5822(19)	177(2)
	N4–H4···O10	0.97(2)	1.76(2)	2.704(2)	162.1(18)
	N4–H4···O11	0.97(2)	2.44(2)	3.035(2)	119.7(15)
	O5–H5···O3	1.12(3)	1.35(3)	2.4559(18)	168(3)
	O7–H6···O12	0.94(3)	1.61(3)	2.5498(18)	173(3)
	O13–H7···O11	1.14(3)	1.32(3)	2.4633(17)	177(3)
	O15–H8···O4*	1.00(3)	1.59(3)	2.5725(17)	169(3)
OA–(3,4-lutidine)$_2$–H_2O	N1–H1···O1	0.933(15)	1.759(15)	2.6480(9)	158.3(14)
	N1–H1···O2*	0.933(15)	2.373(15)	2.9678(9)	121.4(12)
	O3W–H2···O1	0.885(15)	1.910(15)	2.7756(8)	165.5(13)
	O3W–H3···O2*	0.878(17)	1.920(17)	2.7728(8)	163.2(15)
OA–2,3-lutidine	N1–H1···O1	0.938(19)	1.72(2)	2.6619(14)	177.3(19)
	O4–H2···O2*	0.95(2)	1.61(2)	2.5648(14)	173.7(19)

* Atoms generated by symmetry.

In summary of the OA – lutidine materials studied, only the hydrated structure of OA–(3,4-lutidine)$_2$–H_2O forms a complex with the desired 1 : 2 stoichiometry OA : lutidine, which in this case is accompanied by complete H transfer from OA to the lutidines. The structures of OA–3,5-lutidine, OA–2,5-lutidine and OA–2,3-lutidine on the other hand, form 1 : 1 adducts of OA and lutidine. However, due to the different protonation states adopted by OA, OA–3,5-lutidine might be better described as a 3 : 3, and OA–2,5-lutidine as a 2 : 2 complex; in average each OA molecule transfers one H to a lutidine molecule in these 1 : 1 complexes. In all OA – lutidine materials the lutidines are present in the protonated form. Strong N–H···O HBs are found only in OA–2,5-lutidine; all other HBs of this type are moderate in strength, and in cases weak and bifurcated. Aside from the N–H···O HBs, all OA units are involved in further hydrogen bonding to other OA units, or in case of the hydrated structure, OA–(3,4-lutidine)$_2$–H_2O, to the co-crystallising water molecules. Strong HBs of the type O–H(acid)···$^-$OOC are found in OA–3,5-lutidine and in particular in OA–2,5-lutidine where a pronounced electron delocalisation is observed.

5.2.2. Fumaric Acid – Dimethylpyridine Complexes

In the search for strong intermolecular hydrogen bonds, so far PCP and OA have been used as co-crystallisation partners – and HB donors – for the lutidines. While the use of PCP leads to the desired formation of SSHBs which show a ΔpK_a dependent H transfer, the use of OA always results in H transfer upon formation of mostly moderately strong N–H···O HBs. Compared with OA ($pK_{a1,2}$ = 1.2, 4.2), fumaric acid (FA, $pK_{a1,2}$ = 3.03, 4.44) appears to be a more promising H donor because in this case the ΔpK_a range for the first deprotonation step (ΔpK_a = 3.12 – 3.96) is in better pK_a matching distance, which, as we know, is the condition for the formation of SSHBs. The ΔpK_a for the second deprotonation step ranges from 1.71 to 2.55. From the crystal engineering point of view, the target materials are 1 : 2 complexes of FA and lutidine, where FA hydrogen bonds (preferably in a strong manner) to two molecules of lutidine. The co-crystallisation experiments were consequently performed using stoichiometric 1 : 2 ratios of FA and the lutidines. The crystals were grown, as usual, by slow evaporation of the solvent, ethanol or *iso*-propanol in this case. During the experimental work a similar study was published by Haynes, Jones and Motherwell, which investigated the formation of co-crystals and salts[a] by co-crystallising succinic acid and fumaric acid with the series of lutidines.[107] The study was comprehensive but did not analyse the occurrence of strong hydrogen bonding as such. Therefore, the FA – lutidine complexes found during the current experimental work will be presented at this point only with respect to the strong HBs (if present), unless they have not been observed previously in reference [107]. The old and new FA – lutidine complexes are:

FA–(3,5-lutidine)$_2$ ≡ $H_2C_4H_2O_4 \cdot (C_7H_9N)_2$ [107]

FA–(3,4-lutidine)$_2$ ≡ $H_2C_4H_2O_4 \cdot (C_7H_9N)_2$

FA–(2,3-lutidine)$_2$ ≡ $H_2C_4H_2O_4 \cdot (C_7H_9N)_2$ [107]

FA–2,4-lutidine–H_2O ≡ $[HC_4H_2O_4]^- [HC_7H_9N]^+ \cdot H_2O$

The H atoms have been treated during the structure refinements in a manner analogous to that used for the previous PCP and OA – lutidine complexes, i.e. the parameters for the H atoms involved in strong or moderate hydrogen bonding were refined while those for the other H atoms were fixed using the riding model. The parameters for the HBs formed between FA and the lutidines are listed in Table 5-7.

FA – (3,5-Lutidine)$_2$

The original structure of the molecular complex FA–(3,5-lutidine)$_2$ ($\Delta pK_{a1,2}$ = 3.12, 1.71) was determined at 180 K by Haynes *et al*.[107] FA and 3,5-lutidine co-crystallise as the trimeric 1 : 2 adduct envisaged, and SSHBs are formed between both FA carboxylic acid groups and the lutidine bases. Half the formula unit, $H_2C_4H_2O_4 \cdot (C_7H_9N)_2$, is crystallographically independent (FA is situated on an inversion centre) rendering the two

[a] The term "co-crystal" (with or without hyphen) is not used uniformly. Some authors, like in this case Haynes *et al*, define a co-crystal as a multi-component solid state adduct composed of neutral molecules and distinguish ionic adducts as salts. This is neither wrong nor inferior to the definition used in this work where "co-crystal" refers to both neutral and charged multi component adducts – with the advantage that conveniently also partially charged adducts are included, as observed, for example, in materials with centred intermolecular HBs.

SSHBs symmetry equivalent. The SSHB, with an O···N heteroatom distance of 2.542(1) Å at 180 K, is the shortest O–H(acid)···N(pyridine) type HB observed to date in all FA – lutidine complexes. For the purpose of investigating the electronic structure in the SSHB, X-ray structures of this molecular complex have been redetermined at 100 K and at room temperature. Growing crystals of FA–(3,5-lutidine)$_2$ proved to be difficult. FA and 3,5-lutidine dissolved in ethanol or methanol react at ambient conditions to form N-succino-3,5-dimethylpyridine (electrophilic addition to unsaturated C=C bonds, discussed briefly later). Using a less polar solvent to inhibit this reaction, *iso*-propanol in this case, yielded both the addition product and the desired co-crystal of FA–(3,5-lutidine)$_2$ crystallising with plate shaped morphology in the space group $P2_1/c$.[a] The crystals thus obtained were small, weakly diffracting, and unfortunately yielded only datasets of limited quality to $\sin\theta/\lambda$ = 0.64 Å^{-1}. The 100 K structure refined to R_1 = 4.43 % and 7.67 %, and the RT structure refined to R_1 = 4.70 % and 9.57 % for the observed ($F_{obs} > 4\sigma(F_{obs})$) and all data respectively.

The ellipsoid plots of the FA–(3,5-lutidine)$_2$ trimers are shown in Figure 5-32. The trimeric units are only weakly embedded in the 3-dimensional crystalline environment through weak C–H···O and π–π interactions; in the low T structure the shortest H···O contact is 2.57 Å and the distance between the pyridine planes is 3.41 Å. In consequence, the atomic displacements are high, and naturally more pronounced in the RT structure (see Figure 5-32).

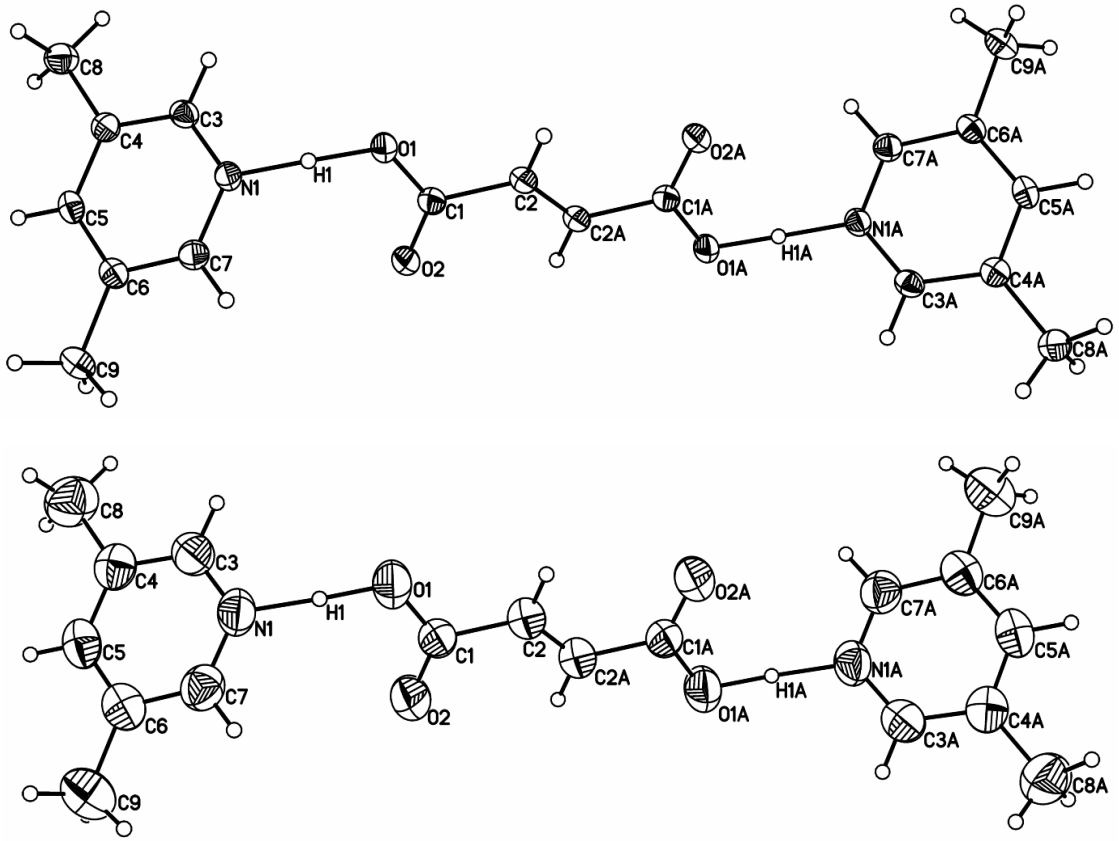

Figure 5-32: Ellipsoid plots of FA–(3,5-lutidine)$_2$, (top) 100 K structure, (bottom) RT structure; for details see Figure 5-1.

[a] The original recipe, cooling a concentrated solution of FA in 3,5-lutidine, was not pursued at this point.

The strong character of the O–H···N HB has been reproduced in both the low and high T structures. The heteroatom distances in the O1–H1···N1 SSHB refine to D = 2.534(2) Å at 100 K and to D = 2.563(2) Å at RT, showing as expected, the shortening and lengthening of this intermolecular contact respectively upon reducing and increasing the temperature in relation to that of the original structure where an intermediate heteroatom distance of D = 2.542(1) Å was found at 180 K. The covalent O1–H1 bond lengths refine to 1.21(3) at 100 K and 1.19(4) Å at RT, pointing out again the elongation of these bonds upon formation of SSHBs. Although the quality of the current X-ray datasets does not justify a detailed interpretation from refined H parameters, the positional parameters appear to be reasonable in this case and coincide well with the density maxima shown in the difference Fourier maps (Figure 5-33). The maps reveal electron density features at a similar level of detail as is observed in the low resolution maps ($\sin\theta/\lambda \sim 0.6$ Å^{-1}) generated for the molecular complexes of IN_2–OA (see Chapter 4.1, Figure 4-1 and Figure 4-2). In other words, not great deal of detail is observed. On the other hand, the electron density distribution in the current SSHB exhibits features similar to these maps which correspond to H atoms occupying substantially centred positions in the SSHB. To conclude, there is strong evidence for a short, strong, centred HB in FA–(3,5-lutidine)$_2$. It belongs, with an O···N distance of 2.534(2) Å, to the shortest O··H··N HBs observed to date and is likely to show interesting features regarding the electronic structure. In the end, a high resolution X-ray diffraction experiment is desirable – preferably in combination with a (variable T) neutron single crystal diffraction study.

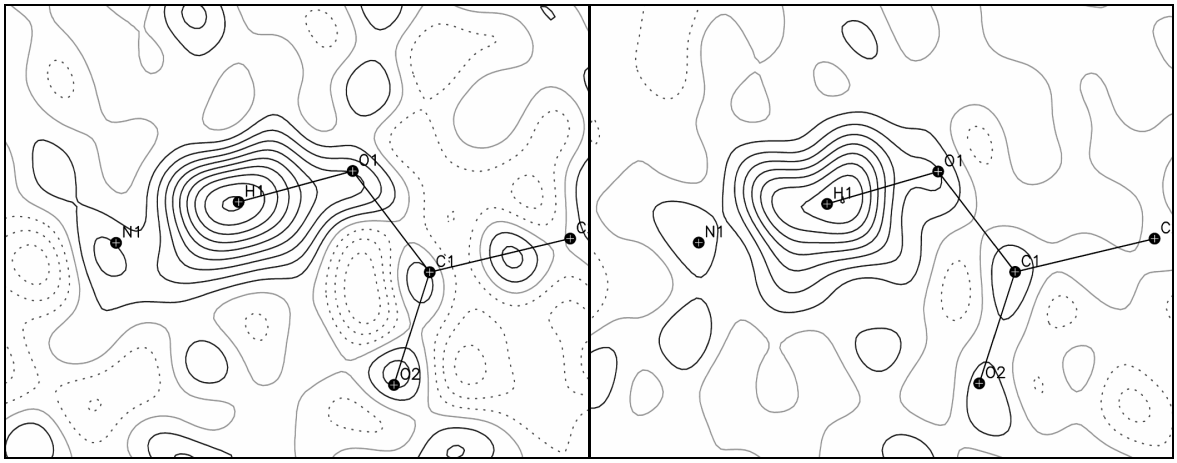

Figure 5-33: Difference Fourier maps for FA–(3,5-lutidine)$_2$ in the C1–O1–N1 plane for the 100 K data (left) and RT (right); $\sin\theta/\lambda < 0.64$ Å^{-1}, for details see Figure 5-5.

FA – (3,4-Lutidine)$_2$

Fumaric acid and 3,4-lutidine ($\Delta pK_{a1,2}$ = 3.43, 2.02) also co-crystallise as the desired 1 : 2 complex, FA–(3,4-lutidine)$_2$. X-ray structures of this complex, crystallising with block shaped morphology in the space group $P2_1/n$, have been determined at 150 K and at room temperature. A structure determination at 100 K was not possible since at a temperature of about 116 K, this material undergoes a sudden and single crystal disrupting (phase) transition. Structure refinement of the low and high T data resulted in R_1 = 5.31 % and 5.81 % for all data to resolutions of $\sin\theta/\lambda$ = 0.78 and 0.70 Å^{-1} respectively.

As in FA–(3,5-lutidine)$_2$, the asymmetric unit of FA–(3,4-lutidine)$_2$ consists of half the formula unit with FA lying on an inversion centre. Strong HBs (consequentially symmetry equivalent) are formed between both FA carboxylic groups and the lutidine N bases. The ellipsoid plots of the complete trimeric 1 : 2 units are shown in Figure 5-34 for both temperature datasets. The trimers can be regarded as isolated units in the 3-dimensional structure since they are interlinked only by weak C–H···O interactions which again manifests in comparably high ADPs, in particular for the RT structure. As a side note, the ADPs are assumed to accurately reflect the external modes (rigid body motion) of the molecules in the crystal as they show the same principal orientations in the low and high T structures, even though two different specimens were used for data collection.

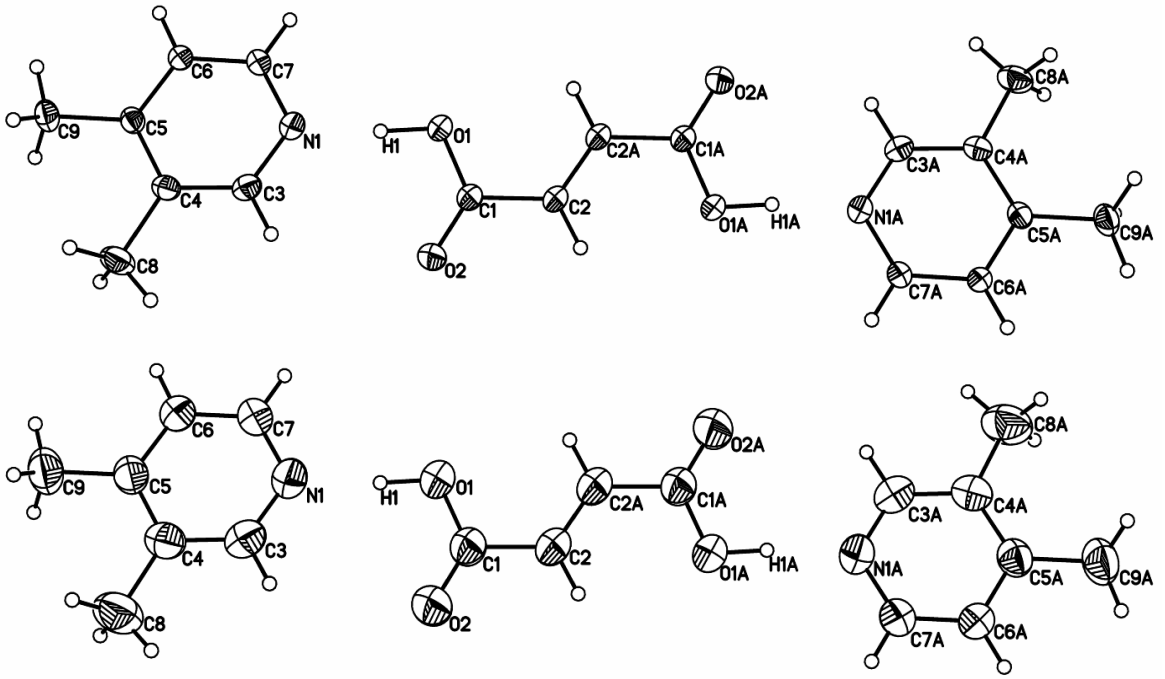

Figure 5-34: Ellipsoid plots of FA–(3,4-lutidine)$_2$, (top) 150 K structure, (bottom) RT structure; for details see Figure 5-1.

The HBs linking FA and the 3,4-lutidines are strong with heteroatom distances for O1···N1 of 2.569(1) and 2.592(1) Å in the low and high T structures respectively. The difference Fourier maps imaging the electron density in these SSHBs are shown in Figure 5-35. They reveal that the H atom in the SSHB O1–H1···N1 is well localised at the O site at both temperatures. The difference Fourier map for the low T data allows a separation of the H1 density from that observed at the N site, which in this case is clearly distinguishable as N lone pair density. The fact that the N lone pairs, when involved in strong hydrogen bonding, are persistently observed to low experimental resolutions is again documented by the lower resolution dataset obtained at RT (Figure 5-35, right). The covalent O–H bond distances show the typical elongation upon the temperature induced reduction of the heteroatom distances, O1···N1. The O1–H1 bond lengths refine to 1.01(2) and 1.03(2) Å at RT and 150 K respectively, and they appear to be accurate in view of the overlay of the refined H positions in the corresponding electron density maps (Figure 5-35). For completion (and later comparison) the heavy atom parameters are mentioned at this point: they refine to 1.311(1), 1.221(1) Å and 118.51(7)º for C1–O1, C1–O2 and C3–N1–C7

respectively (see Table 5-8), and expectedly confirm that this material is a neutral molecular adduct and that no H transfer has occurred.

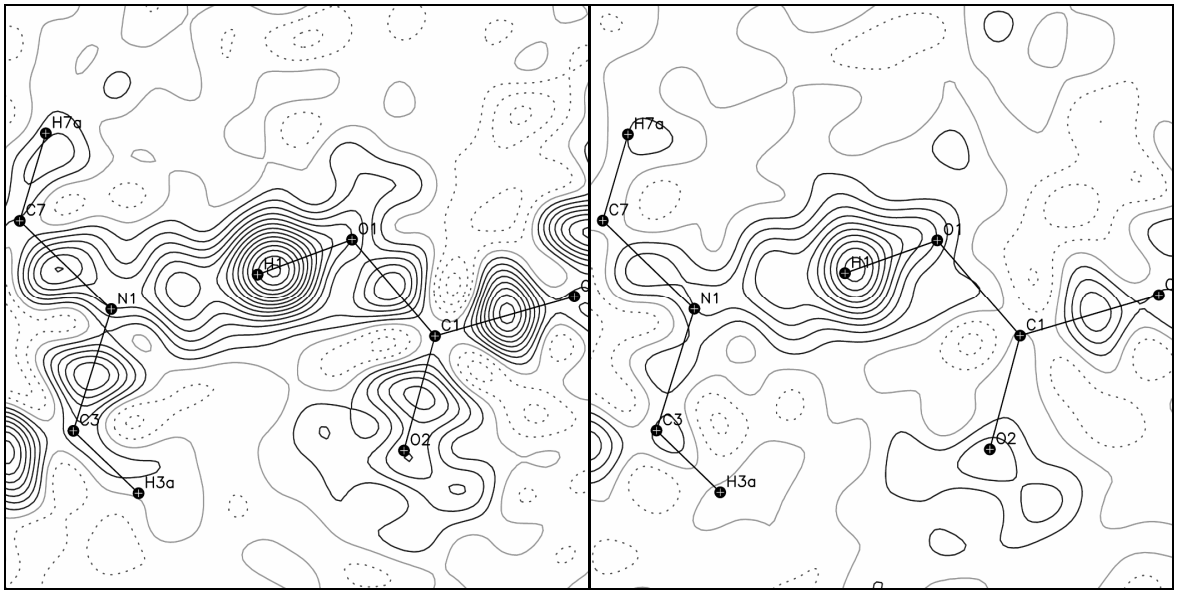

Figure 5-35: Difference Fourier maps for FA–(3,4-lutidine)$_2$ in the C1–O1–N1 plane for the 150 K data (left, $\sin\theta/\lambda < 0.78$ Å^{-1}) and RT (right, $\sin\theta/\lambda < 0.70$ Å^{-1}); for details see Figure 5-5.

FA – (2,3-Lutidine)$_2$

FA–(2,3-lutidine)$_2$ ($\Delta pK_{a1,2}$ = 3.54, 2.13) crystallises as a trimeric complex showing the same hydrogen bonding motif known from FA–(3,5-lutidine)$_2$ and FA–(3,4-lutidine)$_2$. The X-ray structure of this material has previously been published by Haynes *et al* and was determined at a temperature of 180 K.[107] The results from the structure determinations originating from this work, carried out at 100 K and at room temperature, will nevertheless be presented briefly since the hydrogen bonding between FA and the lutidine shows some interesting features. FA–(2,3-lutidine)$_2$ has been obtained from a solution of FA and the lutidine in ethanol and crystallises with stick shaped morphology in the space group $P2_1/n$. The low T dataset was refined to R_1 = 3.90 and 4.71 % for the observed and all data ($\sin\theta/\lambda$ = 0.78 Å^{-1}) respectively; and the high T dataset (obtained from a different sample) to 4.83 % and 7.31 % respectively ($\sin\theta/\lambda$ = 0.70 Å^{-1}).

As in the previous FA – (lutidine)$_2$ complexes, the asymmetric unit of FA–(2,3-lutidine)$_2$ contains half the formula unit (shown in Figure 5-36) with FA lying on an inversion centre, and SSHBs link both FA carboxylic groups with the lutidine bases. The trimeric units of FA–(2,3-lutidine)$_2$ are similarly isolated in the crystal and lack an extended hydrogen bonding network which is again reflected by high ADPs for the RT structure.

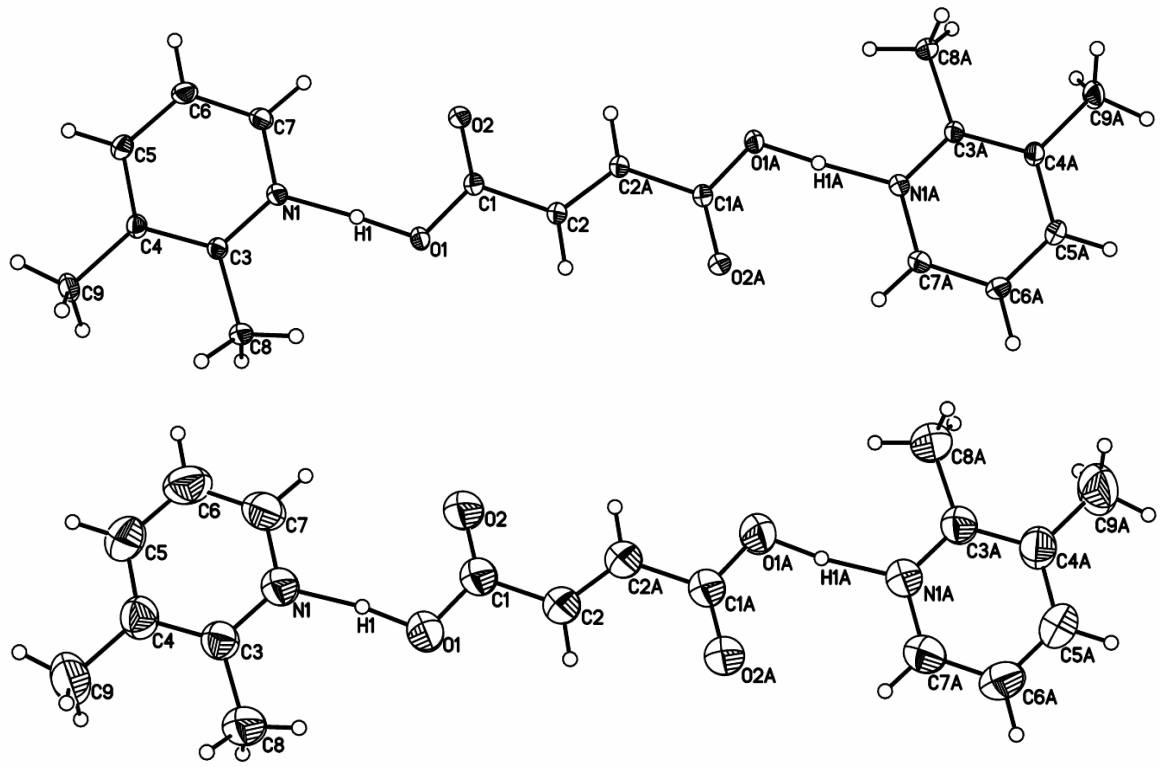

Figure 5-36: Ellipsoid plot of FA–(2,3-lutidine)$_2$, (top) 100 K structure, (bottom) RT structure; for details see Figure 5-1.

The electron densities in the SSHBs (O1–H1···N1) are strongly delocalised at both temperatures (Figure 5-37) and exhibit features familiar to the difference densities observed for the hydrogenous IN$_2$–OA complexes, in particular to that for IN$_2$–OA Form I (compare with Figure 3-4 in Chapter 3). The O1···N1 distances of 2.551(1) and 2.572(1) Å for the 100 K and RT structure respectively, are nearly identical to those found in IN$_2$–OA Form I (2.549(1) and 2.574(1) Å); and also the covalent O1–H1 bond lengths of 1.15(2) Å obtained at both temperatures are comparable to the corresponding bond lengths in IN$_2$–OA (compare the HB parameters in Table 5-7 and Table 3-1). Taking into account all of the above findings we can deduce that the H atom in the SSHB discussed here is not disordered as it might appear in the X-ray difference Fourier maps, but located at the O site. However, the H atom is considerably shifted towards the centre of the SSHB – the shift is likely to be comparable to that in IN$_2$–OA and certainly larger than that observed in FA–(3,4-lutidine)$_2$.[a] These considerations are supported by the heavy atom parameters (Table 5-8) which confirm that a) the carboxylic acid group is still protonated with C1–O1 and C1–O2 distances of 1.309(1) and 1.226(1) Å respectively; and that b) the H1···N1 distance is considerably reduced as the pyridine C3–N1–C7 bond angle of 120.85(6)º is characteristic of an intermediate form between protonated and unprotonated lutidine. For comparison, the CNC bond angles in 2,3-lutidine are 119.44(9)º and 123.57(11)º in the neutral and ionic complexes with PCP and OA respectively.

[a] Educated estimates for FA–(2,3-lutidine)$_2$ and FA–(3,4-lutidine)$_2$ would be O1–H1 = 1.15 and 1.05 Å, respectively.

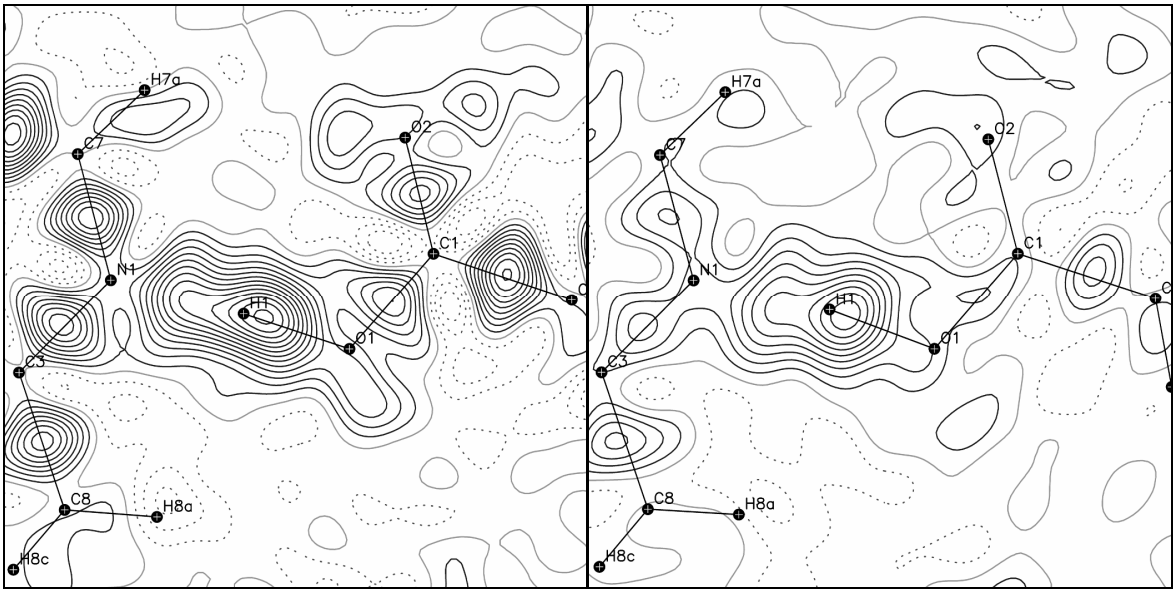

Figure 5-37: Difference Fourier map of FA–(2,3-lutidine)$_2$ in the C1–O1–N1 plane for the 100 K data (left, $\sin\theta/\lambda < 0.78$ Å^{-1}) and RT (right, $\sin\theta/\lambda < 0.70$ Å^{-1}); for details see Figure 5-5. The maps show similar features to those obtained for IN$_2$–OA Form I (compare with Figure 3-4).

FA – 2,4-Lutidine – H_2O

Block shaped co-crystals of FA and 2,4-lutidine ($\Delta pK_{a1,2}$ = 3.96, 2.55) were grown from *iso*-propanol by slow evaporation of the solvent. The X-ray structure determination resulted in a monohydrated complex, FA–2,4-lutidine–H_2O, having abstracted water from the solvent. The dataset obtained at room temperature was refined to R_1 = 5.57 % for the observed, and to 8.55 % for all data to $\sin\theta/\lambda = 0.70$ Å^{-1}.

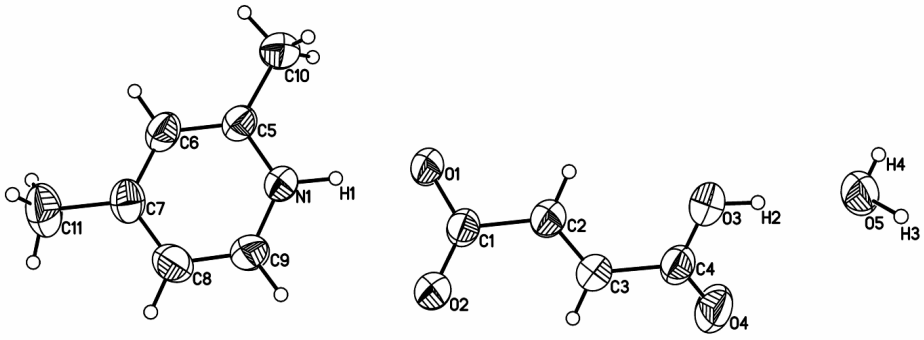

Figure 5-38: Ellipsoid plot of FA–2,4-lutidine–H_2O; for details see Figure 5-1.

This material co-crystallises with a 1 : 1 ratio of FA and 2,4-lutidine and is in this respect comparable to the FA–2,4-lutidine complex published in reference [107]. Aside from the hydration, the two materials differ in that FA exists always in the monoprotonated form in this case, while half a unit of respectively neutral and doubly deprotonated FA are present in the original structure. The asymmetric unit of the current H transfer complex, $[HC_4H_2O_4]^-$ $[HC_7H_9N]^+ \cdot H_2O$, is shown in Figure 5-38, and the extended hydrogen bonded structure formed by this material is shown in Figure 5-39. The strongest HB in FA–2,4-lutidine–H_2O is found between FA and the lutidine, D(N1···O1) = 2.610(2) Å. The difference density map in the plane of this HB (Figure 5-40) shows a slight

polarisation of H1 density towards the HB acceptor O1. The second FA carboxylic acid group remains undissociated and forms a moderate O3–H2···O5 HB with the co-crystallising water (D = 2.632(2) Å) which in turn donates two rather weak HBs to the deprotonated FA carboxylic acid group (D(O5···O1) = 2.777(2) and D(O5···O2) = 2.841(2) Å), see Figure 5-39. The presence of the water molecule thereby leads to the formation of an extended structure which can be visualised as tapes of hydrogen bonded FA–H_2O units with laterally linked lutidinium cations as illustrated in Figure 5-39.

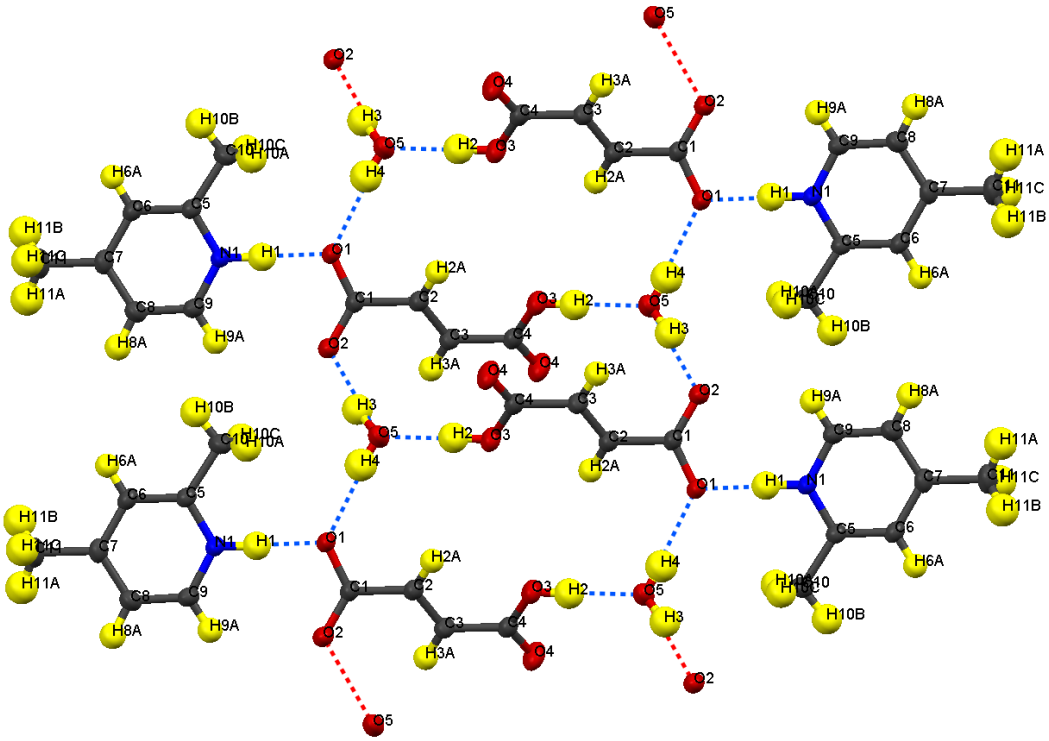

Figure 5-39: Extended hydrogen bonded structure in FA–2,4-lutidine–H_2O.

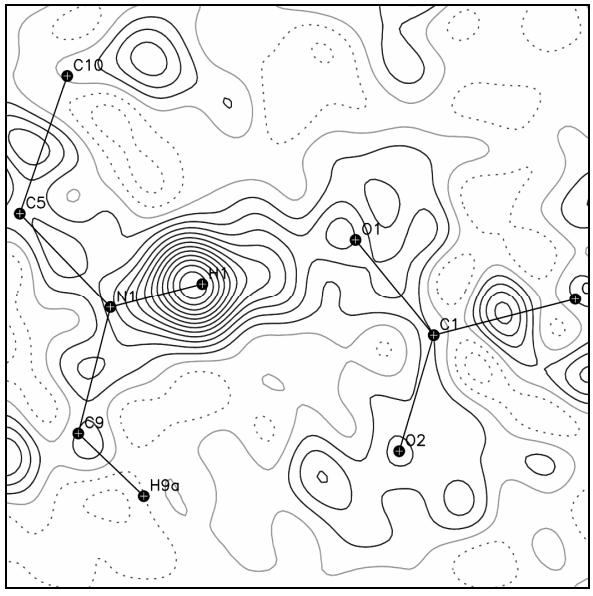

Figure 5-40: Difference Fourier map of FA–2,4-lutidine–H_2O in the C1–O1–N1 plane; $\sin\theta/\lambda < 0.70$ Å^{-1}, for details see Figure 5-5.

Table 5-7: Parameters for the HBs formed between FA and lutidine. H parameters have been refined when errors are given, fixed using the riding model otherwise.

		T	HB	D–H / Å	H···A / Å	D···A / Å	∠DHA / °
FA – lutidine (1 : 2)							
FA–(3,5-lutidine)$_2$		100K	O1–H1···N1	1.21(3)	1.32(3)	2.5341(17)	176(2)
		180K*	O–H···N	1.12(2)	1.42(2)	2.5423(11)	177.4(19)
		RT	O1–H1···N1	1.19(4)	1.38(4)	2.563(2)	176(3)
FA–(3,4-lutidine)$_2$		150K	O1–H1···N1	1.033(18)	1.542(18)	2.5693(10)	172.1(15)
		RT	O1–H1···N1	1.01(2)	1.59(2)	2.5917(13)	174.0(15)
FA–(2,3-lutidine)$_2$		100K	O1–H1···N1	1.146(19)	1.408(19)	2.5513(9)	175.2(17)
		180K*	O–H···N	1.13(2)	1.42	2.553	175.0
		RT	O1–H1···N1	1.15(2)	1.43(2)	2.5719(14)	171.8(18)
FA – lutidine (other)							
FA$_3$–(2,5-lutidine)$_2$*	(3 : 2)	180K	N–H···O	0.86	1.92	2.7758(15)	173.1
FA$_3$–(3,4-lutidine)$_2$*	(3 : 2)	180K	N–H···O	0.88	1.89	2.7715(14)	175.9
FA$_2$–2,3-lutidine*	(2 : 1)	180K	N–H···O	0.92(3)	1.84	2.752	169.6
FA–2,6-lutidine†	(1 : 1)	RT	N–H···O	0.86	1.77	2.619(2)	166.9
FA–2,4-lutidine*	(1 : 1)	180K	N–H···O	0.88	1.71	2.5861(18)	177.0
FA–2,4-lutidine–H$_2$O	(1 : 1)	RT	N1–H1···O1	0.97(3)	1.64(3)	2.6099(18)	178(2)

* from reference [107]; † from reference [108]

Table 5-8: H transfer – ΔpK_a dependence (p$K_{a1,2}$ for FA = 3.03, 4.44) in the FA – lutidine complexes. Geometrical parameters that indicate the protonation states of PCP and the lutidines are also included.

		pK_a (lut)	Δp$K_{a1,2}$	% HT	C–O(H) / Å	C=O / Å	∠CNC / °
FA – lutidine (1 : 2)							
FA–(3,5-lutidine)$_2$		6.15	3.12, 1.71	0	1.3046(19)	1.2240(18)	119.75(14)
FA–(3,4-lutidine)$_2$		6.46	3.43, 2.02	0	1.3110(10)	1.2205(10)	118.51(7)
FA–(2,3-lutidine)$_2$		6.57	3.54, 2.13	0	1.3088(8)	1.2261(8)	120.85(6)
FA – lutidine (other)							
FA$_3$–(2,5-lutidine)$_2$*	(3 : 2)	6.40	3.37, 1.96	100	1.2677(15)	1.2488(14)	123.64(12)
FA$_3$–(3,4-lutidine)$_2$*	(3 : 2)	6.46	3.43, 2.02	100	1.2665(16)	1.2488(16)	122.09(12)
FA$_2$–2,3-lutidine*	(2 : 1)	6.57	3.54, 2.13	100	1.260(2)	1.252(2)	124.0(3)
FA–2,6-lutidine†	(1 : 1)	6.60	3.57, 2.16	100	1.263(2)	1.249(2)	123.92(17)
FA–2,4-lutidine*	(1 : 1)	6.99	3.96, 2.55	100	1.264(2)	1.254(2)	122.02(14)
FA–2,4-lutidine–H$_2$O	(1 : 1)			100	1.2713(18)	1.241(2)	121.80(14)

* from reference [107] measured at 180 K; † from reference [108] measured at RT

The parameters for the O··H··N HBs which are formed between FA and the lutidines are summarised in Table 5-7 for all FA – lutidine complexes found to date. Table 5-8 complements these parameters with the corresponding heavy atom parameters, pK_a data, and the state of H transfer in these materials. With regards to the HB strengths, these data

reveal that short, strong O–H(acid)···N(pyridine) HBs are formed only in the 1 : 2 FA – lutidine complexes, whereas the adducts with a higher relative FA content exhibit only moderately strong HBs. This is reflected by the refined O···N distances, and also the covalent X–H bond lengths which, though determined less reliably, still reproduce the bond elongation typical of SSHBs. The general trend emerging from this comparison is a reduced O··H··N HB strength upon an increased FA content. With regards to H transfer from FA to the lutidine, no dependence on the ΔpK_a values is found. H transfer, as observed in these complexes, depends rather on the stoichiometry of the material: the three 1 : 2 complexes obtained to date are all molecular neutral adducts, and the complexes with an excess of FA are all H transfer adducts. This can, of course, be rationalised by the fact that the carboxylate groups in the H transfer adducts are stabilised by accepting HBs from additional FA units – or water in the case of FA–2,4-lutidine–H_2O. This stabilisation is not possible in the neutral 1 : 2 adducts where the O–H···N HBs are, aside from weak C–H···O interactions, embedded in an apolar environment.

As an aside, the co-crystallisation experiments of FA with 3,5- and 2,5-lutidine, carried out at ambient conditions, yielded additional products of zwitterionic N-succino-lutidines. There is a precedent case documented in the literature where maleic acid has reacted with pyridine in water to N-succinopyridine.[109] Although the crystal structures of the unexpected addition products will not be presented in this work, the reaction scheme resulting in the above compounds will be outlined briefly. The reaction, an auto-catalysed electrophilic addition, is analogous to the acid catalysed hydration of an unsaturated –CH=CH– bond: an electrophilic H^+ (from the same or a second molecule of FA) adds to the double bond and yields a $–CH^+–CH_2–$ carbocation, which in turn acts as an electrophile adding to the lone pair of the pyridyl N atom and forming a C–N bond with the positive charge on the N atom; the negative charge is located on the succino α-carboxylate group. The reaction is favoured by polar solvents (intermediate carbocation) and was observed in methanol in the case of 2,5-lutidine and ethanol in the case of 3,5-lutidine. The use of less polar solvents (ethanol and *iso*-propanol respectively) inhibits the reaction and leads to the co-crystals of FA_3–$(2,5\text{-lutidine})_2$ and FA–3,5-lutidine presented in reference [107].

5.2.3. Conclusion / Discussion

The design of strongly hydrogen bonded materials has been only partially successful and no correlation of H transfer and ΔpK_a values is observed in the complexes of OA and FA with the lutidines.

The co-crystallisation experiments of OA with the lutidines did not result in the desired 1 : 2 complexes, OA – $(\text{lutidine})_2$, and since this was the envisaged condition for the formation of SSHBs, the experiments did also not result in the latter. In retrospect this is not too surprising since oxalic acid, and especially its deprotonated forms, are very strong HB acceptors. As a consequence OA attracts HB donors, i.e. additional molecules of OA or, in case of the hydrated complex, water. The formation of additional, comparatively strong HBs in turn assists the dissociation by stabilising the carboxylate groups and leading to the observed H transfer complexes only, in agreement with the observations made by Lindemann and Zundel for hydrated carboxylic acid – aromatic N base complexes, for which they determined a $\Delta pK_a^{50\%}$ of ~ 0.9.[105] The observed pattern of H transfer implies that the tight range has been missed where centred, hence really strong, SSHBs are formed.

One might argue that the applied approach worked well for co-crystallising OA with the pyridine base isonicotinamide resulting in the analogous 1 : 2 complexes, OA – (isonicotinamide)$_2$ (or in the chosen notation, IN$_2$–OA, see Chapter 3). Ignoring the much lower pK_a of 3.6 for IN which considerably reduces the likelihood of H transfer, IN itself provided HB donors (amide group) to meet the demand of OA for forming HBs. Probably important in this context is the fact that the amide N–H donor is comparably weak and hence does not stabilise a potential carboxylate group so well. Notably, the first ΔpK_a value of 2.4 in IN$_2$–OA ($\Delta pK_{a1,2}$ of 2.4 and -0.6) agrees excellently with $\Delta pK_a^{50\%} \sim 2.3$ determined by Lindemann and Zundel for the N–H···O HB stabilised systems.[105] Another explanation might be that the sterically large IN dimers (resulting from the formation of the diamide HBs) occupy a large portion of space available in the 3-dimensional structure and prevents the inclusion of further OA units. In the end, one has to admit that OA and lutidines have not been well chosen candidates for the current purpose, or refer to the fact that the predictability of co-crystal structures and hence their properties is limited.

The design of SSHBs by co-crystallising the lutidines with FA on the other hand, was successful insofar the 1 : 2 complexes FA – (lutidine)$_2$ are concerned. They all exhibit SSHBs of the type O··H··N embedded in an apolar environment as anticipated. The inclusion of additional FA molecules, or water in case of the hydrated structure, into the crystal structure results in H transfer complexes with HB stabilised hydrogenfumarate or fumarate anions, and furthermore in a weakening of the O···H–N HBs. So far in these systems, the occurrence of H transfer depends on the stoichiometry of the complex, not on the ΔpK_a values, highlighting again the necessary condition for studying ΔpK_a – H transfer relations in molecular crystals: the HB of interest has to be isolated from a polar environment when correlating solution pKa values with solid state systems, as pointed out by Steiner.[8] Thus, in order to establish a ΔpK_a rule for H transfer it is necessary to complete the series of co-crystals containing the trimeric 1 : 2 adducts. It is in particular desirable to obtain an analogous structure with 2,4-lutidine, the strongest lutidine base with a pK_a of 6.99, where H transfer is most likely to occur. As of now, only a lower limit for a $\Delta pK_a^{50\%}$ value can be given to be 3.54 (marked by the molecular complex FA–(2,3-lutidine)$_2$), in agreement with the value of 4.0 found by Lindemann and Zundel.[105] Whether the dissociation constant for first or second deprotonation step is significant in this respect (or an intermediate value), is an altogether different matter. So far, the pK_a for the first deprotonation step seems relevant (as in IN$_2$–OA). What has been observed is that the dicarboxylic acids, hydrogen bonding with both acid groups to N bases, like to share their protons in a symmetrical manner. The H atoms are transferred in unison or not at all. This has been observed not only in the materials studied in this chapter but also on the IN$_2$–OA complexes; the exception is IN$_2$–d-OA Form II where a mixed protonated OA molecule is found.

5.3. PENTACHLOROPHENOL – 1,4-DIAZABICYCLO[2.2.2]OCTANE

Pentachlorophenol (PCP) and 1,4-diazabicyclo[2.2.2]octane (DABCO) have been co-crystallised, forming solid state materials of variable stoichiometric composition. While in Chapter 5.2 (*Carboxylic Acid – Dimethylpyridine Complexes*) diacids were used to complex the family of monobasic lutidines, in this case the monoacid PCP is used to complex the dibase DABCO. The target material is consequently a hydrogen bonded 2 : 1

complex, PCP_2–DABCO. In view of the pK_a values of 4.70 for PCP, and of 2.97 and 8.82 for the first and second deprotonation step of the doubly protonated $[H_2C_6H_{12}N_2]^{2+}$, the first HB formation between PCP and DABCO is expected to be accompanied by a H transfer reaction, while the second HB is expected to show a neutral configuration, see Scheme 5-2 below. Furthermore the formation of SSHBs is envisaged – encouraged by previous co-crystallisation studies with (di)carboxylic acids. They have shown that such (2 : 1) acid – DABCO complexes form, and that a variable degree of H transfer and the formation of SSHBs are observed in some cases.[110, 111, 112]

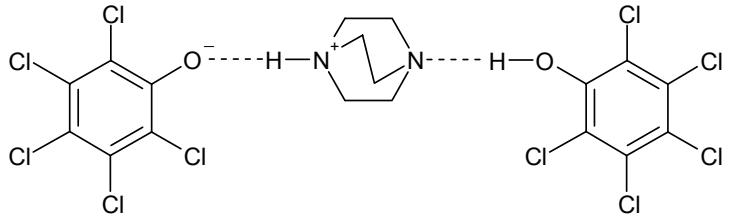

Scheme 5-2: (2 : 1) target complex PCP_2–DABCO.

5.3.1. Stoichiometric Variations

The co-crystallisation experiments were performed by slow evaporation of the solvent for which chloroform and ethanol have been used. To date three complexes of variable PCP : DABCO stoichiometry have been obtained thus and characterised by X-ray diffraction – none of them corresponding to the target compound:

PCP–DABCO $\equiv [C_6Cl_5O]^- [HC_6H_{12}N_2]^+$

PCP_2–DABCO $\equiv C_6Cl_5OH \cdot [C_6Cl_5O]^- [HC_6H_{12}N_2]^+$

PCP_3–$DABCO_2$ $\equiv C_6Cl_5OH \cdot 2[C_6Cl_5O]^- 2[HC_6H_{12}N_2]^+$

Although PCP_2–DABCO crystallises with the desired stoichiometry, the HB scheme differs from the target compound above as we will see later. The asymmetric units of the X-ray structures are shown in Figure 5-41. The structures have been refined according to the previous procedures: the H atoms involved in strong and moderate hydrogen bonding, i.e. those originating from the pentachlorophenol, have been refined whilst the other H atoms were fixed using the riding model. The PCP – DABCO complexes have in common that HBs (some of them strong) are as expected formed between PCP and DABCO and that this HB formation is always accompanied by a H transfer reaction. Unexpectedly however, DABCO always exists in the monoprotonated form, $[HC_6H_{12}N_2]^+$. The strength of the resulting N–H···O HBs appears to depend on additional hydrogen bonding to the pentachlorophenolate anion, which involves the excess molecules of PCP, if present, but also weak C–H···O interactions (all HB parameters are given in Table 5-9). We can attempt to rationalise this behaviour.

PCP–DABCO

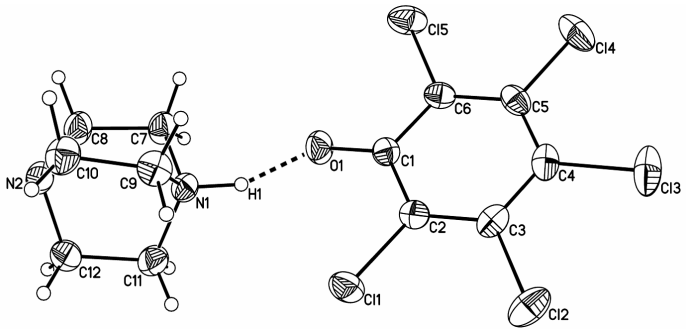

PCP_2–DABCO

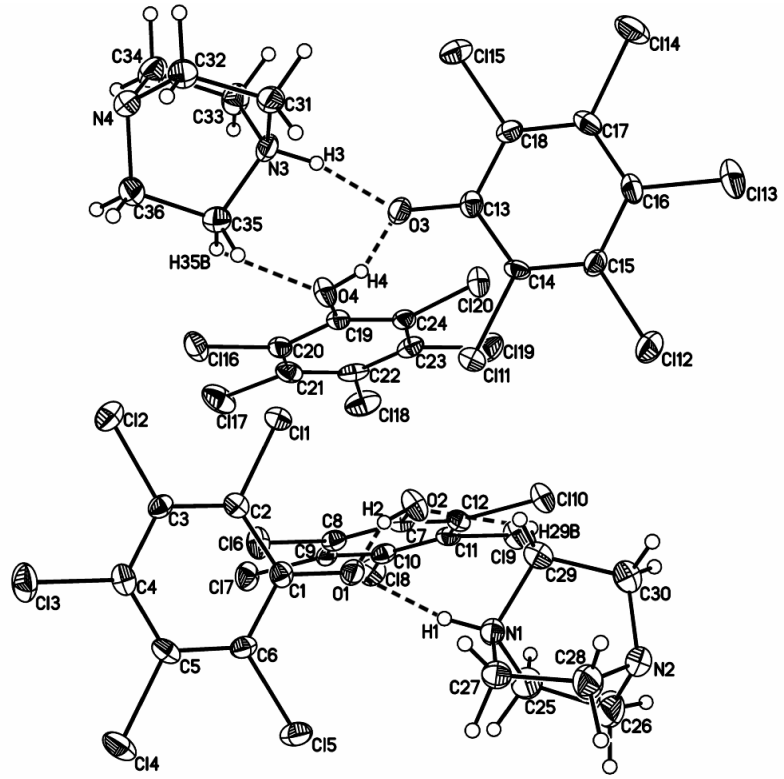

PCP_3–$DABCO_2$

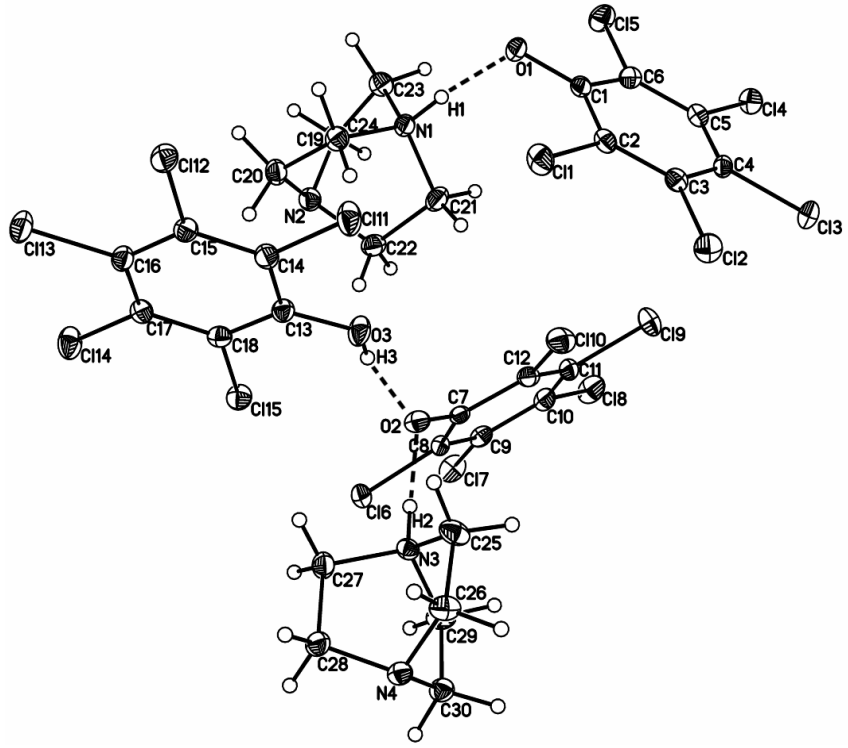

Figure 5-41: Asymmetric units of the PCP – DABCO complexes; for details see Figure 5-1.

PCP – DABCO

Block shaped crystals of PCP–DABCO, crystallising in the space group $P2_1/c$, were grown from a stoichiometric 1 : 1 ratio PCP and DABCO from chloroform. The X-ray structure measured at 150 K[a] was refined to R_1 = 3.42 % and 5.49 % for the observed ($F_{obs} > 4\sigma(F_{obs})$) and all data respectively; the resolution of the dataset was cut off at $\sin\theta/\lambda$ = 0.70 Å^{-1}. As shown in the plot of the asymmetric unit in Figure 5-41, the complex constitutes a hydrogen bonded dimer. The H atom has been transferred from PCP towards one N base of the diamine resulting in an ionic complex $[C_6Cl_5O]^-$ $[HC_6H_{12}N_2]^+$. The short heteroatom distance of 2.546(2) Å in the N1–H1···O1 HB thus formed suggests that this HB is strong. However, the difference Fourier map in the plane of this HB (Figure 5-42) shows no evidence for a pronounced polarisation of the H density towards the phenolate O1 atom as one would expect to observe in a SSHB. The map also reveals N lone pair density for the second amine nitrogen, N2, present in DABCO. Interestingly no HB is formed towards this N lone pair – the closest contact originates from a neighboured C–H group, some 2.80 Å (H11A···N2) away. The phenol oxygen on the other hand, accepts a weak C–H···O HB from a neighbouring molecule of DABCO (H7A···O1 = 2.54 Å). The PCP–DABCO dimers thereby aggregate into the weakly linked tetrameric units shown in Figure 5-43, similar to those observed in some of the dimeric PCP – lutidine complexes (see 5.1.1 *Dimeric 1:1 Structures*).

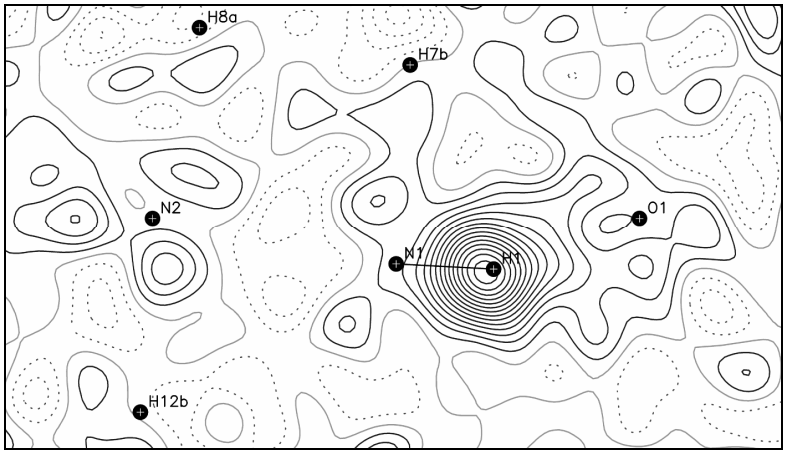

Figure 5-42: Difference Fourier map of PCP–DABCO in the N2–N1–O1 plane; $\sin\theta/\lambda < 0.70$ Å^{-1}, for details see Figure 5-5.

[a] when cooling to 100 K the crystals crack reproducibly but still yield the same lattice parameters.

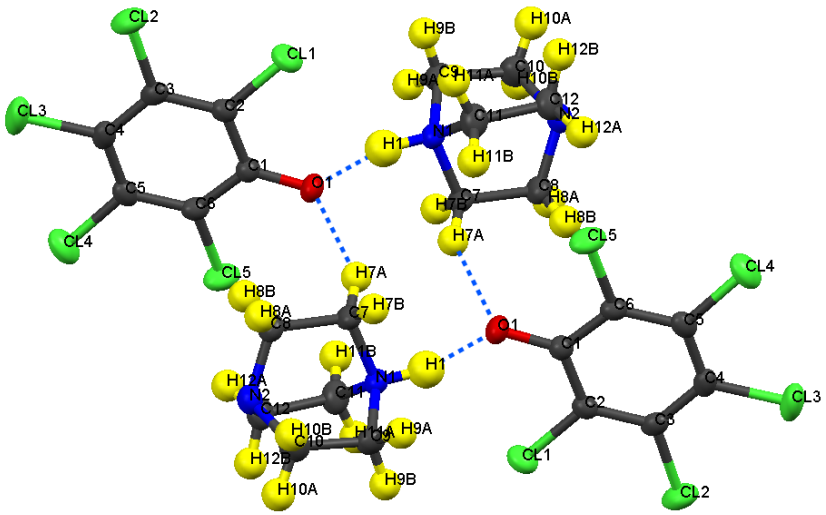

Figure 5-43: Arrangement of the PCP–DABCO dimers into tetramers.

PCP_2 – DABCO

PCP_2–DABCO crystallises from stoichiometric 2 : 1 ratios of PCP and DABCO in a solution of chloroform – forming crystals with a plate shaped morphology in the space group $P2_1/n$. Neither the crystal quality nor the quality of the obtained X-ray dataset proved to be great, but were suitable for a structure determination. The data had to be cut off at a comparably low resolution ($\sin\theta/\lambda$ = 0.64 $Å^{-1}$) and were refined to R_1 = 4.20 % and 9.10 % for the observed and all reflections respectively. This material forms a trimeric, hydrogen bonded 2 : 1 complex of PCP and DABCO, as intended. However, the hydrogen bonding scheme differs from the target complex in that the second DABCO amine group is not involved in the hydrogen bonding. The first PCP molecule forms the expected HB with a DABCO amine group, accompanied by H transfer and thus resulting in an ionic adduct similar to that observed in the dimeric complex PCP–DABCO above. The second PCP molecule however, hydrogen bonds to the deprotonated PCP, instead of forming an independent HB towards the second (and still uncoordinated) amine nitrogen which has to be considered to be a potential HB acceptor. In any case, the HB scheme of the resulting trimeric complex, $C_6Cl_5OH \cdot [C_6Cl_5O]^- [HC_6H_{12}N_2]^+$, has a strong resemblance to that found in the trimeric adducts which pentachlorophenol forms with the 2,5- and 3,4-lutidines (see 5.1.3 *Trimeric 2:1 Structures*). Aside from the HB motif, $O–H\cdots O^-\cdots H–N^+$, the neutral PCP and the amine base (in this case DABCO) are also linked via a C–H···O interaction, if slightly weaker in this case. The C–H···O HB completes the hydrogen bonded cyclic synthon similar to that observed in the PCP_2 – lutidine complexes.

Two formula units of PCP_2–DABCO are crystallographically independent (Z' = 2), they both show the hydrogen bonded cyclic synthon described above. The HBs are indicated by dashed lines in Figure 5-41 in an attempt to visualise the structure, if the relative orientation of the two trimeric units impedes a clear visualisation. The HB lengths in the independent units refine to very similar values: the N···O distances are 2.653(3) and 2.622(3) Å respectively, and the O···O distances are 2.508(3) and 2.481(3) Å respectively. Also, the H···O distances in the C–H···O HBs are comparable, at 2.65 and 2.58 Å, and as a result the two independent adducts can be considered to be equivalent. Difference Fourier

maps in the planes of the HBs are shown in Figure 5-44; they are very noisy due to the poor quality of the X-ray dataset, but they confidently reveal the protonation states in the hydrogen bonded synthons. In comparison to the situation in PCP–DABCO, the N–H···O HBs are elongated by ~0.1 Å and consequently are too weak to be considered SSHBs. This can be rationalised by the fact that in this material the $[C_6Cl_5O]^-$ anions are stabilised by accepting O–H···O HBs from the neutral C_6Cl_5OH molecules. Regarding the homonuclear O–H···O HBs, which are short, the difference densities indicate some polarisation of the H density towards the HB acceptor (in particular in O4–H4···O3), but a classification of these HBs as strong or not strong remains to be seen once better crystallographic data are available.

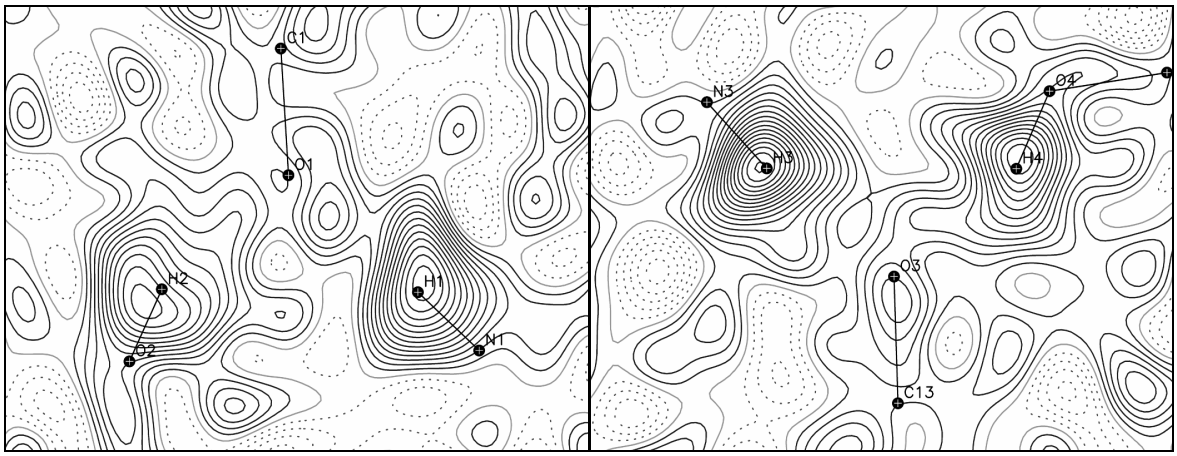

Figure 5-44: Difference Fourier maps in the planes of the hydrogen bonds in PCP_2–DABCO, (left) trimer 1 in the O2–O1–N1 plane, (right) trimer 2 in the O4–O3–N3 plane; $\sin\theta/\lambda < 0.64$ Å^{-1}, for details see Figure 5-5.

PCP_3 – $DABCO_2$

The crystals of PCP_3–$DABCO_2$ were also obtained by co-crystallisation of 2 : 1 ratios of PCP and DABCO. X-ray data collection and subsequent structure refinement resulted in $R_1 = 2.86$ % and 3.90 % for the observed and all data respectively, at $\sin\theta/\lambda = 0.70$ Å^{-1}.

Interestingly, the co-crystal of PCP_3–$DABCO_2$ is composed of a mixture of the dimeric and the trimeric units known from the previous PCP – DABCO complexes; one of each is situated in the asymmetric unit (Figure 5-41). Again, the H atom is transferred to the diamine to form ionic adducts $[C_6Cl_5O]^-$ $[HC_6H_{12}N_2]^+$ which in the case of the trimer is stabilised by the familiar hydrogen bonding to a neutral PCP molecule. In case of the dimeric adduct, some degree of stabilisation of the $[C_6Cl_5O]^-$ ion is achieved by hydrogen bonding to C–H groups of a neighbouring DABCO molecule. The C–H···O HBs are comparatively strong with *d*(H19A···O1) = 2.29 and *d*(H23B···O1) = 2.40 Å respectively, and lead to the formation of, again, tetrameric units as shown in (Figure 5-45). The trimeric adduct on the other hand – which, as a side note, lacks the C–H···O interactions and hence the cyclic synthon observed in PCP_2–DABCO – is not involved in further weak hydrogen bonding and is thus isolated in the crystalline environment. The second DABCO amine groups are not involved in any hydrogen bonding as observed in the previous structures; aside from a weak C–H···N contact with *d*(H25A···N2) = 2.68 Å, which also marks the strongest HB interaction formed by the second amine group of all PCP – DABCO complexes.

The HB in the dimeric adduct is of a comparable strength to that observed in PCP–DABCO. The distance between the heteroatoms in the N1–H1···O1 HB (D = 2.566(2) Å) is elongated by ~0.02 Å, but then the HB shows an increased linearity in this case with an HB angle of ∠N1–H1···O1 = 171(2)º compared to 157(2)º in case of PCP–DABCO. The H1 density (Figure 5-46, left) shows a slight polarisation towards O1 indicating possibly an increased HB strength in this dimeric adduct. With respect to the HB strengths in the trimeric adduct (Figure 5-46, right), the N3–H2···O2 HB (D = 2.568(2) Å) is considerably stronger, and the O3–H3···O2 HB (D = 2.624(3) Å) is considerably weaker than the corresponding N–H···O and O–H···O HBs in PCP_2–DABCO. Remarkably, the same variation in HB strengths has been observed in the trimeric units of the analogous complexes of PCP_2 – lutidine. Also the same "symptom" is observed which appears to trigger the change in HB strengths, namely the absence of a weak C–H···O HB which completes the hydrogen bonded synthons in PCP_2–DABCO. Consequently the explanation is analogous to that given in 5.1.3 on *PCP_2 – 3,4-lutidine*: "The lack of 'stabilisation' the PCP hydroxyl group experiences by the absence of the weak C–H···O HB may prevent this PCP molecule from sharing its H atom to the same extent as is observed in the C–H···O stabilised synthons. In turn, the reduced stabilisation the $[C_6Cl_5O]^-$ anion experiences due to the weakened O–H···O HB might lead to an increased demand for charge balance by forming a stronger interaction to the N–H donor."

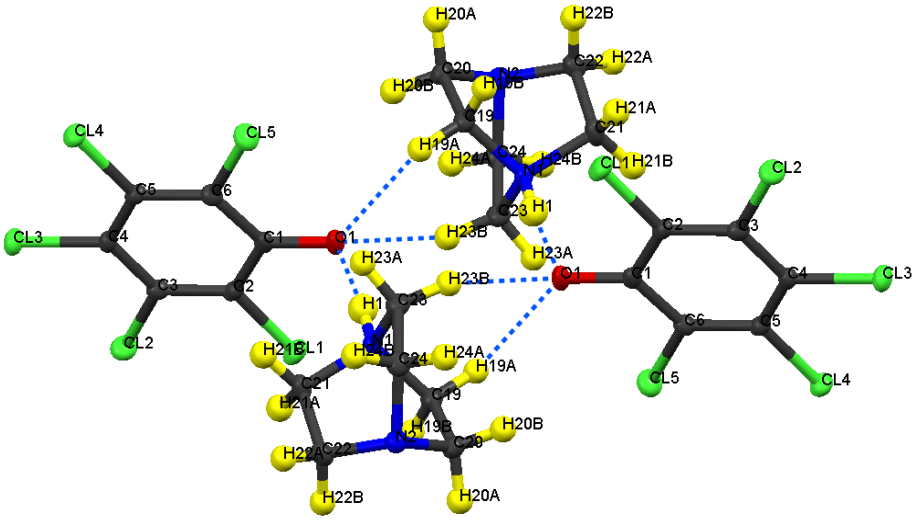

Figure 5-45: PCP – DABCO dimers linking into tetrameric units in PCP_3–$DABCO_2$.

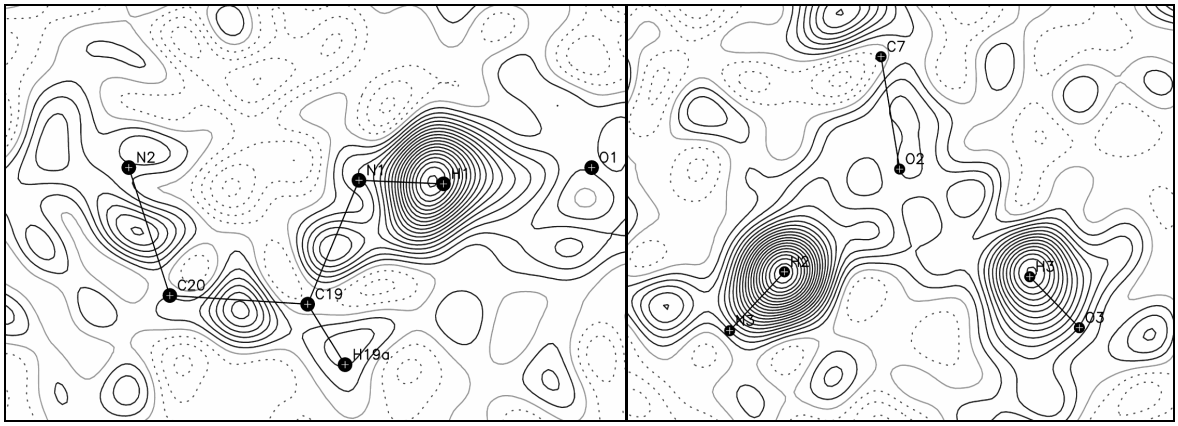

Figure 5-46: Difference Fourier maps of the HBs in PCP_3–$DABCO_2$ in the N2–N1–O1 (left) and in the O3–O2–N2 plane (right); $\sin\theta/\lambda < 0.70$ Å^{-1}, for details see Figure 5-5.

Table 5-9: HB parameters for the PCP – DABCO complexes; H positional and displacement parameters have been refined when errors are given, fixed using the riding model otherwise.

	HB	D–H / Å	H···A / Å	D···A / Å	∠DHA / °
PCP–DABCO	N1–H1···O1	1.00(2)	1.59(2)	2.5462(19)	157(2)
	C7–H7A···O1*	0.99	2.54	3.443(2)	151.4
PCP_2–DABCO	N1–H1···O1	0.88(3)	1.79(3)	2.653(3)	167(3)
	N3–H3···O3	0.92(3)	1.72(3)	2.622(3)	168(3)
	O2–H2···O1	0.81(4)	1.75(4)	2.508(3)	156(4)
	O4–H4···O3	0.87(3)	1.67(4)	2.481(3)	155(3)
	C29–H29B···O2	0.99	2.65	3.413(4)	134.1
	C35–H35B···O4	0.99	2.58	3.302(4)	130.1
PCP_3–$DABCO_2$	N1–H1···O1	0.93(2)	1.64(2)	2.5659(18)	171(2)
	N3–H2···O2	0.882(19)	1.690(19)	2.5676(16)	172.9(19)
	O3–H3···O2	0.80(2)	1.86(2)	2.6237(17)	160(2)
	C19–H19A···O1*	0.99	2.29	3.1334(19)	141.9
	C23–H23B···O1*	0.99	2.40	3.276(2)	147.7

* Atoms generated by symmetry.

5.3.2. Conclusion

Co-crystallisation of PCP and DABCO results in the formation of H transfer complexes $[C_6Cl_5O]^-$ $[HC_6H_{12}N_2]^+$. Additional molecules of PCP retain their molecular form, and hydrogen bond to (and stabilise) the $[C_6Cl_5O]^-$ ions. A correlation has been observed between the availability of weak C–H donors and the HB strengths as seen previously in the PCP_2 – lutidine complexes (5.1.3 *Trimeric 2:1 Structures*), to which the complexes described here show a strong similarity. As the pK_a values for the participating species $[H_2C_6H_{12}N_2]^{2+}$, $[HC_6H_{12}N_2]^+$ and C_6Cl_5OH of respectively, 2.97, 8.82 and 4.70 suggest, DABCO is only present in the monoprotonated form in these materials. However, this should not explain why the formation of a second O–H(pcp)···N(amine) HB seems to be unfavourable. That DABCO is willing to involve both amine groups in hydrogen bonding has been demonstrated (see references [110–112]).

As a final remark, the crystal packing schemes PCP and DABCO can adopt, seem to be flexible and highly variable, and the observed diversity in this material suggests that there are likely further variations in this family to be expected.

6. CONCLUSIONS AND PROSPECTS

The molecular complexes of isonicotinamide with oxalic acid, IN_2–OA, have been investigated. Crystallising in two hydrogenous and two deuterated forms, upon isotopic substitution of the acidic hydrogen by deuterium, they show a profound tendency towards the formation of polymorphs. The hydrogenous forms have been characterised by combined X-ray charge density and single crystal neutron diffraction studies. IN_2–OA Form I and IN_2–OA Form II can be differentiated in a *cis* and a *trans* form respectively, with respect to the OA hydroxyl groups. Both forms show strong hydrogen bonding between OA and IN of the type O–H(acid)···N(pyridine). The neutron diffraction studies have shown that the covalent O–H bonds are considerably elongated, as known to be common for SSHBs, to the extent that in IN_2–OA Form II the H atom occupies a near central position in the SSHB. There is no evidence for H disorder or a particularly pronounced H motion in the SSHB. The X-ray charge density studies have shown that the hydrogen bonding interactions H···N are covalent in nature, confirmed by analysis of the source function, which for the first time has been derived from experimental charge densities. The H···N bonding density arising from this covalency overlaps with the pyridine N lone pair density, and leads in combination with the H density to a strong electronic delocalisation in this type of SSHB. Thereby, the density originating from the charge transfer (N lone pair and H···N bonding density) has the same magnitude as the density corresponding to the H atom. This results in an ambiguity when localising the H atom from difference electron densities, and as a consequence, strong O–H(acid)···N(pyridine) HBs are susceptible to misinterpretation as HBs with a disordered H site.

The occurrence of polymorphism upon isotopic substitution, as observed in IN_2–OA, is known as isotopomeric polymorphism. This H/D isotope in itself is a rare phenomenon for molecular materials. In addition, IN_2–OA shows a pronounced equilibrium H/D isotope effect. The equilibrium O–H/D···N $\leftrightarrow$ O^-···H/D–N^+ becomes considerably shifted to the right upon deuteration and results in transfer of the hydron from the acid to the base. The main structural difference between the IN_2–OA and IN_2–d-OA manifests in bifurcated, weaker hydrogen bonding between OA and IN in the deuterated forms. While the hydrogenous forms can be described as formally neutral, molecular complexes (although IN_2–OA Form II is a borderline case with the H atom occupying a near central position in the SSHB), the deuterated forms, IN_2–d-OA, are clear ionic complexes showing in Form I and Form II 100 % and 50 % D transfer respectively. Overall, the four different polymorphic forms observed to date all exhibit a different degree of hydron transfer.

The molecular complexes IN_2–OA have also been studied by ab-initio DFT calculations in the solid state. Ground state energy calculations have been performed with CASTEP using plane waves, and with CRYSTAL using localised atomic orbitals as descriptors of the wave function. The hydrogenous forms have in addition been studied by quantum molecular dynamic simulations with CASTEP. The calculations have been performed in the crystallographic symmetry (one independent SSHB) and also in a reduced symmetry, rendering the two SSHBs formed by OA independent and allowing for the possibility of the mixed protonated OA, $[HC_2O_4]^-$. It has been shown that the PW calculations did not reproduce the experimental SSHB geometries in the hydrogenous

forms. The ground state energy calculations favour the ionic O···H–N configuration over the O–H···N observed experimentally, suggesting the existence of H transfer complexes only. The QMD simulations also favour the H transfer complexes. For IN_2–OA Form I, the QMD simulations show a high H mobility in the SSHB and the occurrence of several H transfer processes during the simulation period. However, at no time is the neutral configuration for OA observed; at any one time OA exists as $[HC_2O_4]^-$ or $[C_2O_4]^{2-}$. For IN_2–OA Form II, the QMD simulations show a much reduced H mobility with the H atom residing almost exclusively at the N base, and correspondingly OA is observed as $[C_2O_4]^{2-}$ only. The results obtained from the AO calculations are in much better agreement with the experiment. For the hydrogenous forms, the experimental SSHB geometries have been reproduced when using the crystallographic symmetry. However, when using the reduced symmetry, for both polymorphs energy minima are also found for the mixed protonated OA, corresponding to $[HC_2O_4]^-$. In the end, reducing the crystallographic symmetry to allow for the existence of $[HC_2O_4]^-$ (which from the chemical point of view is entirely plausible) has not been helpful in improving the agreement with the experiment, neither for the PW nor for the AO calculations. To conclude, the PW calculations failed to reproduce the experiment with respect to the SSHB, while the AO calculations yielded results in very good agreement with the experiment. The best description of the SSHBs in the hydrogenous forms has been obtained by AO calculations of the adiabatic HB potentials and subsequent inclusion of the zero point energy contributions, yielding O–H expectation values in excellent agreement with the neutron data. On the deuterated forms, the PW and AO calculations performed equally well. The correct HB configurations have been reproduced but the computed HB parameters in places deviate too much from the experiment. Finally, the energy ranking for polymorphism as determined from the AO calculations has been established to be IN_2–OA Form I < IN_2–OA Form II (+2.4 kJ/mol) < IN_2–d-OA Form II (+4.4 kJ/mol) < IN_2–d-OA Form I (+5.9 kJ/mol).

The strong electron delocalisation observed in the SSHBs in IN_2–OA allowed for systematic studies on difference electron density maps obtained for intermolecular SSHBs of the type O··H(acid)··N(pyridine). The studies have been performed for the hydrogenous forms of IN_2–OA discussed above, for PCP–4-methylpyridine showing a centred SSHB at ~100 K, and for dinicotinic acid showing a formally neutral O–H···N HB configuration at RT and a formally ionic $O^-\cdots H–N^+$ HB configuration at low T. For all these materials neutron data, hence accurate H nuclear positions, are available. On IN_2–OA, the dependence of difference electron densities on the resolution of an X-ray diffraction experiment has been investigated. It has been found that N lone pair densities are observed in O··H(acid)··N(pyridine) SSHBs at low experimental resolutions common to standard X-ray diffraction experiments. As a result, the electronic density becomes strongly delocalised if the SSHB is in O–H···N configuration, strongly biasing the localisation of H atoms from difference densities, and suggesting H disorder where there is none. These findings are likely to be transferable to all strong hydrogen bonds involving aromatic N bases. Examples have been found where molecular adducts exhibiting O··H(acid)··N(pyridine) SSHBs are, in our view, documented wrongly in the literature as partial H transfer complexes, implying that neutral materials are characterised misleadingly as ionic. The consequences are apparent for material properties assigned, as well as for the development of design routes for molecular materials (crystal engineering), for example for pharmaceutical purposes. The studies on the centred SSHB in PCP–4-methylpyridine and the nearly centred SSHBs in dinicotinic acid have shown that – once the fact of the

observability of charge transfer effects in these materials is acknowledged – imaging difference electron densities allows a differentiation of O–H···N from centred O··H··N and O···H–N HBs. It has furthermore been shown that the subtle H migration processes in these materials can be reproduced by standard X-ray experiments, even against the background of small absolute differences in H nuclear positions.

Co-crystallisation of pentachlorophenol with the series of dimethylpyridines results in the formation of dimeric (1 : 1) PCP – lutidine complexes, as expected, and for a few lutidines also in the formation of trimeric (2 : 1) PCP_2 – lutidine complexes. All complexes thus obtained show the primary hydrogen bonding motif of an O··H(acid)··N(pyridine) HB (mostly strong) between the lutidine and the pyridine base, as expected. In the series of the dimeric PCP – lutidine complexes these HBs are isolated from a polar environment, and a correlation has been found between proton affinities in solution (expressed by pK_a values) and the degree of H transfer from the phenol to the lutidine in the solid state. In this respect the polymorphic PCP–2,6-lutidine complexes are of interest, as in PCP–2,6-lutidine Form II the two crystallographically independent dimers show a variable degree of H transfer, resulting in a mixture of neutral and ionic PCP–2,6-lutidine adducts in the same solid. This material thereby marks the region of 50 % H transfer which has been determined to $\Delta pK_a^{50\%} \sim 2.0$ for the dimeric PCP – lutidine complexes. The correlation can be explained by the embedding of the O··H··N HBs in an apolar environment which remains comparatively undisturbed by the variation of the lutidine. The introduction of further hydrogen bonding donors, as observed in case of the trimeric PCP_2 – lutidine complexes, disrupts the apolar environment and facilitates H transfer by stabilisation of the pentachlorophenolate anions. Consequently, all 2 : 1 complexes are found to be H transfer complexes. Also, weak C–H···O HBs in the vicinity of the O··H··N HBs are believed to have an effect on the stronger O··H··N and O–H···O HBs. The variable H transfer behaviour in the PCP–2,6-lutidine polymorphs can thus be rationalised by weak C–H···O interactions, but the influence of these weak interactions is admittedly difficult to quantify.

Tentative ab-initio calculations have been performed on the polymorphic structures of PCP–2,6-lutidine using the AO approach. They reproduced the experimental geometries and configuration of the O··H··N HBs. According to the calculations, Form II is the energetically favoured polymorph by ~1.3 kJ/mol. It has been shown that for PCP–2,6-lutidine Form I, calculating the diabatic rather than the adiabatic HB potential yields a better agreement with the experiment, implying that the O–H···N HB in this complex is weaker than those in the hydrogenous forms of IN_2–OA. In order to validate the performance of the AO calculation on this family of molecular materials, further computational studies are required. A determination of the HB potentials observed in the PCP – lutidine complexes is desirable but computationally expensive, in particular for PCP–2,6-lutidine Form II showing the variable SSHB configurations.

Co-crystallisation of the dicarboxylic acids oxalic acid and fumaric acid with the lutidines were intended to yield 1 : 2 acid – lutidine complexes showing strong hydrogen bonding and a variable degree of H transfer. However, this has been successful only when co-crystallising FA with 3,5-lutidine, 3,4-lutidine and 2,3-lutidine. All other experiments result in co-crystallisation of additional molecules of OA and FA respectively, or in some cases in the inclusion of water molecules. As expected, SSHBs are formed in the 1 : 2 FA – lutidine complexes, which, as in the dimeric PCP – lutidine complexes, are embedded in

an apolar environment. The X-ray data suggest a considerable elongation of the covalent O–H bonds and a pronounced covalency of the hydrogen bonding interaction in these SSHBs. For a full description of the electronic structure, however, further investigations will be required, i.e. combined X-ray charge density and neutron diffraction studies. This will also offer the opportunity to perform a systematic study on the electronic structures of SSHBs in a series of related materials. No H transfer has been observed in the ΔpK_a range experimentally available to date, and all 1 : 2 complexes consequently exist in neutral form in the solid state. In this respect it is desirable to complete the series of the FA – $(lutidine)_2$ complexes, and in particular to obtain a structure of the 1 : 2 complex of FA and 2,4-lutidine which would mark the upper end of the ΔpK_a range. The complexes crystallising with a higher acid content, as well as the hydrated complexes, all show H transfer, which is facilitated by stabilisation of the carboxylate groups via the formation of additional O–H···O HBs. As a result, the degree of H transfer was found to be dependent on the stoichiometry of the materials rather than on ΔpK_a values. This has confirmed that the necessary condition for studying ΔpK_a dependencies on H transfer in the solid state is that the corresponding HBs are embedded in an apolar environment. One could argue that such ΔpK_a dependencies could also be established for HBs embedded in a polar environment, but the variations in the strengths, for example, of additional O–H···O HBs, will cause supposedly also a strong variation in "polarity" in these cases, impeding a systematic study.

Co-crystallisation of PCP with the diamine 1,4-diazabicyclo[2.2.2]octane results in the formation of complexes with varying stoichiometry PCP : DABCO. The complexes obtained exhibit dimeric (1 : 1) PCP – DABCO and trimeric (2 : 1) PCP_2 – DABCO adducts, showing a strong resemblance to those found in the PCP – lutidine complexes. The formation of the PCP – DABCO dimer is always accompanied by H transfer, as expected. Unexpectedly, however, additional PCP molecules do not hydrogen bond to the second amine groups of DABCO but to the pentachlorophenolate anion. The reason for DABCO not involving the second amine group in hydrogen bonding in the materials obtained to date could not be rationalised. As in the PCP – lutidine complexes, evidence has been found that weak C–H···O interactions have an effect on the stronger O···H–N and O–H···O HBs, and can alter their relative strengths.

A final comment addresses the difference Fourier density maps provided throughout this work. The problems involved in the localisation of H atoms from X-ray diffraction experiments is well known. On the other hand, it is also well known that the method of choice for determining accurate H parameters, neutron diffraction, has practical limitations. In the absence of neutron data the H atoms have been located from difference Fourier electron density maps in this work. This method is as old as the technique of X-ray diffraction itself but seems to have become out of vogue. At least it has become out of vogue to publish such difference density maps these days (aside from charge density work). This is unfortunate since it has been demonstrated in this work, yet again, that such maps provide valuable information beyond the localisation of H. The density features can reveal charge transfer effects and the nature of HBs, even if obtained from standard X-ray diffraction experiments. Difference density maps aid in an estimation of reasonably accurate H positions, and in the very least they allow an evaluation of the reliability of refined H positional parameters.

APPENDIX

A. EXPERIMENTAL

All co-crystallisation and recrystallisation experiments were carried out by the method of slow isothermal (room temperature) evaporation of the solvent. The chemicals were purchased from Aldrich. In general, various experimental conditions yield the desired compound. The experimental conditions given here specifically are those which yielded the relevant single crystals used for the current structure determination.

Chapter 3 – *Molecular Complexes of Isonicotinamide with Oxalic Acid*:

3.1 Hydrogenous Polymorphs. Both polymorphs of IN_2–OA repeatedly co-crystallise from the same solution, which for the current experiments was water or a mixture of water and ethanol. Form I tends to crystallise prior to Form II. The two forms are easily distinguishable by their morphology, blocks or plates in case of Form I and sticks or needles in case of Form II.

IN_2–OA Form I: IN (156 mg, 1.28 mmol) and OA · $2H_2O$ (80 mg, 0.63 mmol) were dissolved in water (~20 mL) and block shaped crystals were obtained during evaporation of the water. A crystal with the approximate dimensions ($3 \times 2 \times 2$ mm^3) for the single crystal neutron diffraction experiment was obtained from a solution of IN (150 mg, 1.23 mmol) and OA · $2H_2O$ (88 mg, 0.70 mmol) in water – ethanol (1 : 1).

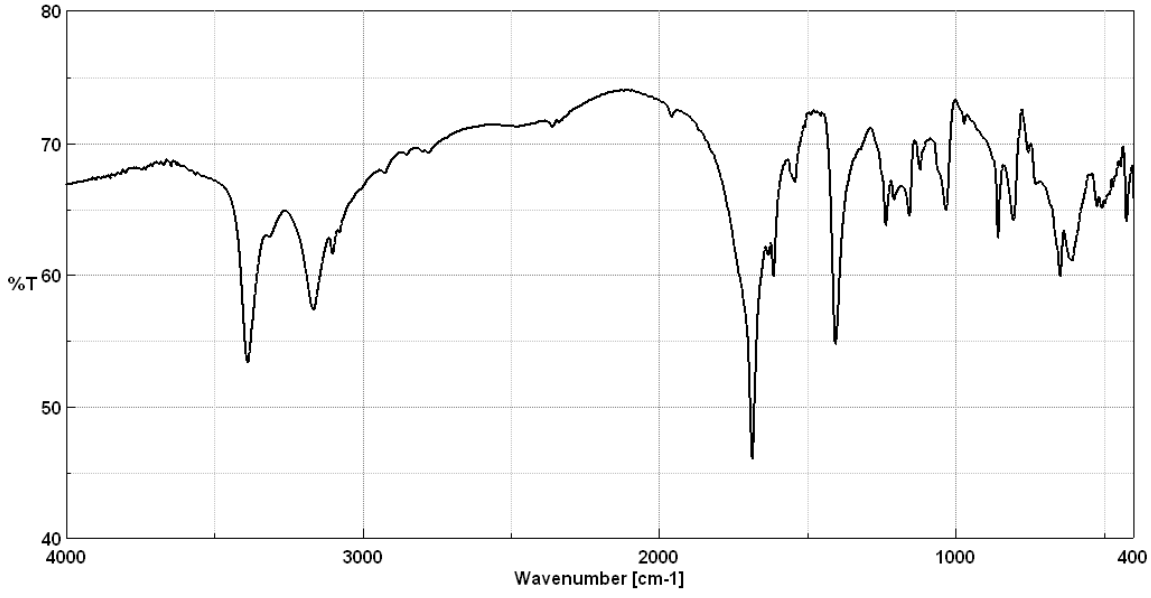

Figure A-1: IR spectrum (KBr) of IN_2–OA Form I. 3388 + 3168 (m) N–H stretch; 3102 (w) C–H stretch; 1685 (s) C=O stretch; 1615 + 1542 (w) N–H bend; 1406 (s) C–N stretch; 1236 (m) C–O stretch; 857 (m) C–H bend; absorption bands for the HBs could not be assigned unambiguously. N–H···O HBs ~3200–2800; O··H··N HB disappeared in continuum?

IN_2–OA Form II: IN (160 mg, 1.31 mmol) and OA · $2H_2O$ (84 mg, 0.67 mmol) were dissolved in water – ethanol (1 : 1) (~20 mL) to yield stick shaped crystals during

evaporation of the solvent. Growing a crystal of sufficient size for the single crystal neutron diffraction experiment required seeding a saturated solution of IN (182 mg, 1.49 mmol) and OA · $2H_2O$ (90 mg, 0.71 mmol) in water with a small specimen. A stick shaped (several centimetres long) but multi-domain crystal was obtained after a couple of weeks during evaporation of the water. Two fragments with the approximate dimensions $1.5 \times 0.8 \times 0.6$ mm^3 and $0.8 \times 0.6 \times 0.4$ mm^3 were separated from this specimen and used for data collection.

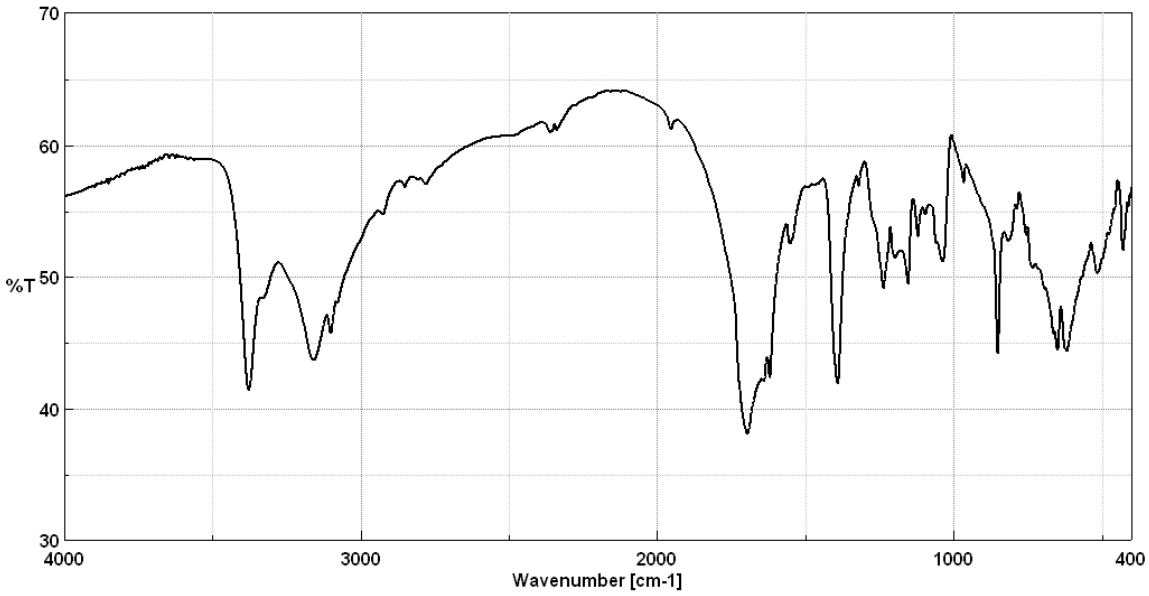

Figure A-2: IR spectrum (KBr) of IN_2–OA Form II. 3379 + 3160 (m) N–H stretch; 3102 (w) C–H stretch; 1697 (s) C=O stretch; 1620 + 1552 (w) N–H bend; 1392 (s) C–N stretch; 1237 (m) C–O stretch; 851 (s) C–H bend; absorption bands for the HBs could not be assigned unambiguously. N–H···O HBs ~3200–2800; O··H··N HB disappeared in continuum?

3.2 Deuterated Polymorphs. As for the hydrogenous forms IN_2–OA, the deuterated forms IN_2–d-OA co-crystallise from D_2O or mixtures of D_2O and deuterated ethanol (C_2H_5OD). All experiments carried out to date yielded a large excess of Form I over Form II. Co-crystallising IN and OA from a mixture of H_2O – D_2O (1 : 1) yields crystals of initially IN_2–d-OA Form I, and later of IN_2–OA Form I.

IN_2–d-OA Form I and *IN_2–d-OA Form II*: The single crystals for both forms have been obtained from the same experiment. IN (30 mg, 0.25 mmol) and OA · $2H_2O$ (15 mg, 0.12 mmol) were dissolved in D_2O (~4 mL) to yield stick shaped crystals of Form I and plate shaped crystals of Form II. Elemental analysis (theoretical values in parenthesis): C 49.53 % (49.41), H 4.11 % (4.11), N 16.29 % (16.46).

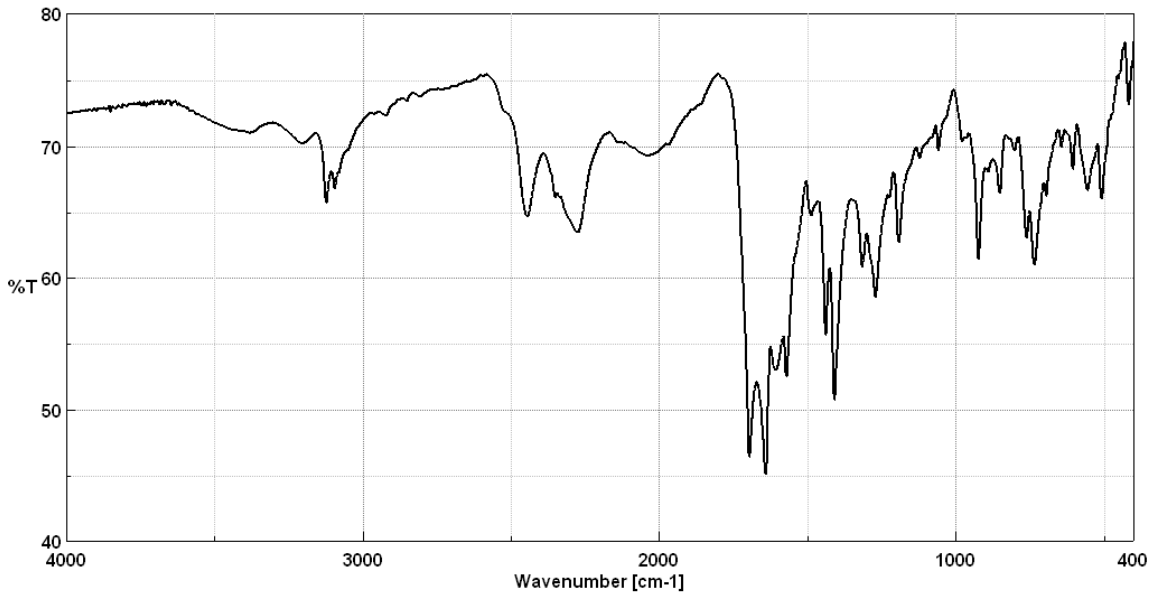

Figure A-3: IR spectrum (KBr) of IN_2–d-OA Form I. 3123 + 3095 (w) C–H stretch; 2445 + 2277 (m) N–D stretch; 2040 (br) N–D···O HB; 1696 (s) C=O amide stretch; 1640 (s) CO_2^- asymmetric stretch; 1607 + 1572 (w) N–D bend; 1439 (s) CO_2^- symmetric stretch; 1409 (s) C–N stretch.

Chapter 4 – *Imaging the Electron Density of Hydrogen in Strong Hydrogen Bonds*:

PCP–4-methylpyridine: PCP (104 mg, 0.39 mmol) was dissolved in chloroform (~2 mL), 4-methylpyridine (40 mg, 0.43 mmol) was added afterwards and crystals in the shape of long plates were obtained.

Dinicotinic acid: recrystallised from ethanol – water (3 : 1).

Chapter 5 – *Design of Strongly Hydrogen Bonded Materials*:

5.1 Pentachlorophenol – Dimethylpyridine Complexes. All complexes can be obtained from various solvents such as methanol, ethanol, chloroform, carbon tetrachloride, and mixtures thereof (volumes range from 2–4 mL); except for PCP_2–3,5-lutidine–H_2O where the presence of water and an appropriate co-solvent is required. The two polymorphic forms of PCP–2,6-lutidine readily and repeatedly co-crystallise from the same batch and are visually indistinguishable.

PCP–3,5-lutidine: PCP (102 mg, 0.38 mmol) was dissolved in carbon tetrachloride, 3,5-lutidine (50 mg, 0.47 mmol) was then added to this solution and thin plates were obtained during evaporation of the solvent. As a side note, the solubility of this material is low in comparison to the other PCP – lutidine complexes. If the concentration of the reactants is sufficiently high, crystals of PCP–3,5-Lutidine form almost immediately in pure form upon addition of the 3,5-lutidine. Due to the highly disordered structure the elemental analysis is given here (theoretical values in parenthesis): C 41.76 % (41.76), H 2.63 % (2.67), N 3.76 % (3.74).

PCP–2,5-lutidine: PCP (106 mg, 0.40 mmol) was dissolved in carbon tetrachloride, an excess of 2,5-lutidine (100 mg, 0.93 mmol) was added and needle shaped crystals were

obtained after evaporation of the solvent. The excess of 2,5-lutidine is required to prevent formation of PCP_2–2,5-Lutidine.

PCP–3,4-lutidine: PCP (100 mg, 0.38 mmol) was dissolved in chloroform and an excess of 3,4-lutidine (100 mg, 0.93 mmol) was added afterwards to obtain plate like crystals. The excess of 3,4-lutidine is required to prevent formation of PCP_2–3,4-Lutidine.

PCP–2,3-lutidine: PCP (64 mg, 0.24 mmol) was dissolved in chloroform, 2,3-lutidine (24 mg, 0.22 mmol) was added and block shaped crystals were obtained.

PCP–2,6-lutidine Form I: PCP (82 mg, 0.31 mmol) was dissolved in ethanol and 2,6-lutidine (36 mg, 0.34 mmol) added. Long plate/stick shaped crystals were obtained.

PCP–2,6-lutidine Form II: PCP (102 mg, 0.38 mmol) was dissolved in ethanol and 2,6-lutidine (40 mg, 0.37 mmol) added. Long plate/stick shaped crystals were obtained.

PCP–2,4-lutidine: PCP (94 mg, 0.35 mmol) was dissolved in ethanol, 2,4-lutidine (~40 mg, 0.37 mmol) was added afterwards, and block shaped crystals were obtained.

PCP_2–3,5-lutidine–H_2O: PCP (78 mg, 0.29 mmol) was dissolved in a mixture of ethanol and water (~2 : 1), 3,5-lutidine was added (30 mg, 0.28 mmol) and stick shaped crystals were obtained during evaporation of the solvent. PCP_2–3,5-Lutidine–H_2O has, like PCP–3,5-lutidine, a comparably low solubility.

PCP_2–2,5-lutidine: PCP (66 mg, 0.25 mmol) was dissolved in ethanol, and 2,5-lutidine (22 mg, 0.21 mmol) was added afterwards. Block shaped crystals were obtained.

PCP_2–3,4-lutidine: PCP (98 mg, 0.37 mmol) was dissolved in ethanol, and 3,4-lutidine (28 mg, 0.26 mmol) was added afterwards. Block shaped crystals were obtained.

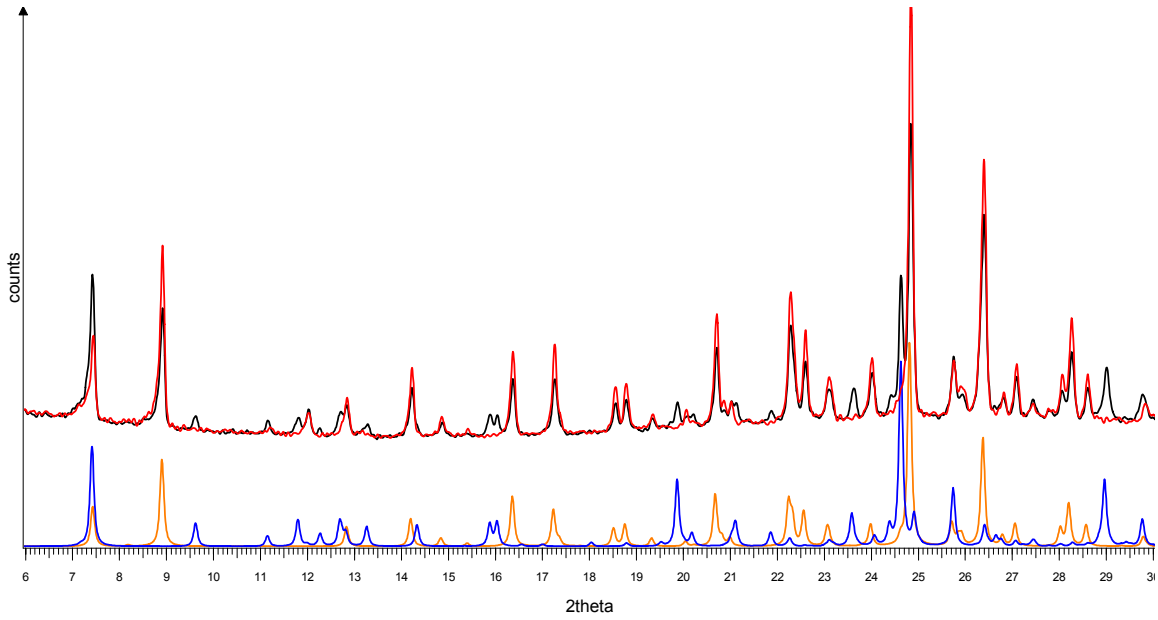

Figure A-4: X-ray powder patterns of the PCP–2,6-lutidine polymorphs showing a mixture of Form I and Form II (black), the same sample measured after 12 h shows Form I only (red). Simulated powder patterns of Form I (orange) and Form II (blue) from single crystal X-ray data.

PCP–3,5-lutidine

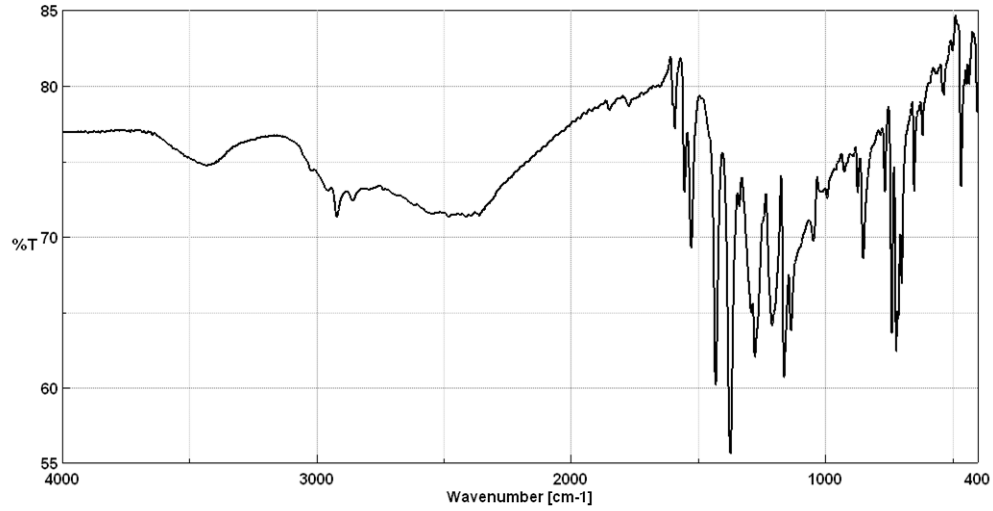

PCP–2,5-lutidine

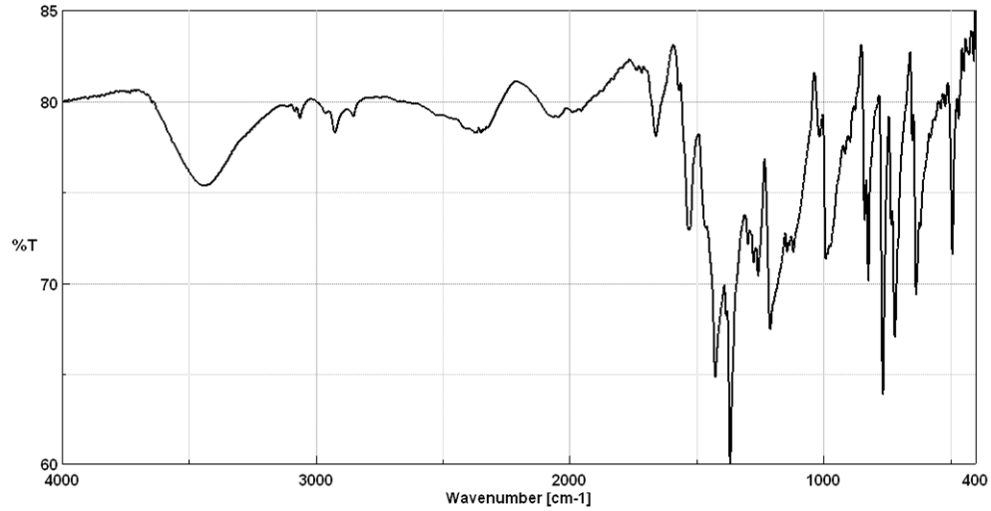

PCP–3,4-lutidine

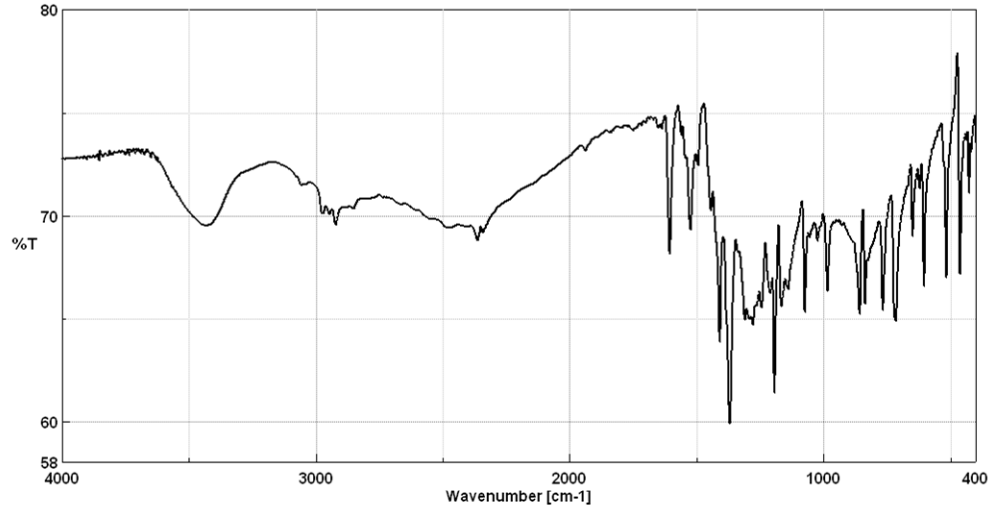

PCP–2,3-lutidine

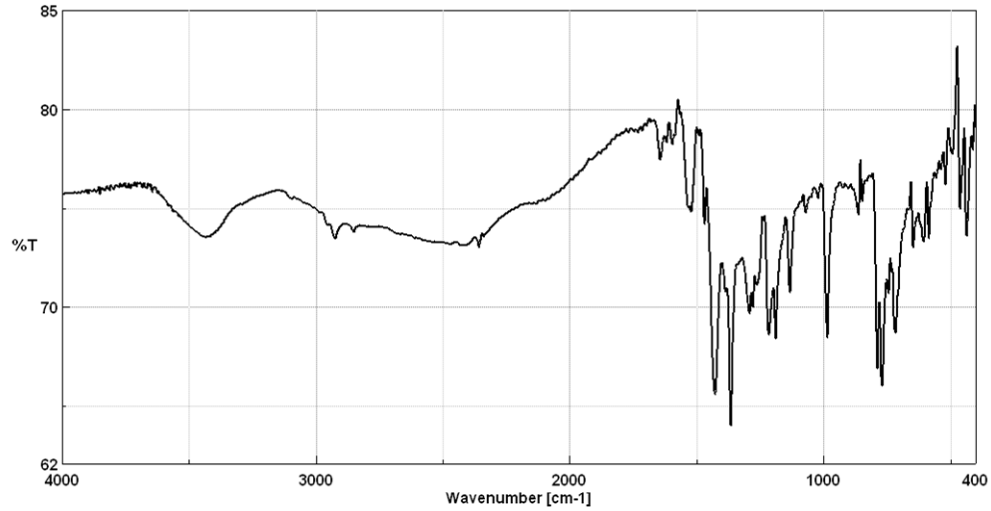

PCP–2,6-lutidine

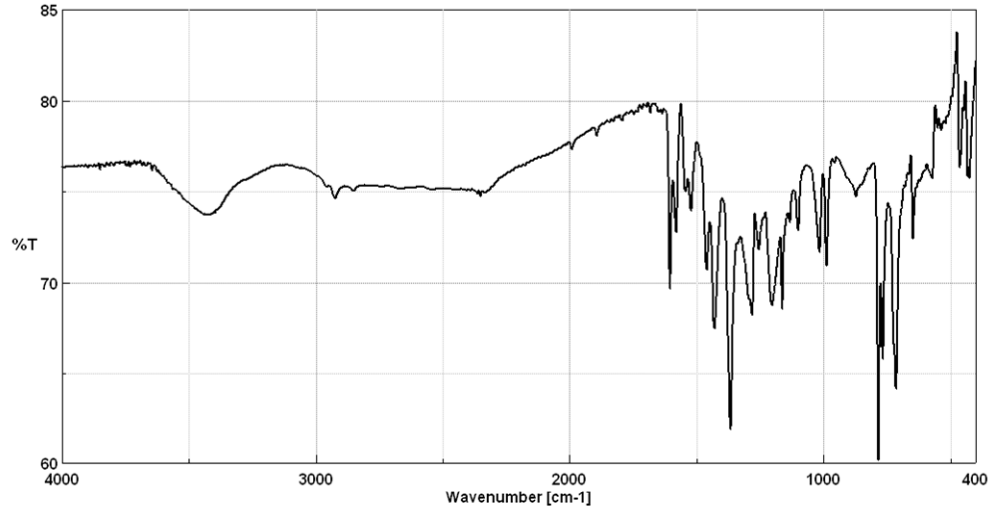

PCP–2,4-lutidine

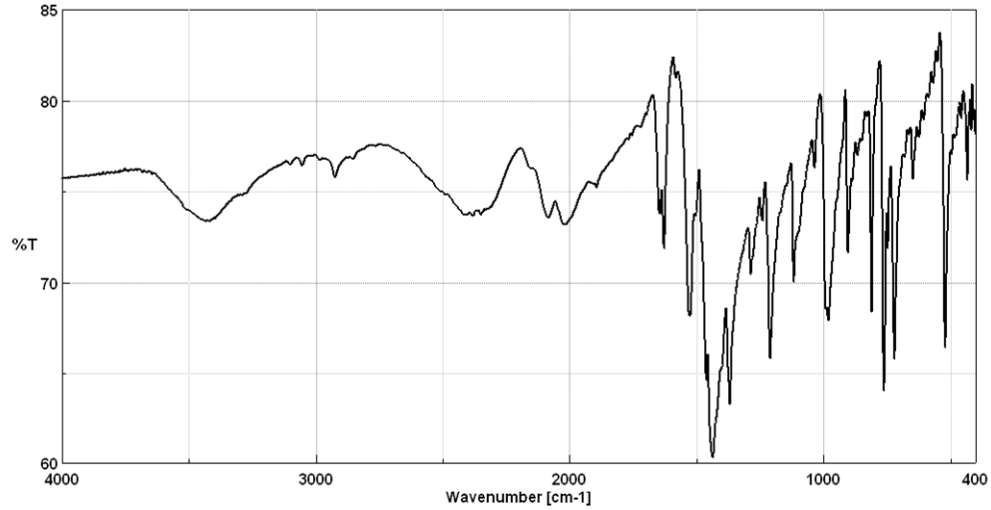

Figure A-5: IR spectra (KBr) of the (1 : 1) PCP – lutidine complexes for reference. Absorption bands for the HBs could not be assigned unambiguously; the H transfer complexes PCP–2,5-lutidine and PCP–2,4-lutidine differ from the neutral complexes in a pronounced absorption ~2370 (br) and ~2050 (br) corresponding to N–H···O HB? O–H··N HB disappeared in continuum?

5.2 Carboxylic Acid – Dimethylpyridine Complexes.

OA–3,5-lutidine: OA · $2H_2O$ (30 mg, 0.24 mmol) was dissolved in ethanol, and 3,5-lutidine (52 mg, 0.49 mmol) was added. Crystals in the shape of long plates were obtained.

OA–2,5-lutidine: OA · $2H_2O$ (30 mg, 0.24 mmol) was dissolved in ethanol, and 2,5-lutidine (56 mg, 0.52 mmol) was added afterwards to yield plate shaped crystals.

OA–(3,4-lutidine)$_2$–H_2O: OA · $2H_2O$ (30 mg, 0.24 mmol) was dissolved in ethanol, and 3,4-lutidine (50 mg, 0.47 mmol) was added afterwards. Block shaped crystals were obtained. The use of water free OA resulted also in crystallisation of the hydrated complex.

OA–2,3-lutidine: OA · $2H_2O$ (30 mg, 0.24 mmol) was dissolved in ethanol, 2,3-lutidine (52 mg, 0.49 mmol) was added afterwards, and plate shaped crystals were obtained.

FA–(3,5-lutidine)$_2$: FA (30 mg, 0.26 mmol) was dissolved in *iso*-propanol, and 3,5-lutidine (60 mg, 0.56 mmol) was added. Plate shaped crystals of FA–(3,5-lutidine)$_2$ were obtained, and, as a side product, block shaped crystals of N-succino-3,5-dimethylpyridine.

FA–(3,4-lutidine)$_2$: FA (32 mg, 0.28 mmol) was dissolved in ethanol, and 3,4-lutidine (70 mg, 0.65 mmol) was added. Block shaped crystals were obtained. A phase transition (not single crystal to single crystal) was observed at a temperature of about 116 K.

FA–(2,3-lutidine)$_2$: FA (30 mg, 0.26 mmol) was dissolved in ethanol, 2,3-lutidine (54 mg, 0.50 mmol) was added, and stick shaped crystals were obtained.

FA–2,4-lutidine–H_2O: FA (30 mg, 0.26 mmol) was dissolved in *iso*-propanol, and 2,4-lutidine (60 mg, 0.56 mmol) was added afterwards to yield block shaped crystals.

5.3 Pentachlorophenol – 1,4-Diazabicyclo[2.2.2]octane. The complexes described here co-crystallise also from ethanol, and as for the PCP – lutidine complexes probably also from a large variety of other solvents.

PCP–DABCO: PCP (72 mg, 0.27 mmol) and DABCO (32 mg, 0.29 mmol) were dissolved in chloroform, and crystals with block or plate shaped morphology were obtained. Crystals of this material crack upon cooling between 150 and 100 K.

PCP$_2$–DABCO: PCP (76 mg, 0.29 mmol) and DABCO (14 mg, 0.13 mmol) were dissolved in chloroform, and plate shaped crystals were obtained.

PCP$_3$–DABCO$_2$: PCP (68 mg, 0.26 mmol) and DABCO (12 mg, 0.11 mmol) were dissolved in water – ethanol (1 : 1), and crystals with block shaped morphology were obtained.

B. CRYSTALLOGRAPHY

The X-ray structures presented in this work were measured on the in-house diffractometers, the CCD detector systems Bruker AXS X8 Apex II and Bruker AXS KappaCCD2000 (both equipped with a 4-circle Kappa goniometer, $Mo_{K\alpha}$ radiation, graphite monochromator), and the image plate diffractometer Rigaku R-Axis Rapid IP (3-circle goniometer, $Mo_{K\alpha}$ radiation, graphite monochromator). The data collection and data processing were performed using the instrument specific software suites summarised in the following:

Bruker AXS X8 Apex II (short Apex II): The data were collected using the latest available version of the APEX2[113] suite, integrated with SAINT[74] and scaled and corrected for absorption with SADABS.[75]

Bruker AXS KappaCCD2000 (short KappaCCD): The data were collected with COLLECT,[114] integrated with DENZO[115] and scaled and corrected for absorption with SADABS.

Rigaku R-Axis Rapid IP (short Rapid IP): The data were collected and integrated with FSPROCESS[116] or TWINSOLVE[117] (both embedded in the CRYSTALCLEAR[118] suite), and scaled and corrected for absorption using FSPROCESS, or SADABS in case of data integration with TWINSOLVE.

The crystal structures were solved with SHELXS and refined with SHELXL, both from reference [39]. Unless stated otherwise the atomic parameters (3 positional and 6 displacement parameters) of the non H atoms were refined, no restraints or constraints have been applied; the refinement of the H parameters was not performed uniformly and the treatment of the H atoms is addressed in the corresponding chapters. An extinction parameter was refined if there was evidence for extinction, i.e. $F_{obs} < F_{calc}$ for strong reflections.

The X-ray charge density experiments were carried out on the Bruker AXS X8 Apex II diffractometer. Details for processing and refining the X-ray charge density data can be found in 3.1.3 *Charge Density Studies*.

The single crystal neutron diffraction experiments were carried out on the instruments SXD and VIVALDI located at the central facilities ISIS, Oxfordshire, and ILL, Grenoble respectively. Details for data collection and data processing can be found in 3.1.2 *Neutron Studies*.

The crystallographic figures were generated with XP[119] (ellipsoid plots) and MERCURY[120] (packing diagrams and HB schemes). The difference Fourier maps were calculated with WINGX and generated with MAPVIEW, both from reference [121]. The graphics in 3.1.3 *Charge Density Studies* were generated with XD[40] and MAPVIEW.

The following tables contain the crystallographic data for the crystal structures presented in this work. Additional information can be obtained from the crystallographic information files (CIF) provided in electronic form in the supplementary CD.

Table B-1: Crystallographic data for IN_2–OA and IN_2–d-OA (X-ray). Chapter 3 *Molecular Complexes of Isonicotinamide with Oxalic Acid*.

	IN_2–OA Form I			IN_2–OA Form II			IN_2–d-OA Form I	IN_2–d-OA Form II	
	100 K	RT	charge density	100 K	RT	charge density		supercell	small cell
Diffractometer	Apex II	Apex II	Apex II*	Apex II	Apex II	Apex II*	Apex II	Apex II	Apex II
Formula	$C_{14}H_{14}N_4O_6$	$C_{14}H_{14}N_4O_6$	$C_{14}H_{14}N_4O_6$	$C_{14}H_{14}N_4O_6$	$C_{14}H_{14}N_4O_6$	$C_{14}H_{14}N_4O_6$	$C_{14}H_8D_6N_4O_6$	$C_{14}H_8D_6N_4O_6$	$C_{14}H_8D_6N_4O_6$
M / g·mol^{-1}	334.29	334.29	334.29	334.29	334.29	334.29	340.33	340.33	340.33
T / K	100	293	100	100	293	100	100	100	100
space group	C2/c	C2/c	C2/c	$P\bar{1}$	$P\bar{1}$	$P\bar{1}$	$P\bar{1}$	$P\bar{1}$	$P\bar{1}$
a / Å	11.6911(12)	11.8864(12)	11.6680(5)	3.6811(7)	3.7561(4)	3.6706(4)	3.7233(3)	6.9765(7)	6.9761(7)
b / Å	9.9945(10)	10.0295(9)	9.9799(4)	7.5913(15)	7.6527(7)	7.6027(8)	7.4294(5)	8.1978(8)	7.3063(6)
c / Å	12.1366(12)	12.2411(11)	12.1407(5)	12.455(2)	12.5120(12)	12.4780(12)	12.3158(10)	13.1421(10)	8.1980(8)
α / °				85.631(9)	85.702(5)	85.523(4)	98.262(4)	106.725(5)	67.428(5)
β / °	102.743(5)	101.432(4)	102.747(2)	87.850(10)	87.832(6)	88.193(4)	90.019(4)	92.458(5)	74.833(6)
γ / °				84.221(10)	85.468(6)	84.252(5)	91.709(5)	105.171(6)	63.972(5)
V / Å^3	1383.2(2)	1430.4(2)	1378.89(10)	345.10(11)	357.33(6)	345.31(6)	336.99(4)	689.04(11)	344.51(6)
Z	4	4	4	1	1	1	1	2	1
ρ_{calc} / g·cm^3	1.605	1.552	1.610	1.609	1.553	1.608	1.677	1.640	1.640
μ / mm^{-1}	0.128	0.124	0.129	0.128	0.124	0.128	0.131	0.129	0.129
θ range / °	2.71 – 33.97	2.68 – 33.72	2.715 – 59.114	1.64 – 34.09	1.63 – 33.95	1.637 – 58.049	1.67 – 33.99	1.63 – 34.11	2.71 – 34.03
refln (meas. / indep.)	10080 / 2782	13102 / 2710	62005 / 9393	8196 / 2773	8325 / 2829	64585 / 8857	10173 / 2744	14726 / 5595	7354 / 2799
R_{int}	0.0299	0.0302	0.0275	0.0217	0.0207	0.0252	0.0216	0.0320	0.0240
refln (obs. $I > 2\sigma(I)$)	2541	1935	7817	2354	2063	7501	2505	3329	2265
completeness / %	98.5	94.8	92.4	98.1	97.9	90.0	100.0	98.9	99.3
data / restr. / param.	2782 / 0 / 136	2710 / 0 / 136	7817 / 0 / 354	2773 / 0 / 137	2829 / 0 / 137	7501 / 0 / 353	2744 / 0 / 138	5595 / 0 / 273	2799 / 0 / 141
GooF on F^2	1.088	1.059	1.336 (on F)	1.051	1.093	0.997 (on F)	1.112	1.005	1.036
R_1 (obs / all)	0.0356 / 0.0383	0.0460 / 0.0684	0.0159 / 0.0302	0.0405 / 0.0474	0.0472 / 0.0650	0.0150 / 0.0274	0.0344 / 0.0373	0.0462 / 0.0860	0.0399 / 0.0518
wR_2 (obs / all)	0.1085 / 0.1110	0.1256 / 0.1432		0.1157 / 0.1220	0.1337 / 0.1484		0.0953 / 0.0981	0.1178 / 0.1423	0.1008 / 0.1089
ρ (max / min) / e·Å^{-3}	0.593 / -0.413	0.380 / -0.295	0.155 / -0.146	0.633 / -0.510	0.411 / -0.315	0.139 / -0.126	0.542 / -0.278	0.588 / -0.289	0.565 / -0.259

* multipole refinement with XD against $F_{obs} > 4\sigma(F_{obs})$

Table B-2: Crystallographic data for the hydrogenous forms IN_2–OA (neutron). Chapter 3 *Molecular Complexes of Isonicotinamide with Oxalic Acid*.

	IN_2–OA Form I					IN_2–OA Form II		
	30 K	100 K	200 K	300 K	350 K	100 K	200 K	RT
Diffractometer	SXD*	SXD*	SXD*	SXD*	SXD*	VIVALDI†	VIVALDI†	VIVALDI†
Formula	$C_{14}H_{14}N_4O_6$	$C_{14}H_{14}N_4O_6$	$C_{14}H_{14}N_4O_6$	$C_{14}H_{14}N_4O_6$	$C_{14}H_{14}N_4O_6$	$C_{14}H_{14}N_4O_6$	$C_{14}H_{14}N_4O_6$	$C_{14}H_{14}N_4O_6$
M / g·mol^{-1}	334.29	334.29	334.29	334.29	334.29	334.29	334.29	334.29
T / K	30	100	200	300	350	100	200	295
space group	C2/c	C2/c	C2/c	C2/c	C2/c	P $\bar{1}$	P $\bar{1}$	P $\bar{1}$
a / Å	11.681(3)	11.720(5)	11.802(3)	11.916(3)	11.964(2)	3.680(3)	3.720(3)	3.760(4)
b / Å	10.009(3)	10.014(6)	10.029(3)	10.043(3)	10.051(2)	7.595(6)	7.626(11)	7.659(8)
c / Å	12.170(3)	12.187(6)	12.225(3)	12.265(3)	12.291(3)	12.501(9)	12.524(7)	12.52(3)
α / °						85.69(5)	85.71(12)	85.66(12)
β / °	103.036(17)	102.70(3)	102.060(18)	101.308(14)	100.918(14)	88.01(5)	87.94(3)	87.81(8)
γ / °						84.22(4)	84.74(4)	85.46(10)
V / Å^3	1386.2(7)	1395.3(12)	1415.0(7)	1439.3(6)	1451.3(5)	346.5(5)	352.6(6)	358.3(9)
Z	4	4	4	4	4	1	1	1
ρ_{calc} / g·cm^3	1.602	1.591	1.569	1.543	1.530	1.602	1.574	1.549
μ / mm^{-1}								
λ range / Å	0.69 – 6.97	0.69 – 6.98	0.70 – 6.97	0.69 – 6.96	0.70 – 6.98	0.84 – 1.90	0.84 – 1.90	0.84 – 1.90
refln (meas. / indep.)	10063 / 10063	8486 / 8486	5899 / 5899	7332 / 7332	7943 / 7943	4633 / 1915	4355 / 1625	2806 / 1132
R_{int}	–	–	–	–	–	0.158	0.132	0.112
refln (obs. $I > 2\sigma(I)$)	10063	8486	5899	7332	7943	1365	1075	893
completeness / %								
data / restr. / param.	10063 / 0 / 178	8486 / 0 / 178	5899 / 0 / 178	7332 / 0 / 181	7943 / 0 / 184	1915 / 0 / 172	1625 / 0 / 172	1132 / 0 / 172
GooF on F^2	1.099	1.064	1.054	1.076	1.119	1.214	1.030	1.256
R_1 (obs / all)	0.0619 / 0.0619	0.0658 / 0.0658	0.0669 / 0.0669	0.0732 / 0.0732	0.0750 / 0.0750	0.0770 / 0.1195	0.0575 / 0.1258	0.0671 / 0.0951
wR_2 (obs / all)	0.1514 / 0.1514	0.1616 / 0.1616	0.1682 / 0.1682	0.1872 / 0.1872	0.1921 / 0.1921	0.1654 / 0.1750	0.1114 / 0.1253	0.1616 / 0.1709
ρ (max / min) / fm·Å^{-3}	3.481 / -2.530	2.581 / -2.088	2.006 / -1.439	1.393 / -1.162	1.244 / -0.931	1.672 / -1.503	0.704 / -0.726	0.769 / -0.811

* refinement against TOF multi-wavelength data; † refinement against wavelength normalised data, R_{int} from LAUENORM

Table B-3: Crystallographic data for PCP–4-methylpyridine and pyridine-3,5-dicarboxylic acid (dinicotinic acid). Chapter 4 *Imaging the Electron Density of Hydrogen in Strong Hydrogen Bonds*.

	PCP–4-methylpyridine	dinicotinic acid 100 K	dinicotinic acid RT
Diffractometer	Apex II	Apex II	Apex II
Formula	$C_{12}H_8Cl_5NO$	$C_7H_5NO_4$	$C_7H_5NO_4$
M / g·mol^{-1}	359.44	167.12	167.12
T / K	100	100	293
space group	$P\bar{1}$	$P2_1/c$	$P2_1/c$
a / Å	7.2614(4)	9.7139(8)	9.7006(6)
b / Å	8.9303(4)	11.1450(10)	11.1545(7)
c / Å	11.6312(6)	6.4750(6)	6.5859(5)
α / °	70.368(3)		
β / °	84.660(3)	108.481(6)	107.839(2)
γ / °	76.453(3)		
V / Å^3	690.55(6)	664.84(10)	678.37(8)
Z	2	4	4
ρ_{calc} / g·cm^3	1.729	1.670	1.636
μ / mm^{-1}	1.038	0.140	0.138
θ range / °	1.86 – 30.00	2.21 – 30.00	2.21 – 30.06
refln (meas. / indep.)	10140 / 4006	8604 / 1936	7163 / 1976
R_{int}	0.0183	0.0281	0.0189
refln (obs. $I > 2\sigma(I)$)	3492	1634	1461
completeness / %	99.4	99.9	99.4
data / restr. / param.	4006 / 0 / 177	1936 / 0 / 130	1976 / 0 / 129
GooF on F^2	1.061	1.045	1.051
R_1 (obs / all)	0.0251 / 0.0311	0.0386 / 0.0470	0.0417 / 0.0598
wR_2 (obs / all)	0.0611 / 0.0644	0.1035 / 0.1111	0.1123 / 0.1255
ρ (max / min) / fm·Å^{-3}	0.568 / -0.244	0.486 / -0.271	0.371 / -0.194

Table B-4: Crystallographic data for the PCP – lutidine complexes. Chapter 5.1 *Pentachlorophenol – Dimethylpyridine Complexes*.

	PCP–3,5-lutidine small cell	large cell	PCP–2,5-lutidine	PCP–3,4-lutidine	PCP–2,3-lutidine	PCP–2,6-lutidine Form I 100 K	200 K	RT
Diffractometer	Rapid IP*	Rapid IP†	Rapid IP*	Apex II‡	Apex II	Apex II	Apex II	Apex II
Formula	$C_{13}H_{10}Cl_5NO$	$C_{13}H_{10}Cl_5NO$	$C_{13}H_{10}Cl_5NO$	$C_{13}H_{10}Cl_5NO$	$C_{13}H_{10}Cl_5NO$	$C_{13}H_{10}Cl_5NO$	$C_{13}H_{10}Cl_5NO$	$C_{13}H_{10}Cl_5NO$
M / g·mol^{-1}	373.47	373.47	373.47	373.47	373.47	373.47	373.47	373.47
T / K	100	100	100	100	100	100	200	293
space group	$P\bar{1}$	$P\bar{1}$	$P2_1/c$	$P\bar{1}$	C2/c	$P\bar{1}$	$P\bar{1}$	$P\bar{1}$
a / Å	6.9077(14)	8.6882(11)	12.3582(3)	7.0777(9)	27.3366(14)	5.4813(3)	5.4966(3)	5.5125(2)
b / Å	8.6625(17)	12.9433(16)	7.1519(2)	8.3607(11)	7.0801(4)	11.4515(6)	11.5609(5)	11.6579(5)
c / Å	12.910(3)	26.788(3)	17.0553(6)	12.9544(18)	19.0097(10)	12.7614(7)	12.8025(6)	12.8697(6)
α / °	77.42(3)	99.376(9)		93.103(8)		68.164(3)	68.460(2)	68.777(2)
β / °	82.55(3)	97.132(9)	100.162(1)	102.685(7)	125.646(2)	82.613(3)	82.641(2)	82.591(2)
γ / °	88.70(3)	102.556(9)		100.184(7)		83.030(2)	83.249(2)	83.350(2)
V / Å^3	747.6(3)	2861.0(6)	1483.78(8)	732.62(17)	2989.9(3)	735.02(7)	748.30(6)	762.39(6)
Z	2	7.5	4	2	8	2	2	2
ρ_{calc} / g·cm^3	1.659	1.626	1.672	1.693	1.659	1.687	1.658	1.627
μ / mm^{-1}	0.963	0.943	0.970	0.982	0.963	0.979	0.962	0.944
θ range / °	3.19 – 27.48	2.43 – 30.00	3.10 – 30.00	1.62 – 30.36	2.64 – 33.86	1.73 – 33.73	1.72 – 33.69	1.70 – 33.73
refln (meas. / indep.)	14213 / 3392	29000 / 15914	29976 / 4305	4254 / 4254	19143 / 5993	21223 / 5864	21574 / 5938	22049 / 6072
R_{int}	0.0825	0.0654	0.0372	0.0421	0.0229	0.0233	0.0249	0.0252
refln (obs. $I > 2\sigma(I)$)	2460	7924	3429	3406	5028	4866	4381	3900
completeness / %	99.5	95.3	99.8	96.7	99.5	99.6	99.5	99.7
data / restr. / param.	3392 / 0 / 183	15914 / 0 / 737	4305 / 0 / 187	4254 / 0 / 188	5993 / 0 / 187	5864 / 0 / 187	5938 / 0 / 187	6072 / 0 / 187
GooF on F^2	1.073	1.025	1.110	0.962	1.069	1.038	1.029	1.015
R_1 (obs / all)	0.1185 / 0.1445	0.1054 / 0.1943	0.0323 / 0.0451	0.0391 / 0.0564	0.0258 / 0.0338	0.0274 / 0.0362	0.0331 / 0.0524	0.0378 / 0.0677
wR_2 (obs / all)	0.2837 / 0.3001	0.2398 / 0.2908	0.0705 / 0.0762	0.0893 / 0.0995	0.0622 / 0.0663	0.0708 / 0.0755	0.0800 / 0.0904	0.0938 / 0.1110
ρ (max / min) / fm·Å^{-3}	2.789 / -2.035	1.683 / -1.108	0.456 / -0.324	0.692 / -0.394	0.553 / -0.312	0.501 / -0.373	0.424 / -0.314	0.336 / -0.340

* processed with FSPROCESS; † processed with TWINSOLVE; ‡ twinned, data merged with TWINABS, R_{int} for singles and composites that include domain 1.

Table B-4 continued: Crystallographic data for the PCP – lutidine complexes. Chapter 5.1 *Pentachlorophenol – Dimethylpyridine Complexes*.

	PCP–2,6-lutidine Form II 100 K	200 K	RT	PCP–2,4-lutidine	PCP_2–3,5-lutidine–H_2O	PCP_2–2,5-lutidine	PCP_2–3,4-lutidine
Diffractometer	Apex II	KappaCCD	KappaCCD	Apex II	Apex II	Apex II	Apex II
Formula	$C_{26}H_{20}Cl_{10}N_2O_2$	$C_{26}H_{20}Cl_{10}N_2O_2$	$C_{26}H_{20}Cl_{10}N_2O_2$	$C_{13}H_{10}Cl_5NO$	$C_{19}H_{13}Cl_{10}NO_3$	$C_{19}H_{11}Cl_{10}NO_2$	$C_{19}H_{11}Cl_{10}NO_2$
M / g·mol^{-1}	746.94	746.94	746.94	373.47	657.80	639.79	639.79
T / K	100	200	293	100	100	100	100
space group	$P2_1/n$	$P2_1/n$	$P2_1/n$	$P2_1/n$	$Pna2_1$	$P\bar{1}$	$P\bar{1}$
a / Å	8.7761(6)	8.8153(18)	8.8601(18)	8.6844(16)	7.0199(6)	9.3420(5)	11.7771(5)
b / Å	14.2399(10)	14.337(3)	14.443(3)	13.449(3)	22.9038(18)	11.5145(7)	12.4154(5)
c / Å	23.7104(17)	23.909(5)	24.116(5)	12.804(2)	15.2538(12)	12.2668(8)	16.9000(7)
α / °						94.367(4)	76.399(2)
β / °	95.9480(10)	96.41(3)	96.97(3)	90.622(4)		104.227(3)	86.657(2)
γ / °						107.084(3)	85.458(2)
V / Å^3	2947.2(4)	3002.9(11)	3063.3(11)	1495.4(5)	2452.5(3)	1206.84(13)	2392.23(17)
Z	4	4	4	4	4	2	4
ρ_{calc} / g·cm^3	1.683	1.652	1.620	1.659	1.782	1.761	1.776
μ / mm^{-1}	0.977	0.959	0.940	0.962	1.162	1.175	1.186
θ range / °	2.40 – 33.73	1.66 – 30.00	1.65 – 27.00	2.20 – 33.96	1.60 – 29.99	1.74 – 30.00	1.24 – 30.00
refln (meas. / indep.)	41576 / 11757	37179 / 8745	24727 / 5960	22961 / 6043	16776 / 6359	20424 / 7029	38411 / 13942
R_{int}	0.0283	0.0456	0.0420	0.0256	0.0279	0.0287	0.0310
refln (obs. $I > 2\sigma(I)$)	9375	5896	3656	5008	5576	5609	11189
completeness / %	99.8	99.7	89.0	99.4	99.9	99.9	100.0
data / restr. / param.	11757 / 0 / 373	8745 / 0 / 373	5960 / 0 / 373	6043 / 0 / 187	6359 / 1 / 316	7029 / 0 / 299	13942 / 0 / 597
GooF on F^2	1.047	1.021	1.033	1.046	1.067	1.023	1.023
R_1 (obs / all)	0.0309 / 0.0435	0.0378 / 0.0733	0.0426 / 0.0885	0.0295 / 0.0392	0.0299 / 0.0380	0.0308 / 0.0429	0.0309 / 0.0435
wR_2 (obs / all)	0.0754 / 0.0820	0.0810 / 0.0934	0.0962 / 0.1150	0.0750 / 0.0799	0.0619 / 0.0658	0.0686 / 0.0747	0.0666 / 0.0722
ρ (max / min) / fm·Å^{-3}	0.559 / -0.295	0.321 / -0.237	0.228 / -0.205	0.563 / -0.295	0.375 / -0.355	0.439 / -0.372	0.467 / -0.341

Table B-5: Crystallographic data for the OA – lutidine and PCP – DABCO complexes. Chapter 5.2.1 *Oxalic Acid – Dimethylpyridine Complexes* and Chapter 5.3 *Pentachlorophenol – 1,4-Diazabicyclo[2.2.2]octane.*

	OA–3,5-lutidine	OA–2,5-lutidine	OA–(3,4-lutidine)$_2$–H_2O	OA–2,3-lutidine	PCP–DABCO	PCP_2–DABCO	PCP_3–$DABCO_2$
Diffractometer	Apex II	Apex II	Apex II	Apex II	Apex II	KappaCCD	Apex II
Formula	$C_{27}H_{33}N_3O_{12}$	$C_{18}H_{22}N_2O_8$	$C_{16}H_{24}N_2O_6$	$C_9H_{11}NO_4$	$C_{12}H_{13}Cl_5N_2O$	$C_{18}H_{14}Cl_{10}N_2O_2$	$C_{30}H_{27}Cl_{15}N_4O_3$
M / g·mol^{-1}	591.56	394.38	340.37	197.19	378.49	644.81	1023.31
T / K	100	100	100	100	150	100	100
space group	C2/c	$P\bar{1}$	$P\bar{1}$	C2/c	$P2_1/c$	$P2_1/n$	$P\bar{1}$
a / Å	14.5215(12)	10.4371(8)	7.0521(9)	11.9999(11)	8.6079(6)	21.7454(5)	9.0541(17)
b / Å	14.0201(11)	13.0973(9)	7.7009(9)	8.7348(8)	9.7567(6)	10.5638(3)	13.599(3)
c / Å	14.4366(12)	15.2677(12)	9.4263(13)	18.0392(16)	18.0930(12)	23.6823(6)	15.851(3)
α / °		67.417(4)	95.339(7)				84.957(5)
β / °	110.739(5)	85.319(4)	109.715(7)	90.288(3)	92.231(4)	115.3060(10)	85.050(4)
γ / °		77.296(4)	115.216(7)				85.692(4)
V / Å^3	2748.7(4)	1879.9(2)	418.80(9)	1890.8(3)	1518.38(17)	4918.1(2)	1932.3(7)
Z	4	4	1	8	4	8	2
ρ_{calc} / g·cm^3	1.429	1.393	1.350	1.385	1.656	1.742	1.759
μ / mm^{-1}	0.113	0.111	0.103	0.110	0.950	1.155	1.108
θ range / °	2.09 – 27.00	1.44 – 27.00	2.39 – 34.10	2.26 – 30.11	2.25 – 30.00	1.07 – 27.00	1.29 – 30.00
refln (meas. / indep.)	13222 / 3002	18561 / 8188	12406 / 3387	5442 / 2240	18344 / 4413	70611 / 10727	32729 / 11272
R_{int}	0.0480	0.0351	0.0221	0.0247	0.0357	0.0993	0.0319
refln (obs. $I > 2\sigma(I)$)	2243	5567	2894	1833	3259	7030	9297
completeness / %	100.0	99.7	98.4	80.2	99.8	99.9	100.0
data / restr. / param.	3002 / 0 / 208	8188 / 0 / 546	3387 / 0 / 123	2240 / 0 / 138	4413 / 0 / 186	10727 / 0 / 593	11272 / 0 / 481
GooF on F^2	1.043	1.017	1.042	1.049	1.014	1.024	1.025
R_1 (obs / all)	0.0398 / 0.0624	0.0443 / 0.0792	0.0372 / 0.0441	0.0378 / 0.0481	0.0342 / 0.0549	0.0420 / 0.0910	0.0286 / 0.0390
wR_2 (obs / all)	0.0864 / 0.0972	0.0968 / 0.1131	0.1060 / 0.1115	0.0921 / 0.0993	0.0721 / 0.0816	0.0654 / 0.0785	0.0670 / 0.0726
ρ (max / min) / fm·Å^{-3}	0.367 / -0.221	0.282 / -0.270	0.525 / -0.199	0.331 / -0.222	0.332 / -0.332	0.464 / -0.423	0.435 / -0.295

Table B-6: Crystallographic data for the FA – lutidine complexes. Chapter 5.2.2 *Fumaric Acid – Dimethylpyridine Complexes*.

	FA–(3,5-lutidine)$_2$		FA–(3,4-lutidine)$_2$		FA–(2,3-lutidine)$_2$		FA–2,4-lutidine–H_2O
	100 K	RT	150 K	RT	100 K	RT	
Diffractometer	KappaCCD	Apex II	Apex II	Apex II	Apex II	Apex II	Apex II
Formula	$C_{18}H_{22}N_2O_4$	$C_{18}H_{22}N_2O_4$	$C_{18}H_{22}N_2O_4$	$C_{18}H_{22}N_2O_4$	$C_{18}H_{22}N_2O_4$	$C_{18}H_{22}N_2O_4$	$C_{11}H_{15}NO_5$
M / g·mol^{-1}	330.38	330.38	330.38	330.38	330.38	330.38	241.24
T / K	100	293	150	293	100	293	293
space group	$P2_1/c$	$P2_1/c$	$P2_1/n$	$P2_1/n$	$P2_1/n$	$P2_1/n$	$P\bar{1}$
a / Å	8.2185(16)	8.3146(6)	12.2389(12)	12.3153(10)	9.9119(17)	9.8650(7)	6.9667(2)
b / Å	16.187(3)	16.4528(13)	5.1709(5)	5.1925(4)	7.0822(13)	7.3831(5)	7.1989(3)
c / Å	6.9014(14)	7.0952(6)	4.5153(15)	14.6437(12)	12.240(2)	12.3115(9)	12.4162(4)
α / °							90.163(2)
β / °	108.12(3)	108.626(4)	105.899(3)	105.672(5)	96.788(4)	96.725(2)	98.040(2)
γ / °							100.600(2)
V / Å^3	872.6(3)	919.77(13)	883.48(15)	901.61(13)	853.2(3)	890.53(11)	605.80(4)
Z	2	2	2	2	2	2	2
ρ_{calc} / g·cm^3	1.257	1.193	1.242	1.217	1.286	1.232	1.323
μ / mm^{-1}	0.089	0.085	0.088	0.086	0.091	0.088	0.105
θ range / °	2.61 – 27.18	2.48 – 26.97	1.93 – 33.75	1.92 – 29.99	2.50 – 33.97	2.51 – 30.02	1.66 – 29.98
refln (meas. / indep.)	12166 / 1932	8298 / 2001	15084 / 3511	11515 / 2630	18130 / 3451	11593 / 2597	9219 / 3507
R_{int}	0.0694	0.0368	0.0259	0.0254	0.0233	0.0278	0.0224
refln (obs. $I > 2\sigma(I)$)	1374	1168	2830	1954	2907	1759	2275
completeness / %	99.2	99.9	99.7	100.0	99.3	99.7	99.5
data / restr. / param.	1932 / 0 / 115	2001 / 0 / 115	3511 / 0 / 115	2630 / 0 / 116	3451 / 0 / 115	2597 / 0 / 115	3507 / 0 / 172
GooF on F^2	1.013	1.031	1.061	1.058	1.059	1.034	1.050
R_1 (obs / all)	0.0443 / 0.0767	0.0470 / 0.0957	0.0425 / 0.0538	0.0431 / 0.0587	0.0390 / 0.0471	0.0483 / 0.0731	0.0557 / 0.0855
wR_2 (obs / all)	0.0970 / 0.1121	0.1015 / 0.1251	0.1176 / 0.1278	0.1226 / 0.1350	0.1048 / 0.1126	0.1355 / 0.1575	0.1562 / 0.1792
ρ (max / min) / fm·Å^{-3}	0.205 / -0.190	0.177 / -0.131	0.464 / -0.179	0.211 / -0.149	0.585 / -0.201	0.213 / -0.157	0.385 / -0.186

C. LIST OF SCHEMES AND FIGURES

D. LIST OF TABLES

REFERENCES

[1] W. M. Latimer, W. H. Rodebush, *J. Am. Chem. Soc.* 1920, **42**, 1419-1433.

[2] M. L. Huggins, *J. Phys. Chem.* 1922, **26**, 601-625.

[3] G. A. Jeffrey, *An Introduction to Hydrogen Bonding*, Oxford University Press, Oxford, 1997.

[4] G. R. Desiraju, T. Steiner, *The Weak Hydrogen Bond in Structural Chemistry and Biology*, Oxford University Press, Oxford, 1999.

[5] S. J. Grabowski (ed.), *Hydrogen Bonding – New Insights*, Springer 2006.

[6] U. Koch, P. L. A. Popelier, *J. Phys. Chem.* 1995, **99**, 9747-9754.

[7] L. Pauling, *The Nature of the Chemical Bond*, Cornell University Press, New York, 3rd edition 1960.

[8] T. Steiner, *Angew. Chem. Int. Ed.* 2002, **41**, 48-76.

[9] C. M. Huggins, G. C. Pimental, *J. Chem. Phys.* 1955, **23**, 1244-1247.

[10] R. Taylor, O. Kennard, *J. Am. Chem. Soc.* 1982, **104**, 5063-5070.

[11] G. A. Jeffrey, H. Maluszynska, *Int. J. Biol. Macromol.* 1982, **4**, 173-185.

[12] M. W. Dougill, G. A. Jeffrey, *Acta Cryst.* 1953, **6**, 831-837.

[13] E. M. D. Keegstra, A. L. Spek, J. W. Zwikker, L. W. Jenneskens, *Chem. Commun.* 1994, 1633-1634.

[14] Z. Malarski, M. Rospenk, L. Sobczyk, E. Grech, *J. Phys. Chem.* 1982, **86**, 401-406.

[15] G. Zundel, *Adv. Chem. Phys.* 2000, **111**, 1-218.

[16] C. Flensburg, S. Larsen, R. F. Stewart, *J. Phys. Chem.* 1995, **99**, 10130-10141.

[17] E. Espinosa, E. Molins, C. Lecomte, *Chem. Phys. Lett.* 1998, **285**, 170-173.

[18] G. Gilli, P. Gilli, *J. Mol. Struct.* 2000, **552**, 1-15.

[19] M. L. Huggins, *J. Chem.* 1936, **40**, 723-731.

[20] J. M. Robertson, A. R. Ubbelohde, *Proc. Roy. Soc. A* 1939, **170**, 222-240.

[21] J. A. Gerlt, P. G. Gassman, *J. Am. Chem. Soc.* 1993, **115**, 11552–11568.

[22] C. C. Wilson, N. Shankland, A. J. Florence, *Chem. Phys. Lett.* 1996, **253**, 103-107.

[23] G. E. Bacon, R. S. Pease, *Proc. Roy. Soc. A* 1955, **230**, 359-381.

[24] S. Horiuchi, R. Kumai, Y. Tokura, *Angew. Chem. Int. Ed.* 2007, **46**, 3497-3501.

[25] T. Steiner, I. Majerz, C. C. Wilson, *Angew. Chem. Int. Ed.* 2001, **40**, 2651-2654.

[26] J. A. Cowan, J. A. K. Howard, G. J. McIntyre, S. M.-F. Lo, I. D. Williams, *Acta Cryst. B* 2003, **59**, 794-801.

[27] A. Parkin, S. M. Harte, A. E. Goeta, C. C. Wilson, *New. J. Chem.* 2004, **28**, 718-721.

[28] J. A. Cowan, J. A. K. Howard, G. J. McIntyre, S. M.-F. Lo, I. D. Williams, *Acta Cryst. B* 2005, **61**, 724–730.

[29] W. W. Bachovchin, *Magn. Reson. Chem.* 2001, **39**, S199-S213.

[30] G. K. H. Madsen, G. J. McIntyre, B. Schiøtt, F. K. Larsen, *Chem. Eur. J.* 2007, **13**, 5539-5547.

[31] I. Majerz, Z. Malarski, T. Lis, *J. Mol. Struct.* 1990, **240**, 47-58.

[32] J. Zhou, Y.-S. Kye, G. S. Harbison, *J. Am. Chem. Soc.* 2004, **126**, 8392-8393.

[33] M. Takasuka, H. Nakai and M. Shiro, *J. Chem. Soc. Perkin Trans. 2* 1982, 1061–1067.

[34] W. Kleber, H. J. Bautsch, J. Bohm, *Einführung in die Kristallographie*, Verlag Technik Berlin, Berlin, 18. Auflage 1998.

[35] W. Massa, *Kristallstrukturbestimmung*, Teubner Verlag, Wiesbaden, 5. Auflage 2007.

[36] C. Giacovazzo (ed.), *Fundamentals of Crystallography*, Oxford University Press, Oxford, 2nd edition 2002.

[37] C. C. Wilson, *Single Crystal Neutron Diffraction From Molecular Crystals*, World Scientific, 2000.

[38] P. Coppens, *Acta Cryst. B* 1974, **30**, 255-261.

[39] SHELXL/SHELXS: G. M. Sheldrick, *Acta Cryst. A* 2008, **64**, 112-122.

[40] XD2006: A. Volkov, P. Macchi, L. J. Farrugia, C. Gatti, P. Mallinson, T. Richter, T. Koritsanszky, 2006.

[41] N. K. Hansen, P. Coppens, *Acta Cryst. A* 1978, **34**, 909-921.

[42] P. Coppens, *X-ray Charge Densities and Chemical Bonding*, Oxford University Press, Oxford 1997.

[43] T. Koritsanszky, P. Coppens, *Chem. Rev.* 2001, **101**, 1583-1627.

[44] UIJXN: R. Blessing, *Acta Cryst. B* 1995, **51**, 816-823.

[45] SHADE: A. O. Madsen, H. O. Sørensen, R. F. Stewart, C. Flensburg, S. Larsen. *Acta Cryst. A* 2004, **60**, 550-561. http://shade.ki.ku.dk/

[46] D. Alfè, M. J. Gillan, G. D. Price, *Nature* 1999, **401**, 462-464.

[47] R. M. Martin, *Electronic Structure – Basic Theory and Practical Methods*, Cambridge University Press, Cambridge, 2004.

[48] A. D. Becke, *J. Chem. Phys.* 1993, **98**, 5648-5652.

[49] C. Lee, W. Yang, R. G. Parr, *Phys. Rev. B* 1988, **37**, 785-789.

[50] CASTEP: S. J. Clark, M. D Segall, C. J. Pickard, P. J. Hasnip, M. J. Probert, K. Refson, M. C. Payne, *Z. Kristallogr.* 2005, **220**, 567-570.

[51] CRYSTAL 2003: V. R. Saunders, R. Dovesi, C. Roetti, R. Orlando, C. M. Zicovich-Wilson, N. M. Harrison, K. Doll, B. Civalleri, I. J. Bush, Ph. D'Arco, M. Llunell.

[52] R. Car, M. Parrinello, *Phys. Rev. Lett.* 1985, **55**, 2471-2474.

[53] R. F. W. Bader, *Atoms in Molecules – A Quantum Theory*, Oxford University Press, Oxford, 1990.

[54] P. Popelier, *Atoms in Molecules – An Introduction*, Pearson Education, Harlow, 2000.

[55] C. Gatti, *Z. Kristallogr.* 2005, **220**, 399-457.

[56] R. F. W. Bader, C. Gatti, *Chem. Phys. Lett.* 1998, **287**, 233-238.

[57] Y. A. Abramov, *Acta Cryst. A* 1997, **53**, 264-272.

[58] R. F. W. Bader, H. Essen, *J. Chem. Phys.* 1984, **80**, 1943-1960.

[59] M. V. Vener, A. V. Manaev, A. N. Egorova, V. G. Tsirelson, *J. Phys, Chem. A* 2007, **111**, 1155-1162.

[60] P. Vishweshwar, A. Nangia, V.M. Lynch, *Cryst. Growth Des.* 2003, **3**, 783-790.

[61] M. C. Etter, *Acc. Chem. Res.* 1990, **23**, 120-126.

[62] M. Schmidtmann, M. J. Gutmann, D. S. Middlemiss, C. C. Wilson, *CrystEngComm* 2007, **9**, 743-745.

[63] F. H. Allen, *Acta Cryst. B* 2002, **58**, 380-388.

[64] A. Angeloni, A. G. Orpen, *Chem. Commun.* 2001, 343-344.

[65] C. J. Adams, P. C. Crawford, A. G. Orpen, T. J. Podesta, *Dalton Trans.* 2006, 4078–4092.

[66] I. Majerz, A. Koll, *Acta Cryst. B* 2004, **60**, 406-415.

[67] D. A. Keen, M. J. Gutmann, C. C. Wilson, *J. Appl. Cryst.* 2006, **39**, 714-722.

[68] L. Pauling, *J. Am. Chem. Soc.* 1947, **69**, 542-553.

[69] P. Coppens *et al*, *Acta Cryst. A* 1984, **40**, 184-195.

[70] Y. Miwa, T. Mizuno, K. Tsuchida, T. Taga, Y. Iwata, *Acta Cryst. B* 1999, **55**, 78-84.

[71] LAUEGEN: J. W. Campbell, Q. Hao, M. M. Harding, N. D. Nguti, C. Wilkinson, *J. Appl. Cryst.* 1998, **31**, 496-502.

[72] ARGONNE_BOXES (a modification of INTEGRATE+): C. Wilkinson, J. A. Cowan, D. A. A. Myles, F. Cipriani, G. J. McIntyre, *Neutron News* 2002, **13**, 37-41.

[73] LAUENORM: J. Campbell, J. Habash, J. R. Helliwell, K. Moffat, *Inf. Q. Protein Crystallogr.* 1986, **18**, 23-31.

[74] SAINT: Bruker AXS 2007.

[75] SADABS: G. M. Sheldrick, University of Göttingen 1997.

[76] SORTAV: R. H. Blessing, *Cryst. Rev.* 1987, **1**, 3-58.

[77] A. Volkov, Y. A. Abramov, P. Coppens, *Acta Cryst. A* 2001, **57**, 272-282.

[78] J. Overgaard, B. Schiøtt, F. K. Larsen, B. B. Iversen, *Chem. Eur. J.* 2001, **7**, 3756-3767.

[79] C. Gatti, F. Cargnoni, L. Bertini, *J. Comput. Chem.* 2003, **24**, 422-436.

[80] D. E. Hibbs, J. Overgaard, R. O. Piltz, *Org. Biomol. Chem.* 2003, **1**, 1191-1198.

[81] J. Sørensen, H. F. Clausen, R. D. Poulsen, J. Overgaard, B. Schiøtt, *J. Phys. Chem. A.* 2007, **111**, 345-351.

[82] J. P. Perdew, K. Burke, M. Ernzerhof, *Phys. Rev. Lett.* 1996, **77**, 3865-3868.

[83] J. P. Perdew, Y. Wang, *Phys. Rev. B* 1992, **45**, 13244-13249.

[84] 1D_SCHRODINGER: D. S. Middlemiss 2007.

[85] J. Poater, M. Solà, M. Duran, J. Robles, *Phys. Chem. Chem. Phys.* 2002, **4**, 722-731.

[86] S. Nosé, *J. Chem. Phys.* 1984, **81**, 511-519.

[87] W. G. Hoover, *Phys. Rev. A.* 1985, **31**, 1695-1697.

[88] S. F. Boys, F. Bernardi, *Mol. Phys.* 1970, **19**, 553-566.

[89] L. B. Jerzykiewicz, Z. Malarski, L. Sobczyk, T. Lis, E. Grech, *J. Mol. Struct.* 1998, **440**, 175-185.

[90] D. M. M. Farrell, G. Ferguson, A. J. Lough, C. Glidewell, *Acta Cryst. B* 2002, **58**, 272-288.

[91] D. M. M. Farrell, G. Ferguson, A. J. Lough, C. Glidewell, *Acta Cryst. B* 2002, **58**, 530-544.

[92] S. H. Dale, M. R. J. Elsegood, M. Hemmings, A. L. Wilkinson, *CrystEngComm* 2004, **6**, 207-214.

[93] Z. M. Jin, M. L. Hu, Z. G. Li, R. C. Xuan, K. B. Yu, *J. Chem. Crystallogr.* 2004, **34**, 567-660.

[94] A. Köroglu, A. Bulut, I. Ucar, G. S. Nichol, R. W. Harrington, W. Clegg, *Acta Cryst. C* 2005, **61**, o678-o680.

[95] Z. Malarski, I. Majerz, T. Lis, *J. Mol. Struct.* 1987, **158**, 369-376.

[96] F. Takusagawa, K. Hirotsu, A. Shimada, *Bull. Chem. Soc. Jpn.* 1973, **46**, 2292-2299.

[97] M. Schmidtmann, C. C. Wilson, *CrystEngComm* 2008, **10**, 177-183.

[98] G. Albrecht, G. Zundel, *J. Chem. Soc. Faraday Trans. 1* 1984, **80**, 553-561.

[99] I. Majerz, Z. Malarski, T. Lis, *J. Crystallogr. Spectrosc. Res.* 1989, **19**, 349-356.

[100] D. D. Perrin, *Dissociation Constants of Organic Bases in Aqueous Solution*, Butterworths, London, 1965 and Supplement 1972.

[101] A. J. Cessna, R. Grover, *J. Agric. Food Chem.* 1978, **26**, 289–292.

[102] K. Wozniak, T. M. Krygowski, B. Kariuki, W. Jones, *J. Mol. Struct.* 1991, **248**, 331-343.

[103] TWINABS: G. M. Sheldrick, University of Göttingen 2007.

[104] CELL_NOW: G. M. Sheldrick, University of Göttingen 2005.

[105] R. Lindemann, G. Zundel, *J. Chem. Soc. Faraday Trans. 2* 1977, **73**, 788-803.

[106] M. Currie, J. C. Speakman, N. A. Curry, *J. Chem. Soc. A* 1967, 1862-1869.

[107] D. A. Haynes, W. Jones, W. D. S. Motherwell, *CrystEngComm* 2006, **8**, 830-840.

[108] Y. J. Pan, Z. M. Jin, C. R. Sun, C. W. Jiang, *Chem. Lett.* 2001, **30**, 1008-1009.

[109] M. N. G. James, M. Matsushima, *Acta Cryst. B* 1976, **32**, 959-961.

[110] C. J. Burchell, C. Glidewell, A. J. Lough, G. Ferguson, *Acta Cryst. B* 2001, **57**, 201-212.

[111] D. Braga, L. Maini, G. de Sanctis, K. Rubini, F. Grepioni, M. R. Chierotti, R. Gobetto, *Chem. Eur. J.* 2003, **9**, 5538-5548.

[112] K. F. Bowes, G. Ferguson, A. J. Lough, C. Glidewell, *Acta Cryst. B* 2003, **59**, 100-117.

[113] APEX2: Bruker AXS 2007.

[114] COLLECT: Bruker AXS 1997-2004.

[115] DENZO: Z. Otwinowski, W. Minor 1997.

[116] FSPROCESS: T. Higashi 2001.

[117] TWINSOLVE: C. Svensson 2005.

[118] CRYSTALCLEAR: Rigaku/MSC 2006.

[119] XP: Bruker AXS 2000.

[120] MERCURY: C. F. Macrae, P. R. Edgington, P. McCabe, E. Pidcock, G. P. Shields, R. Taylor, M. Towler, J. van de Streek, *J. Appl. Cryst.* 2006, **39**, 453-457.

[121] WINGX/MAPVIEW: L. J. Farrugia, *J. Appl. Cryst.* 1999, **32**, 837-838.